Fission Product Diffusion in IG-110 Graphite

A DISSERTATION

Presented to the Faculty of the Graduate School

at the

University of Missouri

In Partial Fulfillment of the Requirements for the Degree of

Doctor of Philosophy

By:

TAYLOR M. WEILERT

Dr. John D. Brockman, Committee Chair

July 2022

The undersigned, appointed by the dean of the Graduate School, have examined the dissertation entitled:

FISSION PRODUCT DIFFUSION IN IG-110 GRAPHITE

Presented by TAYLOR M. WEILERT,

a candidate for the degree of Doctor of Philosophy,

and hereby certify that, in their opinion, it is worthy of acceptance.

_____

Dr. John D. Brockman

_____

Dr. Sudarshan K. Loyalka

_____

Dr. J. David Robertson

_____

Dr. C. Michael Greenlief

_____

Dr. Justin R. Walensky

ACKNOWLEDGEMENTS

First and foremost, I would like to extend my sincerest thanks to my advisor, Dr. John D. Brockman, for his support and patience throughout the years. Your understanding has always been appreciated even if not always acknowledged.

Dr. Sudarshan K. Loyalka and Dr. Kyle L. Walton have both provided incredible assistance on this project. Kyle especially has been of invaluable assistance, from designing and constructing parts of the diffusion cell to performing some stellar COMSOL modelling under a very strict time crunch. I truly appreciate his help and extend a very overdue thanks.

Both Jim Guthrie and Barry Higgins have been immensely helpful in all aspects of ICP-MS operation. Both have always been willing to take the time to help and, unfortunately for them, that means I'll likely be contacting them in the future. Thank you very much to both of you.

Ruth Ann Ngwenyama and Stacy Crane have both helped with performing irradiations and data workup and for that I thank them. I especially thank Ruth Ann for giving me so much of her time and patience.

Mike Glascock has always been willing to lend a helping hand and I sincerely thank him for his help over the years.

Finally, I would like to thank the engineers and machinists at the MURR Science Instrument Shop for fabricating many high-quality parts for this project and for their willingness to accommodate even the oddest of requests.

TABLE OF CONTENTS

LIST OF TABLES

LIST OF FIGURES

LIST OF ABBREVIATIONS

HTGR: High-Temperature Gas-Cooled Reactor

UNECE: United Nations Economic Commission for Europe

IEA: International Energy Agency

LWR: Light Water Reactor

TRISO: Tristructural Isotropic Fuel

PyC: Pyrolytic Carbon / Pyrocarbon

SiC: Silicon Carbide

BISO: Buffer Isotropic / Bistructural Isotropic

UCO: Uranium Oxycarbide

CVD: Chemical Vapor Deposition

MWt: Megawatt Thermal

MWe: Megawatt Electric

SMR: Small Modular Reactor

AVR: Arbeitsgemeinschaft Versuchsreaktor

FSV: Fort St. Vrain

THTR: Thorium Hochtemperatur Reaktor

HEU: Highly Enriched Uranium

LEU: Low Enriched Uranium

FIMA: Fissions per Initial Heavy Metal Atom

HTTR: High-Temperature Test Reactor

HTR-10: 10 MW High-Temperature Reactor

HTR-PM: High-Temperature Reactor Pebble-Bed Module

USNC: Ultra Safe Nuclear Corporation

MMR™: Micro Modular Reactor

DOE: Department of Energy

AGR: Advanced Gas Reactor Fuel Qualification and Development

FCM®: Fully Ceramic Microencapsulated

INL: Idaho National Laboratory

ATR: Advanced Test Reactor

ORNL: Oak Ridge National Laboratory

BWXT: BWX Technologies

ICP-MS: Inductively-Coupled Plasma Mass Spectrometry

INAA: Instrumental Neutron Activation Analysis

PTFE: Polytetrafluoroethylene

MURR: University of Missouri Research Reactor

LA-ICP-MS: Laser-Ablation-ICP-MS

FP: Fission Product

PIE: Post-Irradiation Examination

SEM: Scanning Electron Microscopy

MAE: Mean Absolute Value of the Error

ETAAS: Electrothermal Atomic Absorption Spectroscopy

TAVA: Time-Average Volume-Average

DTF: Designed to Fail

ASA: Active Surface Area

NL-DFT: Non-Local Density Functional Theory

NMR: Nuclear Magnetic Resonance

AAS: Atomic Absorption Spectroscopy

ICP-OES: ICP-Optical Emission Spectroscopy

NIST: National Institute of Standards and Technology

KED: Kinetic Energy Dispersion

LOD: Limit of Detection

HDPE: High Density Polyethylene

PCA: Principal Component Analysis

CRM: Certified Reference Material

ABSTRACT

The threat of global climate change and resultant disasters has never been higher. The promises made by many countries of carbon neutrality by 2050 will be impossible to achieve without nuclear technology. Global public support for nuclear energy is at its highest level in modern history but is still severely hampered by perceptions of safety and issues involving nuclear waste and proliferation. The Fukushima disaster of 2011 and the attack on Ukraine by the Russian Federation in 2022 only served to highlight the dangers of older reactor technology and the potential for large releases of radioactivity either by accident or intentional sabotage. For these reasons most countries have a keen interest in improved reactor technologies, particularly in regards to safety, as they plan to build, or continue building, their nuclear fleets.

Generation-IV reactors are characterized by improved safety, economics, and proliferation resistance compared to current light water reactor designs. The high-temperature gas-cooled reactor (HTGR) exemplifies these characteristics with the additional benefit of process heat production capabilities. Past and current demonstration reactors have proved the technical feasibility of the design and several future reactors are set to enter demonstration phases as early as the late 2020s. Despite strong performance in past and present reactors, there remains several unknown variables, particularly in regards to fission product behavior and transport under differing reactor conditions.

Due to the robust nature of the tristructural isotropic fuel particles used in HTGRs, as well as the large amount of graphite comprising the core, there is little risk of a reactor meltdown. Instead, the primary safety consideration of HTGRs is the release of

radioactive materials from the core, either during normal operation or an off-normal event. Most fission and activation products will be completely retained in either the fuel particle or the surrounding matrix graphite; a few, however, have a demonstrated ability to migrate through all core structures and deposit onto cooling system components. This poses a danger to reactor workers and, if the closed coolant circuit were to be compromised, the public. With that in mind, it is essential to fully understand the transport parameters of these select radionuclides in every component of the reactor core, including the core structural graphite.

This work has measured effective diffusion coefficients of Sr, Ag, Pd, Eu, and Cs in IG-110 structural graphite. A time-release method was utilized to measure these diffusion coefficients at temperatures up to 1973 K using an inductively-coupled plasma mass spectrometer. The effective diffusion coefficients here reported can be used to aid predictive fission product transport programs.

CHAPTER 1:
INTRODUCTION TO HTGRS

The majority of nations have set a goal of 2050 by which to achieve carbon neutrality [1]. Nuclear energy will play a vital role in meeting these carbon reduction goals with some organizations such as the United Nations Economic Commission for Europe (UNECE) and the International Energy Agency (IEA) indicating it may be impossible to do so without nuclear technology [2-3]. The UNECE projects that demand for nuclear generation will increase six-fold by 2050 without major societal, economic, or technological changes [2] while the IEA has reported that nuclear power generation capacity will have to double by 2050 in order to meet the 2 °C international warming goal [3]. The pressing need to reduce carbon emissions has contributed to a shift in global public opinions towards nuclear power. Among countries with long-term polling on public support of nuclear energy, most (5/7) showed increased public support for nuclear energy over the polling period [4]. France showed no change and only Japan showed decreased support.

While public favor has shifted in a positive direction, the public's concerns with nuclear energy remain focused on topics of nuclear waste, terrorism, and proliferation [4]. In contrast, safety remains one of the top priorities of the U.S. Nuclear Regulatory Commission [5]. Advanced nuclear reactor designs hold promise in mitigating all of these concerns and the high-temperature gas-cooled reactor (HTGR) is one of the most prevalent among them.

1.1. HTGR Fuel and Core Design

The fourth generation of nuclear reactors encompasses 6 designs, all of which offer improved economics, safety, proliferation resistance, and environmental performance compared to light water reactors (LWR) [6]. The HTGR is one of these 6 designs and is considered one of the nearest-term reactors with a strong technical feasibility thanks to 8 past and current demonstration reactors.

Whereas light water reactors use water as both coolant and neutron moderator HTGRs use He gas as coolant and a large mass of nuclear grade graphite as moderator. This combination offers numerous advantages. The He coolant is a single phase cooling medium and a highly inert gas thus avoiding chemical interactions with other reactor components [7]. He is also neutronically inert [8]. The large mass of graphite provides a high heat capacity and HTGRs have been described as "meltdown-proof" because of the graphite's ability to retain heat without sustaining damage; graphite does not undergo a phase change until approximately 4000 K, far beyond any projected temperature for HTGRs. Because cooling and neutron moderation are decoupled, HTGRs can accommodate a wide variety of fissile and fertile materials without significant modification to the core design [9].

HTGRs offer high thermal efficiencies with typical He exit temperatures of 700-950 °C. The safety and high-temperature capabilities of the HTGR are directly due to its fully ceramic core and robust fuel, the tristructural isotropic fuel (TRISO) particle. Early iterations of particle fuel used a UO_2 kernel of ~500 μm in diameter covered by a single layer of dense pyrolytic carbon (also called pyrocarbon or PyC). These particles

demonstrated a near complete failure rate under irradiation and were rapidly replaced by buffer-isotropic (BISO) fuel particles [10-11]. The name was later changed to bistructural-isotropic [12]. BISO fuel particles had an added sacrificial buffer layer of porous pyrocarbon between the fuel particle and the dense PyC. This layer accommodated fission gases and fission recoils and exhibited much improved performance over the single layer design. These particles, however, did not perform well at higher temperatures and burnups and were subsequently replaced by TRISO fuel particles. TRISO fuel expanded on the layering design of BISO particles and, in addition to the buffer and first PyC layers, included a layer of SiC and a second layer of dense PyC as the final layer. The addition of SiC meant TRISO particles were able to completely retain the vast majority of fission products produced in the kernel, even at high temperatures and burnups. The outer PyC layer was added to protect the SiC from compressive strain and provide a bonding layer for the matrix graphite component of the fuel elements. TRISO fuel particles with SiC as the main retention layer remain the industry standard for modern TRISO fuel. Alternative designs have been proposed and tested, the most common being the replacement of the SiC layer with ZrC. ZrC is not as susceptible to Pd-induced degradation as SiC and offers better high temperature performance [13]. This design is not favored, however, because of the lower oxidation resistance of ZrC and a more complicated fabrication procedure.

Modern TRISO particles use uranium oxicarbide (UCO) fuel kernels with a diameter of 350-600 μm [14-15]. UCO is a heterogenous mixture of UO_2, UC_2, and UC. UCO was adopted in favor of UO_2 as a means to limit CO production in the kernel while

maintaining the advantage of immobile oxide formation of most fission and activations products [13]. Excess CO in fuel kernels has been linked to degradation of SiC and movement of the fuel kernel across a temperature gradient [13]. UCO kernels are produced using an internal gelation sol-gel process [7]. Once formed and sintered, the UCO kernels are coated with the distinct TRISO layers using chemical vapor deposition (CVD) [7]. The buffer layer is formed by decomposition of acetylene while both PyC layers are formed by the decomposition of a mixture of acetylene and propylene. The SiC layer is formed by the decomposition of methyltrichlorosilane. All of the above coatings take place sequentially in the same fluidized bed. Final TRISO particle diameters are ~1 mm.

To fabricate the graphite fuel elements, TRISO particles are overcoated with matrix graphite powder and then mixed with additional matrix graphite powder and pressed into either a sphere or cylindrical compact. Afterwards the elements are heated to 800 °C in an inert atmosphere to carbonize the phenolic resin component of the matrix and finally annealed at a moderately high temperature, 1900-1950 °C for spheres and 1800 °C for compacts [7]. Matrix graphite acts as a further barrier to fission product release should a TRISO particle fail.

The two basic HTGR core designs are the pebble-bed core and the prismatic block core. These two designs use the above-mentioned fuel forms: the spheres are the fuel form for the pebble-bed reactors and the compacts make up the fuel for the prismatic core design. The pebble-bed design incorporates hundreds-of-thousands (the exact number depends on the power output and core size) of ~60 mm spherical fuel elements

stacked inside a structural graphite-lined core. Structural graphite makes up the side, top, and bottom reflectors; additionally, non-fueled structural graphite pebbles are added to the core before startup and then subsequently replaced with fueled spheres until a critical configuration is reached. The pebble-bed design offers the advantage of online refueling. Spherical fuel elements descend through the core and are then removed automatically and analyzed to assess their burnup. Fuel elements that have reached their specified burnup are permanently removed and stored and replaced with fresh fuel. This automatic refueling allows for very little excess reactivity and reduced U enrichment [7] while the lack of need for frequent reactor outages increase plant capacity factors.

Prismatic core designs utilize cylindrical fuel compacts stacked into a cylindrical graphite sleeve which is then inserted into interlocking hexagonal structural graphite blocks. Fueled blocks are placed in an annular configuration surrounding unfueled blocks and are in turn surrounded by more unfueled reflector blocks. The fueled blocks have additional pre-drilled holes to accommodate control rods and direct He flow. The advantage of the prismatic core design is economy of scale. Pebble-bed modules are limited in power to ~250 MWt per module vs up to 625 MWt per prismatic module [16]. For a full scale multi-module plant with a combined thermal capacity of ~2400-3000 MWt, this equates to 30% lower energy price for a prismatic design [16].

1.2. Matrix and Structural Graphite

Two distinct forms of graphite exist within an HTGR and both offer individual advantages. Matrix graphite is formed using a mixture of natural graphite, electro-

graphite, and a phenolic resin binder. The resulting material has a favorable complement of compressibility due to the natural graphite and toughness as a result of the synthetic graphite. In the fuel compacts, matrix graphite will initially be heated to 800 °C in an inert atmosphere followed by annealing at 1850-1950 °C [7]. The first heating serves to carbonize the resin binder and off-gas resulting volatile organic byproducts while the second helps to harden the matrix graphite and remove impurities. The matrix graphites A3-3 and A3-27 are two of the most studied matrix graphites for HTGRs as they were extensively used in the two German HTGRs. Each had a bulk density ~1.7 g/cm^3 [17]. Modern A3-3 matrix graphite has a bulk density ranging from 1.3-1.7 g/cm^3 [9, 18-19]. The heat treatment at 1850-1950 °C is not hot enough to graphitize the resin binder and as a result matrix graphite contains a high content of amorphous carbon [7]. This constituent is highly sorptive of metallic fission products such as Sr but not of fission gases. Matrix graphite also has a high ratio of interconnected porosity and consequently does not provide significant resistance to the diffusion of fission metals [7].

Structural graphite, sometimes called fuel element graphite, is composed of either pitch or petroleum coke and is graphitized at 2700-2900 °C. Forming methods include extrusion, vibrational molding, and isostatic pressing. Because of the much higher final treatment temperature, structural graphite is denser than matrix graphite and has a more ordered pore structure. The lack of amorphous carbon decreases the sorptivity of this material but the ordered structure means structural graphite is a better barrier to fission product diffusion than matrix graphite [20]. H-451 was the favored structural graphite in US demonstration HTGRs but its source materials are no longer available. Proposed

alternatives include NBG-17 and NBG-18 produced by SGL Carbon, PCEA from GrafTech International, and IG-430 and IG-110 from Toyo Tanso. The latter was the subject of this study. IG-110 is made from petroleum coke and is formed using a cold isostatic pressing process. It has a density of 1.76 g/cm^3 and a total porosity of ~22% [21].

1.3. Environmental, Economic, and Safety Advantages of the HTGR

Global carbon emissions by sector can be broken down as: electricity and heat production 25%; agriculture, forestry, and other land use 24%; buildings 6%; transportation 14%; industry 21%; and other energy 10% [22]. HTGRs can replace a majority of these emissions, either through direct production of electricity and industrial process heat, or indirectly by, for example, the large-scale carbon-free production of hydrogen to be used as transportation fuel.

Most HTGRs fit into the category of small and medium reactors. Small reactors are typically rated as producing under 300 MWe while medium reactors are rated up to 700 MWe [23]. Small and medium sized reactors together make up the small module reactor (SMR) design concept which has significant economic and community interest. Their construction has the potential to be significantly cheaper than large capacity LWR power plants since they offer economies of scale in the form of serial factory production. This production style improves production quality and reduces construction schedules [24]. SMRs can readily fit into brownfield sites to replace decommissioned coal-fired power plants [25], and, due to the small nature of these plants, emergency planning zones

are much smaller than large power reactors, designed to be no more than 300 meters in radius compared to 10 miles [26]. Combined, these can significantly reduce siting costs. Community interest derives from their ability to provide power for remote areas and replace diesel generators [25]. Many prismatic SMR HTGR designs can accommodate up to 5-10 years between refueling.

The large amount of graphite in HTGR cores acts as a heat sink. Both the prismatic and pebble-bed designs have a negative temperature coefficient of reactivity, meaning in the event coolant flow to the core is lost the fission chain reaction will stop without any outside influence, giving the reactors inherent safety. While fuel volumes are up to 20x greater than LWRs of the same output capacity, the fuel is less radiotoxic due to higher burnups [25]. The fuel is also in a readily disposable form and does not require dissolution and vitrification. Most HTGRs are designed to be installed below ground, reducing risks associated with earthquakes and aircraft crashes.

1.4. Safety Considerations

The large mass of graphite which makes up HTGR cores provides a large heat capacity and, combined with the fully ceramic fuel, renders the HTGR design to be very safe. The primary safety consideration for these reactors is the release of radioactive material from the fuel elements [7]. Most fission products are short lived or form stable, immobile oxides in the fuel kernel [7]. Not all fission products, however, will remain in the fuel, due to either manufacturing defects in the TRISO fuel particles or inherent U contamination of the coating layers and graphite. Some fission products are capable of

moving through intact TRISO fuel. Radionuclides located outside of the fuel have the potential to migrate out of the core and into cooler regions of the reactor where they may plate out or adsorb on graphitic dust. These condensed radionuclides then pose a radiation risk to operating personnel; in a worst-case scenario a breach of the closed coolant circuit could result in radioactivity releases outside of the reactor and pose a danger to the surrounding population. It is therefore necessary to be able to predict fission product release rates from fuel elements and estimate deposition concentrations under all expected operation and accident scenarios [7]. Radionuclide migration in the core increases with increasing core temperatures. Loss of forced He coolant circulation would result in a core heat-up event where regions of the core may reach temperatures up to 1600 °C [7].

Radionuclides of concern have been identified based on a combination of their radiological hazard level, fission yield, and transport processes [7]. They can be divided into two groups, the short-lived gaseous fission products and the long-lived metallic fission products. The former category includes isotopes of I, Kr, and Xe; ^{90}Kr and ^{137}Xe are of particular interest because they are precursors to ^{90}Sr and ^{137}Cs, respectively. Metallic radionuclides of interest include isotopes of Cs, Ag, Pd, Sr, and Eu.

The movement of metallic radionuclides through HTGR core materials is dominated by diffusion and modeled as a transient diffusion process. The traditional approach is to utilize experimentally-derived effective diffusion coefficients as input parameters for specialized fission product transport codes. “Effective” here means that any stated diffusion coefficient will encompass all other transport mechanisms into a

single, simplified transport process [27]. This is necessary due to the complex movement of fission products through ceramic materials which can be exacerbated by irradiation- or oxidation-induced microstructural changes.

Measurements of effective diffusivities in core materials can be made on in-pile or out-of-pile samples. That is, diffusion measurements can be made on materials which contain the nuclides of interest as the result of neutron-induced fission and subsequent migration in an operating HTGR (or similar environment), or they can be made in simulated situations in a laboratory setting. The former has the obvious advantage that the material is subjected to the same high-temperature high neutron flux environment as actual HTGRs. Disadvantages include the need to work with radioactive materials and the inability to deconvolute diffusivity changes resulting from interacting processes (for example the influence of one radionuclide on the diffusive behavior of another). There is also uncertainty in temperature and neutron fluence histories of the materials under study. Out-of-pile methods do not necessitate the use of radioactive materials and, if radionuclides are used, they can be applied in a controlled, single-element manner. Temperature and other external variables can also be rigidly controlled. They do not, however, inherently encompass the microstructural changes to reactor materials resulting from irradiation. Fission product modeling codes can benefit from a combination of both in-pile and out-of-pile testing.

Numerous qualified grades of nuclear graphite have been produced since the 1940s. Most of the historical grades which were used in early demonstration or testing programs are no longer available. New materials have been proposed but they require

extensive testing in order to qualify them for reactor use. Each graphite grade has characteristic features due to variations in source materials and forming methods and as such will exhibit different characteristics. These differences will be evident in responses to irradiation, high temperatures, and oxidative environments. Differences will also be seen in the diffusion of fission products given each grades' unique filler particles and pore structures. All of this is to say that all candidate grades much be investigated individually in order to fully understand their behavior in an HTGR environment.

The objective of this work was to measure effective diffusion coefficients of elements of interest in IG-110 nuclear graphite. This grade of graphite has a long history of use in demonstration HTGRs and remains a candidate of interest in future demonstration and power reactors. Effective diffusivities were measured at normal HTGR operating temperatures (800 °C) and up to 1700 °C, exceeding the most severe projected accident temperatures for modular HTGRs. The elements studied were Sr, Ag, Pd, Eu, and Cs. Ag and Pd diffusion coefficients were measured in both single-element and binary systems. Cs diffusion measurements were performed on unoxidized IG-110 and on two oxidized states of IG-110.

1.5. References

[1] Net Zero Tracker. https://zerotracker.net/ (accessed March 8, 2022).

[2] *Technology Brief Nuclear Power*; United Nations Economic Commission for Europe: Geneva, Switzerland, 2021; p 24.

[3] Nuclear. https://www.iea.org/fuels-and-technologies/nuclear (accessed March 14, 2022).

[4] *Public Attitudes to Nuclear Power*; NEA No. 6859; Nuclear Energy Agency - Organisation for Economic Co-operation and Development: Paris, France, 2010; p 54.

[5] *Strategic Plan Fiscal Years 2008-2013*; U.S. Nuclear Regulatory Commission: Washington, DC, 2008; p 24.

[6] Abram, T.; Ion, S., Generation-IV nuclear power: A review of the state of the science. *Energy Policy* **2008,** *36* (12), 4323-4330.

[7] *High Temperature Gas Cooled Reactor Fuels and Materials*; International Atomic Energy Agency: Vienna, Austria, 2010; p 182.

[8] Beck, J. M.; Pincock, L. F. *High Temperature Gas-Cooled Reactors Lessons Learned Applicable to the Next Generation Nuclear Plant*; Idaho National Laboratory: Idaho Falls, ID, 2011; p 62.

[9] Fütterer, M. A.; Fu, L.; Sink, C.; Groot, S. d.; Pouchon, M.; Kim, Y. W.; Carré, F.; Tachibana, Y., Status of the very high temperature reactor system. *Prog. Nucl. Energy* **2014,** *77*, 266-281.

[10] Goeddel, W. V., Coated-Particle Fuels in High-Temperature Reactors: A Summary of Current Applications, Nuclear Applications. *Nucl. Appl.* **1967,** *3* (10), 599-614.

[11] Jaye, S.; Goeddel, W. V., High-temperature gas-cooled reactor fuel and fuel cycles — their progress and promise. *Nucl. Eng. Des.* **1968,** *7* (4), 283-296.

[12] Kania, M. J.; Nabielek, H.; Nickel, H., Coated Particle Fuels for High-Temperature Reactors. *Mater. Sci. Technol.* **2015**.

[13] Demkowicz, P. A.; Liu, B.; Hunn, J. D., Coated particle fuel: Historical perspectives and current progress. *J. Nucl. Mater.* **2019,** *515*, 434-450.

[14] Stinton, D. P.; Lackey, W. J.; Spence, R. D., Production of Spherical UO2-UC2 for Nuclear Fuel Applications Using Thermochemical Principles. *J. Am. Ceram.* **1982,** *65* (7), 321-324.

[15] Phillips, J. A.; Nagley, S. G.; Shaber, E. L., Fabrication of uranium oxycarbide kernels and compacts for HTR fuel. *Nucl. Eng. Des.* **2012,** *251*, 261-281.

[16] *AREVA HTGR Information Kit*; AREVA S.A.: Charlotte, North Carolina, 2014; p 14.

[17] Rind, W., Graphitic matrix for the HTR fuel elements - manufacture and characterization. In *Proceedings of a Colloquium held at Hahn-Meitner-Institut*, Hoinkis, E., Ed. Berlin, 1981; pp 5-10.

[18] Collin, B. P. *AGR-1 Irradiation Test Final As-Run Report*; Idaho National Laboratory: Idaho Falls, ID, 2015; p 99.

[19] Hunn, J. D.; Trammell, M. P. *Data Compilation for AGC-2 Matrix-only Compact Lot A3-H08*; Oak Ridge National Laboratory: Oak Ridge, TN, 2010; p 39.

[20] *A Review of Radionuclide Release From HTGR Cores During Normal Operation*; 1009382; Palo Alto, CA, 2003.

[21] Zheng, G. Q.; Xu, P.; Sridharan, K.; Allen, T. R., Pore Structure Analysis of Nuclear Graphites IG-110 and NBG-18. In *Advances in Materials Science for Environmental and Nuclear Technology II, Volume 227*, Sundaram, S. K.; Fox, K.; Ohji, T.; Hoffman, E., Eds. The American Ceramic Society: 2011; Vol. 227, pp 251-260.

[22] Edenhofer, O.; Pichs-Madruga, R.; Sokona, Y.; Farahani, E.; Kadner, S.; Seyboth, K.; Adler, A.; Baum, I.; Brunner, S.; Eickemeier, P.; Kriemann, B.; Savolainen, J.; Schlömer, S.; Stechow, C. v.; Zwickel, T. *Climate Change 2014: Mitigation of Climate Change*; Cambridge University Press: Cambridge, UK; New York, NY, USA, 2014.

[23] *Small and Medium Power Reactors 1987*; International Atomic Energy Agency: Vienna, Austria, 1987; p 116.

[24] Small Modular Reactors. https://www.nei.org/advocacy/build-new-reactors/small-modular-reactors (accessed March 8, 2022).

[25] Small Nuclear Power Reactors. https://www.world-nuclear.org/information-library/nuclear-fuel-cycle/nuclear-power-reactors/small-nuclear-power-reactors.aspx (accessed March 4, 2022).

[26] Emergency Planning Zones. https://www.nrc.gov/about-nrc/emerg-preparedness/about-emerg-preparedness/planning-zones.html (accessed March 8, 2022).

[27] *Fuel performance and fission product behaviour in gas cooled reactors*; International Atomic Energy Agency: Vienna, Austria, 1997; p 529.

CHAPTER 2:
FISSION PRODUCT DIFFUSION IN IG-110 GRAPHITE

A significant portion of the working knowledge of HTGRs was obtained thanks to five past demonstration reactors which operated in the United Kingdom, the United States, and Germany. These reactors proved the technical feasibility of both the pebble-bed and prismatic core designs and generated vast quantities of knowledge on the uses of fissile and fertile fuels as well as the benefits and drawbacks of different fuel particle designs. This summary will only focus on those gas-cooled reactors which can be defined as HTGRs based on their use of He coolant, graphite moderator, and particle fuel. Other gas-cooled reactors were built and operated but did not, for example, use particle fuel (Ultra-High Temperature Reactor Experiment, Los Alamos National Laboratory, 1959-1971) [1] or He coolant (MAGNOX reactors, UK, 1950s-1970s) [2]. The following is a brief summary of these five initial HTGR demonstration and commercial reactors: Dragon, Peach Bottom Unit 1, Arbeitsgemeinschaft Versuchsreaktor (AVR), Fort St. Vrain (FSV), and the Thorium Hochtemperatur Reaktor (THTR).

2.1. Dragon (UK, 1964-1975)

The Dragon reactor was built in Winfrith, UK and was intended to test fuel, fuel elements, and structural materials. It utilized a prismatic block core and operated at 20 MWt with He inlet and outlet temperatures of 350 °C and 750 °C, respectively [3]. The initial fuel was a mixture of highly enriched uranium (HEU) and thorium but was later

switched to 3.5% low enriched uranium (LEU) [3-4]. Initially, uncoated fuel pellets were imbedded directly into the graphite matrix with the intention that Xe and Kr neutron poisons would be removed from the core. However, these elements were well-retained in the matrix and this led to the development of TRISO fuel particles [5]. The fuel was later imbedded in TRISO fuel particles which demonstrated exceptionally low fission product releases.

2.2. Peach Bottom Unit 1 (US, 1966-1974)

Peach Bottom Unit 1 was built in Delta, PA and operated by the Philadelphia Electric Company. Unlike the Dragon reactor, which was intended solely as a test reactor, Peach Bottom was also designed to produce electricity which it did at 35% thermal efficiency [3-4]. This reactor featured a prismatic block core which produced thermal power of 115 MWt. The He entered the reactor at 327 °C and exited at 700-726 °C. Core reflector graphite consisted of the grades B16-01 and AGOT [3]. The first core loading used uranium and thorium carbide kernels covered with only one layer of PyC. A high incident of coating failures led to the quick replacement of the single-coating particle fuel with BISO particles. This fuel performed well at low temperatures but failed at high temperatures and was subsequently replaced with TRISO fuel. The reactor was shutdown in 1974 after completion of its demonstration mission [3]. Analysis of the primary coolant circuit after shutdown showed that only Cs and Sr isotopes were present at measurable activity levels [3].

2.3. AVR (Germany, 1967-1988)

The AVR was the first operational pebble-bed HTGR and featured on-line refueling capabilities. It was located at the Jülich Research Center in the Federal Republic of Germany. The AVR was designed to be an experimental power station and fuel testing reactor [3]. It produced 46 MWt/15 MWe with He inlet and outlet temperatures of 275 °C and 950 °C, respectively. The initial core consisted of 30,000 fueled and 70,000 non-fueled 60-mm diameter graphite spheres [4]. The particle coating used was BISO although TRISO fuel was also tested. The reactor was used to conduct loss-of-forced cooling tests and showed that the particle fuel would remain below failure temperatures even under such extreme temperature conditions [6]. During decommissioning the AVR was assessed for fission product activity levels located outside of the fuel [7]. A major fraction of the contamination was bound on graphite dust. It was determined that metals were capable of diffusing through fuel kernel coatings and graphite and that their breakthrough took place in long-term normal operation. Activity released from the fuel elements was distributed all over the coolant circuit surfaces and entrained on graphite dust.

2.4. FSV (US, 1974-1989)

FSV was designed by General Atomics based on the Peach Bottom prismatic block design [3]. Located in Platteville, CO, FSV was the first HTGR designed for commercial-scale electricity generation. It operated at 842 MWt/330 MWe and used a

mixture of uranium and thorium carbide TRISO fuel particles. The He coolant entered and exited the reactor at 404 °C and 777 °C, respectively. FSV fuel reached maximum irradiation temperatures of 1300 °C and maximum burnup of 16% fissions per initial metal atom (FIMA) with no accompanying evidence of in-service coating failure [3]. FSV was plagued by moisture ingress issues which caused severe degradation of the permanent core graphite which was made from PGX graphite [4]. The H-327 and H-451 fuel element graphites were also affected, although to a lesser degree. The excess moisture also led to corrosion of carbon steel components, particularly the control rod drive mechanisms. Finally, the added moisture led to positive reactivity in the core, causing a reactor scram event in 1984. The corrosion of the control rod drive mechanisms caused 6 failed insertions during this event. Due to rising maintenance, operations, and fuel costs the decision was made to shutdown FSV by or before mid-1990. An unscheduled shutdown in 1989 revealed significant cracking in the system and the reactor was permanently shut down at that time.

2.5. THTR (Germany, 1985-1991)

Like FSV, the THTR was also built as a commercial-scale demonstration reactor with a power output of 750 MWt/300 MWe. THTR utilized a pebble-bed core and a mixture of uranium and thorium oxide BISO fuel particles [3]. The He coolant entered and exited the reactor at 404 °C and 777 °C, respectively. Despite good technical performance, the THTR was prematurely shut down in 1991 due to a combination of political and economic factors [4].

Three HTGRs are currently operating. These are the High-Temperature Test Reactor (HTTR), the 10 MW High-Temperature Reactor (HTR-10), and the High-Temperature Reactor Pebble-bed Module (HTR-PM). These three reactors have continued to demonstrate the technical feasibility of HTGRs and have successfully performed extreme safety tests to prove the inherent safety features of the design. All three use IG-110 graphite (or the less refined IG-11) as their primary structural graphite.

2.6. HTTR (Japan, 1998)

The HTTR is located on the Japanese Atomic Energy Agency campus in the Ibaraki Prefecture, Tokaimura, Japan [4]. It was built to establish and improve HTGR technologies [3]; its primary intended purpose is to serve as a demonstration plant for process heat production of hydrogen although this system has yet to be constructed. The prismatic reactor produces 30 MWt with He inlet and outlet temperatures of 400 °C and up to 950 °C, respectively. After the reactor was brought up to its maximum operating temperature of 950 °C all radioactivity levels remained below the limit of detection of the fuel failure detection system [3]. The fuel is primarily TRISO-coated 6% enriched uranium oxide [3, 8]. The reactor was taken offline in February 2011 for planned inspections, immediately prior to the Fukushima nuclear accident in March 2011. It was left idle until July 2021 at which time it was restarted after minor changes to the reactor installation to conform with new safety requirements [8].

2.7. HTR-10 (China, 2000)

The HTR-10 was designed and constructed by the Institute of Nuclear and New Energy Technology in China and is located at Tsinghua University in Beijing, China [3-4]. The intended purpose of the pebble-bed reactor is as a test reactor to support the development of larger pebble-bed reactors, namely the HTR-PM. The HTR-10 produces 10 MWt with He inlet and outlet temperatures of 250 °C and 700 °C and uses TRISO-coated UO_2 particles. The HTR-10 has provided useful information on fuel design and expected fuel failures above 1600 °C [3]. It has also been used to conduct numerous safety experiments to verify the inherent safety features of modular HTGRs [9].

2.8. HTR-PM (China, 2021)

The HTR-PM is the most recent HTGR to enter operation at the time of this writing. The dual reactor system reached criticality in November 2021 and the system was connected to the grid in December 2021 [10-11]. It is located in Rongcheng, Shandong Province, China. The reactor design is based on the HTR-10 and features two 250 MWt modular reactors driving a single turbine [9]. Its intended purpose is as a commercial demonstration unit for electricity production. The plant has a combined 211 MWe capacity [12]. He inlet and outlet temperatures are 250 °C and 750 °C, respectively. Each reactor contains 420,000 fuel pebbles, each containing ~12,000 8.5% enriched UO_2 fuel particles [9-10, 12]. An uprated HTR-PM600 system is currently in development

based on this design. It will feature six 250 MWt reactor modules coupled to a single turbine, ultimately producing 655 MWe [13].

Numerous modular HTGRs are currently in the design and planning stages. The following is by no means an exhaustive list and will only focus on reactors intended for commercial use with a strong possibility of construction or initial demonstration by 2030. These are the U-Battery by Urenco, the Xe-100 by X-energy, and the Ultra Safe Nuclear Corporation's (USNC) Micro Modular Reactor (MMR™). A complete list of proposed modular HTGRs can be found in [9, 13].

2.9. U-Battery

The U-Battery by Urenco, a technology developer based in the UK, is technically defined as a micro-modular reactor, producing only 10 MWt/4 MWe per unit [9]. The reactor was designed to use only existing, developed nuclear technology and is intended to service markets which currently rely heavily on diesel or other small fossil fuel technologies. The three intended user-specific applications are to provide heat for industrial application, electricity production, or cogeneration of both heat and power. The He coolant will heat a secondary N_2 coolant system which can in turn directly drive a gas turbine or pass heat to a tertiary fluid for heat applications. The annular prismatic core is composed of twelve fuel columns surrounded by geometry-matched reflector blocks which can replace the fuel blocks if necessary. These are in turn surrounded by permanent graphite reflector blocks. The TRISO-coated fuel particles use <20% enriched

UCO fuel, validated as part of the US Department of Energy's (DOE) Advanced Gas Reactor Fuel Qualification and Development (AGR) Program. Refueling is expected to take place every 5 years [13]. The U-Battery is in the conceptual design phase with plans to operate a pilot reactor at Chalk River Laboratories in Ontario, Canada by 2028.

2.10. Xe-100

The Xe-100 is a pebble-bed modular reactor developed by X-energy, LLC in the US [9]. Each reactor produces 200 MWt/82.5 MWe using 220,000 fuel pebbles with ~18,000 15.5% enriched UCO TRISO particles per pebble. Each pebble is expected to pass through the core six times before final disposal. Target applications are process heat production, desalination, and electricity and heat co-generation. In 2021 X-energy entered into a cooperation agreement with the US-DOE to begin its participation in their Advanced Reactor Demonstration Program [14]. This will allow X-energy to build a commercial-scale demonstration reactor with Energy Northwest in WA state. Current projections are for a reactor start by 2028.

2.11. MMR™

The MMR™ uses a prismatic core design. The reactor is designed to operate for 20 years with no refueling, after which the sealed module would become waste. The fuel compacts are composed of 19.75% enriched UCO TRISO fuel particles imbedded in either traditional graphite matrix, or USNC's novel Fully Ceramic Microencapsulated

(FCM®) fuel which replaces the matrix graphite with fully dense SiC [9]. This combination would provide improved fission product retention over the traditional compact design. The modular reactor is intended to produce 15 MWt/>5MWe for process heat and electricity production. Heat generated in the core will be stored in an Adjacent Plant Molten Salt Heat Storage System. There are plans to begin construction of a demonstration reactor at Chalk River Laboratories in 2023 with 2025 commissioning [13]. This will be followed by a demonstration reactor at the Idaho National Laboratory (INL) and then one at the Urbana-Champaign campus at the University of Illinois to be used as both a power source and a research reactor.

2.12. References

[1] *Ultra High Temperature Reactor Experiment (UHTREX) Hazard Report*; Los Alamos National Laboratory: Los Alamos, New Mexico, 1962; p 164.

[2] Jensen, S. E.; Nonbøl, E. *Description of the Magnox Type of Gas Cooled Reactor (MAGNOX)*; Risø National Laboratory: Roskilde, Denmark, 1998; p 83.

[3] Beck, J. M.; Pincock, L. F. *High Temperature Gas-Cooled Reactors Lessons Learned Applicable to the Next Generation Nuclear Plant*; Idaho National Laboratory: Idaho Falls, ID, 2011; p 62.

[4] Longoni, G.; Gates, R. O.; Mcdowell, B. K. *High Temperature Gas Reactors: Assessment of Applicable Codes and Standards*; Pacific Northwest National Laboratory: Richland, WA, 2015; p 37.

[5] Simon, R. A.; Capp, P. D. In *Operating Experience with the Dragon High Temperature Reactor Experiment*, Conference on High Temperature Reactors, Vienna, Austria, International Atomic Energy Agency: Vienna, Austria, 2002; p 5.

[6] Marnet, C.; Ivens, G.; Ziermann, E., The AVR power plant in its last year of operation. *Energy* **1991,** *16* (1-2), 71-77.

[7] Moormann, R. *A safety re-evaluation of the AVR pebble bed reactor operation and its consequences for future HTR concepts*; ISSN 0944-2952; Forschungszentrum Jülich, Germany, 2008; p 37.

[8] Japanese gas-cooled reactor restarts. https://www.world-nuclear-news.org/Articles/Japanese-gas-cooled-reactor-restarts (accessed January 6, 2022).

[9] *Advances in Small Modular Reactor Technology Developments*; International Atomic Energy Agency: Vienna, Austria, 2020.

[10] Demonstration HTR-PM connected to grid. https://www.world-nuclear-news.org/Articles/Demonstration-HTR-PM-connected-to-grid (accessed January 6, 2022).

[11] Dual criticality for Chinese demonstration HTR-PM. https://www.world-nuclear-news.org/Articles/Dual-criticality-for-Chinese-demonstration-HTR-PM (accessed January 6, 2022).

[12] *Status report 96 - High Temperature Gas Cooled Reactor - Pebble-Bed Module (HTR-PM)*; 2011; p 18.

[13] Small Nuclear Power Reactors. https://www.world-nuclear.org/information-library/nuclear-fuel-cycle/nuclear-power-reactors/small-nuclear-power-reactors.aspx (accessed March 4, 2022).

[14] X-energy formally begins SMR partnership with DOE. https://www.world-nuclear-news.org/Articles/X-energy-formally-begins-SMR-partnership-with-DOE (accessed March 16, 2022).

CHAPTER 3:
MEASUREMENT OF EFFECTIVE Sr DIFFUSION COEFFICIENTS IN IG-110 GRAPHITE

The results of this study were published in 2021 as follows: T.M. Weilert, K.L. Walton, S.K. Loyalka, J.D. Brockman. Measurement of effective Sr diffusion coefficients in IG-110 graphite. *Journal of Nuclear Materials* **2021**. 555, 153102.

3.1. Abstract

Radionuclide transport and release from operating HTGR cores during normal and off- normal operations carries the possibility of increased exposure risk to reactor personnel as well as radionuclide release to the surrounding environment in the event of a depressurization accident. Diffusion is one of the primary processes by which this radionuclide transport takes place. ^{90}Sr is one of several fission products which is commonly investigated within the context of high-temperature gas-cooled reactors due to its low volatility and ability to migrate through intact TRISO fuel particles. Effective diffusion coefficients for strontium in unirradiated IG-110 graphite have been experimentally determined over the temperature range 1773 K – 1973 K using a time-release method coupled to an inductively-coupled plasma mass spectrometer. The results of this work are:

$$D_{Sr,IG-110} = \left(1.7 \times 10^{-1}\, {}^{m^2}/_{s}\right) exp\left(\frac{-3.46 \times 10^{5}\, {}^{J}/_{mol}}{RT}\right)$$

3.2. Introduction

High-temperature gas-cooled reactors (HTGRs) are considered one of the near-term Gen-IV reactor design concepts. This reactor design utilizes the tristructural isotropic (TRISO) fuel form consisting of a kernel of enriched uranium fuel enclosed by successive layers of porous graphite, an inner pyrocarbon layer (IPyC), a SiC layer, and an outer pyrocarbon layer (OPyC); these layers serve in part to retain fission products generated during reactor operation [1-2]. The Advanced Gas Reactor Fuel Qualification and Development (AGR) Program irradiation experiments have been underway at the Idaho National Laboratory (INL) since 2002 to evaluate the performance and fission product retention of modern formulations of TRISO fuel [2]. Irradiations were performed at the Advanced Test Reactor (ATR) at INL and post-irradiation examinations were carried out at both INL and the Oak Ridge National Laboratory (ORNL).

The AGR-1 experiment was conducted as a pilot irradiation of TRISO fuel containing a UCO kernel and produced in small scale [3]. The kernels were produced by BWX Technologies (BWXT) [4] and then coated and compacted at ORNL [5-12]. The release-rate-to-birth-rate ratio (R/B) of strontium in the AGR-1 fuel compact was $<3 \times 10^{-5}$ for all capsules [13]. Strontium was found in the compact matrix graphite suggesting that strontium was released through intact coatings but retained in the compact graphite matrix [3]. In the AGR-2 test, the TRISO fuel particles were formulated from UCO and UO_2 by BWXT [14-18] and compacted on a laboratory scale at ORNL [19-27]. The fuel was irradiated to a %FIMA (fissions per initial heavy metal atom) of 7.3% - 13.2%. In

post irradiation experiments, irradiated AGR-1 TRISO fuel compacts were heated and strontium release from the compacts was recorded at temperatures between 1873 K and 2073 K [28]. These results support the hypothesis that strontium had already migrated through the TRISO particles and was released at temperatures above 1873 K [2]. Similar results were seen in deconsolidation and leach-burn-leach analysis of AGR-2 irradiated compacts [29]. The quantity of strontium leached from outside of the SiC layers was too high to be explained just by the presence of defective particles within the compact, again supporting the ability of strontium to diffuse through intact SiC [29]. These results were correlated with a higher-than-average irradiation temperature for the compact in question [29-30].

The fission product ^{90}Sr is biologically active and is known to mimic calcium in the body. For this reason, as well as its ^{235}U fission yield of 5.7%, ^{90}Sr is one of the primary isotopes of concern in nuclear reactor accidents. Migration of ^{90}Sr through intact TRISO fuel particles and into the primary coolant could lead to potential dose hazards for operations and maintenance (O&M) personnel during routine operation [31]. The fission product source term in the primary loop must be understood to model dose hazards during normal operation and potential release during a reactor accident scenario [31]. The modeling codes FRESCO and PARFUME can be used to track the migration of fission products in reactors. These codes use effective diffusion coefficients that have been compiled from historical grades of nuclear graphite [32]. In this classical approach the term ‘effective’ diffusion coefficient is used to summarize all transport processes, including evaporation, adsorption, diffusion, and trapping, into a single transport process

[33]. PARFUME predictions of AGR-1 capsule heating tests globally over-predicted strontium release and it was noted that release was primarily dominated by intact particles [34].

Previous work on strontium diffusion in graphite has focused both on matrix graphite, which contains high amounts of ungraphitized, amorphous carbon, and structural graphite which is treated to much higher temperatures and is more graphitized [32, 35]. In the present study, the effective diffusion coefficients of strontium were measured in IG-110 graphite. IG-110 is a highly graphitized, fine grain graphite under consideration for use as structural graphite in HTGR designs. In this work, the diffusivity of strontium in IG-110 graphite was measured using a time-release method with inductively-coupled plasma mass spectrometer (ICP-MS)-based detection of the instantaneous strontium release rate. Time-release measurements of strontium diffusivity were made possible from the development of a new method to infuse metals into graphite which utilized a pressurized vessel [36]. In this method graphite spheres were loaded into the pressure vessel with strontium nitrate and the system was pressure cycled to drive strontium into the graphite pore structure. Previous measurements of graphite diffusion coefficients have been made using the depth profiling, permeation, or in-pile diffusion methods [35, 37-42]. While the time-release method is not free from experimental bias, it does not have the same biases as previous methods and will therefore add to a consensus value of effective strontium diffusion coefficients.

Measurements were performed in the temperature range 1773 K – 1973 K. The results presented in this work most closely replicate strontium release as a result of a loss-

of-forced coolant accident. Past research has shown that strontium is effectively retained in the matrix graphite surrounding the TRISO fuel particles at normal operating temperatures [34, 43-44]. At the most extreme accident temperatures there is measurable release of strontium from fuel compacts [34, 43-44]. These releases have the potential to migrate to and into the surrounding structural graphite. Additionally, inherent uranium contamination of structural graphite constitutes an additional source term for radionuclides, including ^{90}Sr. While no studies have focused specifically on the origin of ^{90}Sr in structural graphite, there is some evidence to suggest uranium impurity as the main source of europium radionuclides in graphite balls without nuclear fuel taken from the HTR-10 [45]. Finally, ^{90}Sr release to reactor coolant systems is expected to be dominated by its ^{90}Kr gaseous precursor and ^{90}Rb intermediate [31]. This would represent an additional source-term of ^{90}Sr. The strontium resulting from this decay would be in its metallic form, which is the expected form of diffusant strontium in this study.

3.3. Theory

In this work, the release rate of strontium from a spherical IG-110 graphite sample was measured in a time-release experiment. The time-release experiment has recently been used to measure cesium, iodine, and silver diffusion in graphite [36, 46-49]. The method assumes that release of diffusant from a surface is dominated by diffusion within the graphite and that effects related to adsorption and the presence of trapping contaminants are minimal. This assumption is common in diffusion models and is likewise applied here for structural graphite representing a single retentive layer [33]. The

effective diffusion coefficient D (m^2/s) is determined using Fick's 2nd law in spherical coordinates, where:

$$\frac{\partial C(r,t)}{\partial t} = \frac{1}{r^2}\frac{\partial}{\partial r}\left(Dr^2\frac{\partial C(r,t)}{\partial r}\right) \quad (3.1)$$

$$C(r,0) = C_0 \quad (3.2)$$

$$C(0,t) = finite \quad (3.3)$$

$$C(R,t) = 0 \quad (3.4)$$

Here, $C(r,t)$ is the concentration of strontium (g/m^3) as a function of position and time, r is the radial coordinate (m), R is the radius of the sphere (m), t is the time (s), and C_0 is the known initial concentration of diffusant. This equation can be solved using a series expansion technique. For the case of constant C_0 , one obtains the following cumulative fractional release equation [50-51]:

$$F(t) = \frac{m_{diffused}(t)}{m_0} = 1 - \frac{6}{\pi^2}\sum_{n=1}^{\infty}\frac{1}{n^2}e^{-(\frac{n\pi}{R})^2 Dt} \quad (3.5)$$

Where $F(t)$ is the fractional release of diffusant at a given time, $m_{diffused}(t)$ is the total mass of diffusant (g) that has been released at a given time, and m_0 is the mass of diffusant (g) initially present in the sample. This series converges slowly and therefore 100 terms were used. Effective strontium diffusion coefficients in IG-110 graphite were determined by fitting Eqn. 3.5 to measured cumulative fractional releases.

3.4. Experimental

3.4.1. Materials and Preparation

IG-110 is a structural graphite produced by Toyo Tanso® in Japan using cold isostatic pressing. As mentioned previously, this work was made successful by the implementation of a new method to infuse strontium into the graphite samples. Gas-phase infusion of strontium into IG-110 graphite was previously attempted by Carter [51] using several methods, to very limited success. Briefly, the first attempt utilized evacuated quartz tubes filled with the graphite samples and a $Sr(NO_3)_2$ salt. The tube was heated to ~1373 K for 4 days. The reasoning behind the failure of this method was attributed to insufficient vapor pressure of SrO under the chosen heating conditions [51]. Higher temperatures, along with a different form of strontium, were then tested. A molybdenum container was filled with IG-110 samples and a strontium-laden graphite powder. This assembly was heated to 1400 °C under argon atmosphere. In spite of the argon, oxidation of the molybdenum container began almost immediately, and the experiment was stopped. The molybdenum was then exchanged for a graphite container sealed with a commercial cement and filled in the same manner as the molybdenum. This container was heated to 1400 °C under vacuum for 5 days; afterwards it was discovered the cement seal had failed. Only ~ 340 ng of strontium was measured in each sphere using instrumental neutron activation analysis (INAA).

Spheres of as-received IG-110 graphite were milled to a diameter of 0.32 cm. Strontium was infused into the graphite spheres using a previously described method [36]. Briefly, the graphite spheres were placed in the 45 mL polytetrafluoroethylene (PTFE) sleeve of a Parr Model 4744 parr bomb along with 15 mL of a 1.00 part-per-thousand $Sr(NO_3)_2$ standard solution and 5 mL of high-purity water. The pressure vessel

was capped and heated at 508 K for 2 hours and 373 K for 1 hour; this cycle was repeated four times. Once complete, the spheres were removed from the pressure vessel, rinsed with high-purity water, and dried in a vacuum oven overnight at ~373 K. The next day the spheres were heated to 773 K for 30 minutes to dissociate nitrates remaining within the graphite. The spheres were sanded with Al_2O_3 sandpaper to remove the surface layer of graphite that contained high strontium concentration. The spheres were then sonicated in high purity water to remove dust and dried on a hot plate. The final diameter of each sample was measured with calipers to the nearest 0.025 mm. The average final diameter for the reported samples was 0.316 ± 0.005 cm.

The mass of strontium in the graphite spheres was measured before and after the time-release experiments using standard comparator INAA. Strontium standards were prepared from a commercial ICP-MS standard. The graphite samples and standards were irradiated simultaneously in the row-2 pneumatic tube system at the University of Missouri Research Reactor (MURR) for ten minutes at a thermal neutron flux of 5.5×10^{13} n/cm^2/s. The samples and standards were removed and counted for ten minutes each using a high-purity germanium (HPGe) detector.

The radial profile of strontium in the spheres was measured using laser-ablation inductively-coupled plasma mass spectrometry (LA-ICP-MS). One loaded sphere was selected from the batch and bisected into two hemispheres using a stainless-steel razor blade. The flat faces of both hemispheres were smoothed with Al_2O_3 sandpaper. The concentration profile was determined using a Photon Machines 192 nm laser attached to a NexION® 300x ICP-MS. The laser was operated with a power density of 2 mJ/cm^2, 40

μm spot size, and 10 Hz pulse frequency. The sample was mounted with the flat face directed towards the laser. Samplings were taken every ~100 μm along the diameter of the sample face. After each sampling line was completed, the sampling direction was rotated 45° clockwise; this was repeated four times and the results were averaged.

3.4.2. Diffusion Measurements

Diffusion measurements were carried out using a time-release experiment, depicted in Fig. 3.1 and previously described by Carter et al. [36, 46-49]. The diffusion cell was constructed using SiC tubes purchased from Saint Gobain Hexaloy®. At the start of the experiment, the spherical graphite sample was housed in a chamber above the valve, shown at the top of Fig. 3.1. The valve was partially open to allow helium to displace air from the sample chamber. The diffusion cell was seated within a modified SentroTech high-temperature box furnace (Model ST-1700C-888). The diffusion cell and sample chamber were flushed with helium for most of the duration of the furnace heat-up and for an additional hour prior to the start of the experiment in order to remove air. When the ball valve was opened, the graphite sample dropped into the diffusion chamber and strontium released from the sphere was transported to the ICP-MS system for measurement using a helium jet system [46]. The helium jet was produced by a Palas GFG-1000 carbon aerosol generator that had been modified to work with helium carrier gas at a flow rate of 2 L/min.

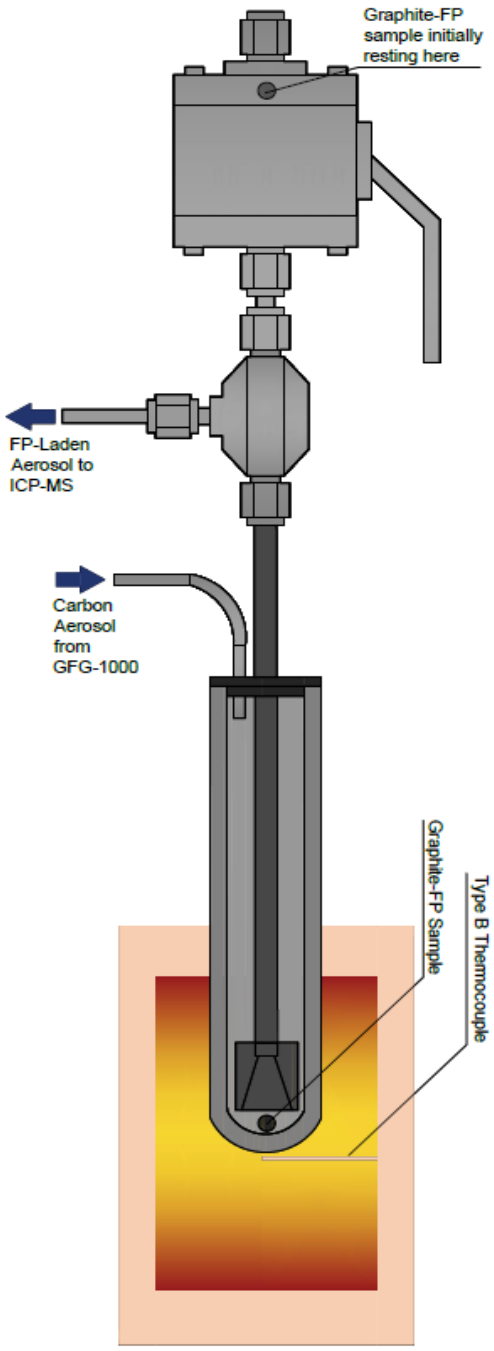

Figure 3.1: The time-release diffusion cell. The spherical graphite sample was initially housed at the top of the chamber. At the start of the experiment, the graphite sample was dropped into the heated portion of the SiC diffusion chamber, depicted at the bottom of the figure. “FP” refers to fission product, however the strontium used was a natural surrogate.

The carbon aerosol-laden helium gas was passed over the graphite sample in the diffusion chamber. Strontium emitted from the surface of the graphite sphere adsorbed to the graphite aerosol and was transported to the ICP-MS instrument. This aerosol was introduced into the argon plasma of the ICP-MS using a dual inlet spray chamber sample introduction system. The second inlet of the spray chamber was used to introduce a 1 ng/g indium internal standard used to correct for instrumental drift throughout the course of the diffusion experiment. The temperature near the graphite sphere in the diffusion chamber was monitored with a Type B Pt/Rh thermocouple. The final strontium concentration in each sample was measured using INAA to determine the total strontium mass loss. Time-release measurements were conducted in the temperature range 1773 K – 1973 K in 50 K intervals.

3.4.3. Data Analysis

The mass spectrometer signal was converted from counts/second to mass loss/second by calibrating to the total strontium mass loss measured by INAA [52]. Prior to the start of an experiment, the background strontium level was collected for approximately 1 hour. The background value used for correction was taken to be the average of the last ten measurements taken before sample introduction (feature A in Fig. 3.2); this average was subtracted from all subsequent measurements. At the start of the experiment, the graphite sample was dropped into the diffusion cell. Strontium released from the cell was transported to the ICP-MS via the carbon aerosol helium jet.

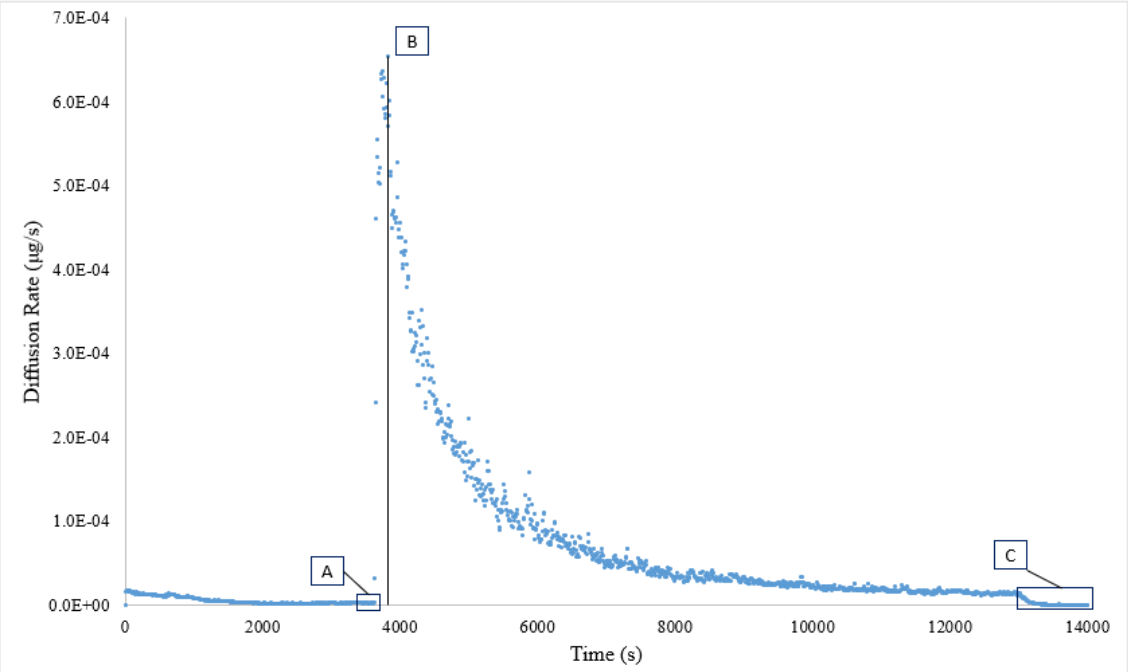

Figure 3.2: Strontium time-release experiment at 1873 K. [A] is the baseline at the start of the experiment. [B] is the peak signal after sample introduction. [C] is the baseline counts at the end of the experiment after the furnace had been shut down.

There was a rapid rise in strontium signal collected when the sphere was introduced. The maximum signal is indicated as feature B in Fig. 3.2. The rapid rise was not used for fitting the data to the cumulative release equation because the graphite sphere was not in thermal equilibrium with the diffusion cell and the initial strontium release was dominated by release of strontium from the surface of the sphere through non-diffusion related mechanisms such as desorption and evaporation [46]. The total mass loss of strontium in this region was calculated and subtracted from the initial mass; the instantaneous fractional release was then determined as described by Carter et al. [46, 52]. After the furnace was turned off, the ICP-MS continued collecting data for 20 minutes. The background-corrected counts collected in this decay region (feature C in Fig. 3.2) constituted much less than 1% of the total counts for the experiment and,

therefore, was not corrected for in the fractional release calculations. The fractional release curve was fit to Eqn. 3.5 using a least squares minimization method. An Arrhenius form, Eqn. 3.6, was used to demonstrate the temperature dependence of the diffusion coefficient:

$$D = D_o e^{-E_a/RT} \tag{3.6}$$

Where D_0 is the pre-exponential factor (m^2/s) and E_a is the activation energy (kJ/mol). Uncertainties in the pre-exponential factor and activation energy were calculated from standard errors of the best fit linear regression.

3.5. Results

The initial radial distribution of strontium in the IG-110 graphite samples is shown in Fig. 3.3. The slope of the distribution curve was 1.40×10^4 counts/cm, 95% CI [-1.67×10^5, 1.39×10^5]. There was not a significant trend between the radial distance and the measured strontium counts ($F_{1,14} = 0.04$, $p = 0.83$). A flat strontium profile was therefore assumed, and Eqn. 3.5 was used to determine the effective diffusion coefficients.

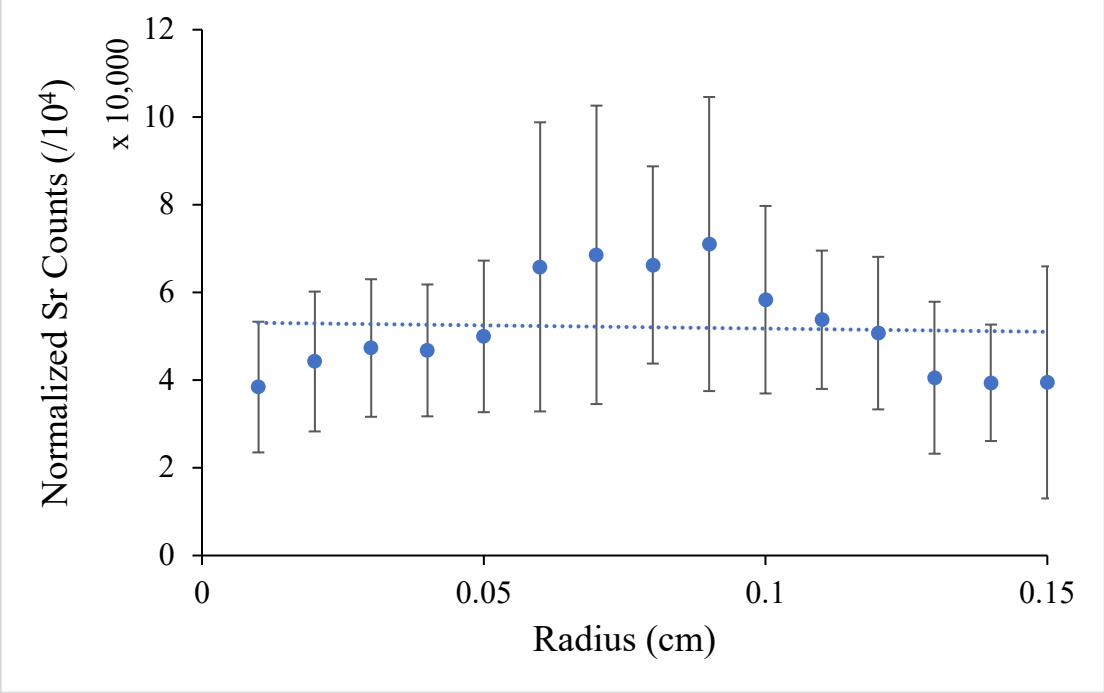

Figure 3.3: Radial distribution of strontium in IG-110 graphite after parr-bomb loading.

The pre- and post-irradiation strontium masses, as measured by INAA, are reported in Table 3.1. The associated fractional release curves at the temperatures listed in Table 3.1 are shown in Fig. 3.4. Table 3.1 lists the diffusion coefficients obtained by fitting Eqn. 3.5 to the release curves using a nonlinear least squares fitting method. The standard error was calculated from the variance-covariance matrix using Mathematica. Table 3.2 reports the calculated Arrhenius parameters obtained by fitting the Arrhenius diffusion coefficient vs. reciprocal temperature data using a weighted linear least squares approach. The Arrhenius plot of strontium diffusion shown in Fig. 3.5 was linear over the experimental temperature range. Experiments were also conducted at 1673 K. In this experiment, a strontium signal was not observed during the 1-hour long experiment and no change in mass was measured using INAA. Diffusivity measurements were successful in the temperature range between 1773 K – 1973 K.

Table 3.1: The experimental temperature, initial and final strontium mass measured using INAA, and the diffusion coefficient. The standard error of the diffusion coefficient is reported in parenthesis.

Test Temperature (K)	Initial Sr Mass (µg)	Final Sr Mass (µg)	Diffusion Coefficient (m^2/s)
1673	1.29	1.28	N/A
1773	1.37	0.27	$1.10\ (0.09) \times 10^{-11}$
1823	0.99	0.16	$2.05\ (0.01) \times 10^{-11}$
1873	0.92	0.14	$4.28\ (0.03) \times 10^{-11}$
1923	1.38	0.12	$5.84\ (0.02) \times 10^{-11}$
1973	1.25	0.07	$1.27\ (0.01) \times 10^{-10}$

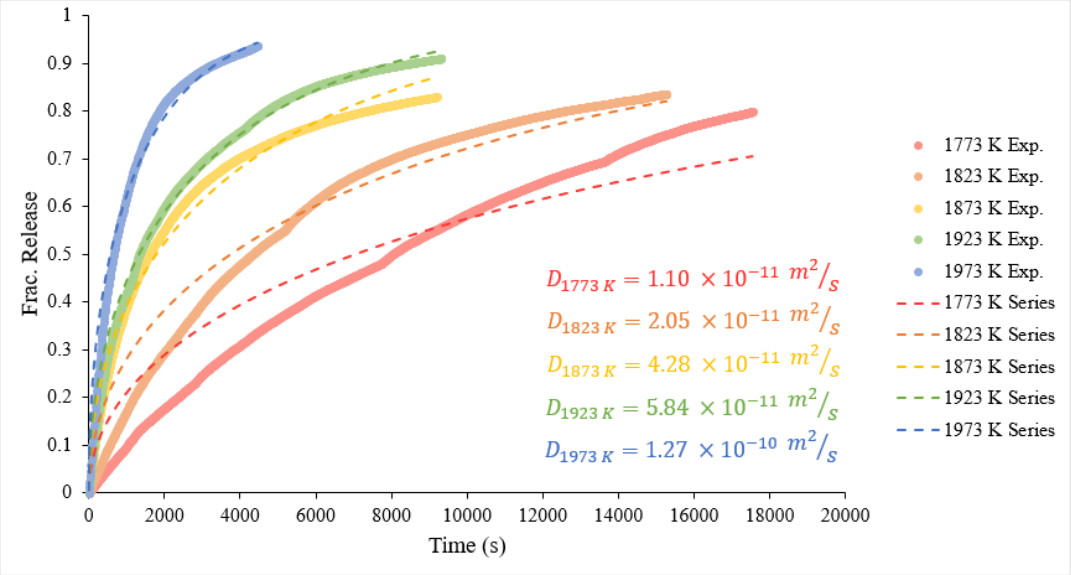

Figure 3.4: Fractional release curves of strontium from IG-110 graphite and their associated diffusivities.

Table 3.2: Calculated Arrhenius parameters of strontium diffusion in IG-110 graphite.

Diffusant	D_0 (m^2/s)	$\pm\Delta D_0$ (m^2/s)	E_a (kJ/mol)	$\pm\Delta E_a$ (kJ/mol)
Sr	1.7×10^{-1}	1.3×10^{-1}	346	22

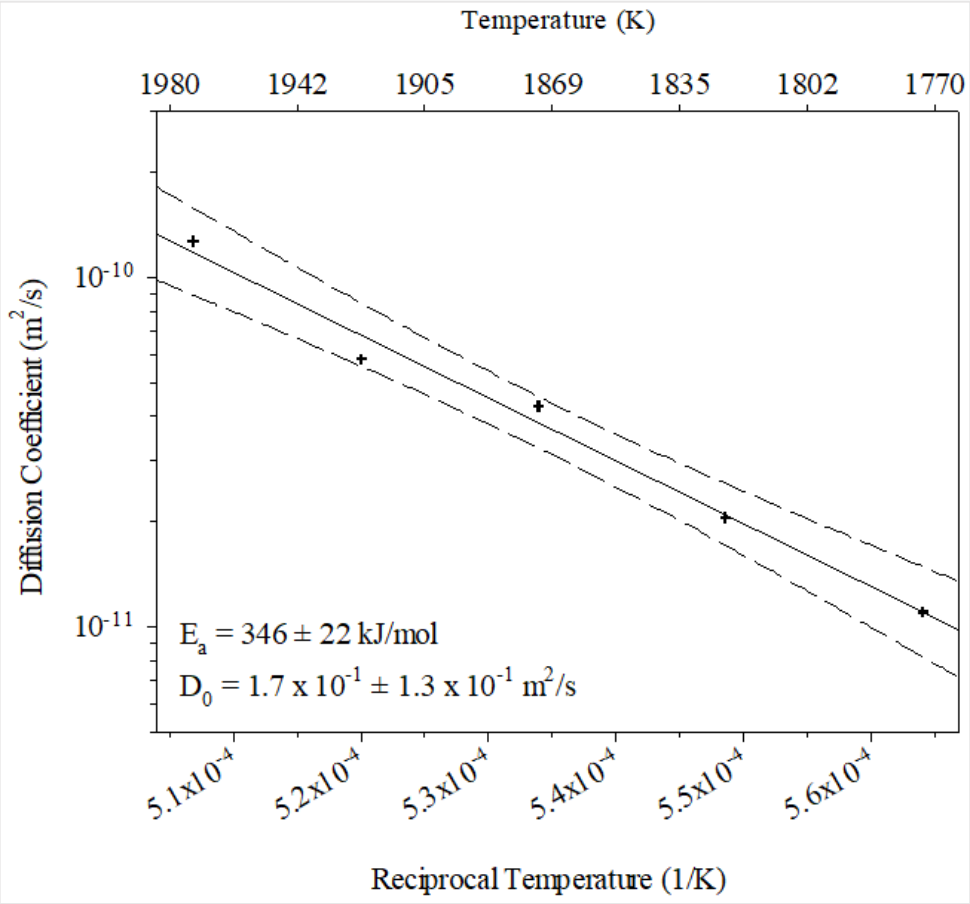

Figure 3.5: Arrhenius plot of strontium diffusion in IG-110 graphite. The dashed lines represent the 95% confidence interval.

3.6. Discussion

An advantage of the time-release method described is that the experiment closely replicates the conditions in an HGTR reactor. The experiment takes place in flowing He with carbon dust and therefore includes evaporative and desorption processes. The time-release method has previously been applied to measurements of cesium, iodine, and silver diffusion coefficients in both NBG-18 and IG-110 graphite [36, 46-49]. Historically, strontium diffusion measurements in graphite have been made using depth profiling,

permeation, or in-pile diffusion methods [35, 37-38]. In the profile and permeation methods, a high concentration of strontium was initially coupled to the graphite. Measurement of the diffusion coefficient of strontium in this way may not adequately account for changes in diffusion related to strontium concentration [35, 38, 41]. Sandalls, et al. [38] reported a concentration dependence of the strontium diffusion coefficient when the concentration exceeded 62 μg Sr/g graphite. One advantage of the time-release method is that strontium can be loaded into graphite at lower concentrations in order to avoid bias related to concentration dependence. Sandalls, et al. demonstrated a decrease in both the activation energy and pre-exponential factor as the concentration increased above 35 μg Sr/g graphite, see Table 3.3. Details were not provided as to how the authors arrived at their 62 μg Sr/g graphite limit. In the present work, IG-110 graphite spheres (ρ = 1.76 g/cm^3) were milled to radii of ~0.16 cm and were loaded with an average of 1.17 μg strontium. This equates to an average concentration of 40 μg Sr/g graphite which should be sufficient to avoid discrepancies caused by a concentration dependence.

The experimental fractional release curves reported in Fig. 3.4 differ from the best-fit theoretical release curves generated using Eqn. 3.5. At 1773 K and 1823 K the model overpredicts the experimental strontium release at short times. This non-Fickian behavior could be caused by several factors. The strontium diffusion profile, Fig. 3.3, was observed to be uniform within experimental uncertainty in a bisected graphite sphere produced at the same time as the experimental sphere. It was assumed that all the graphite spheres in the same production batch had a similar profile. If this were not the case, it could account for some of the observed deviation in the cumulative release profiles. In

previous time-release measurements of silver in IG-110 graphite the use of a measured concentration profile instead of an assumed uniform profile did not significantly alter the silver effective diffusivity values [36]. A radial profile that is not uniform will tend to smooth out during the experiment leading to a smaller-than-expected difference between a system modeled with a uniform diffusant profile and a fitted diffusant profile.

The chemical form of strontium in the graphite sphere could also impact the fractional release curve. In the final steps of the loading procedure the graphite sphere was held at 773 K for 30 minutes to decompose strontium nitrate. Previous work has demonstrated that strontium nitrate atomized on a graphite surface by rapid heating to 2873 K decomposed to produce SrO which further decomposed into strontium metal [53]. The decomposition point of SrO is 3470 K. If strontium is present as SrO then it must desorb from the graphite surface. The desorption of SrO or the conversion of SrO to the metal form through a reaction on the graphite surface may be the rate limiting step at lower temperatures and this could explain why strontium release was not observed at 1673 K despite the temperature being greater than the 1650 K boiling point of strontium metal. Another possibility for the observed non-Fickian behavior at 1773 K and 1823 K is that evaporation or desorption of strontium from the graphite surface could compete with diffusion as the rate-limiting step. In determination of the effective diffusion coefficient it is common to ignore the effects of sorption or trapping [33]. More work is needed to determine the form of strontium in the graphite at the experimental temperatures used in this work and in strontium present in in-pile graphitic materials.

The measured effective diffusion coefficient values were used to derive Arrhenius parameters, reported in Table 3.2. The uncertainty of the activation energy (E_a) and the pre-exponential (D_0) were estimated using a weighted linear least squares regression analysis. Because of the poor fit of the cumulative release curves at 1773 K and 1823 K the Arrhenius parameters were also calculated using only the data at the three highest temperatures. The activation energy and pre-exponential factor over the temperature range 1873 K – 1973 K were 332.8 ± 88 kJ/mol and 0.08 ± 0.16 m^2/s, respectively. There was not a significant difference in the value of the activation energy between the values in Table 3.2 and those calculated at the three highest temperatures, indicating that despite the poor fit to the experimental cumulative release data at 1773 K and 1823 K, the Arrhenius plot was linear and useful over the measured temperature range.

The Arrhenius parameters calculated in this work are compared to historical values in Table 3.3. The present work includes the highest experimental temperatures measured. Our reported activation energy is elevated but still within uncertainty of previously reported data at lower temperatures. The elevated activation energy measured in this study may reflect the increased energy required for evaporation and desorption of strontium from the graphite surface upon evaporation. The diffusivity at 1273 K calculated from the present work is 155 times lower than that of the H-451 irradiated structural graphite reported by Moormann et al. [32].

Table 3.3: Comparison with other results.

Researchers	Graphite Type	Temp. Range (K)	E_a (kJ/mol)	D_0 (m^2/s)	D_{1273K} (m^2/s)	Reference
Hensel, et al.	A3-3 matrix, Unirradiated	1173-1873	303	1.0×10^{-2}	3.7×10^{-15}	[32, 37]

Moormann, et al.	H-451 structural, Irradiated	N/A	268	1.7×10^{-2}	1.7×10^{-13}	[32]
Nabielek	N/A structural, Unirradiated	1123-1673	324	8.3×10^{-1}	4.2×10^{-14}	[32]
Nabielek (2)	N/A matrix, Unirradiated	1473-1873	312	5.6×10^{-2}	8.8×10^{-15}	[32]
Sandalls, et al.	AGL 9 (0 µg Sr/g graphite)	1473-1667	347	2.0×10^{0}	1.2×10^{-14}	[38]
	AGL 9 (35 µg Sr/g graphite)	1450-1667	447	2.1×10^{4}	9.2×10^{-15}	
	AGL 9 (2000 µg Sr/g graphite)	1100-1333	117	7.4×10^{-5}	1.2×10^{-9}	
This Study	IG-110 structural, Unirradiated	1773-1973	346	1.7×10^{-1}	1.1×10^{-15}	

The historical data suggests that neutron irradiation will have a greater effect on strontium diffusion than the type of graphite. It has been observed that the diffusion of cesium and strontium were inversely proportional to the neutron fluence in the highly graphitized graphite grade H-451. For example, cesium effective diffusivity decreased by a factor of 100 in H-451 graphite irradiated to a fast neutron fluence of 4.6×10^{25} n/m^2 [41]. This decrease was well-correlated with an increase in sorptivity. Similar results were reported for strontium [41-42]. Additional work is needed to determine how the diffusivity of strontium will change in irradiated IG-110 graphite.

In studies of the structural graphite sourced from reactor cores, there are measurable levels of fission products which may affect strontium diffusion [35, 39-41]. The presence of cesium and barium have been reported to increase strontium diffusion rates [35]. Studies of the chemical form of fission products in HTGRs most commonly focus on the kernel and coolant circuit regions of the reactors. There are few or no studies that have examined the relative importance of strontium release from the fuel kernel or U contamination as two potential sources of ^{90}Sr in reactor graphite.

3.7. Conclusions and Future Work

Effective diffusion coefficients of strontium have been measured in IG-110 graphite over the temperature range 1773 K – 1973 K using a time-release method. The resulting diffusivities are lower than those reported by other researchers in other forms of graphite using alternative methods. Future work is needed to characterize the chemical form of strontium in the graphite and to examine the effects of neutron irradiation, graphite oxidation, and potential chemical trapping of strontium by other elements. Additional experiments are also needed to re-examine the concentration dependence on the strontium effective diffusion coefficient.

3.8. Acknowledgments

This research has been supported by the U.S. Department of Energy Nuclear Energy University Program grant NEUP-12830. This material is based on work supported under an Integrated University Program Fellowship (DE-NE000118 Mod 007).

3.9. References

[1] *High Temperature Gas Cooled Reactor Fuels and Materials*; International Atomic Energy Agency: Vienna, Austria, 2010; p 182.

[2] Demkowicz, P. A.; Liu, B.; Hunn, J. D., Coated particle fuel: Historical perspectives and current progress. *J. Nucl. Mater.* **2019,** *515*, 434-450.

[3] Demkowicz, P. A.; Hunn, J. D.; Petti, D. A.; Morris, R. N., Key results from irradiation and post-irradiation examination of AGR-1 UCO TRISO fuel. *Nucl. Eng. Des.* **2018,** *329*, 102-109.

[4] Barnes, C. M. *AGR-1 Fuel Product Specification and Characterization Guidance*; EDF-4380, Rev. 8; Idaho National Laboratory: Idaho Falls, ID, 2006a; p 46.

[5] Hunn, J. D.; Lowden, R. A. *Data Compilation for AGR-1 Baseline Coated Particle Composite LEU01-46T*; Oak Ridge National Laboratory: Oak Ridge, TN, 2006a; p 235.

[6] Hunn, J. D.; Lowden, R. A. *Data Compilation for AGR-1 Variant 1 Coated Particle Composite LEU01-47T*; Oak Ridge National Laboratory: Oak Ridge, TN, 2006b; p 192.

[7] Hunn, J. D.; Lowden, R. A. *Data Compilation for AGR-1 Variant 2 Coated Particle Composite LEU01-48T*; Oak Ridge National Laboratory: Oak Ridge, TN, 2006c; p 162.

[8] Hunn, J. D.; Lowden, R. A. *Data Compilation for AGR-1 Variant 3 Coated Particle Composite LEU01-49T*; Oak Ridge National Laboratory: Oak Ridge, TN, 2006d; p 186.

[9] Hunn, J. D.; Montgomery, F. C.; Pappano, P. J. *Data Compilation for AGR-1 Baseline Compact Lot LEU01-46T-Z*; Oak Ridge National Laboratory: Oak Ridge, TN, 2006a; p 51.

[10] Hunn, J. D.; Montgomery, F. C.; Pappano, P. J. *Data Compilation for AGR-1 Variant 1 Compact Lot LEU01-47T-Z*; Oak Ridge National Laboratory: Oak Ridge, TN, 2006b; p 53.

[11] Hunn, J. D.; Montgomery, F. C.; Pappano, P. J. *Data Compilation for AGR-1 Variant 2 Compact Lot LEU01-48T-Z*; Oak Ridge National Laboratory: Oak Ridge, TN, 2006c; p 43.

[12] Hunn, J. D.; Montgomery, F. C.; Pappano, P. J. *Data Compilation for AGR-1 Variant 3 Compact Lot LEU01-49T-Z*; Oak Ridge National Laboratory: Oak Ridge, TN, 2006d; p 44.

[13] Demkowicz, P. A.; Harp, J. M.; Winston, P. L.; Ploger, S. A. *Analysis of Fission Products on the AGR-1 Capsule Components*; Idaho National Laboratory: Idaho Falls, ID, 2013; p 50.

[14] Barnes, C. M. *AGR-2 Fuel Specification*; Idaho National Laboratory: Idaho Falls, ID, 2009.

[15] BWXT *Industrial Fuel Fabrication and Development Lot G73AA-10-69308*; 2008.

[16] BWXT *Industrial Fuel Fabrication and Development Lot G73I-14-69307*; 2008.

[17] BWXT *Industrial Fuel Fabrication and Development Lot G73J-14-93071A, G73J-14-93073A, G73J-14-93074A*; 2008.

[18] BWXT *Industrial Fuel Fabrication and Development Lot G73H-10-93085B*; 2009.

[19] Hunn, J. D.; Montgomery, F. C.; Pappano, P. J. *Data Compilation for AGR-2 UCO Baseline Compact Lot LEU09-OP2-Z*; Oak Ridge National Laboratory: Oak Ridge, TN, 2010; p 132.

[20] Hunn, J. D.; Montgomery, F. C.; Pappano, P. J. *Data Compilation for AGR-2 UCO Variant Compact Lot LEU06-OP1-Z*; Oak Ridge National Laboratory: Oak Ridge, TN, 2009; p 114.

[21] Hunn, J. D.; Montgomery, F. C.; Pappano, P. J. *Data Compilation for AGR-2 UCO Baseline Compact Lot LEU07-OP1-Z*; Oak Ridge National Laboratory: Oak Ridge, TN, 2009; p 130.

[22] Hunn, J. D. *Data Compilation for AGR-2 Baseline Coated Particle Batch G73J-14-93071A*; Oak Ridge National Laboratory: Oak Ridge, TN, 2008; p 15.

[23] Hunn, J. D.; Montgomery, F. C.; Pappano, P. J. *Data Compilation for AGR-2 B&W UO2 Compact Lot LEU11-OP2-Z*; Oak Ridge National Laboratory: Oak Ridge, TN, 2010; p 165.

[24] Hunn, J. D. *Data Compilation for AGR-2 Baseline Coated Particle Batch G73J-14-93072A*; Oak Ridge National Laboratory: Oak Ridge, TN, 2008; p 13.

[25] Hunn, J. D. *Data Compilation for AGR-2 UCO Variant Coated Particle Batch G73J-14-93073A*; Oak Ridge National Laboratory: Oak Ridge, TN, 2008; p 12.

[26] Hunn, J. D. *Data Compilation for AGR-2 UCO Variant Coated Particle Batch G73J-14-93074A*; Oak Ridge National Laboratory: Oak Ridge, TN, 2008; p 12.

[27] Hunn, J. D. *Data Compilation for AGR-2 B&W UO2 Coated Particle Batch G73H-10-93085B*; Oak Ridge National Laboratory: Oak Ridge, TN, 2010; p 18.

[28] Demkowicz, P. A.; Hunn, J. D.; Morris, R. N.; van Rooyen, I.; Gerczak, T.; Harp, J. M.; Ploger, S. A. *AGR-1 Post Irradiation Examination Final Report*; Idaho National Laboratory: Idaho Falls, ID, 2015; p 132.

[29] Hunn, J. D.; Baldwin, C. A.; Montgomery, F. C.; Gerczak, T. J.; Morris, R. N.; Helmreich, G. W.; Demkowicz, P. A.; Harp, J. M.; Stempien, J. D., Initial examination of fuel compacts and TRISO particles from the US AGR-2 irradiation test. *Nucl. Eng. Des.* **2018,** *329*, 89-101.

[30] Stempien, J. D.; Demkowicz, P. A. *AGR-2 Irradiation Experiment Fission Product Mass Balance*; Idaho National Laboratory: Idaho Falls, ID, 2019.

[31] *A Review of Radionuclide Release From HTGR Cores During Normal Operation*; 1009382; Palo Alto, CA, 2003.

[32] Collin, B. P. *Diffusivities of Ag, Cs, Sr, and Kr in TRISO Fuel Particles and Graphite*; Idaho National Laboratory: Idaho Falls, ID, 2016; p 40.

[33] *Fuel performance and fission product behaviour in gas cooled reactors*; International Atomic Energy Agency: Vienna, Austria, 1997; p 529.

[34] Demkowicz, P. A.; Reber, E. L.; Scates, D. M.; Scott, L.; Collin, B. P., First high temperature safety tests of AGR-1 TRISO fuel with the Fuel Accident Condition Simulator (FACS) Furnace. *J. Nucl. Mater.* **2015,** *464*, 320-330.

[35] Myers, B. F.; Bell, W. E. *Strontium transport data for HTGR systems*; General Atomic Company: San Diego, CA, 1974; p 75.

[36] Carter, L. M.; Seelig, J. D.; Brockman, J. D.; Robertson, J. D.; Loyalka, S. K., ICP-MS measurement of silver diffusion coefficient in graphite IG-110 between 1048K and 1284K. *J. Nucl. Mater.* **2018,** *498*, 44-49.

[37] Hensel, W.; Hoinkis, E., The diffusion of Sr in the graphitic Matrix A3-3 in vacuum and in the presence of hydrogen. *J. Nucl. Mater.* **1991,** *184* (2), 88-96.

[38] Sandalls, F. J.; Walford, M. R., Laboratory determinations of strontium diffusion coefficients in graphite. *J. Nucl. Mater.* **1976,** *62* (2-3), 265-272.

[39] Hayashi, K.; Kikuchi, T.; Kobayashi, F.; Minato, K.; Fukuda, K.; Ikawa, K.; Iwamoto, K., Distribution of fission products in irradiated graphite materials of HTGR fuel assemblies: Third and fourth OGL-1 fuels. *J. Nucl. Mater.* **1985,** *136* (2-3), 207-217.

[40] Hayashi, K.; Kobayashi, F.; Minato, K.; Ikawa, K.; Fukuda, K., In-pile release behavior of metallic fission products in graphite materials of an HTGR fuel assembly. *J. Nucl. Mater.* **1987,** *149* (1), 57-68.

[41] Myers, B. F., A review of the diffusion of selected fission product metals in polycrystalline graphite. In *Proceedings of a Colloquium held at Hahm-Meitner-Institut*, Hoinkis, E., Ed. Berlin, 1981; pp 56-67.

[42] Myers, B. F.; Jensen, D. D.; Zumwalt, L. R., The diffusion of cesium and strontium in H-327 graphite during the Peach Bottom Fuel Test Element experiments. In *Proceedings of a Colloquium held at Hahn-Meitner-Institut*, (Ed.), E. H., Ed. Berlin, 1981; pp 166-171.

[43] Schenk, W.; Nabielek, H., High-temperature reactor fuel fission product release and distribution at 1600 to 1800 °C. *Nucl. Technol.* **1991,** *96* (3), 323-336.

[44] Schenk, W.; Pott, G.; Nabielek, H., Fuel accident performance testing for small HTRs. *J. Nucl. Mater.* **1989,** *171*, 19-30.

[45] Liu, X.; Huang, X.; Xie, F.; Jia, F.; Feng, X.; Li, H., Source Term Analysis of the Irradiated Graphite in the Core of HTR-10. *Sci. Technol. Nucl. Install.* **2017,** *2017*, 1-6.

[46] Carter, L. M.; Brockman, J. D.; Loyalka, S. K.; Robertson, J. D., Measurement of cesium diffusion coefficients in graphite IG-110. *J. Nucl. Mater.* **2015,** *460*, 30-36.

[47] Carter, L. M.; Brockman, J. D.; Robertson, J. D.; Loyalka, S. K., ICP-MS measurement of diffusion coefficients of Cs in NBG-18 graphite. *J. Nucl. Mater.* **2015,** *466*, 402-408.

[48] Carter, L. M.; Brockman, J. D.; Robertson, J. D.; Loyalka, S. K., Diffusion of cesium and iodine in compressed IG-110 graphite compacts. *J. Nucl. Mater.* **2016,** *476*, 30-35.

[49] Carter, L. M.; Brockman, J. D.; Robertson, J. D.; Loyalka, S. K., ICP-MS measurement of iodine diffusion in IG-110 graphite for HTGR/VHTR. *J. Nucl. Mater.* **2016,** *473*, 218-222.

[50] Olander, D. R., *Fundamental Aspects of Nuclear Fuel Elements*. Energy Research and Development Administration: 1976; p 629.

[51] Carter, L. M. ICP-MS analysis of fission product diffusion in graphite for high-temperature gas-cooled reactors. University of Missouri - Columbia, Columbia, MO, 2015.

[52] Carter, L. M.; Brockman, J. D.; Loyalka, S. K.; Robertson, J. D., Calibration of a system for measurements of diffusion coefficients of fission products in HTGR/VHTR core materials. *J. Radioanal. Nucl. Chem.* **2016,** *307*, 1771-1775.

[53] Ratliff, J., Investigation of the molecular species produced by the vaporization of the Group IIA metal nitrates from a graphite surface. *Anal. Chim. Acta* **1996,** *333* (3), 285-293.

CHAPTER 4:
EFFECTIVE DIFFUSIVITY OF Ag AND MIGRATION OF Pd IN IG-110 GRAPHITE

The results of this study were published in 2022 as follows: T.M. Weilert, K.L. Walton, S.K. Loyalka, J.D. Brockman. Effective diffusivity of Ag and migration of Pd in IG-110 graphite. *Journal of Nuclear Materials* **2022**. 559, 153427.

4.1. Abstract

Silver-110m transport through intact TRISO fuel particles under normal HTGR operating conditions is a well-documented phenomenon. Recent and past literature has shown the significance of palladium attack on SiC potentially facilitating the transport of silver through this otherwise intact layer. Migration of these fission products through TRISO fuel particles will result in their subsequent deposition into, and transport through, further release barriers including structural graphite. A diffusion cell designed to simulate HTGR conditions was constructed and connected to an ICP-MS and used to perform time-release diffusion measurements at standard and off-normal HTGR operating temperatures (1073 K – 1973 K). Silver and palladium release rates were measured in IG-110 graphite loaded individually or together, the latter of which consisted of silver and palladium co-loaded in the graphite samples. Effective diffusivities of silver and palladium were calculated from these release rates. The results of this work, summarized using the Arrhenius equation, are:

Ag in IG-110 graphite loaded with Ag:

$$D_{Ag,IG-110} = \left(2.7 \times 10^{-1}\, {}^{m^2}/_{s}\right) exp\left(\frac{-2.24 \times 10^{5}\, {}^{J}/_{mol}}{RT}\right)$$

Ag in IG-110 graphite loaded with Ag and Pd:

$$D_{Ag\ (+Pd),IG-110} = \left(8.7 \times 10^{-3}\, {}^{m^2}/_{s}\right) exp\left(\frac{-1.78 \times 10^{5}\, {}^{J}/_{mol}}{RT}\right)$$

Pd in IG-110 graphite loaded with Ag and Pd:

$$D_{Pd\ (+Ag),IG-110} = \left(6.7 \times 10^{0}\, {}^{m^2}/_{s}\right) exp\left(\frac{-3.83 \times 10^{5}\ \ {}^{J}/_{mol}}{RT}\right)$$

*Author's note: When discussing diffusivity measurements on IG-110 graphite loaded with both Ag and Pd, the designation Ag + Pd will be used. When referencing the individual components of this system, Ag (+Pd) and Pd (+Ag) will be used to indicate focus on the Ag and Pd component measurements, respectively.

4.2. Introduction

The current industry-standard fuel form for high-temperature gas-cooled reactors (HTGRs) is the tristructural isotropic (TRISO) coated fuel particle. In TRISO fuel particles, the UO_2 or UCO fuel kernel is coated with successive barriers composed of a porous graphite buffer layer, an inner pyrocarbon layer (IPyC), a SiC layer, and an outer pyrocarbon layer (OPyC). The barriers are designed to minimize breakthrough of fission products over the expected lifetime of the fuel.

Several experiments have evaluated fission product retention of TRISO fuel under normal and off-normal HTGR conditions. The Advanced Gas Reactor Fuel Qualification and Development (AGR) program is led by Idaho National Laboratory (INL) with contributions to post-irradiation examination (PIE) and fuel fabrication from Oak Ridge National Laboratory (ORNL) and BWX Technologies [1-6]. This program has conducted seven fuel performance irradiations of TRISO fuel particles in cylindrical compacts (AGR-1, AGR-2, AGR-3/4, and AGR-5/6/7) [7]. Overall, the TRISO fuel exhibited excellent performance with zero detected failures during the AGR-1 irradiation, and only four detected SiC failures throughout all 72 compacts [8]. Post-irradiation examination of remaining ^{110m}Ag content in these AGR-1 compacts revealed high fractional releases from all compacts during irradiation. Additionally, gamma scanning of select graphite holders of the AGR-2 tests revealed significant Ag deposition outside of some compacts in quantities far greater than contributions solely from damaged TRISO particles [9]. Individually examined particles also revealed significant Ag depletion [10].

The presence of Pd in graphite is of interest because it is known to chemically attack the SiC barrier layer in TRISO fuel [11]. Fission of ^{235}U produces the radioisotope ^{107}Pd ($t_{1/2} = 6.5 \times 10^6$ y) with a cumulative yield of 1.25%, along with several other stable isotopes of Pd. Studies of Pd behavior in HTGRs have so far focused primarily on the interaction of Pd with the SiC retentive layer of TRISO fuel particles. Numerous studies have confirmed the presence of Pd-containing nodules at grain boundaries and triple points of the SiC in irradiated TRISO fuel particles [11-16]. AGR-1 PIE revealed that localized degradation of this layer was highly correlated with failure of the IPyC layer

resulting from buffer shrinkage [17]. This degradation, in turn, was theorized to have provided a path for the escape of volatile fission products, particularly ^{110m}Ag. AGR-2 tests of the same nature, however, did not exhibit any IPyC-adjacent failures to Pd-degraded SiC sites; instead the failures were believed to be the result of higher irradiation temperature or the presence of Ni [10]. Regardless of the nature of the initial release, the above studies indicate a high likelihood of eventual Pd migration through TRISO fuel particles and potentially into the surrounding structural graphite of HTGRs. Indeed, there is already evidence of this occurrence. Leach solutions from graphite holders 1 and 2 of the AGR-1 test revealed the presence of 0.1% - 1% of the predicted capsule inventory of ^{105}Pd [18]. Although Pd is not considered a radiologically significant radionuclide, its ability to form stable alloy complexes with several other metals may alter the behavior of various fission products in all release barriers of HTGR fuels.

^{110m}Ag ($t_{1/2}$ = 250 days) is a gamma emitter produced directly as a blocked fission product with an approximate yield of 0.03%. ^{110m}Ag plates out at relatively high temperatures within an HTGR and is an important contributor to HTGR personnel occupational dose [19]. Ag is the primary design-limiting radionuclide for HTGRs due to its high release from intact TRISO fuel particles at normal operating temperatures, as well as its tendency to deposit directly onto the reactor turbine (specific to a direct cycle HTGR) [19]. Reactor designs are currently required to compensate for the maximum expected occupational dose within a 95% confidence interval. This interval was chosen due to high uncertainties in predicting Ag release in operating HTGRs [19]. Ag and Pd

are both noble metals and mixtures of Ag and Pd are miscible in the solid and liquid phase [20]. Ag in Ag-Pd alloys evaporates at a higher temperature than Ag alone.

The raw materials and forming process dictate the properties of the graphite. The source materials for graphites used in the early fission product diffusion studies are no longer available and therefore new data is needed on currently relevant grades. The modeling codes FRESCO and PARFUME can be used to track the migration of fission products in reactors. These codes use effective diffusion coefficients that have been compiled from historical grades of nuclear graphite [21]. In this classical approach the term 'effective' diffusion coefficient is used to summarize all transport processes, including evaporation, adsorption, diffusion, and trapping, into a single transport process [22]. Pd diffusion is not currently modelled in fission product release codes and its monitoring is solely devoted to SiC penetration depth.

The results presented in this work are intended as an extension to Ag diffusivity measurements made in IG-110 graphite over the temperature range 1048 K – 1284 K [23]. In the present work, time-release diffusion measurements on Ag in unirradiated IG-110 graphite were conducted in the temperature range 1073 K – 1973 K. This range is intended to overlap expected normal operating temperatures as well as temperatures resulting from transient conditions such as a loss-of-forced coolant accident, where maximum temperatures are expected to reach ~1873 K [24]. Diffusion measurements were also made on IG-110 graphite loaded with both Ag and Pd. These experiments explore the possible effects of "metallic traps," initially proposed in Förthmann [25]. Metallic traps are described as small metal droplets in which the Ag becomes dissolved,

thus lowering its vapor pressure and, by extension, decreasing the diffusivity of Ag in the system. Pd time-release measurements were conducted in the graphite spheres loaded with Ag and Pd, and then in graphite spheres loaded with only Pd. These are the first time-release measurements of Pd migration through nuclear grade graphite.

4.3. Theory

The release rates of the Ag and Pd in graphite were measured using a time-release method. The diffusion of an element in a graphite sphere is described using Fick's second law of diffusion with the associated boundary conditions [26]:

$$\frac{\partial C(r,t)}{\partial t} = \frac{1}{r^2}\frac{\partial}{\partial r}\left(Dr^2\frac{\partial C(r,t)}{\partial r}\right) \tag{4.1}$$

$$C(r,0) = C_0 \tag{4.2}$$

$$C(0,t) = finite \tag{4.3}$$

$$C(R,t) = 0 \tag{4.4}$$

Where D is the effective diffusion coefficient (m^2/s), $C(r,t)$ is the concentration of the element of interest as a function of position and time (g/m^3), r is the radial coordinate (m), R is the radius of the sphere (m), t is the time (s), and C_0 (g/m^3) is the known concentration of diffusant. While distribution measurements demonstrated uneven initial distribution of both Ag and Pd, the concentration profiles were assumed to be uniform, thereby satisfying the conditions in Eqn. 4.2. Previous work by this group on Ag has demonstrated only a small change in the calculated effective diffusivities when using the known initial distribution [23]. This assumption, and work demonstrating its validity, will be addressed further in later sections. The fractional release for this system can be

obtained using either a series expansion technique or a Laplace transform [26]. The cumulative fractional release in the series form is shown in Eqn. 4.5:

$$F(t) = \frac{m_{diffused}(t)}{m_0} = 1 - \frac{6}{\pi^2}\sum_{n=1}^{\infty}\frac{1}{n^2}e^{-(\frac{n\pi}{R})^2 Dt} \tag{4.5}$$

Where $F(t)$ is the fractional release of the diffusant at any given time, $m_{diffused}(t)$ is the total mass of diffusant (g) lost at any given time, and m_0 is the initial mass of diffusant (g) in the sample. Diffusion coefficients were determined by fitting Eqn. 4.5 to experimental, cumulative release data. The series in Eqn. 4.5 was limited to 100 terms. In general, when C_0 is a function of r, the cumulative fractional release is:

$$F_{\text{general}}(t) = \frac{4R^2}{m_0}\sum_{n=1}^{\infty} A_n \frac{(-1)^{1+n}}{n}\left(1 - e^{-\left(\frac{n\pi}{R}\right)^2 Dt}\right) \tag{4.6}$$

where the Fourier coefficient for the initial condition is:

$$A_n = \frac{2}{R}\int_0^R C(r,0)\sin\left(\frac{n\pi}{R}r\right)\, r\, dr \tag{4.7}$$

In this work, Eqn. 4.6 was evaluated with both a straight line fit and linear interpolation to $C_0(r,0)$. In particular, for $C(r,0) = \alpha + \beta(r/R)$, Eqn. 4.7 can be evaluated analytically:

$$A_{\text{linear},n} = -\frac{2R}{(n\pi)^3}[2\beta + (-1)^n((n\pi)^2(\alpha+\beta) - 2\beta)] \tag{4.8}$$

where α and β are constants with units g/m^3 and r is the radial coordinate of the sphere. Equation 4.7 can be evaluated numerically when using piecewise linear interpolation or an alternative interpolation of discrete data describing $C(r,0)$. This can be done with Mathematica's NIntegrate with automatic settings, although most quadrature rules for numerical integration are sufficient. Further details on this derivation can be found in Carter, et al. [27].

4.4. Experimental

4.4.1. Materials and Preparation

A block of IG-110 graphite was purchased from the manufacturer, Toyo Tanso®. This as-received block was milled into spheres with approximate radii of 0.16 cm. The spheres were infused with Ag, Pd, and Ag + Pd using a pressurization technique first reported by Carter et al. and later used on Sr [23, 28]. Briefly, the graphite spheres were placed into the 45-mL polytetrafluoroethylene (PTFE) liner of a Parr model 4744 pressure vessel along with 5 mL of high purity water and 15 mL of 1.00 part-per-thousand $AgNO_3$ (High Purity Standards) or $Pd(NO_3)_2$ (Inorganic Ventures) in 2 – 5% v/v nitric. The pressure vessel, once assembled, was heated for four alternating cycles of 2 hours at 508 K and 1 hour at 373 K. The vessel was allowed to cool and afterwards the spheres were removed, rinsed with 18.2 MΩ water, and then heated overnight under vacuum at 373 K to remove moisture. The graphite spheres were heated to 773 K in a furnace for 30 minutes to dissociate the nitrates. $AgNO_3$ begins to decompose at 663 K, producing Ag metal [29]. $Pd(NO_3)_2$ decomposes on graphite surfaces between 573 K and 873 K, forming metallic Pd [30]. The Ag and Pd diffusants are therefore likely to be present in the IG-110 graphite in metallic form after this point. Once cooled, the graphite spheres were sanded with Al_2O_3 sandpaper and sonicated in high purity water to remove dust. The spheres were then dried at 403 K on a hot plate to remove latent moisture.

SEM imaging revealed no visible differences in the graphite microstructure before and after the pressure vessel loading. Selected photos of unloaded IG-110 and IG-110 loaded with Ag are shown in images A and B, respectively, in Fig. 4.1. Ag and Pd

concentrations were too low to determine a loading profile by energy-dispersive x-ray spectroscopy.

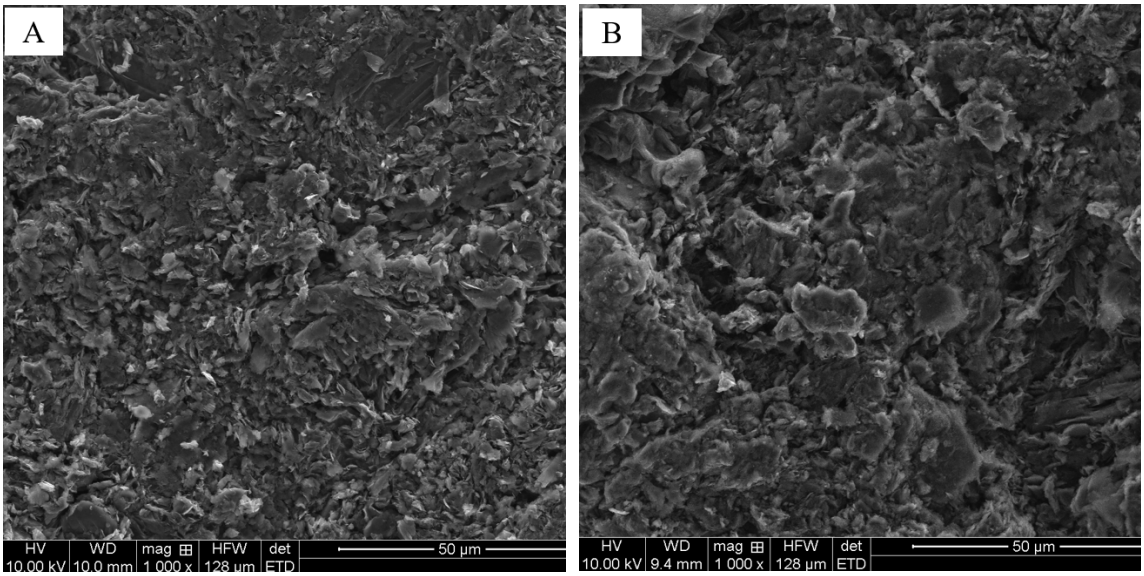

Figure 4.1: Image A is an SEM image of IG-110 graphite before loading and image B is an SEM image of an IG-110 graphite sphere after it had been loaded with Ag.

Distribution of Ag and Pd within the graphite was measured using laser-ablation inductively-coupled plasma mass spectrometry (LA-ICP-MS). Three different analyses were performed, one each on a Ag-only sample, Pd-only sample, and Ag + Pd sample. A loaded graphite sample was bisected using a stainless-steel razor blade and the flat surface was smoothed with 220 grit Al_2O_3 sandpaper. The bisected sample was analyzed using a Photon Machines 192 nm laser coupled to a NexION® 300x ICP-MS. The laser was operated with a power density of 2 mJ/cm^2, and 10 Hz pulse frequency. The laser scan length was 40 µm. Spot samplings were taken in 40 µm line scans every 100 µm across the diameter of the graphite sphere. Scans across the sphere diameter were

collected 4 times for a total of 8 radial measurements; the sample orientation was rotated by 45 degrees around the center axis between each line scan.

The mass loading of Ag or Pd or both into each IG-110 graphite sphere was measured using standard comparator instrumental neutron activation analysis (INAA) [31]. Comparator standards were prepared by drying aliquots of Ag (High Purity Standards) or Pd (Inorganic Ventures) nitrate standards in 0.3 mL high density polyethylene vials. These standards along with the Ag and Ag + Pd samples were irradiated in polyethylene vials for 5 seconds each in a neutron flux of 5.5×10^{13} n/cm^2/s using the row 2 pneumatic tube system at the University of Missouri Research Reactor (MURR). The Pd standards and samples were irradiated for 30 seconds. Neutron activation proceeded through the reactions ^{107}Ag (n,γ)^{108}Ag, ^{109}Ag(n,γ)^{110}Ag, and ^{108}Pd(n,γ)^{109m}Pd which decay via beta emission with associated gamma ray emissions at 633 keV, 658 keV, and 189 keV, respectively. The gamma ray emissions were measured using a high purity germanium (HPGe) detector operated using Canberra Genie 2000 software.

4.4.2. Time-Release Measurements

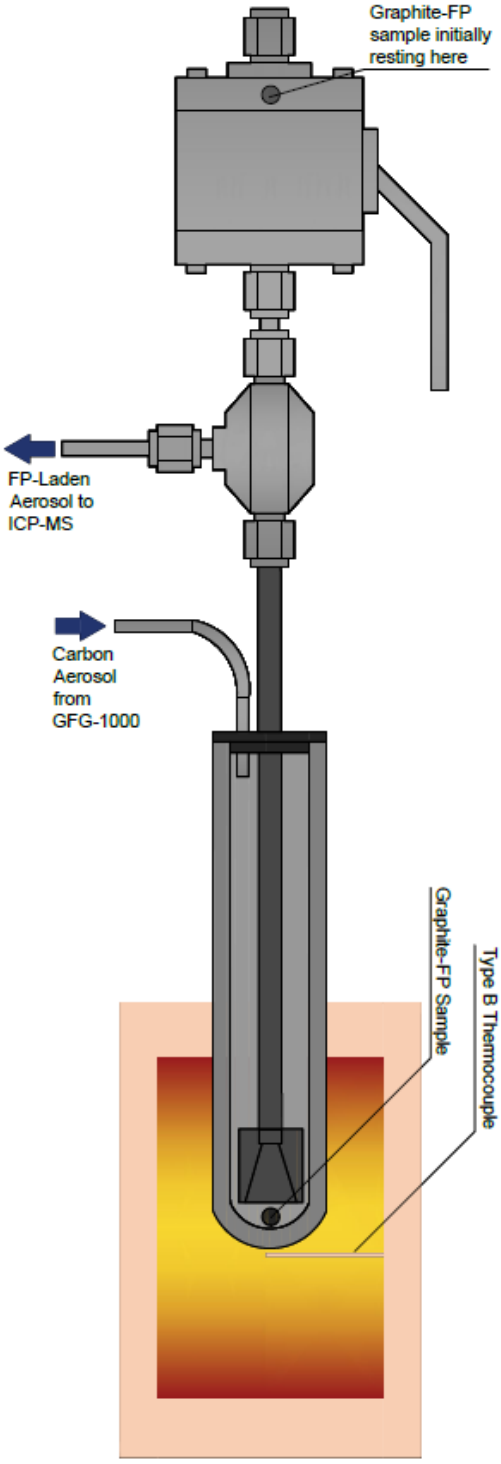

Figure 4. 2: Diffusion cell setup. FP refers to fission product, however the elements used were non-radioactive surrogates [28].

Release rates of Ag and Pd from IG-110 graphite were measured using a method that has been previously described [23, 26-28, 32-33]. The diffusion cell, shown in Fig. 4.2, was located inside of a modified SentroTech high temperature box furnace (Model ST-1700C-888). Briefly, the IG-110 graphite sample was held within a sealed chamber separated from the SiC diffusion cell by a high-temperature ball valve (Swagelok ®). The temperature near the base of the diffusion cell was monitored using a Type B Pt/Rh thermocouple. To begin an experiment, the furnace was heated to the experimental temperature, and He gas flowed through the closed system at a rate of 2 L/min for approximately 1 hour. During the heat-up time, the ball valve was left partially open to allow He to flush room air out of the chamber holding the graphite sphere. Once the experimental temperature was reached the carbon aerosol generator was turned on and mass spectrometer background measurements of the diffusants were collected for 30-60 minutes. The ball valve was then opened which allowed the graphite sphere to fall into the pre-heated diffusion chamber. The diffusant released from the graphite sphere was carried to the detector using a He jet system constructed from a modified Palas carbon aerosol generator [26]. The diffusant release rate was measured using a Perkin Elmer NexION® scanning quadrupole ICP-MS. The ICP-MS used a glass expansion dual-port spray chamber sample introduction system which allowed for the simultaneous introduction of the diffusant and a nebulized 1 ng/g In internal standard, used to correct for instrumental drift. Each time-release experiment was conducted isothermally at temperatures ranging from 1073 K – 1973 K for graphite spheres containing Ag and Ag + Pd, and 1623 K – 1973K for spheres containing only Pd.

At the end of the experiment, diffusant remaining in the graphite sphere was measured using INAA. The mass loss of diffusant measured in each sphere was used to calibrate the instantaneous ICP-MS signal from the count rate to the experimental release rate in g/s. The calibration factor, F_c (g/count), for each sphere was determined using Eqn. 4.9:

$$F_c = \frac{m_D}{K_m} \tag{4.9}$$

Here, m_D is the total mass loss of the diffusant (g) and K_m is the total detector counts measured by the ICP-MS over the experimental time frame for each diffusant. The calibration factor was used to convert the measured instantaneous count rate, k_i (counts/s), to the experimental release rate, Z_r (g/s), using Eqn. 4.10:

$$Z_r = k_i F_c \tag{4.10}$$

From this release rate the fractional release at each measured time point was calculated by integration of the experimental release rate with respect to time to yield the mass of Ag diffused and then dividing by the initial mass of Ag.

4.5. Results

4.5.1. Diffusant Mass Loading and Distribution

The initial mass loadings, final diffusant masses, and test temperatures of the Ag-only, Ag + Pd, and Pd-only experiments are reported in Table 4.1.

Table 4.1: Initial and final masses of Ag and Pd and experimental temperatures.

Tested Diffusant(s)	Temperature (K)	Initial Mass (μg)		Final Mass (μg)		Date of Exp. (YYMMDD)
		Ag	Pd	Ag	Pd	
Ag	1073	0.85		0.55		210616
Ag	1073	0.92		0.61		210618
Ag	1073	1.02		0.70		210620
Ag	1223	0.87		0.00		181014
Ag	1223	1.33		0.00		210213
Ag	1223	1.09		0.00		210218
Ag	1373	0.84		0.00		190426
Ag	1373	0.80		0.00		181013
Ag	1373	1.52		0.00		210220
Ag	1523	1.11		0.00		190410
Ag	1523	1.08		0.00		210223
Ag	1523	1.42		0.00		210225
Ag	1673	0.92		0.00		190408
Ag	1673	0.89		0.00		190207
Ag	1673	1.25		0.00		210228
Ag	1673	1.30		0.00		210302
Ag	1673	1.26		0.00		210304
Ag	1773	0.86		0.00		190227
Ag	1773	0.62		0.00		190302
Ag	1773	1.42		0.00		210306
Ag	1873	0.70		0.00		190323
Ag	1873	0.96		0.00		200127
Ag	1873	0.12		0.00		200129
Ag	1973	0.92		0.00		190422
Ag	1973	0.78		0.00		190423
Ag	1973	0.86		0.00		190417
Ag + Pd	1073	0.61	1.08	0.57	1.02	190503
Ag + Pd	1223	0.45	1.16	0.00	1.02	190429
Ag + Pd	1373	0.61	0.83	0.00	0.88	190424
Ag + Pd	1523	0.46	1.06	0.00	0.90	190513
Ag + Pd	1623	0.47	1.00	0.00	0.54	190401
Ag + Pd	1673	0.42	0.94	0.00	0.58	190403
Ag + Pd	1773	0.57	1.13	0.00	0.28	190509
Ag + Pd	1873	0.47	0.73	0.00	0.00	190507
Ag + Pd	1873	0.66	1.14	0.00	0.00	190511
Ag + Pd	1973	0.73	0.91	0.00	0.00	190504
Pd	1623		1.38		1.31	190413
Pd	1673		1.32		0.38	190321
Pd	1973		1.33		0.00	200307

The radial distributions of diffusant were measured in a bisected graphite sphere using LA-ICP-MS and reported in Figs. 4.3-4.5. Each radial point was constructed from the average and standard deviation of 8 measurements. The slope of the Ag-only profile was 1139 counts/cm, 95% CI [-17959, 20238]. There was no significant effect of radial distance with Ag counts ($F_{1,14} = 0.016$, $p > 0.89$). The slope of the Pd-only profile was 3509 counts/cm, 95% CI [-25653, -10491]. There was a significant trend between radial distance and measured Pd counts ($F_{1,14} = 26.5$, $p < 0.0002$). The slope of the graphite sphere loaded with Ag and Pd was -11461 counts/cm, 95% CI [4922, 18001] for Ag and -523 counts/cm, 95% CI [-1068, 2115] for Pd. There was a significant association between radial distance and Ag ($F_{1,13} = 14.6$, $p < 0.002$) but not between radial distance and Pd ($F_{1,13} = 0.513$, $p < 0.49$).

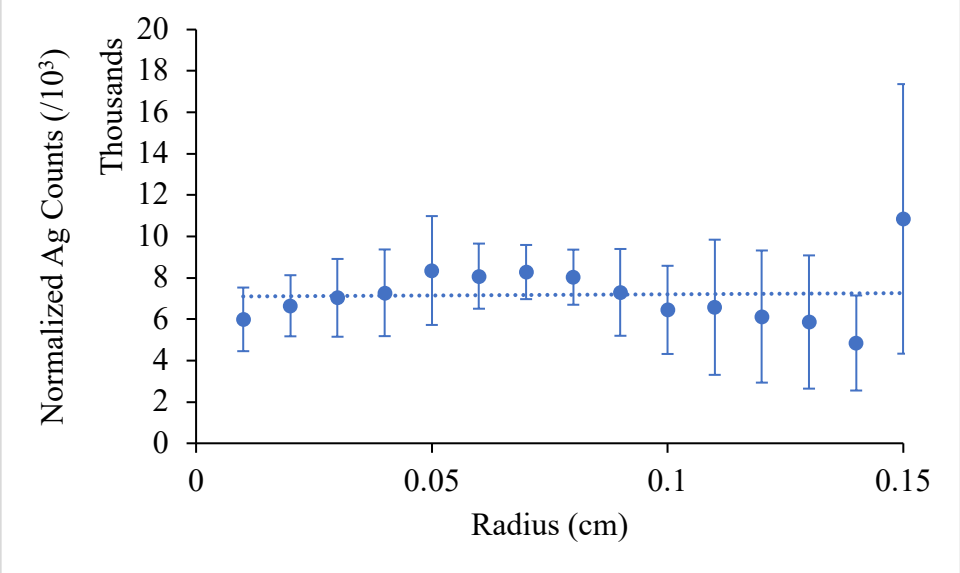

Figure 4.3: Radial distribution of Ag in IG-110 loaded with only Ag.

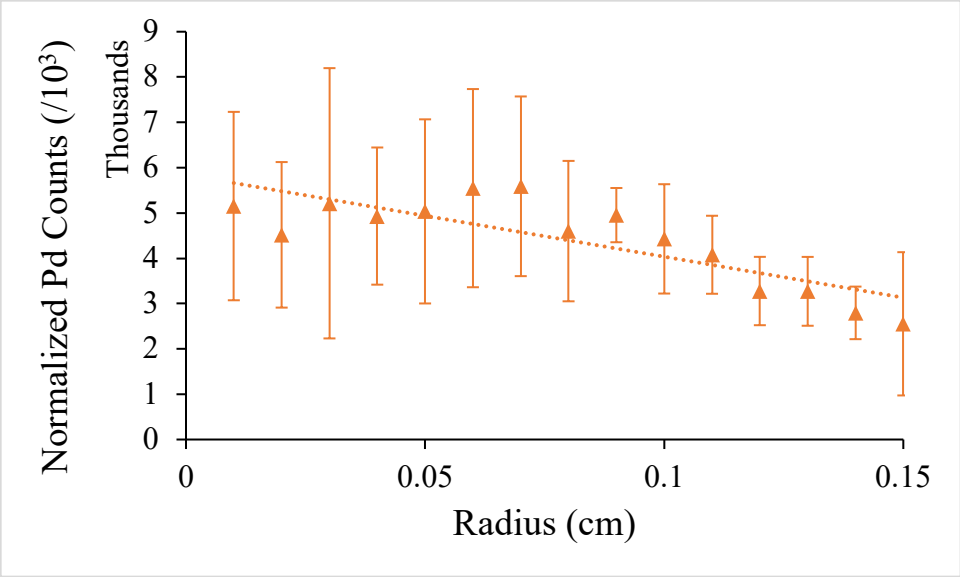

Figure 4.4: Radial distribution of Pd in IG-110 loaded with only Pd.

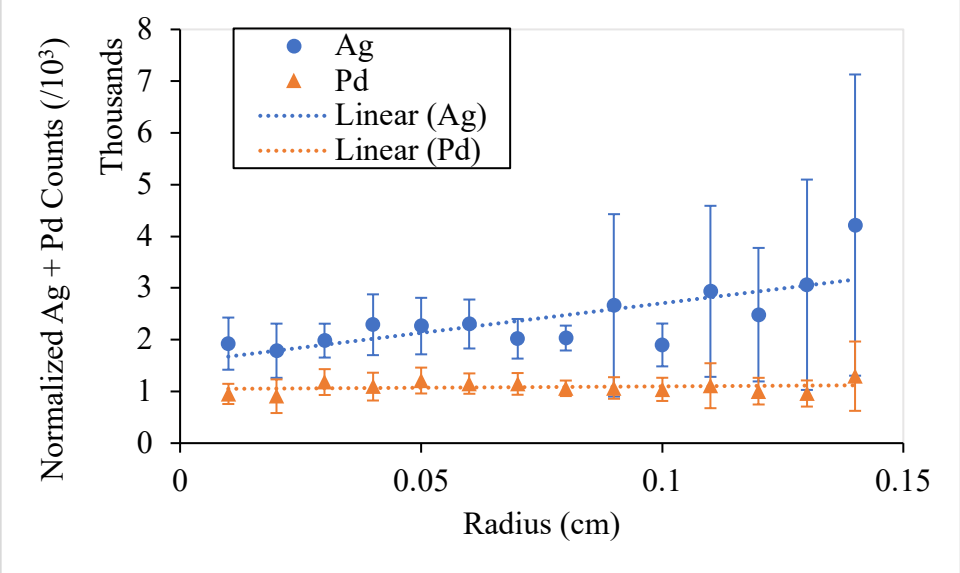

Figure 4.5: Radial distribution of Ag and Pd in IG-110 loaded as a binary system.

4.5.2. Diffusant Release Profiles

The experimental release rates for two Ag-only time-release experiments conducted at 1223 K and 1973 K are shown in Figs. 4.6-4.7, respectively. The total mass

loss of Ag at temperatures above 1073 K was 100%, see Table 4.1. In experiments conducted at temperatures up to 1373 K the Ag signal returned to the pre-experiment baseline level after all of the Ag inventory had diffused. In this temperature range, the Ag background for the duration of the experiment was modeled by taking the average of 10 data points recorded immediately prior to the introduction of the graphite sample.

In experiments conducted at or above 1373 K, the Ag signal did not return to the initial baseline, as shown in Fig. 4.7. A new background value was calculated by averaging the last ten points of the plateau signal at the end of the experiment, seen as $S_{plateau}$ in Fig. 4.7. This new background value was subtracted from all earlier points up to and including the peak. Equation 4.11 was then used to determine the point of 100% fractional release:

$$S_{Ag} = S_{total} - \left(S_{plateau} + 3 * std_{Splateau}\right) \tag{4.11}$$

Where S_{Ag} is the corrected Ag signal, S_{total} is the total Ag signal, $S_{plateau}$ is the average signal calculated from the 10 points at the end of the plateau, and $std_{Splateau}$ is the standard deviation of Ag signal in the last ten points of the plateau region. The point at which S_{Ag} became negative was taken to be the first point after 100% fractional release. The time-release data was used to construct fractional release curves as described in Section 4.2.

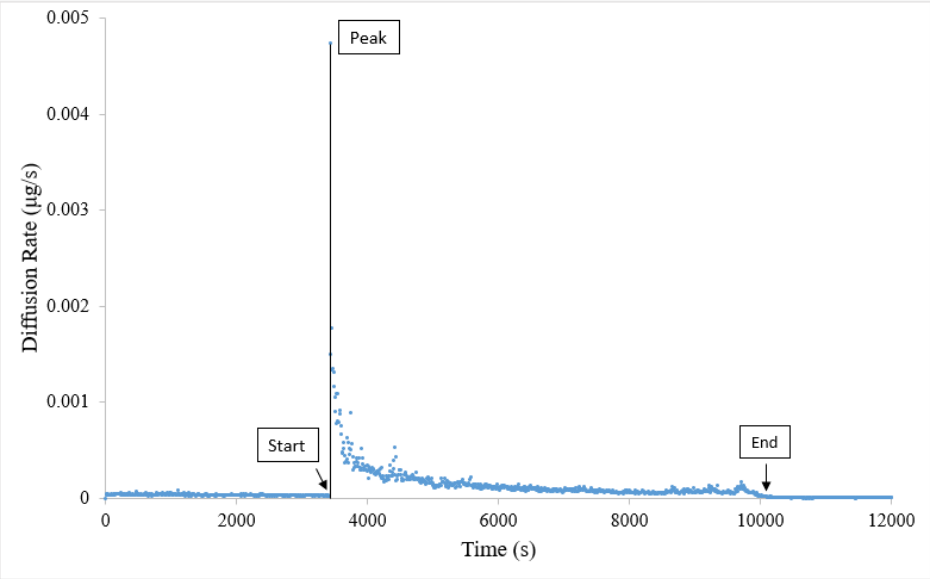

Figure 4.6: Ag release from IG-110 at 1223 K.

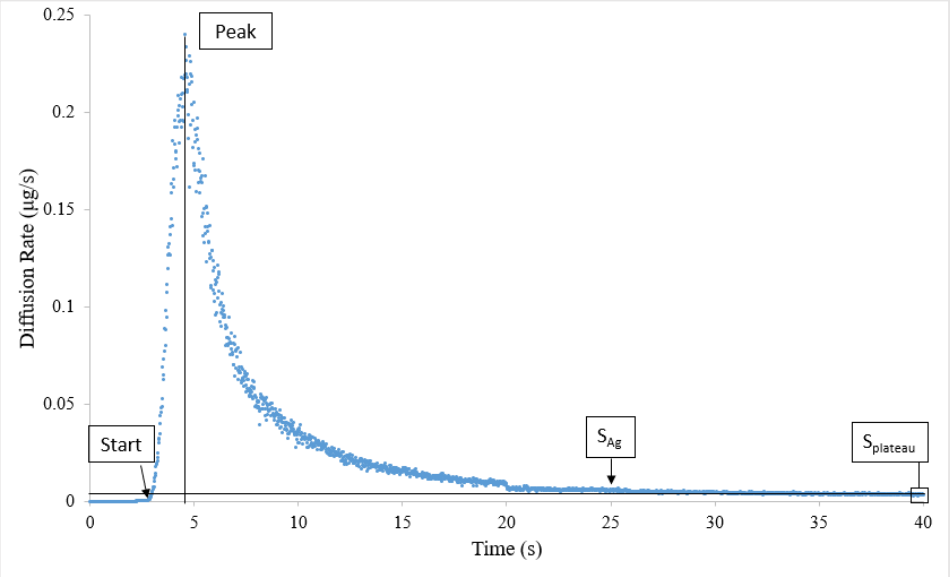

Figure 4.7: Ag release from IG-110 at 1973K.

4.5.3. Fractional Release Curves

The Ag fractional release measurements were run in triplicate except for the 1673 K experiment in which 5 samples were tested. The diffusant profiles measured using LA-ICP-MS demonstrated that the diffusant distributions were not uniform in the graphite spheres. To better understand the effects of a nonuniform diffusant loading, the time-release data for Ag in IG-110 graphite at 1523 K was fit using Eqns. 4.5 and 4.6 using a nonlinear least squares method. For Eqn. 4.6, Eqn. 4.7 was evaluated by both piecewise linear and straight-line fit (Eqn. 4.8) of the Ag profile data reported in Fig 4.3. The radial profiles of Ag in IG-110 are shown in Fig. 4.8. at 0 s, 1 s, 2 s, 4 s, 8 s, and 16 s after the start of the experiment. While LA-ICP-MS found a non-zero concentration at the surface, the radial profiles in Fig. 4.8 reflect the surface's boundary condition (Eqn. 4.4). The three approaches to handling the radial diffusant concentration converge at the 8 s and 16 s time points. Table 4.2 compares the diffusion coefficient of Ag at 1523 K for constant C_0, straight line fit to initial Ag profile, and linear interpolation of the initial Ag profile. The error between the fitted release curves and measured release data is:

$$error = \frac{y - y_{fit}}{y} \tag{4.12}$$

Where y_{fit} is the predicted cumulative release fraction and y is the measured cumulative release fraction. From Eqn. 4.12, a positive error results from a predicted value that is less than the measured value, while a negative error results when the fitted model predicts a higher value than measured. The mean absolute value of the error (MAE) serves as a goodness of fit between the simulated and measured cumulative releases. For constant C_0, the diffusion coefficient was 7.16×10^{-9} m^2/s. The diffusion coefficient from a straight

line fit and linear interpolation was 7.47 × 10^{-9} m^2/s and 7.83 × 10^{-9} m^2/s, respectively. There is an 8.5% difference between the diffusivities derived from the interpolated and constant radial profiles. Since the diffusion coefficients from all three approaches agreed well, Eqn. 4.5 was used for the estimation of the diffusion coefficient for the remaining results.

Table 4.2: Diffusion coefficients of Ag in IG-110 at 1523K using Eqns. 4.5-4.6. MAE is the mean absolute value of the error.

Model	D (m^2/s)	Positive Error (%)		Negative Error (%)		MAE (%)
		Min	Max	Min	Max	
Constant	7.16×10^{-9}	0.0155	4.76	0.03	2183	16.85
Straight Line	7.47×10^{-9}	0.0072	4.74	0.05	1973	16.42
Interpolated	7.83×10^{-9}	0.0183	4.62	0.03	2821	18.87

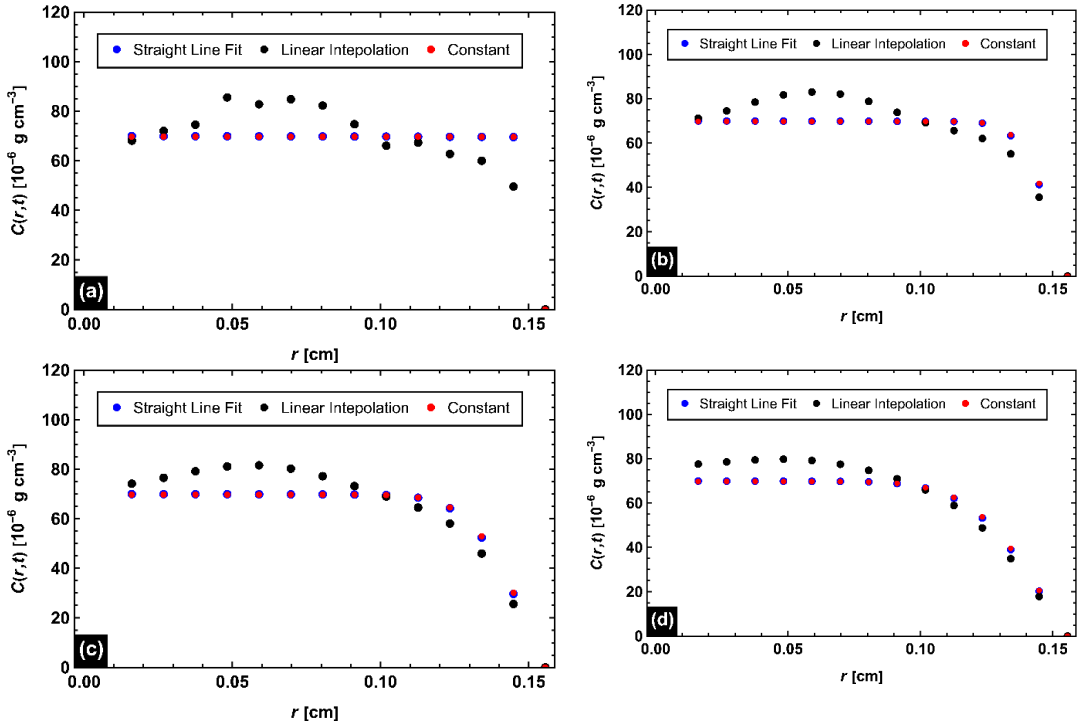

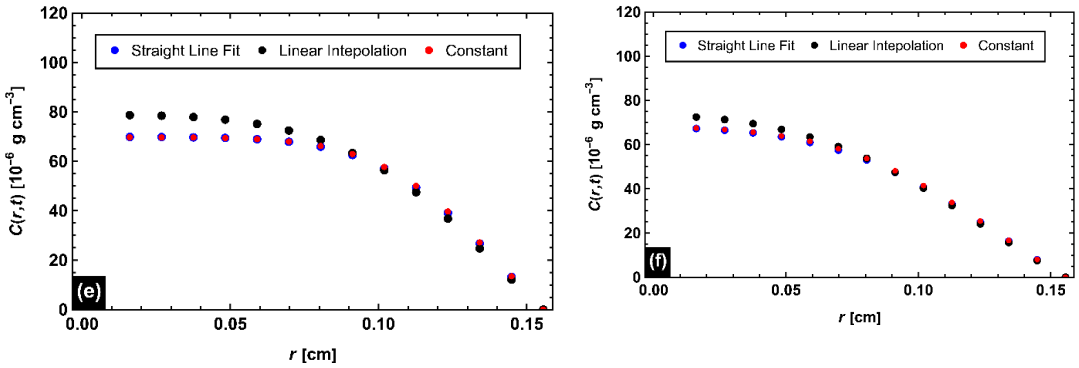

Figure 4.8: The radial profile Ag in IG-110 at select times 0 s (a), 1 s (b), 2 s (c), 4 s (d), 8 s (e), and 16 s (f). The release measurement on this sample was taken at 1523 K and the diffusion coefficient was calculated using Eqn. 4.5 for constant radial profile (red), Eqn. 4.6 for linear interpolation (black), and a straight-line fit (blue) of Fig. 4.3. In this case, the straight-line fit is nearly identical to the constant radial profile.

4.5.3.1. Ag and Ag (+Pd)

Selected experimental Ag fractional release curves from graphite spheres loaded with Ag and Ag + Pd, and the best-fit solutions from Eqn. 4.5, are reported in Figs. 4.9 and 4.10, respectively. The remaining fractional release curves can be found in Appendix A.

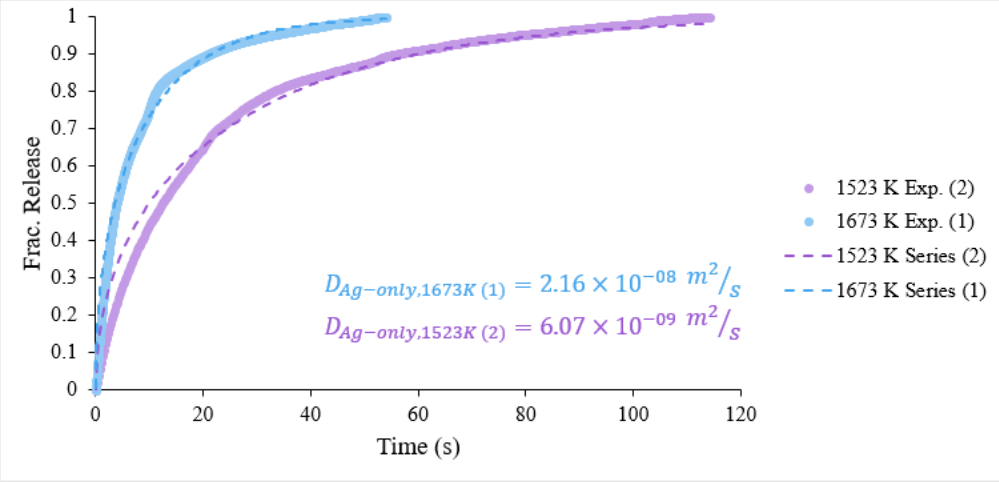

Figure 4.9: Fractional release of Ag from spheres of IG-110 graphite loaded with 1 µg of Ag at 1673 K and 1523 K. The dotted lines represent the best-fit curves, derived using an assumed constant uniform profile. "Series" refers to the series expansion shown in Eqn. 4.5.

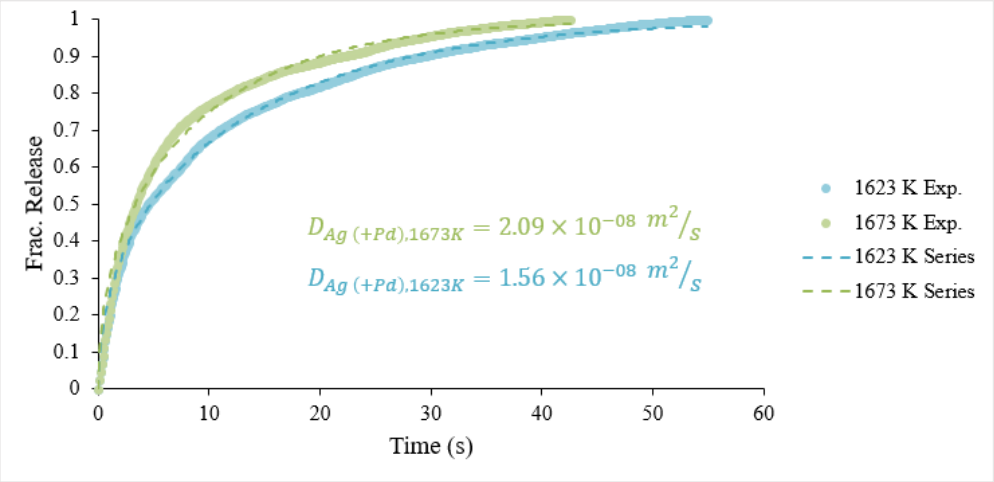

Figure 4.10: Fractional release of Ag from spheres of IG-110 graphite loaded with 0.5 µg of Ag and 1 µg of Pd at 1623 K and 1673 K. The dotted lines represent the best-fit curves, derived using an assumed constant uniform profile. "Series" refers to the series expansion shown in Eqn. 4.5.

4.5.3.2. Pd (+Ag)

Pd release was also measured from the spheres loaded with both Pd and Ag. Selected cumulative fractional release plots of Pd (+Ag) in IG-110 graphite spheres are shown in Fig. 4.11. All other fractional release curves can be found in Appendix A. As with Ag, the fractional release plots shown were made using Eqn. 4.5, assuming a uniform Pd profile.

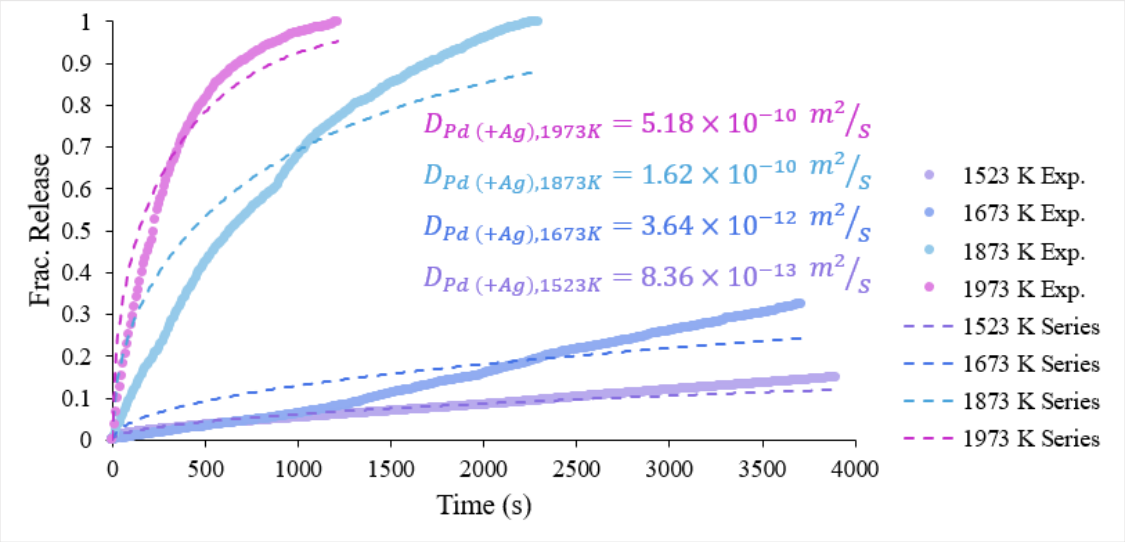

Figure 4.11: Fractional release of Pd from spheres of IG-110 graphite loaded with approximately 1 µg of Pd and 0.5 µg of Ag at temperatures between 1523 K and 1973 K. "Series" refers to the series expansion shown in Eqn. 4.5.

4.5.3.3. Pd

A set of IG-110 graphite spheres was loaded with only Pd. Time-release diffusion experiments were conducted at 1623 K, 1673 K, and 1973 K. Pd released from the IG-110 graphite sphere was detected at the ICP-MS instrument at 1623 K and 1673 K but

not at 1973 K. The fractional release measured at 1623 K was very low and a diffusion coefficient could not be fit from the data.

4.5.4. Arrhenius Plot and Activation Energy

A summary of the effective diffusion coefficients determined by fitting Eqn. 4.5 to the experimental data are presented in Table 4.3. The Ag-only results at 1673 K have been broken into two subsets, 1673 K (1) and 1673 K (2), to be discussed.

Table 4.3: Fitted diffusivities for Ag and Pd in IG-110 graphite spheres. The graphite spheres loaded with only Ag were analyzed in triplicate and the mean diffusion coefficient and the standard deviation have been reported.

	Ag loaded IG-110	Ag + Pd loaded IG-110		Pd loaded IG-110
Temp. (K)	Ag Diffusion Coefficient (m^2/s)	Ag Diffusion Coefficient (m^2/s)	Pd Diffusion Coefficient (m^2/s)	Pd Diffusion Coefficient (m^2/s)
1073	$3.5\ (0.5) \times 10^{-12}$	1.8×10^{-13}	$< 4.5 \times 10^{-14}$	N/A
1223	$8.3\ (1.4) \times 10^{-11}$	1.7×10^{-10}	$< 5.4 \times 10^{-14}$	N/A
1373	$7.1\ (0.9) \times 10^{-10}$	2.8×10^{-9}	$< 5.4 \times 10^{-14}$	N/A
1523	$6.1\ (1.0) \times 10^{-9}$	6.6×10^{-9}	8.4×10^{-13}	N/A
1623	N/A	1.6×10^{-8}	4.0×10^{-12}	N/A
1673 (1)	$3.1\ (1.3) \times 10^{-8}$	2.1×10^{-8}	3.6×10^{-12}	4.1×10^{-13}
1673 (2)	$4.8\ (1.1) \times 10^{-9}$	N/A	N/A	N/A
1773	$1.3\ (0.4) \times 10^{-8}$	2.4×10^{-8}	1.2×10^{-11}	N/A
1873	$2.7\ (1.0) \times 10^{-8}$	1.8×10^{-8}	1.6×10^{-10}	N/A
1973	$3.6\ (0.7) \times 10^{-8}$	2.2×10^{-8}	5.2×10^{-10}	N/A

The classical Arrhenius equation, Eqn. 4.13, was used to describe the temperature dependence of the effective diffusion coefficients in IG-110 graphite:

$$D = D_o e^{-E_a/RT} \tag{4.13}$$

Where D_0 is the pre-exponential factor (m^2/s) and E_a is the activation energy (kJ/mol). The Arrhenius plots of Ag, Ag (+Pd), and Pd (+Ag) in IG-110 graphite are shown in Figs. 4.12 and 4.13. The Ag and Ag (+Pd) E_a and D_0 were calculated using a best fit line at test temperatures up to 1673 K. At temperatures above 1673 K, the association between the natural log of the Ag diffusion coefficient and reciprocal temperature was non-linear. These measurements are therefore not included in the Arrhenius calculations. Table 4.4 reports the values and uncertainties of the pre-exponential factor D_0 and the activation energy E_a for Ag, Ag (+Pd), and Pd (+Ag). The uncertainties of E_a and D_0were calculated from the standard errors of the best fit parameters of the linear regression.

Table 4.4: Pre-exponential and activation energies of the tested diffusants. The +/- values are 1 standard deviation.

System	Diffusant	D_0 (m^2/s)	$\pm\Delta D_0$ (m^2/s)	E_a (kJ/mol)	$\pm\Delta E_a$ (kJ/mol)
Ag	Ag	2.7×10^{-1}	7.5×10^{-2}	224	4
Ag + Pd	Ag	8.7×10^{-3}	2.0×10^{-3}	178	13
Ag + Pd	Pd	6.7×10^{0}	1.2×10^{1}	383	48

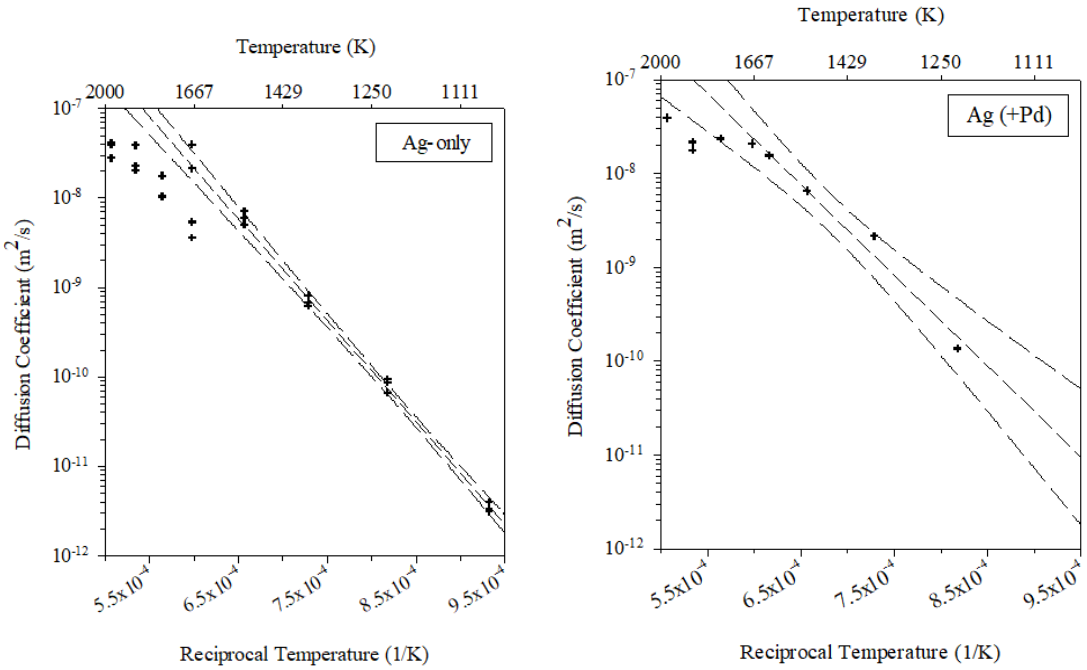

Figure 4.12: On the left is the Arrhenius plot of triplicate measurements of Ag in IG-110 loaded with only Ag and on the right is the Arrhenius plot of Ag in IG-110 loaded with Ag and Pd. The least-squares fit only includes diffusion coefficients at temperatures up to 1673 K. The uncertainty bands represent the 95% confidence interval.

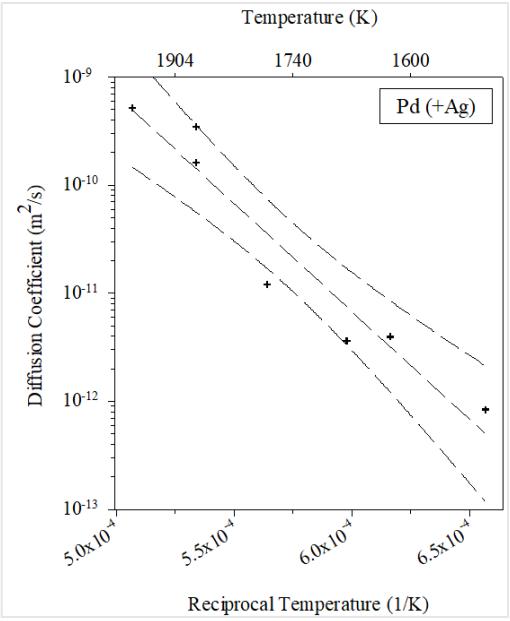

Figure 4.13: Arrhenius plot of Pd in IG-110 graphite loaded with approximately 0.5 µg of Ag and 1 µg of Pd.

4.6. Discussion

The release rates of Ag and Pd diffusant from IG-110 graphite were measured using a time-release experiment. An advantage of the time-release method is that the effective diffusion coefficients are measured in conditions similar to those found in an HTGR, that is the graphite sphere is in flowing He laden with carbon dust. The effective diffusion coefficients, which summarize all transport processes into a single parameter, were determined by fitting Eqn. 4.5 to the cumulative release data using a non-linear least squares approach. The Ag-only experiments were completed at each temperature in triplicate and the standard deviation of the fitted diffusion coefficients ranged from 13% - 37%, see Table 4.3. The mixed Ag and Pd system and the Pd-only experiments were conducted with one sample at each temperature, except for Ag + Pd at 1873 K in which two experiments were performed. Pd was not detected in the time-release experiments conducted in the Ag + Pd system at temperatures between 1073 K and 1373 K. A maximum diffusion coefficient was calculated using Eqn. 4.5 based on a minimum detectable mass loss of 4%, which is the minimum detectable difference of the INAA measurements. The variability in the measured Ag fractional release data is attributed to experimental factors such as differences in the diffusant loading profile and inhomogeneity in the IG-110 graphite.

Selected experimental cumulative Ag release fits are shown in Figs. 4.9-4.10 and the rest can be found in Appendix A. In some cases, the experimental releases exhibited non-Fickian behavior. The model overpredicted the cumulative release curve at short times. A potential explanation for this overestimation was the breakdown of the

assumption of a constant diffusant profile in the graphite spheres. The diffusant profiles are reported in Figs. 4.3-4.5. In the case of diffusion of Ag at 1523 K, the straight line fit of the graphite sphere shown in Fig. 4.3 yielded a diffusivity 4.3% higher than for constant C_0. The diffusion coefficient from the linear interpolation was 9.4% higher than for constant C_0. These deviations fall well within the 17% standard deviation of the three measurements conducted at 1523 K. The three approaches have similar minimum and maximum positive errors and minimum negative errors for their fitted curves, see Table 4.2. The approaches do differ in maximum negative error, thus varying in the overestimation of the fractional release at the onset of Ag diffusion.

The observed non-Fickian behavior could also be caused by sorption, evaporation, or trapping processes if those processes compete with diffusion as the rate-limiting step. The elevated baseline of the Ag signal after complete release of the sample inventory, as described in Section 4.5.2, indicates that Ag release was not simply described by Fick's equations. It is hypothesized that the Ag released from the IG-110 graphite adsorbed onto surfaces in the SiC diffusion cell or He jet outlet tubing, most likely on carbon dust which had built up in the system. Ag desorption from these surfaces would explain the observations that all of the Ag was released from the majority of the graphite samples, see Table 4.1, and yet there remained an elevated Ag signal at the end of the experiments above 1373 K, see Fig. 4.7.

Figure 4.14 shows the fractional release of Ag from IG-110 graphite at 1073 K with and without Pd. The Ag diffusion coefficient decreased by a factor of nearly 20 in the presence of Pd at 1073 K. For this reason, the Ag (+Pd) measurement at 1073 K has

not been included in the Arrhenius calculations. It is hypothesized that at 1073 K, a Ag-Pd alloy was formed. The observed decrease in Ag diffusivity is then explained by a trapping of Ag in the alloy. The Ag-Pd phase diagram indicates that the melting point of the Ag-Pd alloy increases with a higher mole fraction of Pd [20]. At temperatures near 1235 K, the melting point of Ag, the difference in measured diffusion rates of Ag between the Ag-only graphite samples and the Ag + Pd graphite samples is much smaller and the mass loss of Ag was total while Pd remained in the sphere. It is noteworthy that Pd is used as a matrix modifier in trace element analysis by electrothermal atomic absorption spectrometry (ETAAS). In this analytical method, the analyte is placed on a graphite tube furnace and rapidly heated to produce an atomic vapor for the absorption measurement. The addition of Pd reduces the volatility of low melting point elements, providing better measurement conditions [30].

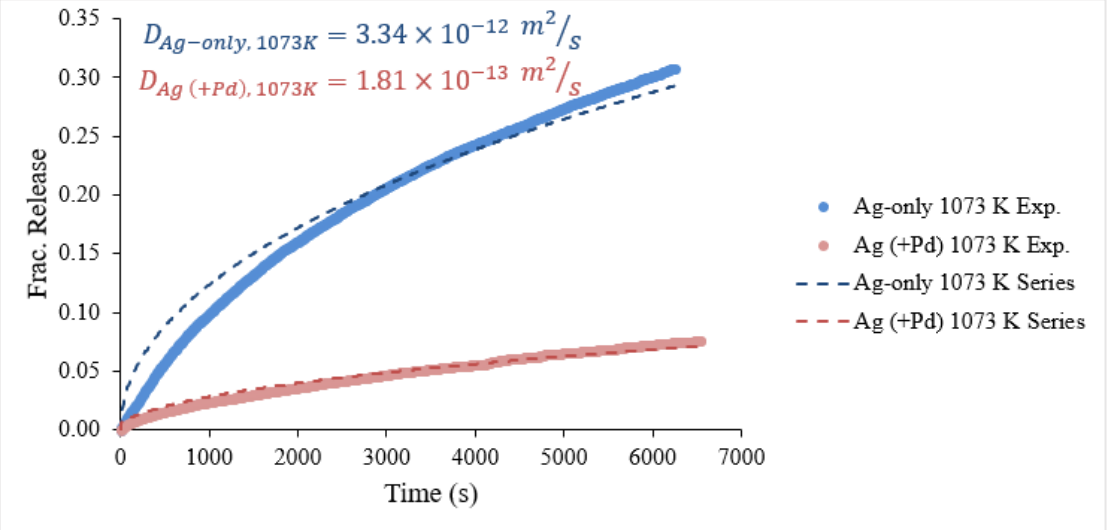

Figure 4.14: Comparative fractional release plots of Ag release at 1073 K with (bottom line) and without (top line) Pd. "Series" refers to the series expansion shown in Eqn. 4.5.

The Ag-only time-release measurements were conducted over a two-year time with good agreement with the exception of the experiments performed at 1673 K. The first time-release measurements at 1673 K fell on the linear regression line of the Arrhenius plot, see Fig. 4.12. When these experiments were repeated approximately two years later the results deviated significantly from the Arrhenius plot and instead aligned with the higher temperature measurements. In the intervening two years the SiC components of the diffusion cell had been replaced and the spacing of the inner tube from the bottom of the outer tube (see Fig. 4.2) may have altered the transport rate of Ag out of the system. No significant difference was seen in repeated experiments performed at the other temperatures which all took place over a similar time frame to that of the 1673 K experiments, including measurements at all reported temperatures below 1673 K and one at 1773 K. Because of the clear separation in diffusivities at 1673 K, these results have been broken into two subsets, 1673 K (1) and 1673 K (2). Only 1673 K (1) has been included in the Arrhenius calculations. This decision was considered valid because exclusion of these results gave Arrhenius parameters of $E_a = 223 \pm 4$ kJ/mol and $D_0 = 2.4 \times 10^{-1} \pm 6.6 \times 10^{-2}$ m^2/s which are within error of the reported results in Fig. 4.12 and Table 4.4.

Non-linearity in the Ag-only and Ag (+Pd) Arrhenius plots was observed at temperatures at and above 1673 K, see Fig. 4.12. There are several potential causes for the non-linear behavior. An experiment was performed at 1673 K with the intention of measuring the absolute release rate of Ag from the system. Ten μL of a ~100 μg/mL Ag standard solution was pipetted onto a small chip of SiC leftover from a previous system

and dried overnight. A time-release experiment was conducted at 1673 K using the method described in Section 4.4.2. It took ~60 s for the Ag signal to return to baseline in this experiment. The 60 s time delay could be due to slow transport of Ag entrained on the helium-transported graphite dust out of the diffusion cell and sorption/desorption of Ag on surfaces in the diffusion cell. It is clear these combined effects will result in a bias at temperatures where diffusion proceeds faster than the time required to transport Ag out of the diffusion cell. This would explain both the poor linear association in diffusion coefficients at 1673 K and higher with lower temperature measurements, as well as the appearance that the measured diffusivities are approaching an asymptotic value of ~4 × 10^{-8} m^2/s. Because of these deviations from expected behavior, the Arrhenius equations for both the Ag-only and Ag (+Pd) sets do not include data from experiments run at 1773 K and above (as well as 1673 K (2) in the case of Ag-only).

The present results are compared with previous works for Ag in structural graphite in Table 4.5. The activation energy measured for Ag in IG-110 graphite in this work was greater than previous results reported by Carter et al. over a narrower temperature range [23]. The concentration of Ag in the samples used by Carter et al. was, on average, 10x greater than the concentrations used in this study. Historically, there is evidence for concentration dependencies of the diffusion coefficient for the elements Sr and Cs [34]. Similar studies for related effects on Ag are not available. For higher loading concentrations the influence from weaker binding sites begins to contribute significantly to diffusion, thus increasing the average speed of migration and the effective diffusivity.

For sufficiently high concentrations the measured diffusivities will no longer increase and the activation energy begins to decrease [34].

Table 4.5: Comparison with other Ag diffusion studies in graphite.

Reference	Graphite Type	Temp. Range (K)	E_a (kJ/mol)	D_0 (m^2/s)	D_{1273K} (m^2/s)
Hayashi [35]	IG-110, irradiated	1173-1303	264	6.3×10^{-3}	9.3×10^{-14}
Causey, et.al. [36]	H-451, unirradiated	753-1073	184	$1.7 \times 10^{+1}$	4.8×10^{-7}
Carter, et.al. [23]	IG-110, unirradiated	1048-1284	174 (12)	6.6×10^{-4}	4.8×10^{-11}
This Study	IG-110, unirradiated	1073-1673	224 (4)	2.7×10^{-1}	1.8×10^{-10}
	IG-110, unirradiated + Pd	1223-1673	178 (16)	8.7×10^{-3}	4.2×10^{-10}

Selected cumulative fractional release curves for Pd in the Ag + Pd system are shown in Fig. 4.11. The poor fits for Pd derived from Eqn. 4.5 indicate that Pd transport is poorly modeled using Fickian diffusion kinetics. The Arrhenius plot of Pd diffusion coefficients from the Ag + Pd system, shown in Fig. 4.13, shows a linear relationship between reciprocal temperature and the natural logarithm of the diffusion coefficient reported in Table 4.3. This suggests that effective diffusion coefficients may still be useful for describing Pd diffusion in IG-110 graphite containing Ag.

Pd diffusion measurements in the absence of Ag were notably different than their Pd (+Ag) counterparts. It was only possible to measure Pd release from the graphite sphere loaded with Pd-only at 1673 K. An attempt was made to measure Pd release from a Pd-only sample at 1973 K. Even though the post-experiment INAA results, reported in

Table 4.1, indicated there was complete loss of Pd from the graphite, there was no corresponding increase of Pd signal above background during the time-release experiment. Additional modeling is needed to elucidate the behavior of Pd migration in IG-110 graphite. There is also a need for more exploration into the behavior of Pd in graphite dust as this may have significance for the behavior of Pd in the HTGR cooling circuit.

4.7. Conclusions and Future Work

Effective diffusion coefficients have been determined for Ag and Pd in IG-110 graphite in the temperature range 1073 K – 1973 K. These results represent the highest temperature Ag diffusion measurements so far performed on unirradiated structural graphite. Ag time-release measurements at and above 1673 K resulted in lower-than-expected diffusivities. It is hypothesized that at temperatures where diffusion proceeds faster than the diffusant can be eliminated from the system the measured diffusion coefficient will be inaccurate, leading to lower-than-expected effective diffusion coefficients at and above 1673 K. In IG-110 graphite loaded with Ag and Pd, the diffusivity of Ag decreased at 1073 K and the diffusivity of Pd increased at 1673 K. This suggests that the presence of Pd, and potentially other platinum group elements, could reduce the diffusion of Ag in graphite at operational temperatures in the HTGR below what is predicted by the Arrhenius parameters. At higher temperatures, the presence of Pd did not significantly alter Ag diffusivity.

Additional work is needed in order to understand the behavior of Pd in both graphite and carbon dust. Alternative diffusion measurement techniques may be better suited to the study of Pd diffusion in graphite. The results reported here show Pd does not behave in a predictable manner in a carbon aerosol atmosphere, and this may have significant implications in modelling of HTGR cooling circuits.

4.8. Acknowledgments

This research has been supported by the U.S. Department of Energy Nuclear Energy University Program grant NEUP-12830. This material is based on work supported under an Integrated University Program Fellowship (DE-NE000118 Mod 007).

The authors wish to express their sincerest gratitude to Ruth-Ann Ngwenyama, Jim Guthrie, and Barry Higgins for their patience and technical support, as well as the MURR Science Instrument Shop for mechanical support.

4.9. References

[1] Demkowicz, P. A.; Liu, B.; Hunn, J. D., Coated particle fuel: Historical perspectives and current progress. *J. Nucl. Mater.* **2019,** *515*, 434-450.

[2] Barnes, C. M. *AGR-1 Fuel Product Specification and Characterization Guidance*; EDF-4380, Rev. 8; Idaho National Laboratory: Idaho Falls, ID, 2006a; p 46.

[3] Barnes, C. M. *AGR-2 Fuel Specification*; Idaho National Laboratory: Idaho Falls, ID, 2009.

[4] BWXT *Industrial Fuel Fabrication and Development Lot G73J-14-93071A, G73J-14-93073A, G73J-14-93074A*; 2008.

[5] BWXT *Industrial Fuel Fabrication and Development Lot G73H-10-93085B*; 2009.

[6] Barnes, C. M. *AGR-3 & 4 Fuel Product Specification*; EDF-6638, Rev. 1; Idaho National Laboratory: Idaho Falls, ID, 2006b.

[7] Gougar, H. D.; Petti, D. A.; Demkowicz, P. A.; Windes, W. E.; Strydom, G.; Kinsey, J. C.; Ortensi, J.; Plummer, M.; Skerjanc, W.; Williamson, R. L.; Wright, R. N.; Li, D.; Caponiti, A.; Feltus, M. A.; O'Connor, T. J., The US Department of Energy's high temperature reactor research and development program - Progress as of 2019. *Nucl. Eng. Des.* **2020,** *358*, 1-15.

[8] Demkowicz, P. A.; Hunn, J. D.; Ploger, S. A.; Morris, R. N.; Baldwin, C. A.; Harp, J. M.; Winston, P. L.; Gerczak, T. J.; van Rooyen, I. J.; Montgomery, F. C.; Silva, C. M., Irradiation performance of AGR-1 high temperature reactor fuel. *Nucl. Eng. Des.* **2015,** *306*, 2-13.

[9] Harp, J. M.; Demkowicz, P. A.; Stempien, J. D., Fission Product Inventory and Burnup Evaluation of the AGR-2 Irradiation by Gamma Spectrometry. *Nucl. Eng. Des.* **2016,** *329*, 134-141.

[10] Hunn, J. D.; Baldwin, C. A.; Montgomery, F. C.; Gerczak, T. J.; Morris, R. N.; Helmreich, G. W.; Demkowicz, P. A.; Harp, J. M.; Stempien, J. D., Initial examination of fuel compacts and TRISO particles from the US AGR-2 irradiation test. *Nucl. Eng. Des.* **2018,** *329*, 89-101.

[11] Demkowicz, P. A.; Hunn, J. D.; Petti, D. A.; Morris, R. N., Key results from irradiation and post-irradiation examination of AGR-1 UCO TRISO fuel. *Nucl. Eng. Des.* **2018,** *329*, 102-109.

[12] Lillo, T. M.; van Rooyen, I. J., Associations of Pd, U and Ag in the SiC layer of neutron-irradiated TRISO fuel. *J. Nucl. Mater.* **2015,** *460*, 97-106.

[13] Olivier, E. J.; Neethling, J. H., The role of Pd in the transport of Ag in SiC. *J. Nucl. Mater.* **2013,** *432* (1-3), 252-260.

[14] Rooyen, I. J. v.; Lillo, T. M.; Wu, Y. Q., Identification of silver and palladium in irradiated TRISO coated particles of the AGR-1 experiment. *J. Nucl. Mater.* **2014,** *446* (1-3), 178-186.

[15] van Rooyen, I. J.; Olivier, E. J.; Neethling, J. H., Fission products silver, palladium and cadmium identification in neutron-irradiated SiC TRISO particles using a Cs-Corrected HRTEM. *J. Nucl. Mater.* **2016,** *476*, 93-101.

[16] Wen, H.; van Rooyen, I. J., Distribution of fission products palladium, silver, cerium, and cesium in the un-corroded areas of the locally corroded SiC layer of a neutron irradiated TRISO fuel particle. *J. Eur. Ceram.* **2017,** *37* (10), 3271-3284.

[17] Hunn, J. D.; Baldwin, C. A.; Gerczak, T. J.; Montgomery, F. C.; Morris, R. N.; Silva, C. M.; Demkowicz, P. A.; Harp, J. M.; Ploger, S. A., Detection and analysis of particles with failed SiC in AGR-1 fuel compacts. *Nucl. Eng. Des.* **2016,** *306*, 36-46.

[18] Demkowicz, P. A.; Harp, J. M.; Winston, P. L.; Ploger, S. A. *Analysis of Fission Products on the AGR-1 Capsule Components*; Idaho National Laboratory: Idaho Falls, ID, 2013; p 50.

[19] *A Review of Radionuclide Release From HTGR Cores During Normal Operation*; 1009382; Palo Alto, CA, 2003.

[20] Ghosh, G.; Kantner, C.; Olson, G. B., Thermodynamic Modeling of the Pd-X (X = Ag, Co, Fe, Ni) Systems. *J. Phase Equilibria* **1999,** *20* (3), 295-308.

[21] Collin, B. P. *Diffusivities of Ag, Cs, Sr, and Kr in TRISO Fuel Particles and Graphite*; Idaho National Laboratory: Idaho Falls, ID, 2016; p 40.

[22] *Fuel performance and fission product behaviour in gas cooled reactors*; International Atomic Energy Agency: Vienna, Austria, 1997; p 529.

[23] Carter, L. M.; Seelig, J. D.; Brockman, J. D.; Robertson, J. D.; Loyalka, S. K., ICP-MS measurement of silver diffusion coefficient in graphite IG-110 between 1048K and 1284K. *J. Nucl. Mater.* **2018,** *498*, 44-49.

[24] *High Temperature Gas Cooled Reactor Fuels and Materials*; International Atomic Energy Agency: Vienna, Austria, 2010; p 182.

[25] Förthmann, R., Influence of metallic traps on the diffusion of silver and caesium in graphitic matrix. In *Hahn-Meitner-Institut fur Kernforschung Berlin GmbH*, Hoinkis, E., Ed. Berlin, Germany, 1981; pp 108-112.

[26] Carter, L. M.; Brockman, J. D.; Loyalka, S. K.; Robertson, J. D., Measurement of cesium diffusion coefficients in graphite IG-110. *J. Nucl. Mater.* **2015,** *460*, 30-36.

[27] Carter, L. M.; Brockman, J. D.; Robertson, J. D.; Loyalka, S. K., ICP-MS measurement of diffusion coefficients of Cs in NBG-18 graphite. *J. Nucl. Mater.* **2015,** *466*, 402-408.

[28] Weilert, T. M.; Walton, K. L.; Loyalka, S. K.; Brockman, J. D., Measurement of effective Sr diffusion coefficients in IG-110 graphite. *Journal of Nuclear Materials* **2021,** *555*, 153102.

[29] Otto, K.; Oja Acik, I.; Krunks, M.; Tõnsuaadu, K.; Mere, A., Thermal decomposition study of HAuCl4·3H2O and AgNO3 as precursors for plasmonic metal nanoparticles. *Journal of Thermal Analysis and Calorimetry* **2014,** *118* (2), 1065-1072.

[30] Volynsky, A. B., Mechanisms of action of platinum group modifiers in electrothermal atomic absorption spectrometry. *Spectrochim. Acta B* **2000,** *55* (2), 103-150.

[31] Greenberg, R. R.; Bode, P.; De Nadai Fernandes, E. A., Neutron activation analysis: A primary method of measurement. *Spectrochimica Acta Part B: Atomic Spectroscopy* **2011,** *66* (3), 193-241.

[32] Carter, L. M.; Brockman, J. D.; Robertson, J. D.; Loyalka, S. K., ICP-MS measurement of iodine diffusion in IG-110 graphite for HTGR/VHTR. *J. Nucl. Mater.* **2016,** *473*, 218-222.

[33] Carter, L. M.; Brockman, J. D.; Robertson, J. D.; Loyalka, S. K., Diffusion of cesium and iodine in compressed IG-110 graphite compacts. *J. Nucl. Mater.* **2016,** *476*, 30-35.

[34] Myers, B. F.; Jensen, D. D.; Zumwalt, L. R., The diffusion of cesium and strontium in H-327 graphite during the Peach Bottom Fuel Test Element experiments. In *Proceedings of a Colloquium held at Hahn-Meitner-Institut*, (Ed.), E. H., Ed. Berlin, 1981; pp 166-171.

[35] Hayashi, K.; Kobayashi, F.; Minato, K.; Ikawa, K.; Fukuda, K., In-pile release behavior of metallic fission products in graphite materials of an HTGR fuel assembly. *J. Nucl. Mater.* **1987,** *149* (1), 57-68.

[36] Causey, R. A.; Wichner, R. P., Silver transport in H-451 graphite. In *Colloquium on the transport of Fission Products in Matrix and Graphite*, Berlin, Germany, 1981.

CHAPTER 5:
EUROPIUM DIFFUSION IN IG-110 NUCLEAR GRAPHITE

The results of this study were published in 2022 as follows: T.M. Weilert, K.L. Walton, S.K. Loyalka, J.D. Brockman. Europium diffusion in IG-110 nuclear graphite. *Journal of Nuclear Materials* **2022**. 561, 153544.

5.1. Abstract

Europium diffusion in graphite has been recognized to be of interest in high-temperature gas reactor safety analyses, particularly as an indicator of strontium diffusion. However, no measurements of europium diffusion coefficients have been reported in the literature. In this work, the effective diffusion coefficient of europium was measured using a time-release method. Natural europium was loaded into pre-milled unirradiated IG-110 graphite spheres using a pressurized acid digestion vessel. The time-release experiments were performed in the temperature range 1823 K – 1973 K using a SiC diffusion cell connected to an inductively-coupled plasma mass spectrometer (ICP-MS) via a He gas line. The results of this work are:

$$D_{Eu,IG-110} = \left(1.5 \times 10^{-3}\ {}^{m^2}/_{s}\right) exp\left(\frac{-2.87 \times 10^5\ {}^{J}/_{mol}}{RT}\right)$$

This effective diffusion coefficient can be used to aid in predictive modelling of europium transport in HTGRs.

5.2. Introduction

The high-temperature gas-cooled reactor (HTGR) uses a multi-layered fuel form consisting of a low-enriched uranium oxicarbide (UCO) or uranium oxide (UO_2) kernel surrounded by a buffer carbon layer, a dense inner pyrocarbon (PyC) layer, SiC, and a final outer layer of PyC. These multi-layered fuels, known as tristructural isotropic (TRISO) fuels, boast excellent fission product retention at operating temperatures between 700 ºC – 950 ºC [1-2]. TRISO particles, once manufactured, are coated with a carbonaceous matrix material and then formed into either right cylindrical compacts or spheres, followed by heating to 800 ºC – 1800 ºC to cure the resin and reduce the impurity content [2]. Compacts are stacked within the structural graphite core of a prismatic reactor while the spheres make up the core of a pebble-bed reactor design. Flowing He is used to transfer the heat from the core, either directly to turbines or a steam generator.

Eu isotopes are low-yield, medium-lived fission products. ^{154}Eu and ^{155}Eu are often observed in post-irradiation analyses and heating tests and are sometimes used as an analog for ^{90}Sr release [3]. Several studies have examined Eu release from irradiated TRISO fuel particles and compacts with in-irradiation and post-irradiation investigations. Minato et al. [4] performed post-irradiation heating tests on irradiated UO_2 TRISO fuel particles sourced from deconsolidated fuel compacts. Despite there being no detected particle failures or observed Pd-induced decomposition of SiC, ^{154}Eu and ^{155}Eu were among several isotopes detected on the surrounding structural graphite sink. These Eu fractional releases were as high as Cs in some cases [4].

Release of Eu from TRISO fuel was also observed in the Idaho National Laboratory's (INL) ongoing Advanced Gas Reactor Fuel Qualification and Development (AGR) Program. In AGR-1, UCO fuel kernels that were coated and compacted on a laboratory scale were irradiated at the Advanced Test Reactor (ATR) [5-13]. Post-irradiation examination (PIE) of AGR-1 capsules indicated release of Eu in excess of one TRISO particle equivalent [14-16]. This released Eu was retained in the surrounding matrix graphite and was only released during heating tests conducted between 1600 ºC – 1800 ºC [15-17]. PIE of the test train found ^{154}Eu in the metal capsule components, as well as the graphite fuel holders indicating Eu released further during the irradiation [14]. There were no detected TRISO failures throughout the course of the AGR-1 irradiation and the amount of Eu release exceeded the amount produced in a single TRISO particle, suggesting that Eu migrated through the SiC boundary during irradiation [14, 17].

In the AGR-2 test, some capsules were heated to higher average and peak temperatures compared to AGR-1 with Capsule 2 achieving a maximum time-average volume-average (TAVA) temperature of 1252 ºC at the end of irradiation and a time-average peak temperature of 1360 ºC. This was 163 ºC higher than the maximum temperature of any capsule in the AGR-1 irradiation [17-18]. The AGR-2 test utilized UCO and UO_2 kernels produced in an industrial scale coater and compacted on a laboratory scale at ORNL [19-32]. PIE of the AGR-2 test train showed Eu release through intact SiC with ^{154}Eu detected in the graphite fuel holder of Capsule 2 [3, 15, 33]. The level of ^{154}Eu outside of intact SiC layers in a compact from Capsule 2 exceeded what could be explained by observed coating failures [33]. Throughout all of Capsule 2,

the total measured amount of ^{154}Eu was equivalent to 1410 particles' worth, or 3.7% of the capsule inventory [3].

The AGR-3/4 experiment was designed to measure fission product transport through compact matrix and structural graphite. This was achieved through the addition of 20 designed-to-fail (DTF) fuel particles in each of the 48 compacts (4 compacts per capsule) within the test train. [5, 34-36]. The fuel kernels of the DTF particles were identical to those of the driver particles and coated with only a thin layer of PyC [37-38]. Capsule 7 was the highest temperature capsule in the AGR-3/4 irradiation with a TAVA temperature of 1345 ºC and a time-averaged peak temperature of 1418 ºC [39]. ^{154}Eu was detected in the inner matrix graphite ring of Capsule 7 in an amount equivalent to 229 particles, more than the 80 DTF particles originally present in the 4 compacts of the capsule [40-41]. The AGR experiments demonstrate that Eu release is associated with increased temperature of the TRISO fuel and supports the possibility that Eu is capable of migrating through intact SiC [15]. Another potential source of Eu in structural graphite is from fission of U that is intrinsically present in the graphite [42].

Eu is well-retained in matrix graphite and it is not expected to migrate during normal reactor operation. Off-normal events such as a loss-of-forced coolant accident have the potential to raise the core temperature to 1620 ºC [2]. These temperatures could enable enhanced Eu diffusion in the core. Structural and matrix graphite are both high-purity, fine-grain, high graphitization, high-isotropy graphites. Modern A3 matrix graphite is produced with different raw materials, manufactured using a hot-pressing method, and annealed at 1850 °C [43]. It has an average particle size of 11.3 μm [44], a

bulk density of 1.3 – 1.7 g/cm^3 [43, 45-46], and a total porosity of 20% [47]. IG-110 structural graphite is prepared using cold isostatic pressing with an annealing temperature at 2900 °C, has a grain size of 20 μm, and a density of 1.76 g/cm^3. The total porosity of IG-110 graphite is 22.3% [48]. IG-110 graphite contains lower concentrations of amorphous carbon and binder as well as a denser, more ordered pore structure. These properties offset each other as it relates to fission product diffusion and radionuclide transport in matrix and structural graphite has historically been treated as a collective process [49]. In previous experiments on Sr diffusion in A3 matrix graphite and structural graphite the reported activation energies ranged from 242 – 303 kJ/mol and 268 – 346 kJ/mol, respectively [50-51]. This suggests that measurement of Eu diffusion in IG-110 allows for estimation of Eu diffusion in matrix graphite. The codes FRESCO and PARFUME could be used to track the migration of Eu in reactors. These codes utilize a single parameter to summarize the transport processes evaporation, adsorption, diffusion, and trapping into a single transport process known as the effective diffusion coefficient [50, 52].

There is little information on fission product diffusion in modern graphite grades and large experimental variation in experiments conducted on historical graphite. Several studies have attempted to measure Eu diffusion, but no diffusivity values have been provided. Cowan and Orth [53] examined diffusion rates of various fission products, including Eu, in irradiated slugs of graphite loaded with ^{235}U. They did not report noticeable diffusion of Eu except at 2400 ºC after heating for 240 s. Orth [54] also examined trends in lanthanide and actinide diffusion in graphite at temperatures between

1600 ºC – 2600 ºC. While no diffusion constants were given, the author noted a strong correlation between diffusion rates and the boiling points of the elements under study. Hayashi et al. [55-56] examined fission product distributions in OGL fuel assemblies taken from the Japan Materials Testing Reactor. The axial profiles of the block and graphite sleeve of the assembly were examined by means of high-purity germanium (HPGe) detection and the radial profiles were measured by lathe sectioning followed by HPGe detection of the graphite powder. Both ^{154}Eu and ^{155}Eu were detected, though only in the inner surface of the graphite sleeve. The Eu was theorized to be attributed solely to nuclear fission and not Eu impurity of the graphite [56]. Myers et al. [57] investigated the diffusion of Eu in a fuel test element of the Peach Bottom reactor. The source material contained precursors of the elements of interest which were then created through transmutation in the reactor. Radial profiles were created from the center post and crucible wall regions of these samples and while the authors stated they were able to fit the Eu profiles with the classical diffusion model no such fits were given. The successes and shortcomings of the above studies demonstrate a need for more quantitative exploration of Eu diffusion in graphite.

In this work, the effective diffusion of Eu was measured in IG-110 structural graphite using a time-release method. IG-110 is currently used in the primary core structures of the High Temperature Test Reactor in Japan and the HTR-10 and HTR-PM test reactors in China. Eu was loaded into pre-milled unirradiated IG-110 graphite spheres using a pressurized acid digestion vessel. The time-release experiments were performed in the temperature range 1823 K – 1973 K using a SiC diffusion cell

connected to an inductively-coupled plasma mass spectrometer (ICP-MS) via a He gas line.

5.3. Theory

The time-release experiment described in this work has previously been successfully applied to effective diffusion measurements of Cs, I, Ag, and Sr in several types of graphite [51, 58-64]. The experiment assumes that migration and release of the Eu diffusant from the graphite is dominated by diffusion, and that effects from adsorption and trapping are minimal [52]. The applicable diffusion equation in spherical coordinates is:

$$\frac{\partial C(r,t)}{\partial t} = \frac{1}{r^2}\frac{\partial}{\partial r}\left(Dr^2\frac{\partial C(r,t)}{\partial r}\right) \tag{5.1}$$

Together with the initial and boundary conditions:

$$C(r,0) = C_0 \tag{5.2}$$

$$C(R,t) = 0 \tag{5.3}$$

Where D is the effective diffusion coefficient (m^2/s); $C(r,t) \geq 0$ is the concentration (g/m^3) of diffusant, in this case Eu, as a function of position and time; r is the radial coordinate (m); R is the radius of the sphere (m); t is the time (s); and C_0 is the known initial concentration (g/m^3) of diffusant. We also have that,

$$C(0,t) = finite \tag{5.4}$$

A uniform initial profile has been assumed for this work and subsequently Eqn. 5.1 has been solved via series expansion with the initial and boundary conditions described in Eqns. 5.2-5.4 to give the following cumulative fractional release equation:

$$F(t) = \frac{m_{diffused}(t)}{m_0} = 1 - \frac{6}{\pi^2}\sum_{n=1}^{\infty}\frac{1}{n^2}e^{-(\frac{n\pi}{R})^2 Dt} \quad (5.5)$$

Where $F(t)$ is the fractional release of diffusant at a given time, $m_{diffused}(t)$ (g) is the cumulative mass of Eu diffused at a given time, and m_0 (g) is the total mass of Eu initially present in the sample. For the purposes of this work, n was limited to 100 terms.

In time-release measurements of Ag diffusion, the authors compared results obtained from Eqn. 5.5, which assumes a uniform initial distribution of diffusant, to results obtained using the experimentally-determined concentration profile [63]. The difference in diffusivities obtained from the two assumptions were not statistically significant and therefore the authors have chosen to apply the same assumption of uniform distribution and use Eqn. 5.5 to fit the experimental data.

5.4. Experimental

5.4.1. Materials and Preparation

IG-110 structural graphite was milled to spheres with diameters of ~0.32 cm. The pre-milled spheres were placed in the 45 mL polytetrafluoroethylene (PTFE) sleeve of a Parr Model 4744 pressurized acid digestion vessel to which was added 15 mL of a 1000 part-per-million (ppm) $Eu(NO_3)_2$ standard (Inorganic Ventures, 7% (v/v) HNO_3) and 5 mL of high-purity water. The parr bomb was assembled and then heated for four alternating cycles of 508 K for 2 hours and 373 K for 1 hour. After cooling, the vessel was disassembled, and the spheres were removed and placed in a vacuum oven at ~373 K where they remained overnight. The next day they were heated to 773 K for 30 minutes

to dissociate remaining nitrates. The spheres were then individually sanded with Al_2O_3 sandpaper, sonicated in high-purity water to remove dust, and then dried on a hot plate. The final diameter of each sphere was measured with calipers to the nearest 0.025 mm. This method produced IG-110 spheres with an average mass of 1.64 μg Eu and average diameter of 0.312 ± 0.003 cm.

The above-stated average mass of Eu in the samples was measured using standard comparator instrumented neutron activation analysis (INAA). Standards containing ~3 μg each of Eu were prepared by drying aliquots of a 1000 ppm standard on filter paper. The samples, once prepared, were irradiated with the standards in the University of Missouri Research Reactor for 5-10 seconds at a thermal neutron flux of 5.5×10^{13} n/cm^2/s. The samples and standards were then counted for 20 minutes each on a high-purity germanium (HPGe) detector; the 842 keV decay line was used for quantification.

A sample was selected from the batch for radial distribution measurements. The sample was bisected with a stainless-steel razor blade and the flat faces were smoothed with Al_2O_3 sandpaper. One of the flat faces was then set facing a Photon Machines 192 nm laser which was connected to a NexION® 300x ICP-MS. The laser operated with a power density of 2 mJ/cm^2 and 10 Hz pulse frequency. The laser produced 40 μm spot sizes and samplings were taken every 100 μm across the diameter of the sample. The sampling direction was rotated 45° clockwise after every completed line; this was repeated four times and the results were averaged. This procedure was used on a random sample selected from the initial loading batch and was repeated on the sample which was used to measure the Eu diffusion coefficient at 1873 K.

5.4.2. Diffusion Measurements

The time-release method used here has been described in previous publications and is only briefly described here [51, 58-64]. In Fig. 5.1, a Eu-loaded graphite sample was left in the top of a ball valve set on top of a Saint Gobain Hexaloy® SiC diffusion cell. The cell was set in a Model ST-1700C SentroTech box furnace with a maximum temperature capability of 1700 °C. While the furnace heated to the experimental temperature, ultra-high purity He flowed through the cell to displace room air. The ball valve was left in a partially open position to allow He to flow into the sample chamber without letting the sample fall through. The He was first directed through a Palas GFG-1000 carbon aerosol generator, modified for use with He. The operating specifics of this generator have been described in Carter, et al. [58]. The generator produced carbon nanoparticles entrained in He flowing at 2 L/min. The He flow was reduced to 1 L/min prior to entering the SiC chamber using a splitter valve. After the furnace had reached the experimental temperature the ICP-MS was started and optimized. Background Eu measurements were taken for approximately 1 hour, after which the ball valve was opened, allowing the sample to drop into the preheated diffusion cell. Released Eu was carried to the ICP-MS via the He-carbon aerosol and injected through a dual-inlet spray chamber.

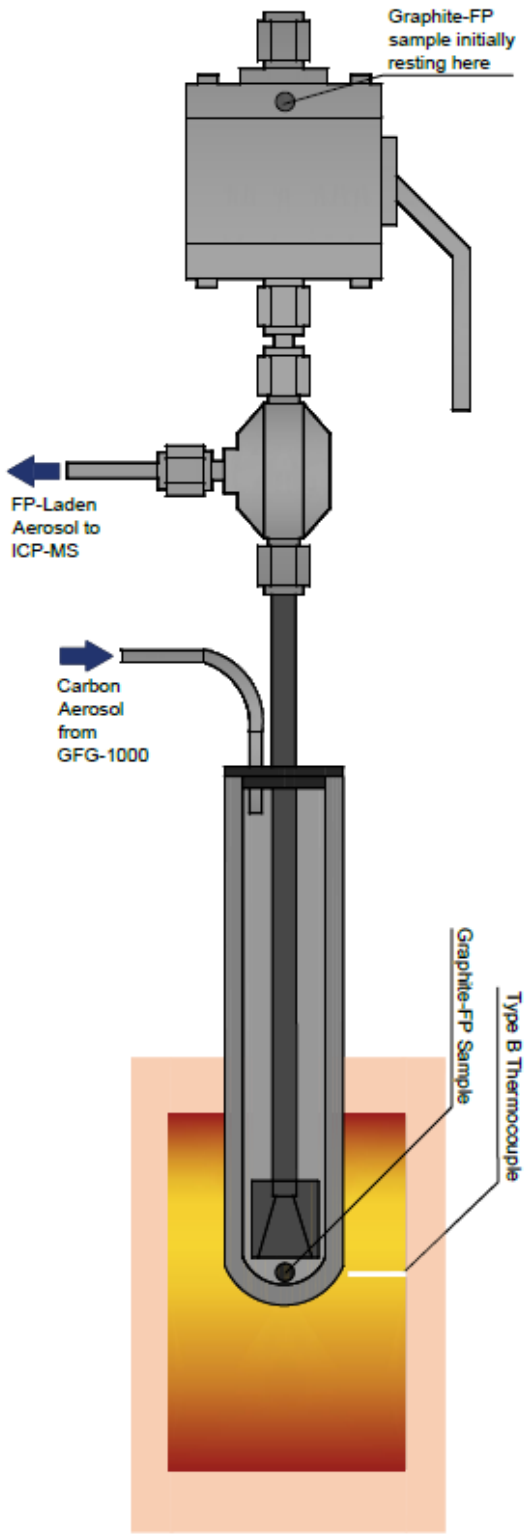

Figure 5.1: The SiC time-release diffusion cell. “FP” refers to fission product however the Eu used was from a natural source [51].

The second inlet was used to introduce a 1 ng/g In internal standard which allowed for correction of instrumental drift. Temperature monitoring was achieved through a Pt/Rh thermocouple installed in the furnace and placed at the base of the diffusion cell, see Fig. 5.1. These time-release measurements were conducted in the temperature range 1823 K – 1973 K in 50 K intervals. A COMSOL multi-physics model, described in Appendix C, was used to demonstrate a negligible temperature distribution near the sample location.

5.4.3. Data Analysis

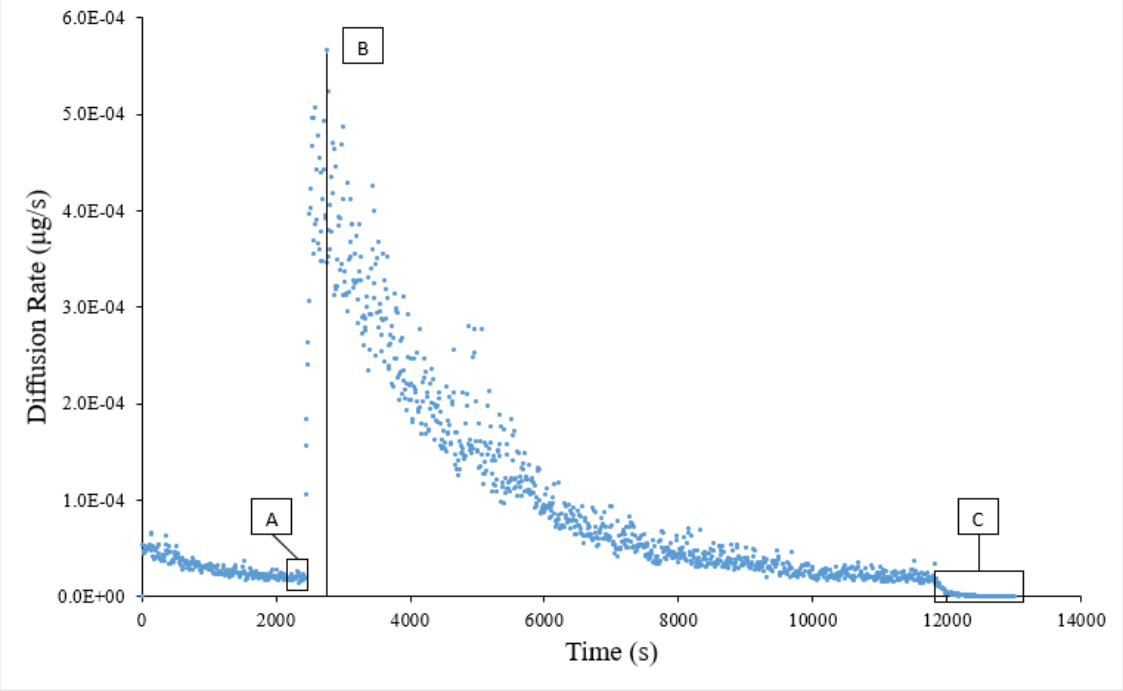

Figure 5.2: Europium time-release experiment at 1873 K. [A] is the baseline just before the sample was dropped into the diffusion cell. [B] is the peak rate of diffusion after sample introduction. [C] is the signal recorded after the furnace had been shut down.

Once experiments were complete, INAA was performed on the samples in the same manner as previously described in order to determine the total mass loss of Eu over

the course of each experiment. This mass loss was used to convert the mass spectrometer signal of counts/second to units of mass loss/second. A background correction was applied to each experiment in one of two ways: by calculating a constant background based on an average of the last ten measurements before sample introduction (feature A in Fig. 5.2) and subtracting that value from all subsequent measurements, or by fitting the background to a best-fit exponential equation and subtracting the values derived from that equation from the remainder of the measurements. In general, the first method was favored due to its greater simplicity. However, in some cases the sample was introduced into the chamber before the background had adequately decayed. The difference in the calculated diffusivities when comparing these two methods was an average of 4%.

After the sample was introduced, the Eu signal rapidly increased until it reached a peak, shown as feature B in Fig. 5.2. After several hours, when the release signal had decayed nearly to baseline (indicating a majority of the Eu had been released), the furnace was stopped and ICP-MS measurements continued for 20 minutes as the temperature decreased. This is shown as feature C in Fig. 5.2. The counts in this region make up less than 1% of the total counts for the experiment and therefore this decay period is not corrected for. The signal acquired before the peak was not used in the cumulative release fit as it was attributed to release of Eu from the graphite surface and nondiffusion-dominated processes. The signal before the peak was summed, converted to mass loss, and subtracted from the initial mass of Eu present in the sample. The remainder of the curve was converted to instantaneous fractional release by multiplying by a calibration factor, $F_{calibration}$ (g/count), which was equal to the corrected mass loss

divided by the total background-corrected counts in the diffusion region. The calibration factor was then multiplied by the count rate (counts/s) at each time point to calculate the release rate (g/s). Finally, the total fractional release was calculated at each time point by integration of the release rate over the region of interest to calculate the mass diffused and dividing by the initial mass of Eu present in the sample, as described in Carter et al. [58]. The experimental fractional release was then fit to Eqn. 5.5, as previously described. All of the above steps occurred after normalizing to the signal of the In standard.

The Arrhenius equation was used to demonstrate the temperature dependence of the Eu diffusion coefficient, Eqn. 5.6:

$$D = D_o e^{-E_a/RT} \tag{5.6}$$

Where D_0 is the pre-exponential factor (m^2/s) and E_a is the activation energy (kJ/mol). Uncertainties in the pre-exponential factor and activation energy were calculated from standard errors of the best fit linear regression.

5.5. Results

Figure 5.3 presents the results of the radial distribution measurements of Eu after the pressure vessel loading. The slope of the average distribution was 17,534 counts/cm, 95% CI [-24,104 59,173]. An F-test revealed there was no significant relationship between the radial distance and the Eu distribution ($F_{1,13} = 0.84$, $p = 0.38$). A flat diffusant profile was assumed, and Eqn. 5.5 was used to calculate the effective diffusion coefficients. Previous work with Ag has indicated no significant difference between effective diffusivities calculated using the measured profile vs. a flat profile [64].

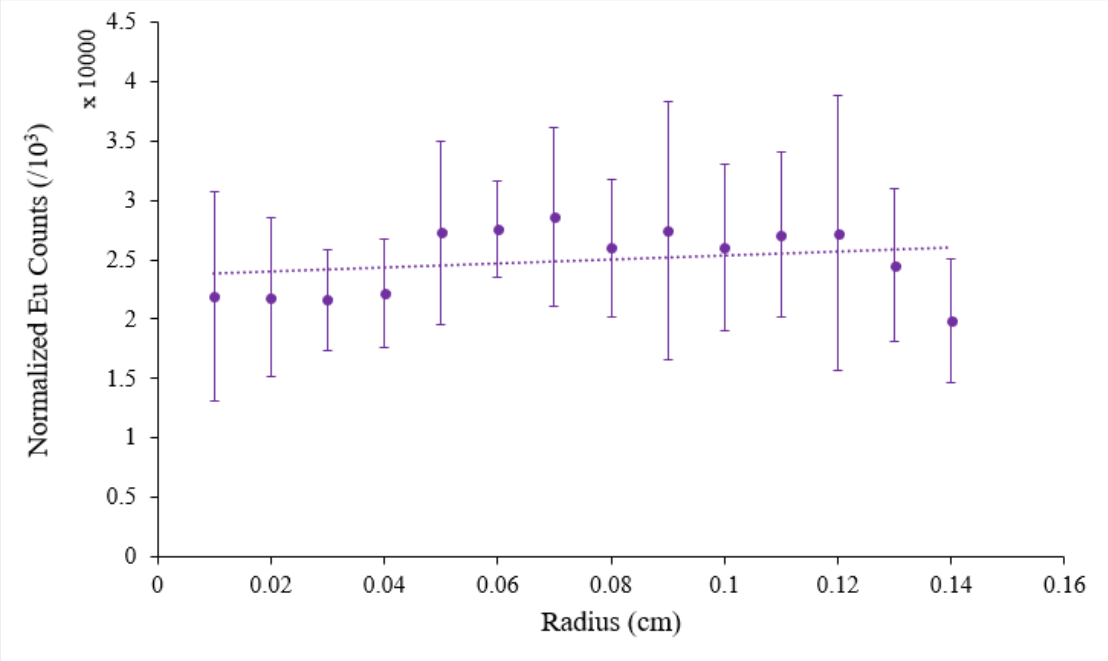

Figure 5.3: Radial distribution of Eu in an IG-110 sphere loaded using a pressure vessel.

Diffusion measurements were performed at four temperatures, beginning with 1823 K. Table 5.1 presents the test temperature, initial and final Eu mass, and the effective diffusivity of Eu, the variance, the mean absolute value of the error, and the exposure time for each experiment performed. The variance, thus standard error, was calculated from the Hessian matrix of the least squares fit using Excel [65]. The mean absolute value of the error (MAE) is reported as a goodness of fit between the simulated and the measured cumulative release using Eqn. 5.7.

$$error = \left|\frac{y - y_{fit}}{y}\right| \tag{5.7}$$

Where y_{fit} is the predicted cumulative release fraction and y is the measured cumulative release fraction. These results are shown again in Fig. 5.4 in the form of the

experimentally derived fractional release curves with the best-fit solutions to Eqn. 5.5 super-imposed on the accompanying curve.

Table 5.1: The experimental temperature, initial and final Eu mass, calculated diffusion coefficient, MAE, and exposure time for each experiment.

Test Temperature (K)	Initial Eu Mass (µg)	Final Eu Mass (µg)	Diffusion Coefficient (m^2/s)	MAE	Exposure Time (s)
1823	1.40	0.62	$8.87\ (1.8) \times 10^{-12}$	10.5%	9390
1873	1.69	0.42	$1.51\ (0.20) \times 10^{-11}$	17.0%	14190
1923	1.86	0.45	$2.74\ (0.47) \times 10^{-11}$	14.2%	8190
1973	1.62	0.36	$3.58\ (0.75) \times 10^{-11}$	22.5%	5790

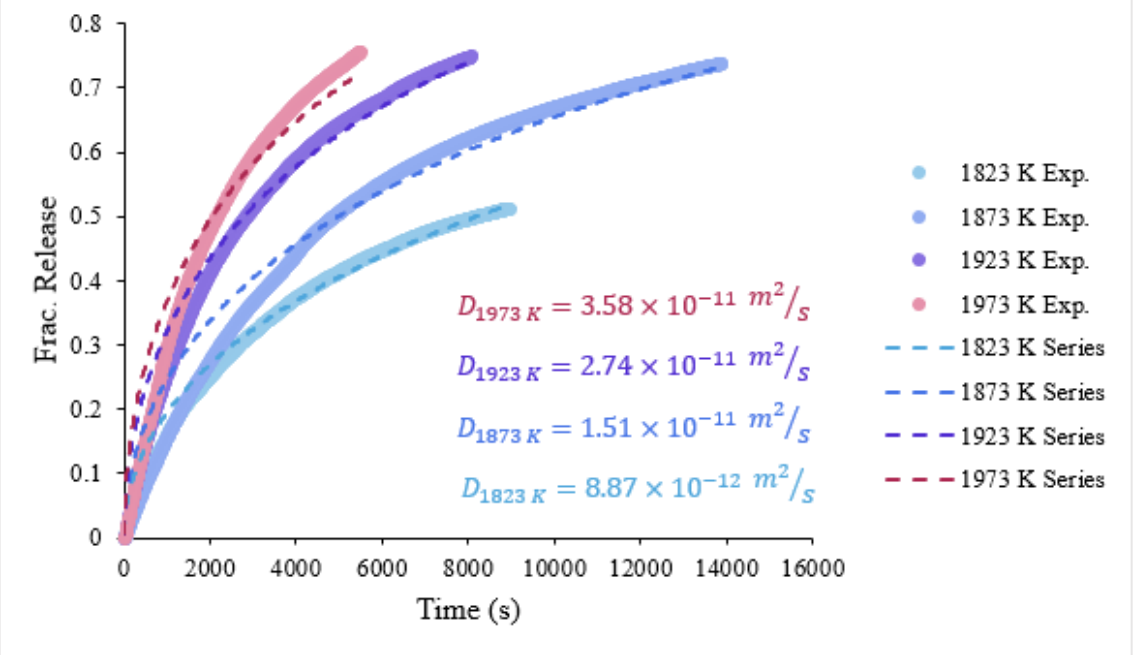

Figure 5.4: Experimental fractional release curves of Eu in IG-110 graphite taken between 1823 K and 1973 K and the best-fit solutions to Eqn. 5.5.

The Arrhenius parameters, shown in Table 5.2, were derived by fitting the Arrhenius diffusion coefficient to the reciprocal temperature using a weighted linear least

squares approach. The results were linear over the experimental temperature range. The accompanying Arrhenius plot is presented in Fig. 5.5 along with results of earlier measurements for Sr diffusion over a similar temperature range using the same time-release method [51].

Table 5.2: Calculated Arrhenius parameters of Eu diffusion in IG-110 graphite between 1823 K – 1973 K.

Diffusant	D_0 (m^2/s)	$\pm\Delta D_0$ (m^2/s)	E_a (kJ/mol)	$\pm\Delta E_a$ (kJ/mol)
Eu	1.5×10^{-3}	3.8×10^{-4}	287	26

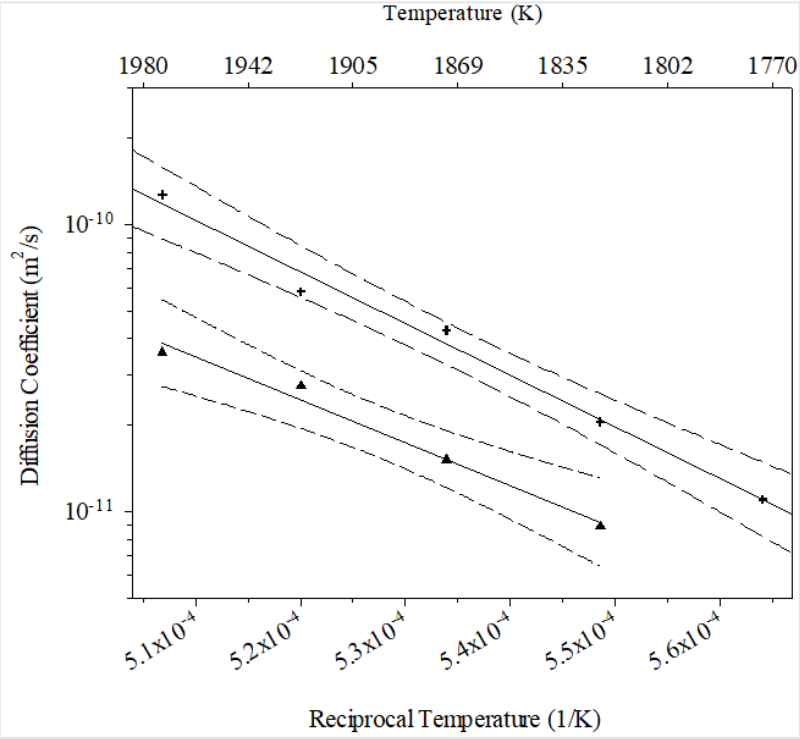

Figure 5.5: Arrhenius plot of Sr and Eu diffusion in unirradiated IG-110 graphite [51]. The Sr plot is the upper curve and the Eu plot is shown below. The dashed lines represent the respective 95% confidence intervals.

5.6. Discussion

The time-release method described in this work has previously been successfully applied to diffusion measurements of Cs, I, Ag, and most recently Sr in several types of nuclear graphite [51, 58-63]. The Arrhenius parameters of Sr were E_a = 346 (± 22) kJ/mol and D_0 = 1.7 (± 1.3) × 10^{-1} m^2/s over the temperature range 1773 K – 1973 K [51]. The individual Sr diffusion measurements had resulting diffusivities approximately 3 times greater than the temperature-equivalent Eu measurements. The slope of the best-fit line for Sr was such that it would intersect the Eu best-fit line at 1516 K, below which Eu would exhibit greater diffusivities. This is in keeping with observations obtained from AGR experiments, discussed earlier, in which Eu and Sr were known to exhibit similar diffusive behaviors with Eu release in general greater than that of Sr [3].

Concentration dependencies of diffusion are an important consideration in diffusivity studies. One advantage of the time-release method used in this work over the depth profiling method is that experiments can be conducted at low diffusant concentrations. The high energy binding sites dominate diffusion processes at low diffusant concentrations. As the concentration of diffusant increases, weaker binding sites begin to contribute to diffusion processes resulting in increased rates of migration [66]. Cs and Sr are known to exhibit relevant changes in diffusion rates when the concentration of the element under study increases above a certain point [66-68]. For example, the "limit" of concentration for Sr in graphite, under which diffusion is believed to not be affected by concentration, is 62 μg Sr/g graphite [68]. Eu is expected to exhibit a similar concentration dependency above a threshold concentration value, however, to the best of

the authors' knowledge, the value of the threshold is unknown. The graphite samples used in this study had an average radius of 0.156 cm and an average Eu loading content of 1.64 μg. Considering the stated density of IG-110 of 1.76 g/cm^3, this equates to an average concentration of 59 μg Eu/g graphite. This amount is close to the accepted limit for Sr but a direct comparison cannot be made. Further investigations into a possible Eu concentration dependency should be made in future studies.

Similar to the Sr diffusion studies [51], the Eu experimental fractional releases did not initially align well with the best-fit solutions to Eqn. 5.5. In the four fractional release plots shown in Fig. 5.4, Eqn. 5.5 overpredicts the release rate in the first 1000 s – 4000 s of the experiments, after which the series solution was in good agreement with the experimental releases. In diffusion studies it is common to ignore effects related to sorption or trapping; these are factored into the effective diffusion coefficient, but their contributions are considered minimal [52]. Despite that, the overprediction of Eqn. 5.5 in the first few thousand seconds of each experiment could be the result of sorption at the surface of the sphere competing with diffusion as the rate limiting step or, alternatively, some transport effects (e.g., free flight of molecules) other than diffusion playing a role. In the Eu distribution, see Fig. 5.3, Eu was measured at the surface of the sphere which is a violation of the initial condition reported in Eqn. 5.3. This violation could have led to deviation of Eqn. 5.5, particularly early in the experiments. To test the impact of the poor early time fits, diffusion coefficients were calculated wherein the first 10%, 20%, 30%, and 40% of the total fractional release was ignored and Eqn. 5.5 was only fit to the remainder of the curve. For all four time-release experiments over all four tested

conditions the change in the effective diffusion coefficient was no more than 8%. This is well within the uncertainties reported in Table 5.1 and indicates that the reported effective diffusivities are a good representation of the experimental fractional release curves.

The chemical form of diffusant could also have a significant effect on its rate of diffusion. The heating step to 773 K, described in Section 5.4, was intended to dissociate $Eu(NO_3)_3$. This dissociation likely led to the Eu being in the chemical form of either Eu_2O_3 or EuO. Thermodynamic calculations on the suitability of binary oxides for epitaxy source materials reported that at low partial pressures of O_2, the dominant form of Eu over the two Eu oxides was Eu metal at temperatures above 1800 K [69]. Near 1800 K the calculated partial pressure of EuO and Eu metal were similar, and both could thermodynamically be present in the graphite sphere. In the high-purity He environment of the diffusion cell the O_2 partial pressure would be very low and would promote the decomposition of the Eu oxide to Eu metal. The presence of both EuO and Eu at the beginning of the experiments could account for the overprediction of the experimental data early in the release profile.

The temperature of the furnace was measured using a thermocouple located 2.5 cm from the sample position inside the SiC chamber. It is possible that the temperature inside of the SiC tube housing the test sample was cooled by the flow of He entering the chamber. A COMSOL multi-physics model, described in Appendix C, was used to determine the temperature distribution near the sample location. The model indicates a temperature drop of 40 – 48 K over the experimental temperature range of 1823 K – 1973

K. The model does not account for the heat exchange between the tube assembly and the insulation or the fact that the thermocouple regulating the oven temperature is 2.5 cm from the sample location. The model predicts a sample temperature of 1783 K at the experimental temperature of 1823 K, which is 21 K lower than the boiling point of Eu. This suggests that the COMSOL model overpredicts the temperature drop at the sample location. Calculating the Arrhenius parameters using the COMSOL model temperatures instead of the experimental temperatures results in an activation energy of 288 ± 26 kJ/mol and a pre-exponential factor of 2.48 ± 0.71 m^2/s. The activation energy is unchanged, while the pre-exponential factor is different than the values reported in Table 5.2.

The IG-110 graphite used in this study is manufactured using a cold isostatic molding method and is a fine-grained, petroleum coke-based nuclear graphite with a porosity volume of 22.3% [48]. Variations in these stated properties (e.g. molding method, grain size, coke source, and porosity) will affect both base diffusion rates and microstructural changes resulting from oxidation and neutron irradiation which will in turn also affect fission product diffusion. IG-110 was chosen due to its prevalence in currently operating HTGRs and the work presented here has established a baseline of information on Eu diffusion in structural graphite and initiated an approximation of Eu diffusion in fuel component graphite materials. While IG-110 graphite is not the representative of diffusion in matrix and PyC, analysis of diffusion in structural graphite provides an approximation of diffusion behavior in fuel component graphite materials and accurate insight into diffusion of Eu in structural graphite components. Much work is

still needed on comparative studies with alternative grades of structural graphite as well as matrix graphites to assess the validity of the current standard of treating fission product diffusion in these differing materials as a collective process [49].

5.7. Conclusions and Future Work

The diffusion of Eu in graphite has often been overlooked. As a result, little is known about its rates of diffusion, what influence other fission products may have in slowing or increasing those diffusion rates, as well as various effects related to structural damage of the graphite and concentration dependencies. In this work, Eu diffusion in IG-110 structural graphite was measured using a time-release method with resulting Arrhenius parameters of E_a = 287 (26) kJ/mol and D_0 = 1.5 (0.38) × 10^{-3} m^2/s. This has provided accurate information on the diffusion of Eu in structural graphite and an approximation of Eu diffusion in graphitic matrices.

5.8. Acknowledgments

This research has been supported by the U.S. Department of Energy Nuclear Energy University Program grant NEUP-12830, and an Integrated University Program Fellowship grant (DE-NE000118 Mod 007) towards support of T.M. Weilert.

5.9. References

[1] Verfondern, K.; Nabielek, H.; Kendall, J. M., Coated particle fuel for high temperature gas cooled reactors. *Nucl. Eng. Technol.* **2007,** *39* (5), 603-616.

[2] *High Temperature Gas Cooled Reactor Fuels and Materials*; International Atomic Energy Agency: Vienna, Austria, 2010; p 182.

[3] Stempien, J. D.; Demkowicz, P. A. *AGR-2 Irradiation Experiment Fission Product Mass Balance*; Idaho National Laboratory: Idaho Falls, ID, 2019.

[4] Minato, K.; Ogawa, T.; Fukuda, K.; Sekino, H.; Miyanishi, H.; Kado, S.; Takahashi, I., Release behavior of metallic fission products from HTGR fuel particles at 1600 to 1900°C. *J. Nucl. Mater.* **1993,** *202* (1-2), 47-53.

[5] Barnes, C. M. *AGR-1 Fuel Product Specification and Characterization Guidance*; EDF-4380, Rev. 8; Idaho National Laboratory: Idaho Falls, ID, 2006a; p 46.

[6] Hunn, J. D.; Lowden, R. A. *Data Compilation for AGR-1 Baseline Coated Particle Composite LEU01-46T*; Oak Ridge National Laboratory: Oak Ridge, TN, 2006a; p 235.

[7] Hunn, J. D.; Lowden, R. A. *Data Compilation for AGR-1 Variant 1 Coated Particle Composite LEU01-47T*; Oak Ridge National Laboratory: Oak Ridge, TN, 2006b; p 192.

[8] Hunn, J. D.; Lowden, R. A. *Data Compilation for AGR-1 Variant 2 Coated Particle Composite LEU01-48T*; Oak Ridge National Laboratory: Oak Ridge, TN, 2006c; p 162.

[9] Hunn, J. D.; Lowden, R. A. *Data Compilation for AGR-1 Variant 3 Coated Particle Composite LEU01-49T*; Oak Ridge National Laboratory: Oak Ridge, TN, 2006d; p 186.

[10] Hunn, J. D.; Montgomery, F. C.; Pappano, P. J. *Data Compilation for AGR-1 Baseline Compact Lot LEU01-46T-Z*; Oak Ridge National Laboratory: Oak Ridge, TN, 2006a; p 51.

[11] Hunn, J. D.; Montgomery, F. C.; Pappano, P. J. *Data Compilation for AGR-1 Variant 1 Compact Lot LEU01-47T-Z*; Oak Ridge National Laboratory: Oak Ridge, TN, 2006b; p 53.

[12] Hunn, J. D.; Montgomery, F. C.; Pappano, P. J. *Data Compilation for AGR-1 Variant 2 Compact Lot LEU01-48T-Z*; Oak Ridge National Laboratory: Oak Ridge, TN, 2006c; p 43.

[13] Hunn, J. D.; Montgomery, F. C.; Pappano, P. J. *Data Compilation for AGR-1 Variant 3 Compact Lot LEU01-49T-Z*; Oak Ridge National Laboratory: Oak Ridge, TN, 2006d; p 44.

[14] Demkowicz, P. A.; Harp, J. M.; Winston, P. L.; Ploger, S. A. *Analysis of Fission Products on the AGR-1 Capsule Components*; Idaho National Laboratory: Idaho Falls, ID, 2013; p 50.

[15] Hunn, J. D.; Baldwin, C. A.; Montgomery, F. C.; Gerczak, T. J.; Morris, R. N.; Helmreich, G. W.; Demkowicz, P. A.; Harp, J. M.; Stempien, J. D., Initial examination of fuel compacts and TRISO particles from the US AGR-2 irradiation test. *Nucl. Eng. Des.* **2018,** *329*, 89-101.

[16] Demkowicz, P. A.; Reber, E. L.; Scates, D. M.; Scott, L.; Collin, B. P., First high temperature safety tests of AGR-1 TRISO fuel with the Fuel Accident Condition Simulator (FACS) Furnace. *J. Nucl. Mater.* **2015,** *464*, 320-330.

[17] Demkowicz, P. A.; Hunn, J. D.; Morris, R. N.; van Rooyen, I.; Gerczak, T.; Harp, J. M.; Ploger, S. A. *AGR-1 Post Irradiation Examination Final Report*; Idaho National Laboratory: Idaho Falls, ID, 2015; p 132.

[18] Collin, B. P. *AGR-2 Irradiation Test Final As-Run Report*; Idaho National Laboratory: Idaho Falls, ID, 2014; p 87.

[19] Barnes, C. M. *AGR-2 Fuel Specification*; Idaho National Laboratory: Idaho Falls, ID, 2009.

[20] BWXT *Industrial Fuel Fabrication and Development Lot G73AA-10-69308*; 2008.

[21] BWXT *Industrial Fuel Fabrication and Development Lot G73I-14-69307*; 2008.

[22] BWXT *Industrial Fuel Fabrication and Development Lot G73J-14-93071A, G73J-14-93073A, G73J-14-93074A*; 2008.

[23] BWXT *Industrial Fuel Fabrication and Development Lot G73H-10-93085B*; 2009.

[24] Hunn, J. D. *Data Compilation for AGR-2 Baseline Coated Particle Batch G73J-14-93071A*; Oak Ridge National Laboratory: Oak Ridge, TN, 2008; p 15.

[25] Hunn, J. D. *Data Compilation for AGR-2 Baseline Coated Particle Batch G73J-14-93072A*; Oak Ridge National Laboratory: Oak Ridge, TN, 2008; p 13.

[26] Hunn, J. D. *Data Compilation for AGR-2 UCO Variant Coated Particle Batch G73J-14-93073A*; Oak Ridge National Laboratory: Oak Ridge, TN, 2008; p 12.

[27] Hunn, J. D. *Data Compilation for AGR-2 UCO Variant Coated Particle Batch G73J-14-93074A*; Oak Ridge National Laboratory: Oak Ridge, TN, 2008; p 12.

[28] Hunn, J. D. *Data Compilation for AGR-2 B&W UO2 Coated Particle Batch G73H-10-93085B*; Oak Ridge National Laboratory: Oak Ridge, TN, 2010; p 18.

[29] Hunn, J. D.; Montgomery, F. C.; Pappano, P. J. *Data Compilation for AGR-2 UCO Baseline Compact Lot LEU07-OP1-Z*; Oak Ridge National Laboratory: Oak Ridge, TN, 2009; p 130.

[30] Hunn, J. D.; Montgomery, F. C.; Pappano, P. J. *Data Compilation for AGR-2 UCO Variant Compact Lot LEU06-OP1-Z*; Oak Ridge National Laboratory: Oak Ridge, TN, 2009; p 114.

[31] Hunn, J. D.; Montgomery, F. C.; Pappano, P. J. *Data Compilation for AGR-2 B&W UO2 Compact Lot LEU11-OP2-Z*; Oak Ridge National Laboratory: Oak Ridge, TN, 2010; p 165.

[32] Hunn, J. D.; Montgomery, F. C.; Pappano, P. J. *Data Compilation for AGR-2 UCO Baseline Compact Lot LEU09-OP2-Z*; Oak Ridge National Laboratory: Oak Ridge, TN, 2010; p 132.

[33] Harp, J. M.; Demkowicz, P. A.; Stempien, J. D., Fission Product Inventory and Burnup Evaluation of the AGR-2 Irradiation by Gamma Spectrometry. In *2016 International Topical Meeting on High Temperature Reactor Technology (HTR 2016)*, Las Vegas, NV, 2016; p 11.

[34] BWXT *Industrial Fuel Fabrication and Development Lot G73V-20-69303*; 2006.

[35] Kercher, A. K.; Jolly, B. C.; Montgomery, F. C.; Silva, C.; Hunn, J. D. *Data Compilation for AGR-3/4 Designed-To-Fail (DTF) Fuel Particle Batch LEU03-07DTF*; Oak Ridge National Laboratory: Oak Ridge, TN, 2011; p 70.

[36] Hunn, J. D.; Lowden, R. A. *Data Compilation for AGR-3/4 Driver Fuel Coated Particle Composite LEU03-09T*; Oak Ridge National Laboratory: Oak Ridge, TN, 2007; p 187.

[37] Barnes, C. M. *AGR-3 & 4 Fuel Product Specification*; EDF-6638, Rev. 1; Idaho National Laboratory: Idaho Falls, ID, 2006b.

[38] Marshall, D. W. *AGR-3/4 DTF Fuel and Capsule Component Material Specifications*; SPC-1214, Rev. 1; 2011.

[39] Collin, B. P.; Demkowicz, P. A.; Petti, D. A.; Hawkes, G. L.; Palmer, J.; Pham, B. T.; Scates, D. M.; Sterbentz, J. W., The AGR-3/4 fission product transport irradiation experiment. *Nucl. Eng. Des.* **2018,** *327*, 212-227.

[40] Stempien, J. D.; Demkowicz, P. A.; Harp, J. M.; Winston, P. L. *AGR-3/4 Experiment Preliminary Mass Balance*; Idaho National Laboratory: Idaho Falls, ID, 2018; p 62.

[41] Harp, J. M.; Demkowicz, P. A.; Stempien, J. D., Initial Gamma Spectrometry Examination of the AGR-3/4 Irradiation. In *2016 International Topical Meeting on High Temperature Reactor Technology (HTR 2016)*, Las Vegas, NV, 2016.

[42] Liu, X.; Huang, X.; Xie, F.; Jia, F.; Feng, X.; Li, H., Source Term Analysis of the Irradiated Graphite in the Core of HTR-10. *Sci. Technol. Nucl. Install.* **2017,** *2017*, 1-6.

[43] Fütterer, M. A.; Fu, L.; Sink, C.; Groot, S. d.; Pouchon, M.; Kim, Y. W.; Carré, F.; Tachibana, Y., Status of the very high temperature reactor system. *Prog. Nucl. Energy* **2014,** *77*, 266-281.

[44] Pappano, P. J.; Burchell, T. D.; Hunn, J. D.; Trammell, M. P., A novel approach to fabricating fuel compacts for the next generation nuclear plant (NGNP). *J. Nucl. Mater.* **2008,** *381* (1-2), 25-38.

[45] Collin, B. P. *AGR-1 Irradiation Test Final As-Run Report*; Idaho National Laboratory: Idaho Falls, ID, 2015; p 99.

[46] Hunn, J. D.; Trammell, M. P. *Data Compilation for AGC-2 Matrix-only Compact Lot A3-H08*; Oak Ridge National Laboratory: Oak Ridge, TN, 2010; p 39.

[47] Verfondern, K.; Liu, B.; Nabielek, H.; Wang, T.; Allelein, H. J.; Tang, C. H., Release Rates of Short-lived Fission Gases from Modern Spherical Fuel Elements with TRISO-coated Particles. *J. Phys.: Conf. Ser.* **2021,** *2048*, 1-12.

[48] Zheng, G. Q.; Xu, P.; Sridharan, K.; Allen, T. R., Pore Structure Analysis of Nuclear Graphites IG-110 and NBG-18. In *Advances in Materials Science for Environmental and Nuclear Technology II, Volume 227*, Sundaram, S. K.; Fox, K.; Ohji, T.; Hoffman, E., Eds. The American Ceramic Society: 2011; Vol. 227, pp 251-260.

[49] *HTGR Mechanistic Source Terms White Paper*; Idaho National Laboratory: Idaho Falls, ID, 2010; p 95.

[50] Collin, B. P. *Diffusivities of Ag, Cs, Sr, and Kr in TRISO Fuel Particles and Graphite*; Idaho National Laboratory: Idaho Falls, ID, 2016; p 40.

[51] Weilert, T. M.; Walton, K. L.; Loyalka, S. K.; Brockman, J. D., Measurement of effective Sr diffusion coefficients in IG-110 graphite. *J. Nucl. Mater.* **2021,** *555*.

[52] *Fuel performance and fission product behaviour in gas cooled reactors*; International Atomic Energy Agency: Vienna, Austria, 1997; p 529.

[53] Cowan, G. A.; Orth, C. J., Diffusion of fission products at high temperatures from refractory matrices. In *Second United Nations International Conference on the Peaceful Uses of Atomic Energy*, U.S. Government Printing Office: 1958; p 17.

[54] Orth, C. J., Diffusion of Lanthanides and Actinides from Graphite at High Temperatures. *Nucl. Sci. Eng.* **1961,** *9* (4), 417-420.

[55] Hayashi, K.; Kikuchi, T.; Kobayashi, F.; Minato, K.; Fukuda, K.; Ikawa, K.; Iwamoto, K., Distribution of fission products in irradiated graphite materials of HTGR fuel assemblies: Third and fourth OGL-1 fuels. *J. Nucl. Mater.* **1985,** *136* (2-3), 207-217.

[56] Hayashi, K.; Kobayashi, F.; Minato, K.; Ikawa, K.; Fukuda, K., In-pile release behavior of metallic fission products in graphite materials of an HTGR fuel assembly. *J. Nucl. Mater.* **1987,** *149* (1), 57-68.

[57] Myers, B. F.; Jensen, D. D.; Zumwalt, L. R., The diffusion of cesium and strontium in H-327 graphite during the Peach Bottom Fuel Test Element experiments. In *Proceedings of a Colloquium held at Hahn-Meitner-Institut*, (Ed.), E. H., Ed. Berlin, 1981; pp 166-171.

[58] Carter, L. M.; Brockman, J. D.; Loyalka, S. K.; Robertson, J. D., Measurement of cesium diffusion coefficients in graphite IG-110. *J. Nucl. Mater.* **2015,** *460*, 30-36.

[59] Carter, L. M.; Brockman, J. D.; Loyalka, S. K.; Robertson, J. D., Calibration of a system for measurements of diffusion coefficients of fission products in HTGR/VHTR core materials. *J. Radioanal. Nucl. Chem.* **2016,** *307*, 1771-1775.

[60] Carter, L. M.; Brockman, J. D.; Robertson, J. D.; Loyalka, S. K., ICP-MS measurement of diffusion coefficients of Cs in NBG-18 graphite. *J. Nucl. Mater.* **2015,** *466*, 402-408.

[61] Carter, L. M.; Brockman, J. D.; Robertson, J. D.; Loyalka, S. K., ICP-MS measurement of iodine diffusion in IG-110 graphite for HTGR/VHTR. *J. Nucl. Mater.* **2016,** *473*, 218-222.

[62] Carter, L. M.; Brockman, J. D.; Robertson, J. D.; Loyalka, S. K., Diffusion of cesium and iodine in compressed IG-110 graphite compacts. *J. Nucl. Mater.* **2016,** *476*, 30-35.

[63] Carter, L. M.; Seelig, J. D.; Brockman, J. D.; Robertson, J. D.; Loyalka, S. K., ICP-MS measurement of silver diffusion coefficient in graphite IG-110 between 1048K and 1284K. *J. Nucl. Mater.* **2018,** *498*, 44-49.

[64] Weilert, T. M.; Walton, K. L.; Loyalka, S. K.; Brockman, J. D., Effective diffusivity of Ag and migration of Pd in IG-110 graphite. *J. Nucl. Mater.* **2022,** *559*.

[65] Hughes, I. G.; Hase, T. P. A., *Measurements and their Uncertainties: A Practical Guide to Modern Error Analysis*. Oxford University Press: 2010.

[66] Myers, B. F., A review of the diffusion of selected fission product metals in polycrystalline graphite. In *Proceedings of a Colloquium held at Hahm-Meitner-Institut*, Hoinkis, E., Ed. Berlin, 1981; pp 56-67.

[67] Myers, B. F.; Bell, W. E. *Strontium transport data for HTGR systems*; General Atomic Company: San Diego, CA, 1974; p 75.

[68] Sandalls, F. J.; Walford, M. R., Laboratory determinations of strontium diffusion coefficients in graphite. *J. Nucl. Mater.* **1976,** *62* (2-3), 265-272.

[69] Adkison, K. M.; Shang, S.-L.; Bocklund, B. J.; Klimm, D.; Schlom, D. G.; Liu, Z.-K., Suitability of binary oxides for molecular-beam epitaxy source materials: A comprehensive thermodynamic analysis. *APL Mater.* **2020,** *8* (8), 081110-1-18.

CHAPTER 6:
DIFFUSION OF CESIUM IN OXIDIZED AND UNOXIDIZED IG-110 NUCLEAR GRAPHITE

The results of this study were submitted to the *Journal of Nuclear Materials* on April 12, 2022 for review as: T.M. Weilert, K.L. Walton, S.K. Loyalka, J.D. Brockman. Diffusion of cesium in oxidized and unoxidized IG-110 nuclear graphite.

6.1. Abstract

Time-release diffusion measurements of cesium have been conducted over the temperature range 1073 K – 1973 K on oxidized and unoxidized IG-110 graphite. Four cesium concentrations were tested to investigate the concentration dependence of the diffusion coefficient. Two levels of oxidation were tested and compared to unoxidized concentration-matched sets to explore the effects of graphite oxidation. The results demonstrate that the cesium diffusion coefficient in unoxidized IG-110 graphite is independent of concentration within the range 34 – 163 $\mu g_{Cs}/g_{graphite}$. Above this, the effective cesium diffusion coefficient changes with concentration. The diffusion coefficient was increased by a factor of 2-12 in the oxidized set with 7.8% mass loss. These results can be used to aid predictive modelling of cesium diffusion in HTGR cores.

6.2. Introduction

The outlook for the high-temperature gas-cooled reactor (HTGR) has grown increasingly positive due to several recent developments. To name a few, the US Department of Energy announced $80 million in funding for X-energy's Xe-100 modular pebble-bed reactor in October 2020 [1], the Japanese high-temperature test reactor (HTTR) was successfully restarted in August 2021 [2], and the Chinese HTR-PM reached dual criticality and was connected to the electricity grid in late 2021 [3-4]. Finally, the United Kingdom announced that a modular HTGR will become the focus of their Advanced Modular Reactor Research, Development, and Demonstration Program [5]. These successes have been made possible due to industry confidence in the HTGR and its robust fuel design, the tristructural isotropic (TRISO) fuel particle, a multilayered ceramic fuel characterized by high-temperature resistance to degradation and excellent retention of nearly all fission products.

There are, however, several fission products which are not quantitatively retained in the fuel particles. These non-retained fission products have the potential to migrate through the core graphite and into the primary cooling system to eventually deposit in cooler regions of the reactor. This presents a potential dose hazard to operating personnel and, under the most severe accident conditions, the public [6]. The elements known to migrate include Cs, Ag, Sr, and Eu [7].

^{137}Cs is an important medium-lived fission product due to a comparatively high yield of 6.1% from ^{235}U fission and a half-life of 30 years. It is effectively retained by the SiC layer in the TRISO fuel particle [8]. In rare cases where the SiC layer becomes

compromised, 20-100% of the ^{137}Cs inventory escapes from the TRISO fuel particle [9]. ^{137}Cs measured outside of irradiated TRISO fuel was an indicator of SiC failure in experiments conducted by the Advanced Gas Reactor Fuel Qualification and Development (AGR) Program [8, 10-11]. Released ^{137}Cs migrates through the surrounding matrix graphite at normal operating temperatures and can continue to migrate into core structural graphite (in the case of a prismatic core) or directly enter the primary cooling loop [10]. The majority of the gamma activity in past operational HTGR cooling circuits has been from Cs [12].

Fission product transport in HTGRs under normal and off-normal operating conditions are modeled using computer codes such as FRESCO and PARFUME. Graphite makes up much of the fuel and core structures of both the prismatic and pebble-bed HTGR designs. These codes use effective diffusion coefficients in UCO, SiC, and graphite to describe fission product transport. In this classical approach, diffusion is assumed to be the rate limiting step and the presumed effective diffusion coefficient encompasses evaporation, sorption, trapping and diffusion. Experimentally-measured effective diffusion coefficients are available for historical grades of nuclear graphite and have recently been measured in several modern grades [13]. One of the limitations of this approach is that changes in the graphite microstructure alter fission product migration. Both neutron irradiation and oxidation are known to alter graphite microstructure [14]. Microstructural changes caused by neutron irradiation are a factor in the difference between effective diffusion coefficients measured using in-pile vs out-of-pile experiments. Graphite oxidation is caused by ingress of water vapor, CO_2, and O_2 into the

primary cooling loop [15] and can be catalyzed by trace elements in the graphite, including Ba which is produced through ^{137}Cs decay [14, 16]. Oxidation of core graphite can reduce its structural integrity and lead to increased rates of fission product diffusion [17].

Some fission product modeling approaches compensate for graphite oxidation by making the effective diffusion coefficient a function of weight-percent burnoff [8]. Others simply input a release fraction equal to the corrosion degree of the graphite (or the corrosion degree of the binder material in the case of matrix graphite) [18]. These approaches do not account for variations in oxidation characteristics among different graphites. These differences can arise from variations in the production method, coke source materials, grain size, porosity, and relative pore size. Changes in the effective diffusivities may not be uniform among graphitic materials with equal percent weight loss. The IG-110 graphite used in this study is a superfine grade graphite with petroleum coke precursor. The pore size distribution of IG-110 graphite consists of a majority of fine pores (~0.005-0.05 μm) and a small fraction of medium size pores (~0.05-0.5 μm) [19] for a total pore volume of 22.7% [20]. This porosity is higher than that of other nuclear graphite grades such as IG-430 and NBG-18 and is correlated with a higher active surface area (ASA) [20]. Highly porous graphites such as this have increased oxidation rates in oxidation Regime II (the regime used in this work) due to increased rates of oxygen transport [21]; higher ASA is also associated with greater degrees of oxidation [20]. To the best of the authors' knowledge there are currently no studies with

information on Cs diffusion in oxidized IG-110 and very few on structural graphites in general [22].

A second topic explored in this work is the concentration dependency of the Cs diffusion coefficient. Diffusivity changes related to sample concentration are a well-known phenomenon and can inhibit the applicability of experimental work to real-world situations where concentrations are much lower. Little is currently known about the concentration dependency of Cs. Small concentration effects were found by Myers and Bell [8, 23], however Myers later stated that the Cs concentration dependence was similar to that of Sr which has a demonstrated concentration dependence above 62 $\mu g_{Sr}/g_{graphite}$ [22, 24]. Myers, et al. [25] also stated the Cs diffusion coefficient was expected to be independent of concentration below 0.55 $\mu g_{Cs}/g_{source\ material}$. Katscher et al. [18] discussed potential concentration dependencies after saturation occurred at ~0.1-1 $mmol_{Cs}/kg_c$.

In this work, time-release diffusion measurements of Cs were performed on sets of unoxidized IG-110 graphite and two sets of IG-110 graphite which had been oxidized in air for 30 and 60 minutes. Time-release measurements were also performed on four sets of unoxidized IG-110 loaded with a wide range of Cs concentrations. These experiments were performed in the temperature range 1073 K – 1973 K.

6.3. Theory

Studies of fission product diffusion in graphite generally assume that effects of sorption and trapping are minimal relative to diffusion and that diffusion is the rate-limiting step [8]. Fission product transport processes in graphite are encompassed into an

overall “effective diffusion coefficient”. This assumption is also made in this work. The time-release method used here has been previously applied to measurements of Cs diffusion in various types of graphite, as well as measurements of I, Ag, Sr, and Eu diffusion in IG-110 graphite [26-34]. Here, Eqn. 6.1, was solved using a series expansion with the initial and boundary conditions set out in Eqns. 6.2-6.4:

$$\frac{\partial C(r,t)}{\partial t} = \frac{1}{r^2}\frac{\partial}{\partial r}\left(Dr^2\frac{\partial C(r,t)}{\partial r}\right) \tag{6.1}$$

$$C(r,0) = C_0 \tag{6.2}$$

$$C(0,t) = finite \tag{6.3}$$

$$C(R,t) = 0 \tag{6.4}$$

These initial and boundary conditions state that a known initial concentration of diffusant, C_0 (g/m^3), is evenly distributed throughout a spherical sample with no diffusant present at the surface. In the above equations, D is the effective diffusion coefficient (m^2/s), r is the radial coordinate (m), R is the radius of the sphere (m), and t is the time (s). The cumulative fractional release of the diffusant is then given by:

$$F(t) = \frac{m_{diffused}(t)}{m_0} = 1 - \frac{6}{\pi^2}\sum_{n=1}^{\infty}\frac{1}{n^2}e^{-(\frac{n\pi}{R})^2 Dt} \tag{6.5}$$

Where $F(t)$ is the cumulative fractional release of diffusant at a given time, $m_{diffused}(t)$ (g) is the cumulative mass of Cs diffused at the given time, and m_0 (g) is the total mass of Cs initially present in the sample. In this work, n was limited to 100 terms.

The assumption of a uniform diffusant distribution has been shown to be good, even in cases where experimental measurements have demonstrated a non-uniform distribution. This was demonstrated in Carter et al. and Weilert et al., both of which

showed that deviation of the Ag distribution from uniformity resulted in statistically insignificant changes in the calculated diffusivities [31, 33].

6.4. Experimental

6.4.1. Oxidation and Pore Characterization of the Graphite

Cyclic oxidation of IG-110 graphite spheres were performed in a three-zone tube furnace. Details of the apparatus are given in Al Zubaidi et al. [35] for the oxidation of low-alloy steels. The furnace tube was evacuated with a mechanical vacuum pump to a pressure of 13 kPa to 40 kPa during heating and cooling steps to minimize oxidation. A synthetic blend of nitrogen (bal.) and oxygen (20% to 22%) with a dew point of 211 K was introduced into the tube furnace once the desired temperature was reached. A mass flow controller maintained a flow rate of 150 mL/min. Batches of pre-milled IG-110 spheres were oxidized at 923 K for 30 and 60 minutes. BET surface area and pore volume distributions were obtained after each oxidation cycle with an N_2 gas adsorption surface analyzer. N_2 adsorption and desorption isotherms at 77 K were obtained to allow multipoint BET and non-local density functional theory (NL-DFT) calculations for surface area and pore volume distributions, respectively. Thirty-four spheres of IG-110 with a combined mass of approximately 1.224 g were needed get a successful N_2 surface area measurement. Five spheres were removed from the batch of spheres following each oxidation cycle to be used for diffusion measurements. The mass of the spheres was measured before and after each oxidation cycle with an analytical balance. No spallation or degradation of the graphite spheres were observed with oxidations up to 60 minutes.

6.4.2. Sample Preparation

Cs was infused into both the oxidized and unoxidized graphite spheres using a pressure vessel loading procedure. Variations in the procedure were used to create a range of sample concentrations as well as compensate for expanded surface area in the oxidized samples. The general method was as follows: commercially purchased solutions of $CsNO_3$ with concentrations of 1,000 μg/g or 10,000 μg/g were mixed with high-purity water to a total volume of 20 mL. This mixture was placed in a 45 mL polytetrafluoroethylene (PTFE) vessel along with pre-milled IG-110 graphite spheres. The vessel was capped and placed in a Parr Model 4744 parr bomb and heated in a box furnace for four cycles of 508 K for 2 hours and 373 K for 1 hour. Following this, the samples were removed and placed in a vacuum oven to dry overnight. The next day the samples were heated at 773 K for 30 minutes to dissociate nitrates, sanded to remove the outer layer, and lastly sonicated in high-purity water to remove dust created in the sanding process. Only 5 spheres were available for each oxidized set and therefore 1 sphere was selected to test the initial loading procedure. This procedure was modified afterwards based on the initial results.

The Cs concentration in each sample was measured using instrumental neutron activation analysis (INAA). Standards with 3 μg each of Cs were prepared by drying aliquots of $CsNO_3$ ICP-MS standard on a piece of filter paper set in a 0.3 mL high-density polyethylene vial. These standards were irradiated with the samples in the University of Missouri Research Reactor at a neutron flux of approximately 5×10^{13} $n/cm^2/s$. Irradiation times were either 60 s or 90 s depending on the irradiation position

used. After irradiation the samples and standards were counted for 600 s each and decay-corrected back to the start of the first count. Neutron activation proceeded via the reaction ^{133}Cs (n, γ) ^{134m}Cs which has a 2.9-hour half-life and decays partially by emission of a 127.5 keV gamma ray.

The Cs concentration distributions were then measured by laser ablation ICP-MS (LA-ICP-MS). One unoxidized sample was randomly selected from each batch. For the oxidized samples, given the limited number available, the initial test sample was also used for laser ablation. The selected samples were bisected with a stainless-steel razor blade and the flat faces were lightly sanded with 220-grit Al_2O_3 sandpaper. The samples were then placed in the laser ablation system with the flat faces oriented towards a Photon Machines 192 nm laser. This system was connected to a NexION® 300x ICP-MS. The laser operated with a power density of 2 mJ/cm^2 and 10 Hz pulse frequency producing a 40 μm spot size. The sampling procedure was repeated every 100 μm across the diameter of each sample; once complete the sampling direction was rotated 45° clockwise. This was repeated 4 times which produced a total of 8 radial measurements across each sample face. These were averaged to generate an average radial profile. Cs counts were normalized to a solid In standard with measurements taken immediately before and after each sample to correct for drift.

6.4.3. Diffusion Measurements

Time-release diffusion measurements were conducted over two different temperature ranges. Sample set B contained measurements at eight temperatures ranging

from 1073 K – 1973 K while the remaining sets, due to their limited number of samples, were measured from 1223 K – 1973 K at four different temperatures. The time-release method utilized in this work has been previously used to measure diffusion coefficients of Cs, I, Ag, Sr, and Eu [26, 28-34]. The diffusion cell was constructed with the bottom portion set into a Sentro-Tech high-temperature box furnace (Model ST-1700C-888), as shown in Fig. 6.1. Both the outer tube and inner tube were made from Saint Gobain Hexaloy® SiC; the end cap was stainless steel as were the Swagelok high-temperature ball valve and fittings. The He gas inlet tubing was first directed through a Palas GFG-1000 carbon aerosol generator which had been modified for use with He. The outlet tubing was connected to a dual-inlet spray chamber, the other inlet of which was used to continuously introduce a 1 ppb In standard used for signal normalization. Once constructed, a graphite sample was placed in the upper portion of the ball valve which was set at a partially open position, enough to allow He in without allowing the sample to fall through. While the furnace heated to the experimental temperature, He was continuously circulated to displace room air and prevent oxidation of the graphite sample and SiC components at high temperatures. Once heated, the ICP-MS was started and tuned. Background measurements were taken for ~1 hour after which the ball valve was fully opened, allowing the sample to drop into the heated portion of the cell. The He-laden carbon aerosol continuously passed over the sample and diffused Cs adsorbed to the carbon nanoparticles and was subsequently transported to the ICP-MS. After the signal sufficiently decayed the furnace was stopped while the ICP-MS continued scanning for an additional 20 minutes. Fig. 6.2 shows a typical release plot generated at

1223 K on a sample from set B using the above method. [A] shows the final background measurements taken before sample introduction. [B] shows the peak signal after sample introduction and [C] shows the decrease in Cs signal during the 20-minute cooling period.

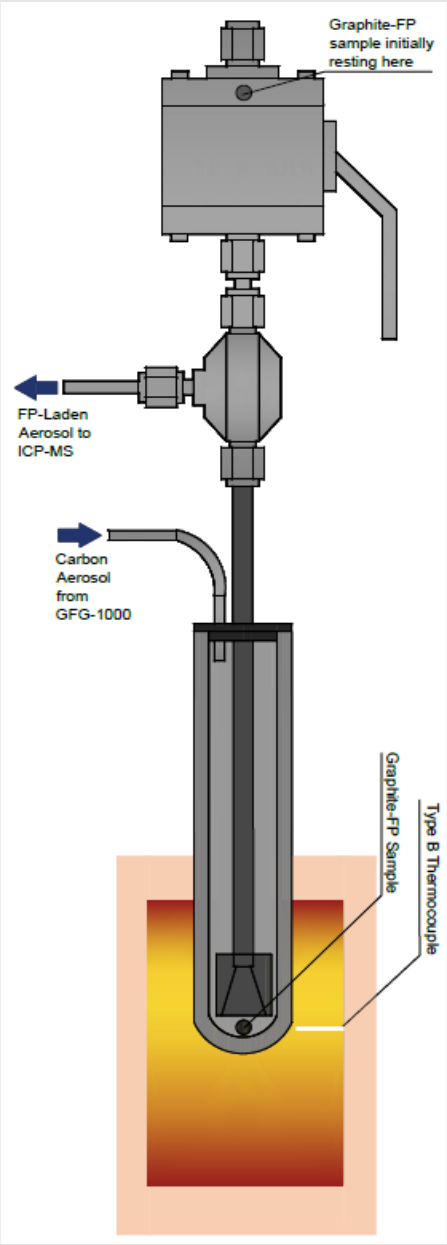

Figure 6.1: The SiC time-release diffusion cell. "FP" refers to fission product however the Cs used was from a natural source [32].

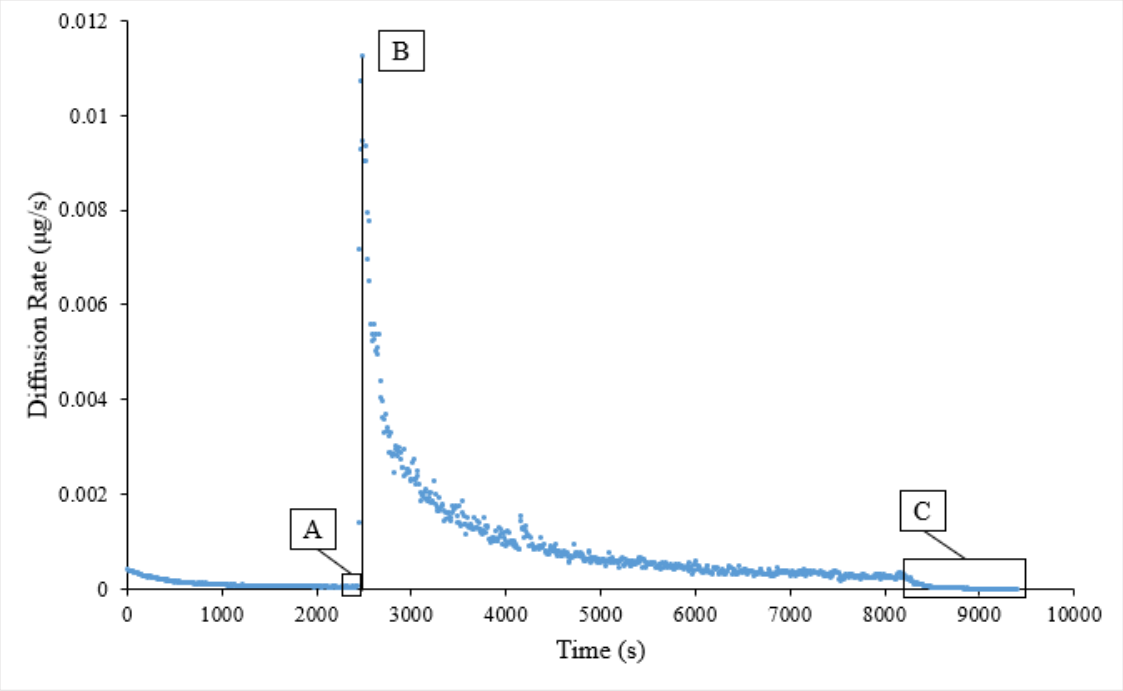

Figure 6.2: Cs time-release experiment in unoxidized IG-110 graphite at 1223 K. [A] is the baseline before sample introduction, [B] is the peak signal after sample introduction, and [C] is the decrease in signal after the furnace was shut down.

6.4.4. Data Analysis

Background corrections were made using three separate methods which were chosen based on the experiment. The first background correction method utilized the average of the last 10 data points taken before sample introduction; this average was subtracted from the remainder of the experimental data points and the end point of the experiment (only in cases with 100% fractional release) was the point immediately before the signal difference became negative. The second background correction method constituted a best-fit decay equation which was fit to the initial background measurements and then extended to the end of the experiment. It was generally used when the overall fit to Eqn. 6.5 was improved by its use. These first two methods were

used for experiments performed at 1523 K and below. Above 1523 K, the Cs signal did not always return to the initial baseline value even after 100% of the Cs was released. Instead it reached a plateau with a higher signal than the initial baseline. This increase in background signal was attributed to the more rapid release of Cs at these higher temperatures causing some Cs to deposit in the system, likely on graphite dust present in the tubing. A similar effect was seen in Ag time-release measurements taken over a similar temperature range [33]. For experiments performed above 1523 K, two corrections were used for each experiment. First, the background signal up to the peak was taken as the average of the ten points immediately prior to the introduction of the sample. Then, the average of the last ten points of the plateau region was used for the background subtraction of the peak and all subsequent points. In order to determine the end point of the experiment, Eqn. 6.6 was used:

$$S_{Cs} = S_{total} - \left(S_{plateau} + 3 * std_{Splateau}\right) \tag{6.6}$$

Where S_{Cs} was the corrected Cs signal, S_{total} was the total Cs signal, $S_{plateau}$ was the average signal calculated from the last ten points of the plateau, and $std_{Splateau}$ was the standard deviation of Cs signal in the last ten points of the plateau region. The point at which S_{Cs} became negative was considered the first point after 100% fractional release.

The INAA results taken before and after each diffusion experiment were used to calculate the total mass loss of Cs for each sample used. Once the above-described background corrections had taken place a calibration factor, $F_{calibration}$ (g/count), was calculated by dividing the total mass loss by the sum of all counts in the diffusion region. This calibration factor was then used to calculate the release rate (g/s) at each

measurement point by multiplication with the count rate (counts/s). Finally, the total fractional release was calculated by integrating the release rate over the region of interest and dividing by the initial mass, creating a total fractional release for each measurement point. This was then fit to Eqn. 6.5 used a least-squares minimization approach.

The temperature dependence of the Cs diffusion coefficient was demonstrated using the classic Arrhenius equation, Eqn. 6.7:

$$D = D_0 e^{-E_a/RT} \tag{6.7}$$

Where D_0 is the pre-exponential factor (m^2/s) and E_a is the activation energy (kJ/mol). Uncertainties in the pre-exponential factor and activation energy were calculated from standard errors of the best fit linear regression.

6.5. Results

The pore-size distribution results are shown in Fig. 6.3. The calculated wt% mass loss for the 30- and 60-minute oxidized sets was 3.6% and 7.8%, respectively.

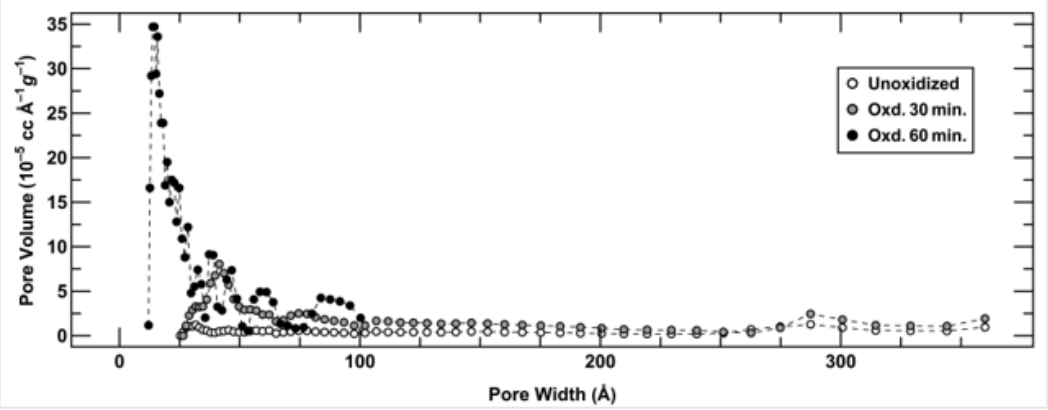

Figure 6.3: Differential pore volume distribution of IG-110 for unoxidized, 30-minute, and 60-minute oxidations.

Table 6.1 shows the number of spheres, type of standard, volume of standard, final average Cs mass, and final Cs concentration of each sample set used in this work. For the concentration-matched samples, ox30 control and ox60 control refers to the concentration matched sets for ox30 and ox60, respectively. The final average Cs concentration per sample has been provided in units of both $\mu g_{Cs}/g_{graphite}$ and $mmol_{Cs}/kg_{graphite}$ for ease of comparison to the literature in later sections. Sample masses were determined gravimetrically to avoid discrepancies in densities caused by oxidation.

Table 6.1: Conditions for loading Cs into the graphite sphere using the loading procedure. Samples labeled (test) were used to test the loading procedure.

Sample Set	Number of Spheres	Cs Standard concentration (ppm)	Vol. Standard (mL)	Final Avg. Cs Content (μg)	Final Average Cs Concentration ($\mu g_{Cs}/g_{graphite}$ | $mmol_{Cs}/kg_{graphite}$)
B	17	1,000	15	7.1 (0.8)	276 (23) | 2.1 (0.2)
C	6	1,000	5	0.9 (0.1)	34 (2) | 0.26 (0.01)
ox30 (test)	1	1,000	15	6.1 (-)	N/A
ox30	4	1,000	5	4.2 (0.5)	141 (13) | 1.1 (0.1)
ox30 control	4	10,000	4.85-5	4.1 (0.6)	163 (26) | 1.2 (0.2)
ox60 (test)	1	1,000	4	0.4 (-)	N/A
ox60	4	1,000	6	1.6 (0.1)	57 (3) | 0.43 (0.02)
ox60 control	4	10,000	1.6-2	1.6 (0.2)	49 (8) | 0.37 (0.06)

The results of the LA-ICP-MS experiments are shown below in Figs. 6.4-6.8. In order, the samples were selected at random from batches B, C, and ox60 control; the last two were the test samples from the ox30 and ox60 loadings, respectively. In all cases there was not a significant relationship between radius and Cs concentration.

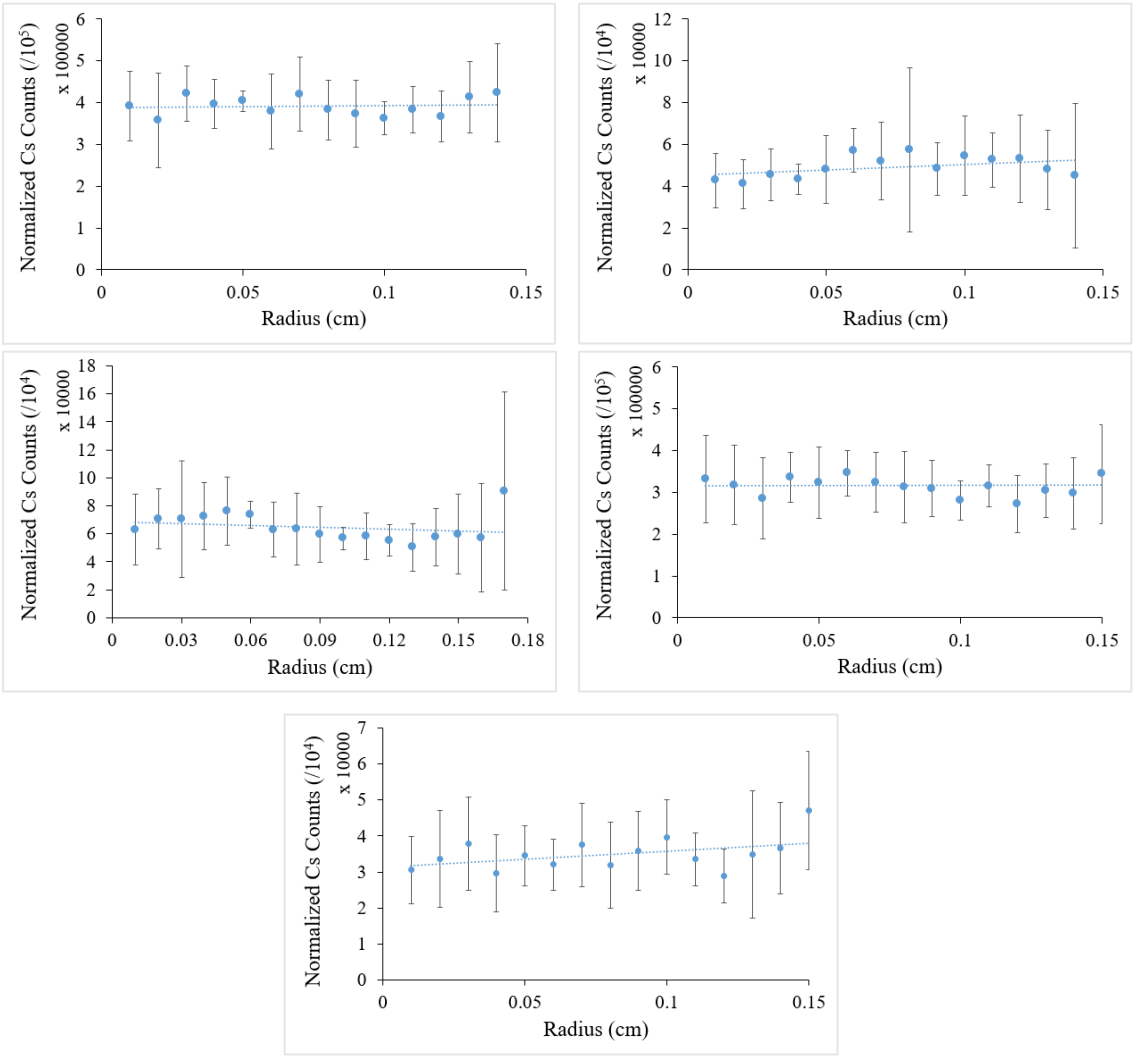

Figures 6.4, 6.5, 6.6, 6.7, 6.8: Selected samples from batches B, C, and ox60 control, and test samples from the ox30 and ox60 test loadings, respectively.

The results for the time-release experiments are provided in Table 6.2. This includes the sample set, experimental temperature, pre- and post-experiment Cs masses, the effective diffusivity calculated by fitting the experimental fractional release to Eqn. 6.5, the variance of each effective diffusion coefficient, and the mean absolute value of the error (MAE). The variance was calculated from the Hessian matrix of the least

squares fit [36]. The MAE describes the goodness of fit between the measured and simulated cumulative fractional release and was calculated using Eqn. 6.8:

$$error = \left|\frac{y - y_{fit}}{y}\right| \tag{6.8}$$

Where y_{fit} is the simulated cumulative release fraction and y is the measured cumulative release fraction.

Figure 6.9 shows an example of an experimental fractional release plot with the best-fit solution to Eqn. 6.5 superimposed on the curve. All other fractional release plots can be found in Appendix B. Figures 6.10-6.12 show the Arrhenius plots for all 6 sample sets with ox30 and ox30 control shown in Fig. 6.10, ox60 and ox60 control shown in Fig. 6.11, and sets B and C in Fig. 6.12. Finally, Table 6.3 shows the activation energy, E_a (kJ/mol), and pre-exponential, D_0 (m^2/s), for each set along with their respective uncertainties.

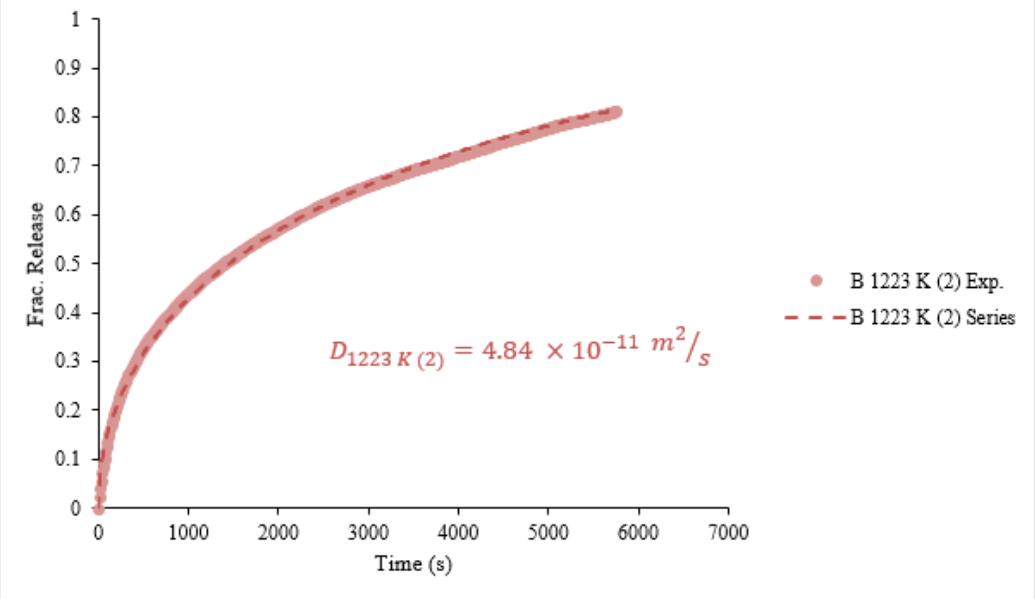

Figure 6.9: Experimental fractional release, taken from a sample from set B measured at 1223 K. "Series" refers to the series solution in Eqn. 6.5.

Table 6.2: Results for all time-release experiments. Includes the experimental temperature, initial and final Cs masses, and the calculated effective diffusion coefficient.

Sample Set	Experimental Temperature (K)	Initial Cs mass (μg)	Final Cs mass (μg)	Effective Diffusion Coefficient (m^2/s)	MAE
B	1073	7.00	1.20	$2.02\ (0.43) \times 10^{-11}$	20%
	1073	8.29	3.21	$2.05\ (0.48) \times 10^{-11}$	8%
	1223	7.62	0.47	$7.85\ (1.61) \times 10^{-11}$	8%
	1223	6.76	1.25	$4.84\ (0.96) \times 10^{-11}$	2%
	1223	6.13	0.13	$9.76\ (2.10) \times 10^{-11}$	5%
	1373	7.73	0.17	$2.56\ (0.72) \times 10^{-10}$	4%
	1523	6.51	0.05	$5.48\ (2.24) \times 10^{-10}$	5%
	1673	6.67	0.00	$1.04\ (0.19) \times 10^{-9}$	9%
	1773	7.86	0.00	$1.64\ (0.44) \times 10^{-9}$	4%
	1873	8.07	0.00	$2.94\ (0.96) \times 10^{-9}$	1%
	1973	6.54	0.00	$3.88\ (1.34) \times 10^{-9}$	4%
C	1223	0.77	0.03	$3.04\ (0.58) \times 10^{-11}$	35%
	1523	1.01	0.03	$1.71\ (0.42) \times 10^{-10}$	4%
	1773	0.85	0.00	$2.63\ (0.90) \times 10^{-9}$	1%
	1973	0.86	0.00	$4.42\ (0.94) \times 10^{-9}$	3%
ox30	1223	4.29	0.58	$4.79\ (0.96) \times 10^{-11}$	7%
	1523	4.04	0.07	$3.03\ (0.97) \times 10^{-10}$	4%
	1773	4.36	0.03	$1.56\ (0.38) \times 10^{-9}$	1%
	1973	3.35	0.00	$5.29\ (1.09) \times 10^{-9}$	3%
ox30 control	1223	4.55	0.77	$3.95\ (0.81) \times 10^{-11}$	19%
	1523	3.86	0.06	$1.84\ (0.51) \times 10^{-10}$	3%
	1773	4.58	0.00	$3.32\ (1.26) \times 10^{-9}$	2%
	1973	3.25	0.00	$5.41\ (1.05) \times 10^{-9}$	4%
ox60	1223	1.67	0.00	$1.51\ (0.43) \times 10^{-10}$	18%
	1523	1.70	0.00	$2.03\ (0.41) \times 10^{-9}$	2%
	1773	1.67	0.00	$7.10\ (1.37) \times 10^{-9}$	9%
	1973	1.40	0.00	$9.84\ (2.03) \times 10^{-9}$	2%
ox60 control	1223	1.53	0.06	$5.79\ (1.14) \times 10^{-11}$	26%
	1523	1.83	0.02	$1.68\ (0.48) \times 10^{-10}$	15%
	1773	1.44	0.00	$2.72\ (0.85) \times 10^{-9}$	1%
	1973	1.41	0.00	$4.74\ (0.90) \times 10^{-9}$	5%

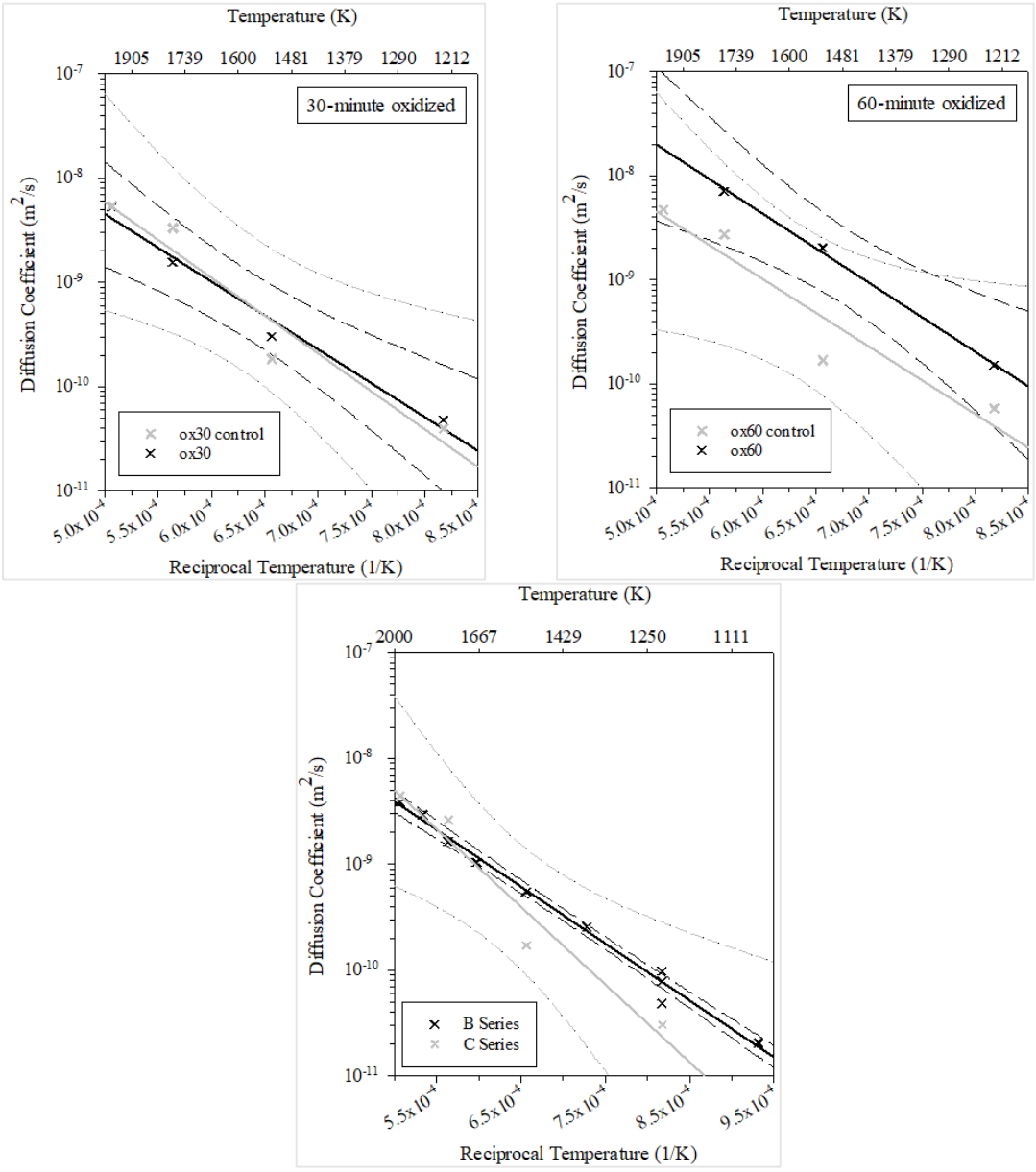

Figures 6.10, 6.11, 6.12: The top left Arrhenius plot shows the 30-minute oxidized samples (black) compared to the concentration-matched control samples (gray). The top right plot shows the same for the 60-minute oxidized samples (black) and their concentration-matched control counterparts (gray). The bottom Arrhenius plot shows the results from set B, the highest concentration set, in black and set C, the lowest concentration set, in gray. In each, the solid line shows the best-fit line while the dashes represent the 95% confidence interval.

Table 6.3: Arrhenius parameters of the Cs diffusion coefficient of all tested sets and their uncertainties.

Sample Set	Oxidation time (m)	Cs concentration (μg/g)	D_0 (m^2/s)	$\pm\Delta D_0$ (m^2/s)	E_a (kJ/mol)	$\pm\Delta E_a$ (kJ/mol)
B	0	276 (23)	1.9×10^{-6}	4.2×10^{-8}	103	3
C	0	34 (2)	2.3×10^{-5}	3.7×10^{-6}	140	22
ox30	30	141 (13)	7.7×10^{-6}	6.3×10^{-7}	124	13
ox30 control	0	163 (26)	2.6×10^{-5}	4.8×10^{-6}	139	26
ox60	60	57 (3)	4.2×10^{-5}	2.0×10^{-6}	127	6
ox60 control	0	49 (8)	8.1×10^{-6}	1.5×10^{-6}	124	28

6.6. Discussion

Figure 6.3 shows the pore volume distributions for unoxidized, 30-min oxidized, and 60-min oxidized samples. In moving from unoxidized to 30-min oxidized there was an increase in the volume of fine pores of ~0.005-0.01 μm but little change beyond that size. This was most likely caused by preferential oxidation of the binder material which is known to develop fine pores upon oxidation [37]. The 60-min oxidized samples showed the appearance of micropores, possibly due to the exposure of previously blind pores in the graphite filler particles. There was a complete disappearance of pores >0.01 μm and this may have been caused by an enlargement of the existing pores beyond the range of what can be analyzed using nitrogen adsorption (~0.1 μm).

Cs diffusion coefficients were measured and compared for two sets each of oxidized and unoxidized IG-110 graphite. The samples were oxidized in synthetic air at 923 K for either 30 or 60 minutes. The diffusion coefficients were measured in sets of IG-110 graphite loaded with four different concentrations ranging from 34-276

$\mu g_{Cs}/g_{graphite}$, see Table 6.1. The Cs concentration in two of the non-oxidized control groups matched the concentration of Cs in the oxidized samples. The concentration matched control samples eliminated concentration-dependent effects that may have obscured oxidation induced changes in the effective diffusivities. Three replicate experiments were performed at 1223 K on samples taken from set B. These resulted in a standard deviation of the effective diffusion coefficient of 33%. This is in the observed range of 13% - 37% for triplicate experiments of Ag diffusion performed over the temperature range 1073 K – 1973 K [33]. Therefore, a change in diffusivity of >33% of a measurement from one set compared to another was considered a significant difference. Both oxidized sets showed significant changes in diffusivities compared to their concentration-matched control samples. Changes to the 30-minute oxidized set were smaller than those of the 60-minute oxidized set. In unoxidized samples, concentration dependent changes in diffusivity were not observed until the concentration exceeded 163 $\mu g_{Cs}/g_{graphite}$ (or ~1.2 $mmol_{Cs}/kg_{graphite}$). Above 163 $\mu g_{Cs}/g_{graphite}$ the activation energy decreased.

Cs transport in graphite is dominated by diffusion through pores where the Cs atoms are in constant contact with the grain surfaces and grain volume [18]. The diffusion mechanism of Cs in graphite below 1573 K is described by a diffusion trapping model in which “traps” are defined as sites with increased binding energy [38]. Such sites have been theorized to be pores of $\leq$ 1 nm and irregularly-shaped cavities with an increased negative charge density [22, 38]. Cs is ionized in graphite and is attracted to the negatively charged cavities [38]. Hoinkis [38], studying oxidized and unoxidized matrix

A3-3, observed that this trapping effect was not uniform over all temperatures or all oxidized states. Instead, Cs diffusivity studies revealed that above 1573 K the diffusion-trap model was no longer applicable in unoxidized samples and Cs diffusion followed simple Fickian kinetics. In oxidized samples, the diffusion mechanism changed from a diffusion-trap model to classical diffusion. In both cases this change in diffusion mechanism was attributed to a reduction in trapping sites.

An increase in the diffusion coefficient at 1523 K was observed in the oxidized sets. This change is most likely due to a reduction in trapping pores. Figures 6.10-6.11 show the Arrhenius plots of the ox30 and ox60 sets, respectively, compared to their concentration-matched sets. In both cases, the trends for the oxidized samples were linear while the unoxidized samples deviated from their best-fit lines. In all of the unoxidized sets, except the highest concentration set, there was a consistent decrease in diffusivity at 1523 K versus what would be expected based on the surrounding measurements. This may be due to the increased influence of trapping sites at temperatures below 1573 K [38]. In the set with the highest Cs concentration, unoxidized set B, the effective diffusion coefficients were linear over the entire tested temperature range. This could be explained by saturation of the highest energy traps with lower energy sites therefore contributing to diffusion, resulting in a normalization effect over the temperature range. As the concentration increases, lower-energy sites increasingly contribute to diffusion and the average speed of migration increases [22].

Set C was the lowest concentration set tested in this work and had an average concentration of 34 μg $Cs/g_{graphite}$ (0.26 mmol $Cs/kg_{graphite}$) per sample. The time-release

system used in this work does not have adequate sensitivity to measure samples with concentrations much lower than this, as evidenced by a failure to measure a signal from two samples containing 0.07 μg_{Cs} or ~10% the concentration of the samples in set C. Myers, et al. [25] reported a concentration dependence for Cs at concentrations ≥ 0.55 $\mu g_{Cs}/g_{source\ material}$. Katscher, et al. [18] published a less conservative concentration-dependent value of ~0.1 - 1 $mmol_{Cs}/kg_{C}$, based on estimates of saturation effects in graphite. These values are below the minimum Cs concentrations measurable in this work and therefore these values could not be verified. Within the context of this work, there was not a significant change in diffusion coefficients between samples from set C and set ox30 control (163 $\mu g_{Cs}/g_{graphite}$, 1.2 $mmol_{Cs}/kg_{graphite}$). Therefore, it is reasonable to conclude that diffusion is independent of concentration between 34 – 163 $\mu g_{Cs}/g_{graphite}$ (0.26 – 1.2 $mmol_{Cs}/kg_{graphite}$). Below and above these values there exists the possibility that diffusion will be affected by concentration.

Most studies looking at the effects of graphite oxidation on fission product sorption and diffusion have focused on matrix graphite and report that the binder content of graphite heavily influences its fission product retention. The binder is the primary contributor to the greater sorption capacity for fission products in matrix graphite vs structural graphite [18]. Graphite binder adsorbs 100x more Cs than graphite filler particles [39]. This binder, however, also oxidizes to a much greater extent than graphite filler particles and subsequently sorption rapidly decreases with oxidation due to preferential oxidation of binder material [18, 22]. Cs diffusion coefficients in oxidized matrix A3 graphite were increased by factors of 6-330 for burnoffs of <5 wt% [22].

Given the much lower concentration of binder content in IG-110 vs A3 matrix, similar increases in diffusivities would not be expected, nor were they observed in this work. Instead, the 30 minute-oxidized samples (wt% loss = 3.6%) showed only moderate changes in effective diffusion coefficients with the highest changes occurring at 1523 K and 1773 K. At 1523 K the effective diffusivity increased by 65%, most likely due to a reduction in binder content and trapping pores. The diffusivity at 1773 K, on the other hand, decreased by over 50% compared to the unoxidized set. It is possible that the increased pore volume hindered Cs transport given that traps are not expected to be effective at this high temperature. The 60 minute-oxidized samples (wt% loss = 7.8%) experienced greater increases in diffusivities for all tested temperatures with the greatest change occurring at 1523 K where the diffusion coefficient increased by a factor of 12. This increase is attributed to a decrease in trapping sites and increase in interconnected pore volume.

The diffusion coefficient of Cs in the 60-minute oxidized set was measured over the same temperature range as its concentration-matched set (1223 K – 1973 K), however, its measured diffusivity at 1973 K was not used in the Arrhenius calculation nor was the measurement point included in the Arrhenius plot shown in Fig. 6.11. The measured diffusivity at 1973 K was ~50% of the expected value. Similar decreases in diffusivity were observed in Ag measurements at temperatures of 1673 K and higher and were attributed to the time required for released diffusant to completely exit the system, measured to be ~60 s [33]. This corresponds to a diffusion coefficient of $\sim 1 \times 10^{-8}$ m^2/s

which was similar to the diffusivity of the 60-minute oxidized sample in this work, which had a measured diffusivity of 9.84×10^{-9} m^2/s.

There are currently two methods utilized in fission product modelling to compensate for graphite oxidation. One makes the effective diffusion coefficient a function of weight-percent burnoff [8] while the other uses a release fraction equal to the degree of graphite corrosion [18]. The observed temperature dependence of Cs diffusion in this work suggests that these correction methods are too simplistic. Efforts should be made in future studies to expand the range of oxidation to lower and higher wt% losses.

The rate of graphite oxidation is influenced by several factors including the graphitization temperature of the graphite and subsequently its binder content, the pore structure, and the oxidation temperature. Four oxidation regimes have been identified based on their respective rates of oxygen transport into the graphite microstructure vs the rate of oxygen consumption [21]. Regime II was the targeted regime in this work and is typically defined as occurring in the temperature range of 550-800 °C; it is dominated primarily by competition between in-pore diffusion and the rate of chemical reaction [40]. This competition means the concentration of reactant (and burnoff) will vary exponentially with depth and lead to an oxidation burn-off profile [40]. A limitation of this work was that sanding was necessary to remove high levels of Cs present at the surface of the graphite. Removal of the outer layer of the samples through sanding could have altered the pore structure and accounted for a disproportionately larger fraction of the wt% loss and increased pore size in the oxidized samples. The reported diffusivities

for the oxidized samples may therefore be under representative of diffusivities for the reported weight loss values.

Table 6.4 presents comparative results of the unoxidized samples at the high and low ends of the Cs concentration range in the present study to those published previously. The closest comparison to the current results are those presented in Carter et al. [26] which were measured using a similar time-release system. The current study produced diffusivities that were 1-2 orders of magnitude greater than those measured in Carter et al. The difference between these studies was the Cs loading procedure. Carter used a gaseous infusion technique. In the present work a pressure vessel infusion method, described in Section 6.4.2, was employed. Hayashi, et al. [41] reported order-of-magnitude increases in diffusivities when using different source preparation methods. IG-110 samples which were heated at 1073 K in open air experienced diffusivities ~10x less than those heated to 1173 K under flowing Ar [41]. It is clear then that modification of a loading procedure can result in large changes in diffusivities and this is likely the cause of the discrepancies between this work and Carter, et al's.

Table 6.4: Comparison of historical results to those of this work.

Reference	Graphite Type	Temp. Range (K)	E_a (kJ/mol)	D_0 (m^2/s)	D_{1273K} (m^2/s)
Hayashi, et al. [41]	IG-110, unirradiated [A]	873-1273	112	1.2×10^{-4}	3.0×10^{-9}
	IG-110, unirradiated [B]	873-1273	95	1.7×10^{-4}	2.2×10^{-8}

Hayashi, et al. [42]	IG-110, irradiated	1023-1303	157	9.0×10^{-6}	3.3×10^{-12}
Moormann [43]	H-451, irradiated	N/A	149	1.7×10^{-6}	1.3×10^{-12}
Carter, et al. [28]	NBG-18, unirradiated	1090-1395	123	1.0×10^{-7}	9.0×10^{-13}
Carter, et al. [26]	IG-110, unirradiated	1100-1300	110 (28)	1.0×10^{-7}	3.1×10^{-12}
This Study	IG-110, unirradiated [B]	1073-1973	103 (3)	1.9×10^{-6}	1.2×10^{-10}
	IG-110, unirradiated [C]	1223-1973	140 (22)	2.3×10^{-5}	4.0×10^{-11}

One area of great importance not explored in this work is the influence of neutron irradiation on the Cs diffusion coefficient and how this may change with oxidation. Neutron irradiation alters the microstructure of graphite filler particles and binder and creates sites with higher-than-average binding energies [22]. Consequently, in highly graphitized materials such as IG-110, fission product sorptivity increases with increasing neutron fluence, leading to a decrease in the effective diffusion coefficient and an increase in the activation energy. This can be seen quite clearly in Table 6.4 and has been studied in depth in in-pile graphite. However, to the best of the authors' knowledge, no studies have examined how the competing processes of neutron irradiation and oxidation will interact to influence fission product diffusion; this should be explored in future studies.

6.7. Conclusions

Cs diffusion coefficients have been measured in unoxidized and oxidized IG-110 graphite over a range of sample concentrations. Oxidation led to an increase in the effective Cs diffusion coefficient, particularly in the more oxidized set. Diffusion coefficients were independent of concentration between 34 – 163 $\mu g_{Cs}/g_{graphite}$, above which the diffusion coefficient and mechanism was affected by concentration. These results can aid in predictive modeling of Cs diffusion in HTGR cores.

6.8. Acknowledgments

The authors thank Dr. Jeremy Watts at University of Missouri Science and Technology for his aid with the BET measurements reported in this work.

This research has been supported by the U.S. Department of Energy Nuclear Energy University Program grant NEUP-12830, and an Integrated University Program Fellowship grant (DE-NE000118 Mod 007) towards support of T.M. Weilert.

6.9. References

[1] US DOE selects advanced reactor designs for demonstration plants. https://www.world-nuclear-news.org/Articles/US-DOE-selects-advanced-reactor-designs-for-demons (accessed June 9).

[2] Japanese gas-cooled reactor restarts. https://www.world-nuclear-news.org/Articles/Japanese-gas-cooled-reactor-restarts (accessed January 6, 2022).

[3] Demonstration HTR-PM connected to grid. https://www.world-nuclear-news.org/Articles/Demonstration-HTR-PM-connected-to-grid (accessed January 6, 2022).

[4] Dual criticality for Chinese demonstration HTR-PM. https://www.world-nuclear-news.org/Articles/Dual-criticality-for-Chinese-demonstration-HTR-PM (accessed January 6, 2022).

[5] UK selects HTGR for advanced reactor demonstration. https://www.world-nuclear-news.org/Articles/UK-selects-HTGR-for-advanced-reactor-demonstration (accessed January 6, 2022).

[6] *High Temperature Gas Cooled Reactor Fuels and Materials*; International Atomic Energy Agency: Vienna, Austria, 2010; p 182.

[7] Zhou, X.-w.; Tang, Y.-p.; Lu, Z.-m.; Zhang, J.; Liu, B., Nuclear graphite for high temperature gas-cooled reactors. *New Carbon Materials* **2017,** *32* (3), 193-204.

[8] *Fuel performance and fission product behaviour in gas cooled reactors*; International Atomic Energy Agency: Vienna, Austria, 1997; p 529.

[9] Hunn, J. D.; Baldwin, C. A.; Gerczak, T. J.; Montgomery, F. C.; Morris, R. N.; Silva, C. M.; Demkowicz, P. A.; Harp, J. M.; Ploger, S. A., Detection and Analysis of Particles with Failed SiC in AGR-1 Fuel Compacts. In *Proceedings of the HTR 2014*, Weihai, China, 2016; p 12.

[10] *A Review of Radionuclide Release From HTGR Cores During Normal Operation*; 1009382; Palo Alto, CA, 2003.

[11] Demkowicz, P. A.; Hunn, J. D.; Morris, R. N.; van Rooyen, I.; Gerczak, T.; Harp, J. M.; Ploger, S. A. *AGR-1 Post Irradiation Examination Final Report*; Idaho National Laboratory: Idaho Falls, ID, 2015; p 132.

[12] Evans, R. B., III; Davis, W., Jr.; Sutton, A. L., Jr. *Cesium Diffusion in Graphite*; Oak Ridge National Laboratory: Oak Ridge, TN, 1980; p 130.

[13] Miller, G. K.; Petti, D. A.; Maki, J. T.; Knudson, D. L.; Skerjanc, W. F. *PARFUME Theory and Model Basis Report*; Idaho National Laboratory: Idaho Falls, ID, 2018; p 74.

[14] Mohanty, S.; Majumdar, S. *HTGR Graphite Core Component Stress Analysis Research Program - Task 1 Technical Letter Report*; U.S. Nuclear Regulartoy Commission: 2011; p 115.

[15] Castle, B. *NGNP Reactor Coolant Control Study*; Idaho National Laboratory: Idaho Falls, ID, 2010; p 32.

[16] Pointud, M. L.; Karcher, W.; Pollitt, N.; Lothe, J. *Catalytic Influence of Different Metals on the Corrosion Rate of Graphite*; Dorset, England, 1965; p 62.

[17] Kane, J. J.; Contescu, C. I.; Smith, R. E.; Strydom, G.; Windes, W. E., Understanding the reaction of nuclear graphite with molecular oxygen: Kinetics, transport, and structural evolution. *J. Nucl. Mat.* **2017,** *493*, 343-367.

[18] Katscher, W.; Moormann, R.; Verfondern, K.; Decken, C. B. v. d.; Iniotakis, N.; Hilpert, K., Fission product behaviour and graphite corrosion under accident conditions in the HTR. *Nucl. Eng. Des.* **1990,** *121* (2), 219-225.

[19] Contescu, C. I.; Guldan, T.; Wang, P.; Burchell, T. D., The effect of microstructure on air oxidation resistance of nuclear graphite. *Carbon* **2012,** *50* (9), 3354-3366.

[20] Huang, W.-H.; Tsai, S.-C.; Yang, C.-W.; Kai, J.-J., The relationship between microstructure and oxidation effects of selected IG- and NBG-grade nuclear graphites. *J. Nucl. Mat.* **2014,** *454* (1-3), 149-158.

[21] Lo, I.-H.; Tzelepi, A.; Patterson, E. A.; Yeh, T.-K., A study of the relationship between microstructure and oxidation effects in nuclear graphite at very high temperatures. *J. Nucl. Mat.* **2018,** *501*, 361-370.

[22] Myers, B. F., A review of the diffusion of selected fission product metals in polycrystalline graphite. In *Proceedings of a Colloquium held at Hahm-Meitner-Institut*, Hoinkis, E., Ed. Berlin, 1981; pp 56-67.

[23] Myers, B. F.; Bell, W. E. *Strontium transport data for HTGR systems*; General Atomic Company: San Diego, CA, 1974; p 75.

[24] Sandalls, F. J.; Walford, M. R., Laboratory determinations of strontium diffusion coefficients in graphite. *J. Nucl. Mater.* **1976,** *62* (2-3), 265-272.

[25] Myers, B. F.; Jensen, D. D.; Zumwalt, L. R., The diffusion of cesium and strontium in H-327 graphite during the Peach Bottom Fuel Test Element experiments. In

Proceedings of a Colloquium held at Hahn-Meitner-Institut, (Ed.), E. H., Ed. Berlin, 1981; pp 166-171.

[26] Carter, L. M.; Brockman, J. D.; Loyalka, S. K.; Robertson, J. D., Measurement of cesium diffusion coefficients in graphite IG-110. *J. Nucl. Mater.* **2015,** *460*, 30-36.

[27] Carter, L. M.; Brockman, J. D.; Loyalka, S. K.; Robertson, J. D., Calibration of a system for measurements of diffusion coefficients of fission products in HTGR/VHTR core materials. *J. Radioanal. Nucl. Chem.* **2016,** *307*, 1771-1775.

[28] Carter, L. M.; Brockman, J. D.; Robertson, J. D.; Loyalka, S. K., ICP-MS measurement of diffusion coefficients of Cs in NBG-18 graphite. *J. Nucl. Mater.* **2015,** *466*, 402-408.

[29] Carter, L. M.; Brockman, J. D.; Robertson, J. D.; Loyalka, S. K., ICP-MS measurement of iodine diffusion in IG-110 graphite for HTGR/VHTR. *J. Nucl. Mater.* **2016,** *473*, 218-222.

[30] Carter, L. M.; Brockman, J. D.; Robertson, J. D.; Loyalka, S. K., Diffusion of cesium and iodine in compressed IG-110 graphite compacts. *J. Nucl. Mater.* **2016,** *476*, 30-35.

[31] Carter, L. M.; Seelig, J. D.; Brockman, J. D.; Robertson, J. D.; Loyalka, S. K., ICP-MS measurement of silver diffusion coefficient in graphite IG-110 between 1048K and 1284K. *J. Nucl. Mater.* **2018,** *498*, 44-49.

[32] Weilert, T. M.; Walton, K. L.; Loyalka, S. K.; Brockman, J. D., Measurement of effective Sr diffusion coefficients in IG-110 graphite. *J. Nucl. Mater.* **2021,** *555*.

[33] Weilert, T. M.; Walton, K. L.; Loyalka, S. K.; Brockman, J. D., Effective diffusivity of Ag and migration of Pd in IG-110 graphite. *J. Nucl. Mat.* **2022,** *559*.

[34] Weilert, T. M.; Walton, K. L.; Loyalka, S. K.; Brockman, J. D., Europium diffusion in IG-110 nuclear graphite. *J. Nucl. Mat.* **2022,** *561*.

[35] Zubaidi, F. N. A.; Walton, K. L.; Tompson, R. V.; Ghosh, T. K.; Loyalka, S. K., The effect of long-term oxidation on the total hemispherical emissivity of Type 316L stainless steel. *Nucl. Technol.* **2018,** *205* (6), 790-800.

[36] Hughes, I. G.; Hase, T. P. A., *Measurements and their Uncertainties: A Practical Guide to Modern Error Analysis*. Oxford University Press: 2010.

[37] Wang, P.; Contescu, C. I.; Yu, S.; Burchell, T. D., Pore structure development in oxidized IG-10 nuclear graphite. *J. Nucl. Mat.* **2012,** *430* (1-3), 229-238.

[38] Hoinkis, E., The determination of diffusion coefficients of cesium and silver by the release method in as-received, oxidized, and neutron-irradiated graphitic matrix. In *Proceedings of a Colloquium held at Hahm-Meitner-Institut*, Hoinkis, E., Ed. Berlin, 1981; pp 77-102.

[39] Moormann, R., Fission Product Transport and Source Terms in HTRs: Experience from AVR Pebble Bed Reactor. *Sci. Technol. Nucl. Install.* **2008,** *2008*, 14.

[40] Xiaowei, L.; Jean-Charles, R.; Suyuan, Y., Effect of temperature on graphite oxidation behavior. *Nucl. Eng. Des.* **2004,** *227* (3), 273-280.

[41] Hayashi, K.; Fukuda, K., Diffusion coefficients of cesium in un-irradiated graphite and comparison with those obtained from in-pile experiments. *J. Nucl. Mat.* **1989,** *168* (3), 328-336.

[42] Hayashi, K.; Kobayashi, F.; Minato, K.; Ikawa, K.; Fukuda, K., In-pile release behavior of metallic fission products in graphite materials of an HTGR fuel assembly. *J. Nucl. Mater.* **1987,** *149* (1), 57-68.

[43] Collin, B. P. *Diffusivities of Ag, Cs, Sr, and Kr in TRISO Fuel Particles and Graphite*; Idaho National Laboratory: Idaho Falls, ID, 2016; p 40.

CHAPTER 7:
CONCLUDING REMARKS AND FUTURE WORK

This work has expanded the knowledge base of fission product diffusion in structural graphite, particularly in regards to diffusion in oxidized graphites and potential retention effects of Pd in the presence of other noble metals. It has also provided the first diffusion coefficients for Eu in any type of graphite.

Given the success of measuring Cs diffusion in oxidized IG-110, it would be beneficial to expand the range of oxidized states over both shorter and longer oxidation times to establish a better means of predicting diffusivity changes in oxidized IG-110. Coupling the pore size distribution measurements with imaging or spectroscopy techniques would allow for a better assessment of the binder content and would provide a more accurate means of evaluating microstructural changes and the coincident effects on fission product diffusion. Past methods used to assess binder content in nuclear graphites include transmission electron microscopy, scanning electron microscopy, and Raman spectroscopy. Diffusion measurements in oxidized IG-110 should be expanded to Sr and Eu; given these elements' greater adsorption to binder content than Cs, diffusivity changes may be even more extreme with oxidation. Diffusion measurements in oxidized graphite should also be extended to other grades of structural and matrix graphites.

The Ag + Pd binary measurements showed considerable changes in Ag diffusion coefficients at 1073 K in the presence of Pd. Those samples contained an approximately 1:2 ratio of Ag:Pd which is far greater than fission yield ratios resulting from U and Pu

fissions. Tailoring the loading procedure to produce a more realistic ratio may show whether or not this retentive behavior could be expected in an operating reactor.

The failure to measure Pd-only diffusion at all tested temperatures but one may have been the result of the released Pd not interacting with the carbon aerosol in a traditional manner. Figures 7.1-7.2 show the results of temperature ramping experiments on Pd-only samples. In Fig. 7.1 the furnace was preheated to 1673 K and a Pd-only loaded sample was dropped in. The furnace decreased in temperature by 50 K every 20 minutes until the temperature reached 1373 K, after which the furnace was stopped. Total Pd fractional release was 31%. In Fig. 7.2 the experiment was conducted in reverse; the furnace was preheated to 1073 K after which the sample was dropped in. The temperature was then raised 50 K every 15 minutes until it reached 1973 K. Total Pd fractional release was 100%. In both experiments the Pd signal changed dramatically with temperature in a non-linear manner. Figure 7.1 shows a sharp increase in the Pd signal when the temperature dropped from 1673 K to 1623 K. The same can be seen in Fig. 7.2 where the Pd signal decreased when the temperature increased from 1623 K to 1673 K. The Pd signal also decreased when the temperature increased from 1423 K to 1473 K. This temperature dependence of Pd transport to the ICP-MS may reflect non-traditional Pd interaction with graphitic dust or Pd interaction with the SiC tubing; both hypotheses are worth further investigation.

Eu diffusion should be measured in matrix graphite to assess the suitability of using Eu diffusion measurements conducted in structural graphite to estimate Eu diffusion in matrix graphites.

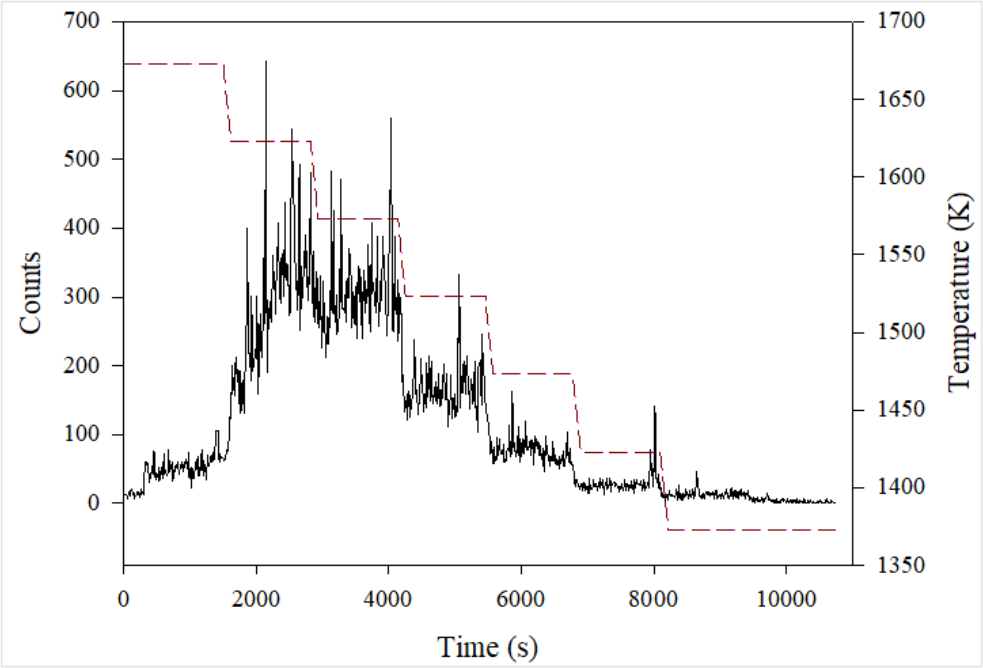

Figure 7.1: Temperature dependence of Pd detection at the ICP-MS. The black track corresponds to the ICP-MS signal for Pd and the red track shows the furnace temperature. The tested temperature range was 1673 K – 1373 K.

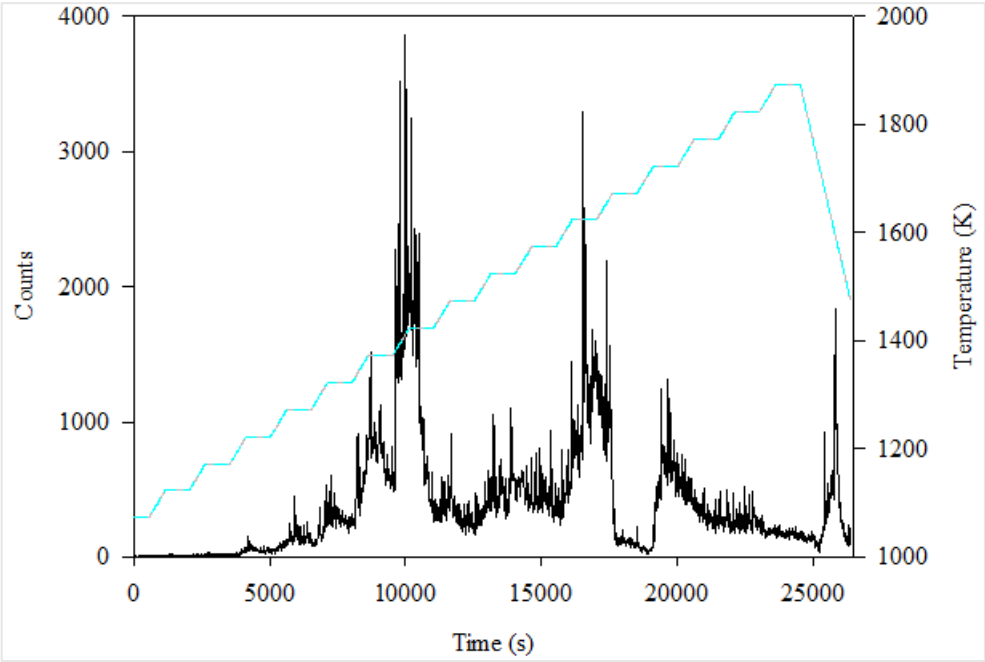

Figure 7.2: Temperature dependence of Pd detection at the ICP-MS. The black track corresponds to the ICP-MS signal for Pd and the blue track shows the furnace temperature. The tested temperature range was 1073 K – 1973 K.

CHAPTER 8:
NEUTRON ACTIVATION ANALYSIS AND ICP-MS FOR PROVENANCE OF HONEY COLLECTED FROM AMERICAN MIDWEST REGION

The results of this study were submitted to the *Journal of Radioanalytical and Nuclear Chemistry* on April 20, 2022 for review as: T.M. Weilert, C.L. Ray, J.A. Gawenis, J.D. Brockman. Neutron activation analysis and ICP-MS for provenance of honey collected from American Midwest region.

8.1. Abstract

The elemental analysis of honey is a useful tool for regional and botanical authentication of honey, particularly when combined with palynology and carbohydrate analysis. A comprehensive database that includes trace element levels in honey with known regional and botanical sources is needed to evaluate its usefulness for honey source provenance. In this study, honey samples collected from discrete sources in Montana, North Dakota, and South Dakota were analyzed by ICP-MS and INAA. Sucrose was measured by NMR to confirm that samples were not adulterated with sugar. Palynology was used to assess the pollen source. The elements B, Na, Mg, Al, P, K, Ca, Mn, Fe, Cu, Zn, Rb, Sr, Co, Mo, Cs, Ba, and Ce, among others, were measured by ICP-MS, and the elements Na, Cl, Sc, Cr, Fe, Zn, Se, Br, and Hg were measured by INAA. The duplicate elements from the two methods were compared. A cluster analysis and a

principal component analysis were conducted to determine if the regional or botanical sources could be distinguished by their trace element content. The results have demonstrated that elemental analysis may be useful in discriminating honey sourced from Montana against honey sourced from North and South Dakota.

8.2. Introduction

As of 2020, of the top 10 honey-producing states in the United States, North Dakota (ND), South Dakota (SD), and Montana (MT) ranked as numbers 1, 2, and 5, respectively, with a combined total honey production of 62.5 million pounds [1]. This was over 40% of the total US honey production in that year. ND has consistently ranked as the United States' #1 honey producer since 2004 and is a popular summer feeding stop for pollination colonies travelling around the country [2-3]. While the US remains a net importer of honey, exports, primarily to Canada, South Korea, and Japan, totaled USD$19.2 million in 2019 making the US the 23rd largest exporter of honey in the world [4].

The global market price of honey has increased on a year-over-year basis and this trend is expected to continue through at least 2028 [5]. This increase has been attributed to population growth and increased consumer desire for natural sweeteners [3, 5]. The pharmaceutical industry, too, has shown increased interest in the use of honey due to its antibacterial properties and presence of beneficial health substances such as amino acids, enzymes, and minerals [5]. Coincident with the demand for increased honey is an increase fraudulent practices [6]. These practices include dilution with sugar syrup and

falsifying the honey origin, both on a geographic and botanical basis. Because of this, honey is recognized as the third most frauded product in the global food market [7]. This has led to a negative impact on market growth and a loss of profits to high-quality honey producers as they are forced to compete with low-priced low-quality honey [5].

A number of methods have emerged as a means to identify adulterated and falsely labelled product, including assay of the amino acid and proteins, volatile aroma compounds, flavonoid and phenolic compounds, and carbohydrate ratios [6]. Melissopalynology is used to assay the pollen contained in honey; it is a means of identifying both geographic and botanical origin. While being a favored technique of authenticating honey this method is limited due to a lack of qualified practitioners and the use of ultrafiltration for pollen removal [6]. Stable isotope ratios of C, H, S, and N have been used to identify honey adulteration with counterfeit sugars and for geographical provenance [6]. Likewise, chemical fingerprinting has been identified as a promising method to verify honey origin, provided a suitable reference database exists [6]. The last two methods are only applicable to those regions that have sufficient data libraries for available for provenance studies.

This study has focused on measurements of the trace element composition of American-produced honeys as a potential tool for provenance studies. Previous studies have measured the elemental composition of honey using atomic absorption spectroscopy (AAS), neutron activation analysis (NAA), inductively-coupled plasma (ICP)-optical emission spectrometry (ICP-OES) and ICP-mass spectrometry (ICP-MS). NAA, including INAA, RNAA, and k_0-NAA, has been used in the past to measure trace

elements in honeys originating from several countries including Brazil [8], Slovenia [9], the United States [10-11], and Ghana [12]. ICP-MS and ICP-OES have been used to investigate trace element concentrations in honey in several publications. Zhou, et al. [13-14] analyzed honeys from Australia and around the world, Caroli, et al. [15] analyzed Italian honeys, Baroni, et al. [16] and Camina, et al. [9] examined Argentinean honeys, Devillers, et al. [17] examined French honeys, Döker, et al. [18] examined Turkish honeys, Fernandez-Torres, et al. [19] examined Spanish honeys, Voica, et al. [20] examined Romanian honeys, and Bogdanov et al. [21] examined Swiss honeys. Few studies, however, have examined American honeys.

As far back as the late 1800s and early 1900s, researchers were measuring many of the macroelements in American-produced honey, namely Fe, Cu, Mn, P, Ca, Mg, S, Cl, Na, and K. Some of the earliest information on this topic were provided by Schuette, et al. [22-25] in their 4-part series on the Mineral Constituents of Honey 1932-1939. Despite this early work, few researchers since have examined the elemental content of American-produced honeys. Iskander [10-11], using instrumental neutron activation analysis (INAA), examined the trace metal content of 4 commercial honey brands available for purchase in Austin, Texas (TX), USA as well as honey produced on uranium mining reclaimed land, also in TX. While many of the elements under investigation were successfully measured, the results have limited use in a provenance database given that no information on botanical origin was provided and the production location was only provided for one sample. Zhou, et al. [13], in a comparative study of 100 honeys produced in regions throughout the globe, used ICP-MS to analyze and

compare the elemental contents of the samples; included in the batch were 9 honeys produced in North America, 2 from Canada and 7 from the United States. Like the previous study, however, no further information was provided for botanical or state-origin.

This emphasis on the need for knowledge of botanical origin is due to the species-dependent nature in which plants uptake nutrients [26]. The mineral composition of honey can be further affected by variables such as the apiary location, soil composition, climate, pollution, and farming practices [26]. Any decrease in the number of unknown variables will improve the quantitative nature of the study and reduce uncertainties in eventual reference databases.

In this work, 28 honey samples produced in MT, ND, and SD were obtained from a proprietary commercial source via Sweetwater Science Labs. The authenticity of the samples was verified by NMR analysis of the sugar profiles and melissopalynology was performed to obtain information on the botanical origin. ICP-MS and INAA were performed on all samples to assess the elemental content. Statistical methods, including hierarchical cluster analysis and principal component analysis, were performed on the resulting data matrix to ascertain whether the samples could be separated based on state or botanical origin.

8.3. Materials and Methods

8.3.1. Sample Collection and Authentication

The honey samples were obtained from a proprietary commercial source by way of Sweetwater Science Labs (Glasgow, MO). A total of 28 samples originating from unique bee yards located in MT (n=9), ND (n=10), and SD (n=9) were supplied. The location of each bee yard is proprietary information; it is known that the bee yards were located a minimum of 5 miles apart. The honeys were collected in 2019, processed under normal conditions, and stored in lined steel barrels. The honey samples were collected from the storage barrels and shipped to Sweetwater Science Labs in polypropylene containers maintained at 20-27°C.

8.3.2. Chemicals and Reagents

Trace metal grade HNO_3 (Fisher Scientific) was used for all digestions and dilutions. Ultra-pure water with a resistivity of 18.2 MΩ/cm was obtained from a Milli-Q water purification system. Polypropylene tubes were purchased from Stockwell Scientific and PFA evaporation dishes were purchased from Savillex. All tubes were cleaned in 2% HNO_3 before use. PFA dishes were soaked in 10% HNO_3 for a minimum of 1 hour between uses. High purity single and multielement ICP-MS standards were purchased from High Purity Standards and Inorganic Ventures and diluted to appropriate concentrations with 2% HNO_3. NIST 1568a Rice Flour was used to assess recovery of certified elements.

8.3.3. Sugar Profiles and Melissopalynology

The sugar profile was measured in each honey sample using a 400 MHz Bruker NMR equipped with the Bruker Food Screener Honey Profiler software, v2.0.4. Melissopalynology was performed by PaleoResearch Institute (Golden, CO).

8.3.4. Elemental Analysis by ICP-MS

The honeys samples were obtained from Sweetwater Science Labs in 15 mL polypropylene tubes and stored at room temperature until use. Six samples were selected to test a microwave digestion procedure. The sample tubes were heated at 60-65 ºC for a minimum of 30 minutes to decrease viscosity and solubilize the sugars. The closed tubes were inverted 5 times to mix the contents before pipetting. Approximately 400 mg of honey was pipetted into preweighed MARS 6 Xpress microwave digestion vessels with 6 mL of concentrated HNO_3. The mixtures were predigested by submerging the bottom portion of the open vessels in a water bath held at ~80 °C for 20 minutes. Once cooled, the vessels were closed. The 6 sample vessels and 2 blanks were ramped to 200 °C in 20 minutes at a power of 200 W and were intended to be held at 200 °C for 15 minutes. Approximately 2 minutes after the samples reached temperature one of the vessels off gassed and the microwave was stopped following cooldown. Because of the potential for sample overpressure, an open vessel digestion was developed for this study.

In the open vessel digestion, aliquots of 300-500 µL were pipetted by mass into cleaned pre-weighed 15 mL falcon tubes. A lint-free wipe was secured to the top of each

tube and the samples were lyophilized. The mass was recorded at 24-hour intervals until a stable mass was achieved at 72 hours. The dried samples were stored in a freezer until digested.

Digestions were carried out in the same tubes used for freeze-drying. 350 μL of concentrated HNO_3 was pipetted into each sample tube and allowed to sit at room temperature for 20 ± 4 hours. The liquid was then transferred to a precleaned PFA evaporation dish; the tubes were rinsed with 2% HNO_3 to ensure complete transfer of the honey digestate. Drying occurred on a hot plate at 120 ºC until dry, ~1 hour. The residue was brought up in 2% HNO_3, transferred to the digestion tube and reweighed. Method blanks and the quality control material NIST 1568a Rice Flour (RF) were prepared using the same procedure. The latter was used to assess recovery of certified elements. All samples were digested in triplicate using this method.

Dilutions were made at 10x and 100x levels. Sc and Rh were used for internal standards. Six samples were used for spike recovery measurements of select elements. Spiked samples were prepared with 3-10x the element concentration of the unspiked sample solution. External standard calibration curves were used for quantification; single element Ca standards were made separately to avoid interference of Sr^{2+} in the multielement standard. Measurements were made using a PerkinElmer® NexION 300x ICP-MS operated in kinetic energy dispersion (KED) mode at helium flow rates of 2.5 and 4.5 mL/min. Further operating specifics for the ICP-MS are provided in Table 8.1 along with the measured isotopes of each analyzed element.

Table 8.1: Operating specifics of the ICP-MS.

ICP RF power, W	1600
Plasma gas, L/min	18
Carrier gas, L/min	0.97
Cones	Nickel
Nebulizer	Quartz
Spray chamber	PFA 47 mm Spray Chamber
Acquisition mode	Peak hopping
Isotopes	^{11}B, ^{23}Na, ^{24}Mg, ^{27}Al, ^{31}P, ^{39}K, ^{44}Ca, ^{55}Mn, ^{56}Fe, ^{63}Cu, ^{66}Zn, ^{85}Rb, ^{88}Sr, ^{7}Li, ^{9}Be, ^{47}Ti, ^{51}V, ^{53}Cr, ^{59}Co, ^{60}Ni, $^{69/71}$Ga, ^{75}As, ^{78}Se, ^{89}Y, ^{95}Mo, ^{101}Ru, ^{105}Pd, ^{107}Ag, ^{111}Cd, ^{118}Sn, ^{121}Sb, ^{133}Cs, ^{137}Ba, ^{139}La, ^{140}Ce, ^{141}Pr, ^{146}Nd, ^{147}Sm, ^{153}Eu, ^{157}Gd, ^{159}Tb, ^{163}Dy, ^{165}Ho, ^{166}Er, ^{169}Tm, ^{172}Yb, ^{175}Lu, ^{193}Ir, ^{195}Pt, ^{205}Tl, ^{208}Pb, ^{209}Bi, ^{232}Th, ^{238}U
Integration time, ms	500
Replicates	5

8.3.5. Elemental Analysis by Instrumental Neutron Activation Analysis

All irradiations were performed in the University of Missouri Research Reactor (MURR). Gamma peak acquisitions were made with HPGe detectors using the GENIE™ 2000 Basic Spectroscopy Software.

The mass fraction of an element was determined by standard comparator INAA using the equation:

$$C_x = \left(C_z \cdot \frac{A_{0x}}{A_{0z}} \cdot R_\theta \cdot R_\varphi \cdot R_\sigma \cdot R_{eff} - B\right) \cdot \frac{m_z}{w \cdot m_x} \quad (8.1)$$

Where C_x is the mass fraction of the unknown, m_x is the mass of the sample, C_z is the mass fraction of the primary standard, m_z is the mass of the standard, and w is the mass correction factor (wet to dry ratio). The terms A_{ox} and A_{oz} are the decay corrected counting rate for the standard (z) and the unknown (x), respectively. The term B is the

mass of analyte in the quartz vial blank. The terms R_θ, R_φ, R_σ, R_{eff} are the sample to standard ratio of the isotopic abundance (θ), neutron fluence (φ), cross section (σ), and detector efficiency, respectively [27]. The term A_0 is:

$$A_0 = \frac{N \cdot \lambda \cdot e^{\lambda \cdot t_d}}{1 - e^{-\lambda \cdot t_c}} \tag{8.2}$$

In this equation N is the number of counts in the gamma-ray photo peak, λ is the decay constant, t_d is the decay time, and t_c is the count time. INAA LOD was calculated using Eqn. 8.3:

$$LOD_{INAA} = \frac{\sqrt{bkgd} \cdot 3}{cts/\mu g_{std}} \tag{8.3}$$

8.3.5.1. Cl Measurement

Comparator standards containing 200 µg of Cl were prepared from commercial ICP-MS standards purchased from High Purity Standards. The standards were dried on filter paper circles in identical 1.5 mL high-density polyethylene (HDPE) vials. Quality control material included 3 samples of NIST 1577 Bovine Liver and 3 samples of NIST 909b Human Serum Level 1 and Level 2. The honey samples were heated in 15 mL tubes and mixed as previously described in Section 2.4. Aliquots of 50-100 µL were pipetted into cleaned and pre-weighed 1.5 mL HDPE vials. The samples were covered with lint free wipe, lyophilized for 72 hours, and reweighed to obtain the dry weight. Of the 28 honey samples, 6 were prepared in duplicate. The samples, standards, and quality control materials were irradiated in series in the Row 1 pneumatic tube irradiation position at the MURR for 5 seconds in a flux of 9×10^{13} n/cm^2/s. The samples were decayed for 15

seconds and the gamma ray spectrums were measured for 30 seconds on the face of a 20% relative efficiency HPGe detector. Dead time was corrected using loss free counting and the measured dead times for all samples was less than 10%.

An additional experiment was conducted to test for the presence of F. The samples were irradiated for 5 seconds, allowed to decay for 12 seconds and counted for 15 seconds on the detector face. The 1633 keV peak from ^{20}F decay was not observed.

8.3.5.2. Na and Br Measurement

A 'mid' irradiation was conducted to measure Na and Br. The empty 1.5 mL HDPE vials contained unacceptable levels of Br and therefore the honey samples were reprepared in cleaned quartz vials (Herarus). The precleaned quartz tubes were heated in a sand bath held at ~80 ºC. Disposable transfer pipettes were trimmed at the top and bottom to serve as funnels and these were placed in the quartz tubes. The bulk honey samples were heated to 60-65 ºC for 30 minutes, inverted five times, and then 30-50 µL aliquots were pipetted into the top of the trimmed transfer pipettes. When the honey had pooled in the bottom of the tube the transfer pipette was removed and the quartz tube was reweighed. The quartz samples were lyophilized for 72 hours and a dry weight was obtained. The vials were then sealed using a natural gas-oxygen torch. Br comparator standards were prepared from commercial ICP-MS standards and NCS DC 73347 hair was prepared as a quality control material.

Prior to irradiation, the samples were cleaned in an aqua regia bath. The samples, standards, and quality control material were bundled and irradiated in a rotating position

in the graphite reflector region of the MURR for 4 hours in a neutron flux of 5×10^{13} n/cm^2/s. The bundle was removed and decayed for 24 hours before the quartz vials were cleaned in aqua regia. The samples and standards were counted approximately 2 cm from the face of 38% relative efficiency HPGe detectors connected to automatic sample changes. The measured dead-time for all samples was less than 10%. Details of the comparator INAA experiment have been previously published [28].

8.3.5.3. Sc, Cr, Fe, Zn, Se, and Hg INAA

Following a decay time of one month the samples were analyzed for Sc, Cr, Fe, Zn, Se, and Hg using standard comparator INAA. The samples, standards, and quality control materials were bundled into an Al can and irradiated for 40 hours in a rotating position in the graphite reflector region of the MURR at a flux of approximately 5.5×10^{13} n/cm^2/s. The Al can was flooded during the irradiation to minimize sample heating. The quartz vials were cleaned in an aqua regia bath prior to analysis by standard comparator INAA. The sample bundle contained 28 samples, 6 duplicate samples, 6 comparator standards, 12 quality control materials, and 6 empty quartz vial method blanks. The quality control materials were NIST 1577 Bovine Liver, NIST 1633 Orchard Leaves, and NSC DC 77347 Hair. The irradiated samples were decayed for 10 days and then counted for 4 hours each, 1 cm from an HPGe detector. The quartz vials were rotated in front of the HPGe detector during the measurement. The dead-time was handled using a live-time correction and measured dead-times were less than 10% for all

samples. Details of the comparator INAA experiment have been previously published [28].

8.3.6. Statistical Methods

A hierarchical cluster analysis was performed using SPSS® Statistics software. The Average Linkage (Between Groups) method was used with the squared Euclidean distance as association criterion. SPSS® Statistics and Microsoft Excel were used to calculate the Pearson correlation coefficients for all element pairings. A two-tailed significance level was provided for each Pearson coefficient by SPSS®. SigmaPlot® was used to conduct a principal component analysis (PCA) on the covariance matrix of the samples and elemental data. Elemental concentrations in μg/g were scaled on a log10 basis.

8.4. Results

All of the honey samples had a measured sucrose content of <5% and were considered to be authentic and not diluted with sucrose [29]. The melissopalynology analysis showed the honey samples were collected from beehives pollenating clover (n = 15), alfalfa (n = 8), and canola (n = 5) with all 3 states represented in both clover and alfalfa and MT and ND in canola. Floral source was designated by >50% floral presence of the stated pollen type.

The measured moisture content of each sample based on the dehydration of the triplicate ICP-MS samples varied between 11.3% and 15.5%. ND samples had, on average, 1% greater moisture content than the MT samples. The average moisture content of SD samples was almost directly in between that of MT and ND. All results reported for this work have been converted back to wet-mass values, with the exception of one dendrogram.

The measured elemental concentrations in the honey samples, element recovery of NIST 1568a Rice Flour (RF) certified elements, and spike recovery values are reported in Table 8.2 for the most important elements. The remaining elemental concentrations are reported in Appendix D. Spike recoveries for all spiked elements were 96%-112%. Recovery values for the certified elements in RF were between 94%-113% for all but four measured elements. The ICP-MS limits of detection (LOD) were calculated based on the average instrument LOD over all sample runs and the average 10x total dilution value for all samples. The INAA LODs were calculated using Eqn. 8.3. Elemental concentrations determined using INAA are marked with an asterisk.

Hg was present at levels less than the LOD in all samples in the INAA experiments. The elements Na, Cl, Sc, Cr, Fe, Zn, and Br were successfully measured by INAA. Na concentrations averaged 94 ± 4% agreement with the ICP-MS results, Zn averaged 108 ± 13% agreement, Fe averaged 76 ± 24% agreement, and Cr averaged 83 ± 42% agreement. The difference in recovery could be the result of systematic bias associated with the counting geometry. The honey samples were loaded in quartz vials. Following the 40-hour irradiation the honey had visibly covered most of the interior

surface area of the quartz vials. We did not attempt to make a geometry correction. The difference could also be due to the smaller sample aliquots used in the INAA samples vs the ICP-MS samples. If the elements were present as foreign material they may have been heterogeneously mixed in the honey. Cr concentrations in some samples were near the LOD. The Sc, Cl, and Br levels were only measured by INAA. The Cl measured in NIST SRM 909c Sera Level 2 (n=3) was 4369 ± 117 μg/mL and the certified value was 4234 ± 30 μg/mL. The Br level measured in reference material NCS DC 73347 Hair (n=3) was 0.34 ± 0.01 μg/g and the accepted value is 0.36 μg/g.

A cluster analysis was performed on both the dry- and wet-mass values of the results shown in Table 8.2 and the associated dendrograms are provided in Figs. 8.1-8.2. PCA was also performed on both the dry- and wet-mass values however only the wet-mass results are shown. The first 3 PCs encompassed 71% of the total variability in the data and the first 6 PCs encompassed 91% of the total variability. The component scores and component loadings of PC1 vs PC2, PC1 vs PC3, and PC2 vs PC3 are shown in Figs. 8.3-8.8. Select Pearson correlation coefficients are provided in Table 8.3 only for pairings with coefficients >0.75 and < -0.75; all coefficients shown had p-values <<0.01 based on a two-tailed significance with the highest being 4×10^{-6} for Cs:K. The full correlation matrix for the pairings of elements shown in Table 8.2 is provided in Appendix D.

Table 8. 2: NIST 1568a Rice Flour recoveries, spike recoveries, and concentrations of select trace elements in honeys from MT, ND, and SD. Elements marked with an asterisk were measured using INAA, all other values were measured using ICP-MS.

µg/g	RF Rec	Spike Rec	Montana (N = 9)		North Dakota (N = 10)		South Dakota (N = 9)		LOD ICP-MS	LOD INAA
			Mean ± S.D.	Range	Mean ± S.D.	Range	Mean ± S.D.	Range		
B	-	96%	5.98 ± 1.29	4.59 – 8.18	9.88 ± 1.84	7.06 – 11.87	10.86 ± 1.81	8.71 – 13.64	0.25	-
Na	289%	100%	11.92 ± 5.04	6.63 – 20.21	14.15 ± 6.16	8.86 – 30.82	10.90 ± 1.25	9.25 – 13.64	0.050	0.060
Mg	-	100%	9.73 ± 1.34	7.89 – 11.56	14.51 ± 2.89	10.53 – 19.24	12.90 ± 2.91	9.56 – 16.49	0.039	-
Al	-	103%	0.12 ± 0.04	0.06 – 0.17	0.15 ± 0.08	0.08 – 0.30	0.11 ± 0.03	0.07 – 0.18	0.051	-
P	-	100%	35.45 ± 4.72	28.90 – 41.31	40.64 ± 6.68	30.60 – 52.12	40.39 ± 9.56	27.54 – 55.95	1.74	-
Cl*	-	-	99.47 ± 36.20	49.64 – 157.6	70.83 ± 15.55	41.59 – 93.16	73.65 ± 29.14	45.26 – 137.0	-	13.0
K	102%	98%	229.7 ± 69.1	130.6 – 355.2	196.7 ± 51.8	145.2 – 325.2	179.5 ± 37.3	135.1 – 243.6	0.53	-
Ca	97%	102%	43.04 ± 9.06	32.72 – 59.09	56.03 ± 9.71	44.55 – 71.32	64.91 ± 12.53	39.98 – 77.29	1.37	-
Mn	102%	102%	0.20 ± 0.07	0.14 – 0.37	0.37 ± 0.07	0.26 – 0.50	0.44 ± 0.07	0.34 – 0.55	0.0031	-
Fe	51%	99%	0.57 ± 0.28	0.38 – 1.28	1.13 ± 0.62	0.37 – 2.10	0.54 ± 0.20	0.34 – 0.97	0.038	0.300
Cu	94%	98%	0.09 ± 0.02	0.07 – 0.12	0.09 ± 0.02	0.07 – 0.12	0.11 ± 0.03	0.07 – 0.17	0.00086	-
Zn	100%	101%	0.27 ± 0.05	0.23 – 0.36	0.38 ± 0.19	0.22 – 0.74	0.28 ± 0.06	0.19 – 0.36	0.032	0.040
Br*	-	-	0.15 ± 0.06	0.08 – 0.28	0.17 ± 0.06	0.08 – 0.30	0.27 ± 0.25	0.12 – 0.86	-	0.020
Rb	113%	107%	0.29 ± 0.13	0.12 – 0.52	0.23 ± 0.06	0.16 – 0.35	0.22 ± 0.08	0.14 – 0.37	0.00057	-
Sr	-	99%	0.11 ± 0.04	0.05 – 0.17	0.15 ± 0.08	0.06 – 0.27	0.20 ± 0.08	0.06 – 0.27	0.0047	-
ng/g	RF Rec	Spike Rec	Mean ± S.D.	Range	Mean ± S.D.	Range	Mean ± S.D.	Range	LOD ICP-MS	LOD INAA
Co	67%	98%	2.37 ± 0.78	1.41 – 3.58	5.03 ± 1.52	2.90 – 7.72	6.20 ± 2.49	4.20 – 12.40	0.25	-
Mo	105%	112%	5.26 ± 2.09	2.02 – 7.29	4.59 ± 2.09	2.10 – 7.47	4.95 ± 2.00	1.92 – 8.03	1.00	-
Cs	-	110%	1.19 ± 1.08	0.22 – 3.71	0.45 ± 0.41	0.11 – 1.45	0.21 ± 0.09	0.11 – 0.35	0.10	-
Ba	-	106%	60.48 ± 13.74	32.60 – 72.55	70.18 ± 36.08	17.46 – 117.1	80.35 ± 33.24	17.95 – 109.8	1.21	-
Ce	-	110%	0.31 ± 0.11	0.16 – 0.49	0.42 ± 0.19	0.21 – 0.83	0.32 ± 0.07	0.14 – 0.37	0.088	-

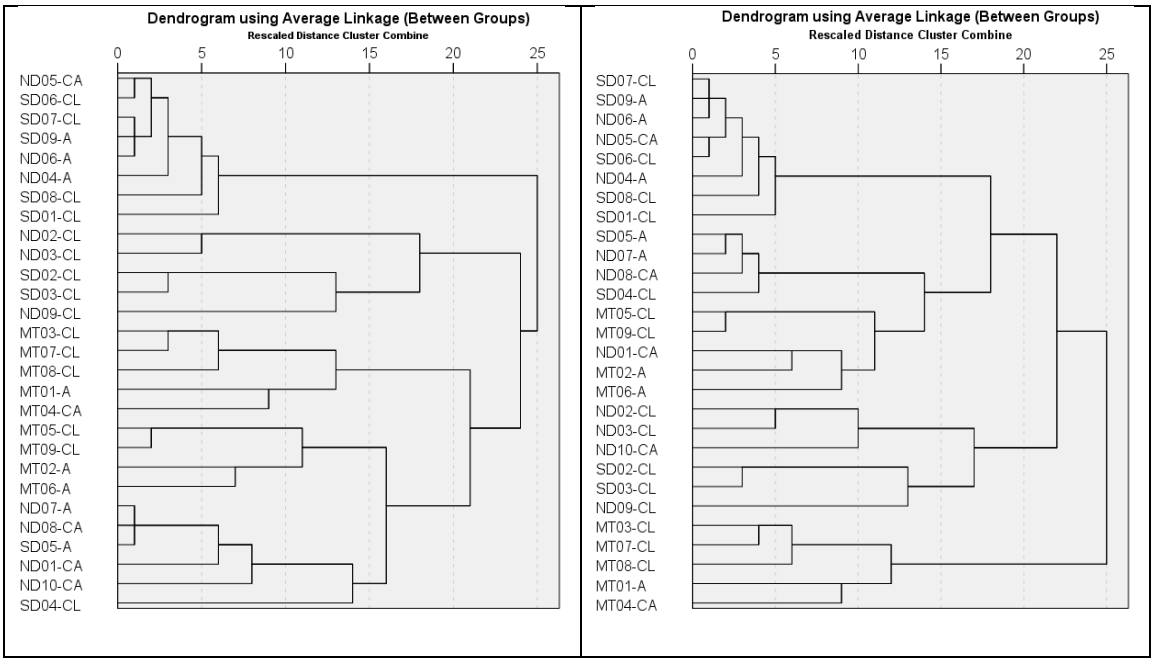

Figures 8.1, 8.2: Dendrograms produced using dry- and wet-mass values of Table 8.2, respectively. (Clover = CL, Alfalfa = A, and Canola = CA).

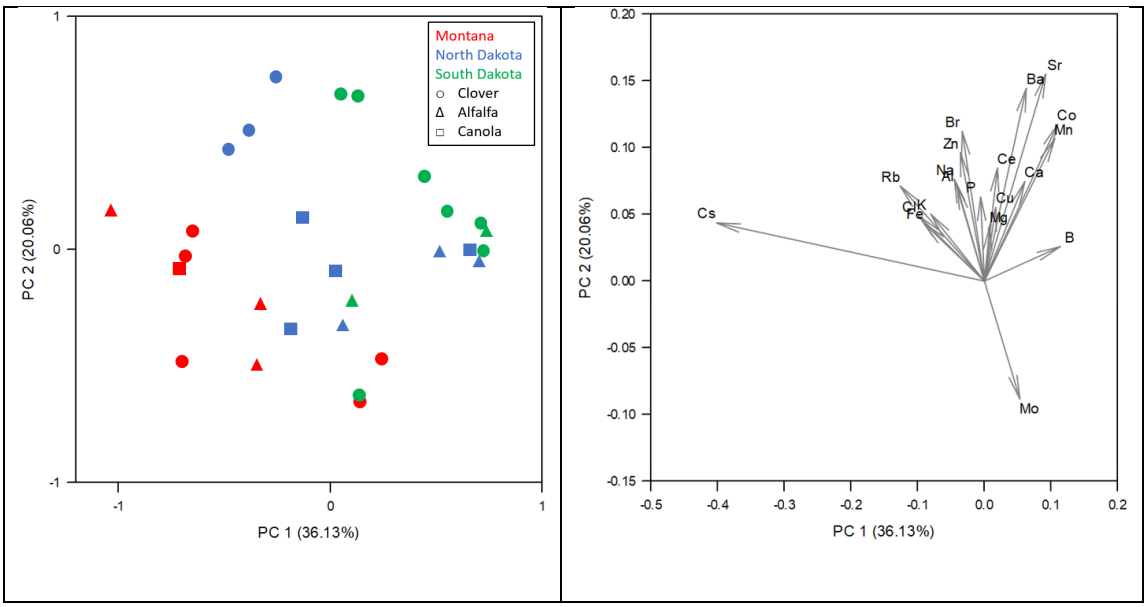

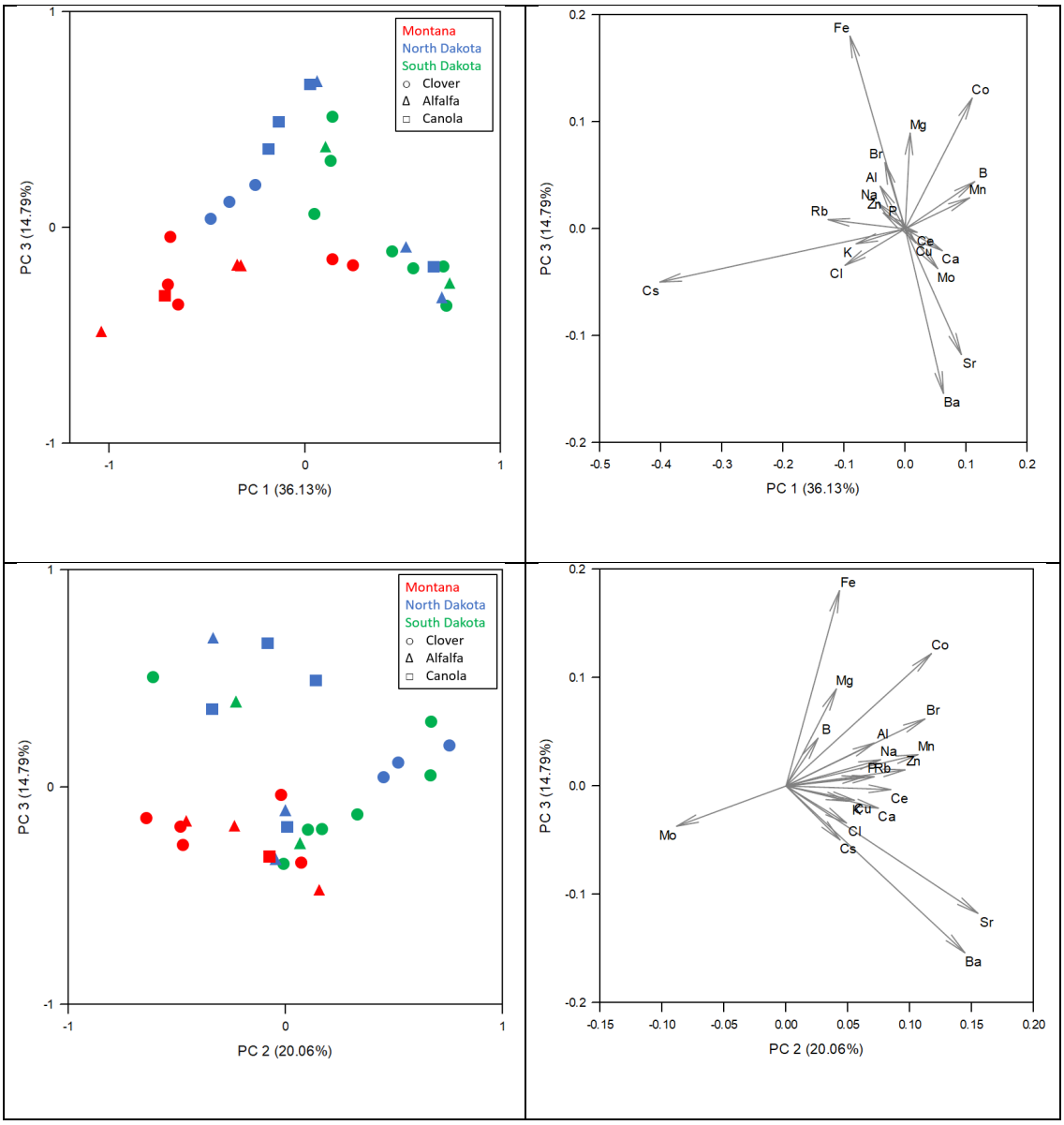

Figures 8.3, 8.4, 8.5, 8.6, 8.7, 8.8: Component score and component loading plots of PC1 vs PC2, PC1 vs PC3, and PC2 vs PC3.

Table 8.3: Select Pearson correlation coefficients.

	B	Cl	K	Ca	Mn	Rb	Sr	Cs	Ba
B	1								
Cl		1							
K			1						
Ca				1					
Mn				0.783	1				
Rb		0.770	0.804			1			
Sr				0.860			1		
Cs	-0.755		0.754			0.798		1	
Ba							0.774		1

8.5. Discussion

The moisture content measured in the honey samples in this work ranged from 11.3% to 15.5%. White [30] published values of the average moisture content for honey samples taken from 47 out of 50 American states. ND was not represented in the sample set, however MT and SD had moisture content values of 16.1% and 16.6%, respectively.

There is no certified reference material for honey. In this study, the high-carbohydrate CRM NIST 1568a Rice Flour was used as a suitable analog for the ICP-MS experiments [26]. The digested honey samples were clear while the CRM RF had visible particles in solution. This was possibly due to the high starch content of RF compared to honey matrix. The RF recoveries, shown in Table 8.2, were between 94%-113% for all certified elements with the exceptions of Se, Fe, Co, and Na. Fe and Co recoveries were 51% and 67%, respectively. Na recovery was 300%. The concentration of Na in the honey samples measured by INAA and ICP-MS agreed, with a recovery of 94 ± 4% over all samples. This suggests that contamination occurred before or during preparation and analysis.

The samples in this study were of either clover, alfalfa, or canola origin. All three of these honey varieties are considered “light” and as such would be expected to have lower overall elemental concentrations than darker honeys. In 1932-1939, Schuette et al. [22-25] examined up to 35 honey samples from states across the US and separated results by color. Light honeys were considered either water white or white and consisted primarily of clover and alfalfa honeys. The elements examined were Na, Mg, P, Cl, K, Ca, Mn, Fe, and Cu, as well as S which was not measured in this work. Most of the element concentrations measured in light honeys were in good agreement with those of this work with the exceptions of Fe and Cu. Schuette measured average values of 4.8 μg/g and 0.25 μg/g for Fe and Cu, respectively, in light honeys, both of which are more than twice the highest values measured in this work. This may be the result of decreased contamination from stainless steels and other containers in the modern samples compared to those honey samples which were collected nearly a century ago. Both Fe and Cu can be both naturally occurring and of anthropogenic origin in honey [31].

Zhou, et al. [13] examined 9 North American honey samples, 7 originating from the US and 2 from Canada. All of the elements shown in Table 8.2 were measured with the exceptions of Cl, Br, Cs and Ce. Among the measured concentrations of the common elements between Zhou et al. and this work, all average concentrations were of the same magnitude except for two. K and Ca average concentrations were 10x higher and 10x lower, respectively, in Zhou’s work. Floral and state-of-origin information were not provided for the samples. In the work by Schuette, et al., dark honeys had much higher K concentrations compared to lighter colored samples (>2000 μg/g vs 205 μg/g). In

contrast, Schuette et al. observed lower average Ca concentrations in dark honeys compared to all other colors, although the Ca concentrations in the dark honeys covered a wide range of 5-266 μg/g. It is possible that Zhou, et al. may have had darker honey samples than those measured in this work, highlighting the need for information on both floral and geographic origins in studies of this nature. Comparisons of Na, Mg, P, and Mn would also support this conclusion. Despite this, the decision tree provided in Zhou, et al. would have correctly identified the samples in this study as originating from North America based on concentrations of Sr, P, and K.

Only 3 other modern studies have examined honeys originating from the United States, 1 for honeys produced in New York state [32] and 2 for honeys purchased or produced in TX [10-11]. In the former, Tong, et al. [32] measured 47 elements in 19 honey samples collected throughout New York state, most from industrialized or polluted areas. The concentrations of many of those measured elements were over 1000x higher those measured in this paper. It is unclear if the high concentrations were representative of the unadulterated honey samples or reflected contamination during collection, processing, or analysis. Iskander [10-11] used INAA to measure 24 trace elements in 4 honey brands commercially available in Austin, TX, as well as honey produced on land which had previously been used for U mining. Nearly all of the results were elevated in comparison to those reported here with the exceptions of K, Na, and Rb. No information was published on the region of production or the floral origin of the honey samples.

Dendrograms created using the dry- and wet-mass values reported in Table 8.2 are shown in Figs. 8.1-8.2. The two dendrograms were not identical. Using the wet-mass

values there was no visual clustering by state-of-origin or floral type. The samples were mixed with only small clusters of clover samples. The MT samples were separated into 3 groups. Conversely, when the dry-mass values were used there were two noticeable trends. First, the MT samples were located together towards the bottom half of the plot. Second, nearly all of the clover samples (10/15) were located together. This suggests that variation in moisture content should be controlled. In the literature, elemental levels in honey are reported as wet mass values.

The PCA component score plots did not show a significant difference in clustering when using dry- or wet-mass values. For this reason, only the PCA plots derived from wet-mass values are provided. PC1 vs PC3 showed good separation based on state-of-origin with MT samples in the bottom half of the plot, 7/10 ND samples in the upper left quadrant, and finally SD samples in the upper right quadrant. In both PC1 vs PC2 and PC1 vs PC3 there was a distinct cluster of ND and SD samples from all 3 pollen types corresponding to the uppermost grouping in the dendrograms. It is possible these samples were produced in neighboring regions given that ND and SD share a border. Specific regional information is proprietary and this hypothesis cannot be verified. Overall, discrete separation was poor in PC1 vs PC2 and PC2 vs PC3. The sample set was relatively small and the samples were produced in neighboring states from similar pollen types.

Pearson correlation coefficients were calculated for element pairs of the elements shown in Table 8.2 over all 28 samples in order to discover potential trends in element groupings. Correlation coefficients >0.75 and < -0.75 indicate very strong correlations in

a positive and negative direction, respectively. Table 8.3 shows coefficients derived from this work corresponding only to values >0.75 and < -0.75, the remainder are provided in Appendix D. Table 8.4 shows comparisons of select coefficients between this work and works studying samples produced in Greece [33], Cyprus [33], Egypt [33], Serbia [34], Romania [20], and Jordan [35] (one sample was not included in calculations for Cyprus as it was an outlier). As can be seen, no element grouping shows strong correlation in all of the studied regions. This indicates that correlations and pairs of correlations may be indicative of specific geographic regions. It should be noted that some of the correlations in this study were state dependent. For example, the coefficient for Al:Zn for MT was -0.860 while ND and SD had coefficients of 0.959 and 0.718, respectively. Some element pairings had strong correlations regardless of state-of-origin and these were K:P, K:Rb, Cs:Rb, and Ca:Sr. All of the samples produced in Egypt were clover honeys. When Pearson coefficients for this work were calculated using just clover samples there were still differences between this work and those from Egypt, notably Mg:Ca had no significant correlation (0.291) and there was only moderate correlation for Mg:Mn (0.632). Ca:Mn and Al:Zn did however have similar strong correlations of 0.753 and 0.732, respectively. Additional work would be needed to attribute these differences in agricultural practices or geology.

Table 8.4: Comparison of Pearson correlation coefficients of various element pairings for honeys from multiple countries.

Elements	This Work	Greece [33]	Cyprus [33]	Egypt [33]	Serbia [34]	Romania [20]	Jordan (unifloral) [35]
Ca:Mn	**0.783**	0.078	**0.946**	**0.827**	-0.137	0.352	-
Ca:Sr	**0.860**	-	-	-	-	**0.785**	**-**
Sr:Ba	**0.774**	-	-	-	-	0.37	**0.840**
Fe:Zn	0.435	0.318	**0.868**	0.169	0.184	-	-
Al:Zn	0.650	-0.150	0.297	**0.807**	-	0.285	-
Al:P	0.345	**0.925**	0.071	-0.084	-	-	-
Mg:Ca	0.158	-0.226	0.634	**0.862**	0.043	**0.930**	**0.890**
Mg:Mn	0.512	0.696	0.496	**0.810**	-0.006	0.558	-

8.6. Conclusions

This work has provided information on elemental concentrations of North American honey, specifically honey produced in Montana, North Dakota, and South Dakota. Trace element concentrations were measured using both ICP-MS and INAA. These concentrations were compared to those provided in other studies on North American honey. While not the primary objective of this study, cluster analyses were undertaken in order to determine if the samples could be separated on either a state-of-origin or botanical basis. Concentrations based on dry samples were shown to have better hierarchical clustering of both state and botanical origin vs clusters obtained using wet-mass concentrations. Principal component analysis showed only moderate success in separating samples by state with PC1 vs PC3 showing the greatest separation. Pearson correlation coefficients were calculated based on element pairings over all samples, samples separated by state, and samples separated by botanical origin. Some pairings with high correlations were shown to be state-dependent while others were consistently high across all states. These coefficients were compared to those provided by or

calculated from other works and it was shown that no element pairing had high correlations across all regions, indicating that Pearson correlations may show promise as an indicator of honey provenance.

8.7. Acknowledgements

The authors would like to extend their sincere thanks to Jim Guthrie, Ruth Ann Ngwenyama, Stacy Crane, and Mike Glascock for their assistance in performing this work.

8.8. References

[1] *Honey - National Agricultural Statistics Service - USDA*; United States Department of Agriculture: 2021; pp 1-6.

[2] North Dakota leads nation in honey production for 15th year 2019. https://apnews.com/article/5749289cc5ee41cf83c5e8a59825e3ac (accessed Feburary 4, 2022).

[3] Matthews, W. A.; Summer, D. A.; Hanon, T. *Contributions of the U.S. Honey Industry to the U.S. Economy*; National Honey Board: 2019; pp 1-53.

[4] Honey in United States 2019. https://oec.world/en/profile/bilateral-product/honey/reporter/usa?redirect=true (accessed Feburary 4, 2022).

[5] Honey Market Size, Share & COVID-19 Impact Analysis, By Type (Alfalfa, Buckwheat, Wildflower, Clover, Acacia, and Others), Application (Food & Beverages, Personal Care & Cosmetics, Pharmaceuticals, and Others), Packaging (Glass Jar, Bottle, Tub, Tube, and Others), and Regional Forecast, 2021-2028 *Food Processing and Processed Food* [Online]. https://www.fortunebusinessinsights.com/industry-reports/honey-market-100551 (accessed Feburary 4, 2022).

[6] McComb, K.; Frew, R., Using new analytical approaches to verify the origin of honey. In *New Analytical Approaches For Verifying the Origin of Food*, Woodhead Publishing Series in Food Science, Technology and Nutrition: 2013; pp 216-242.

[7] United States Pharmacopeia: 2018.

[8] Vasconcellos, M. B. A.; Maihara, V. A.; Munita, C. J. A. S.; Fávaro, D. I. T.; Armelin, M. J. A. *Application of Neutron Activation Analysis to the Monitoring of Trace Elements in Brazilian Foodstuffs*; International Atomic Energy Agency (IAEA): Vienna, Austria, 1994; p 27.

[9] Camiña, J. M.; Cantarelli, M. A.; Lozano, V. A.; Boeris, M. S.; Irimia, M. E.; Gil, R. A.; Marchevsky, E. J., Chemometric tools for the characterisation of honey produced in La Pampa, Argentina, from their elemental content, using inductively coupled plasma optical emission spectrometry (ICP-OES). *J. Apic. Res.* **2015,** *47* (2), 102-107.

[10] Iskander, F. Y., Assessment of trace elements in honey produced on uranium mining reclaimed land. *Sci. Total Environ.* **1996,** *192* (1), 119-122.

[11] Iskander, F., Trace and minor elements in four commercial honey brands. *J. Radioanal. Nucl. Chem.* **1995,** *201* (5), 401-408.

[12] Boateng, R. Monitoring of Elemental Composition of Honey from Selected Regions of Ghana Using Instrumental Neutron Activation Analysis and Atomic Absorption Spectroscopy. University of Ghana, Accra, Ghana, 2015.

[13] Zhou, X.; Taylor, M. P.; Salouros, H.; Prasad, S., Authenticity and geographic origin of global honeys determined using carbon isotope ratios and trace elements. *Sci. Rep.* **2018,** *8*, 1-11.

[14] Zhou, X.; Taylor, M. P.; Davies, P. J.; Prasad, S., Identifying Sources of Environmental Contamination in European Honey Bees (Apis mellifera) Using Trace Elements and Lead Isotopic Compositions. *Environ. Sci. Technol.* **2018,** *52* (3), 991-1001.

[15] Caroli, S.; Forte, G.; Iamiceli, A. L.; Galoppi, B., Determination of essential and potentially toxic trace elements in honey by inductively coupled plasma-based techniques. *Talanta* **1999,** *50* (2), 327-336.

[16] Baroni, M. V.; Podio, N. S.; Badini, R. G.; Inga, M.; Ostera, H. A.; Cagnoni, M.; Gautier, E. A.; García, P. P.; Hoogewerff, J.; Wunderlin, D. A., Linking soil, water, and honey composition to assess the geographical origin of Argentinean honey by multielemental and isotopic analyses. *J. Agric. Food Chem.* **2015,** *63* (18), 4638-4645.

[17] Devillers, J.; Doré, J. C.; Marenco, M.; Poirier-Duchéne, F.; Galand, N.; Viel, C., Chemometrical Analysis of 18 Metallic and Nonmetallic Elements Found in Honeys Sold in France. *J. Agric. Food Chem.* **2002,** *50* (21), 5998-6007.

[18] Döker, S.; Aydemir, O.; Uslu, M., Evaluation of Digestion Procedures for Trace Element Analysis of Cankiri, Turkey Honey by Inductively Coupled Plasma Mass Spectrometry. *Anal. Lett.* **2014,** *47* (12), 2080-2094.

[19] Fernández-Torres, R.; Pérez-Bernal, J. L.; Bello-López, M. A.; Callejón-Mochón, M.; Jiménez-Sánchez, J. C.; Guiraúm-Pérez, A., Mineral content and botanical origin of Spanish honeys. *Talanta* **2005,** *65* (3), 686-691.

[20] Voica, C.; Iordache, A. M.; Ionete, R. E., Multielemental characterization of honey using inductively-coupled plasma mass spectrometry fused with chemometrics. *J. Mass Spectrom.* **2020,** *55* (7), 13.

[21] Bogdanov, S.; Haldimann, M.; Luginbühl, W.; Gallmann, P., Minerals in honey: environmental, geographical and botanical aspects. *J. Apic. Res.* **2007,** *46* (4), 269-275.

[22] Schuette, H. A.; Remy, K., Degree of pigmentation and its probable relationship to the mineral constituents of honey. *J. Am. Chem. Soc.* **1932,** *54* (7), 2909-2913.

[23] Schuette, H. A.; Huenink, D. J., Mineral constituents of honey II. Phosphorous, calcium, magnesium. *J. Food Sci.* **1937,** *2* (6), 529-538.

[24] Schuette, H. A.; Triller, R. E., Mineral constituents of honey III. Sulphur and chlorine. *J. Food Sci.* **1938,** *3* (5), 543-547.

[25] Schuette, H. A.; Woessner, W. W., Mineral constituents of honey. IV. Sodium and potassium. *J. Food Sci.* **1939,** *4* (4), 349-353.

[26] Pohl, P.; Stecka, H.; Sergiel, I., Different Aspects of the Elemental Analysis of Honey by Flame Atomic Absorption and Emission Spectrometry: A Review. *Food Anal. Methods* **2012,** *5* (4), 737-751.

[27] Zeisler, R.; Lindstrom, R. M.; Greenberg, R. R., Instrumental neutron activation analysis: A valuable Link in chemical metrology. *Journal of Radioanalytical and Nuclear Chemistry* **2005,** *263* (2), 315-319.

[28] Carioni, V. M. O.; Brockman, J. D.; Morris, M. C.; Ngwenyama, R. A.; Schell, L. A.; Spate, V. L.; Crane, S., Instrumental neutron activation analysis, a technique for measurement of Se, Hg, Fe, Zn, K, Mn, Br, and the Hg:Se ratio in brain tissue samples with results from the Memory and Aging Project (MAP). *J. Radioanal. Nucl. Chem.* **2018,** *318*, 43-48.

[29] *Revised Codex Standard for Honey Codex Stan 12-1981, Rev. 1 (1987), Rev. 2 (2001)*; Codex Alimentarius Commission: 1981; pp 1-8.

[30] White, J. W., *Composition of American Honeys*. U.S. Department of Agriculture: 1962; p 124.

[31] Stankovska, E.; Stafilov, T.; Šajn, R., Monitoring of trace elements in honey from the Republic of Macedonia by atomic absorption spectrometry. *Environ. Monit. Assess.* **2008,** *142* (1-3), 117-126.

[32] Tong, S. S. C.; Morse, R. A.; Bache, C. A.; Lisk, D. L., Elemental Analysis of Honey as an Indicator of Pollution. *Arch. Environ. Health* **1975,** *30* (7), 329-332.

[33] Karabagias, I. K.; Louppis, A. P.; Kontakos, S.; Drouza, C.; Papastephanou, C., Characterization and Botanical Differentiation of Monofloral and Multifloral Honeys Produced in Cyprus, Greece, and Egypt Using Physicochemical Parameter Analysis and Mineral Content in Conjunction with Supervised Statistical Techniques. *J. Anal. Methods Chem.* **2018,** *2018*, 10.

[34] Spirić, D.; Ćirić, J.; Đorđević, V.; Nikolić, D.; Janković, S.; Nikolić, A.; Petrović, Z.; Katanić, N.; Teodorović, V., Toxic and essential element concentrations in different honey types. *Int. J. Environ. Anal. Chem.* **2019,** *99* (5), 474-485.

[35] Tahboub, Y. R.; Al-Ghzawi, A. A.-M. A.; Al-Zayadneh, S. S.; AlGhotani, M. S., Levels of trace elements and rare earth elements in honey from Jordan. *Environ. Sci. Pollut. Res.* **2022,** *29*, 11469-11480.

APPENDIX A:

SUPPLEMENTARY INFORMATION FOR CHAPTER 4

A.1. Ag-only

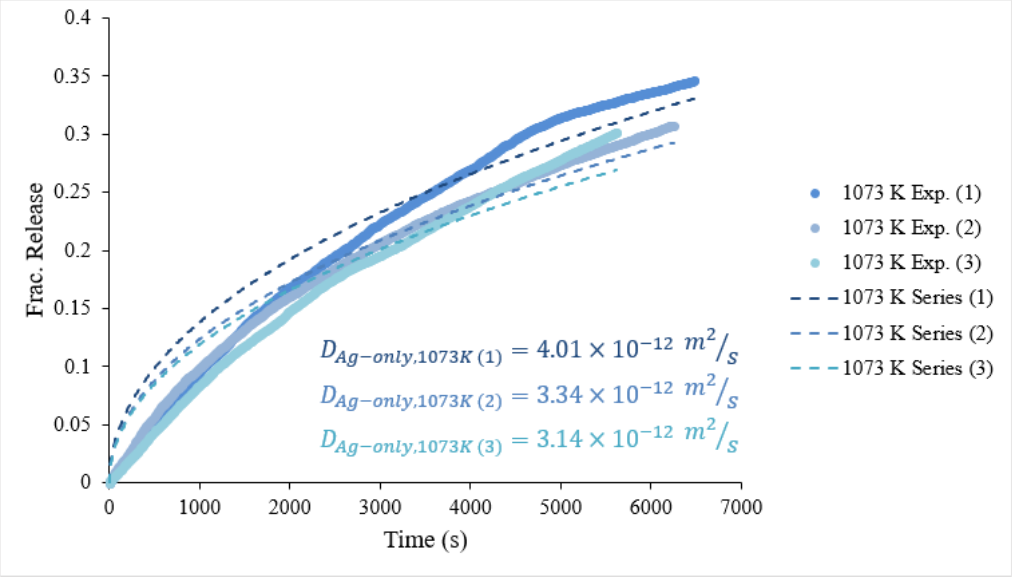

Figure A.1: Fractional release of Ag from spheres of IG-110 graphite loaded with Ag-only at 1073 K.

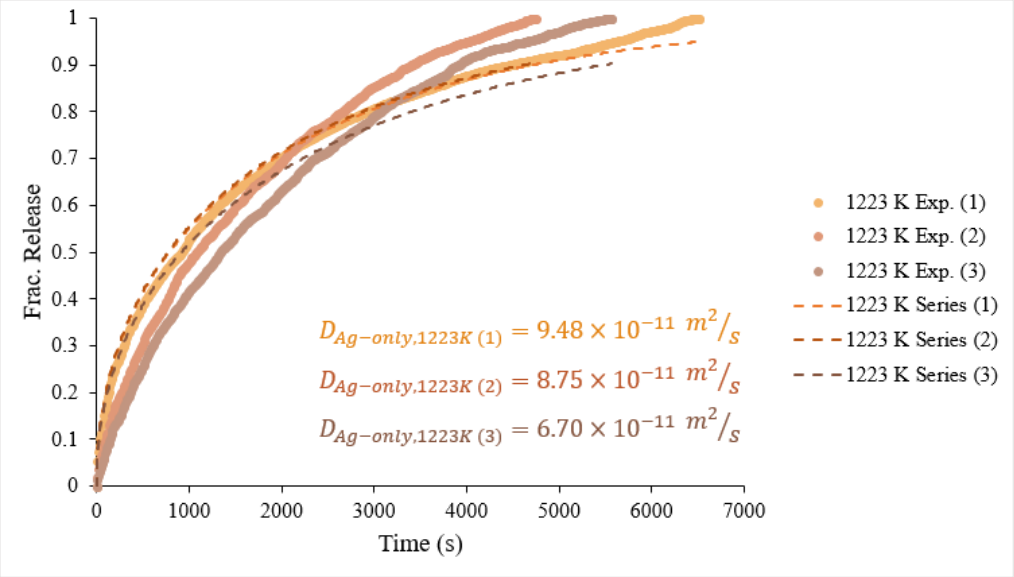

Figure A.2: Fractional release of Ag from spheres of IG-110 graphite loaded with Ag-only at Ag-only 1223 K.

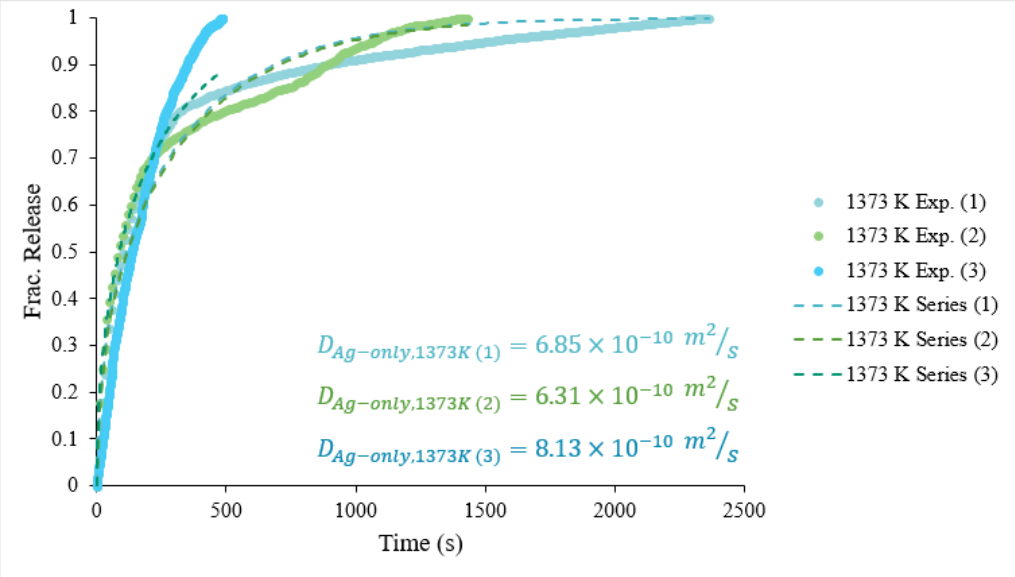

Figure A.3: Fractional release of Ag from spheres of IG-110 graphite loaded with Ag-only at Ag-only 1373 K.

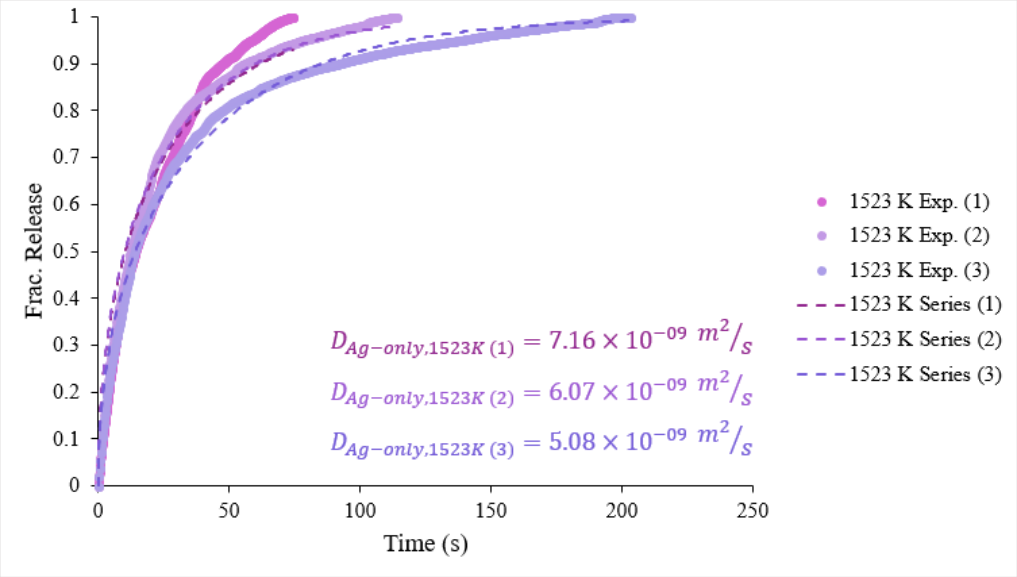

Figure A.4: Fractional release of Ag from spheres of IG-110 graphite loaded with Ag-only at Ag-only 1523 K.

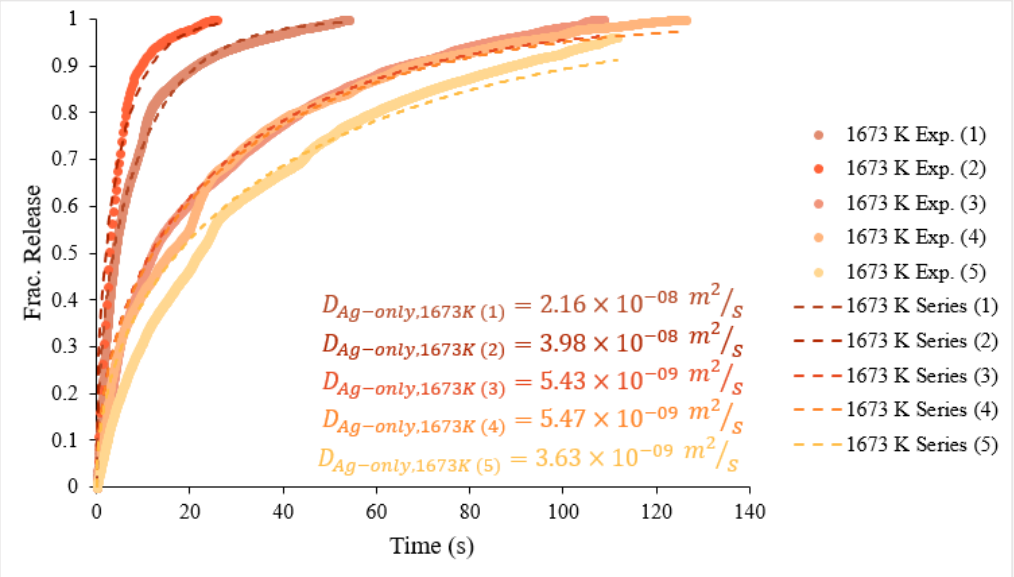

Figure A.5: Fractional release of Ag from spheres of IG-110 graphite loaded with Ag-only at Ag-only 1673 K.

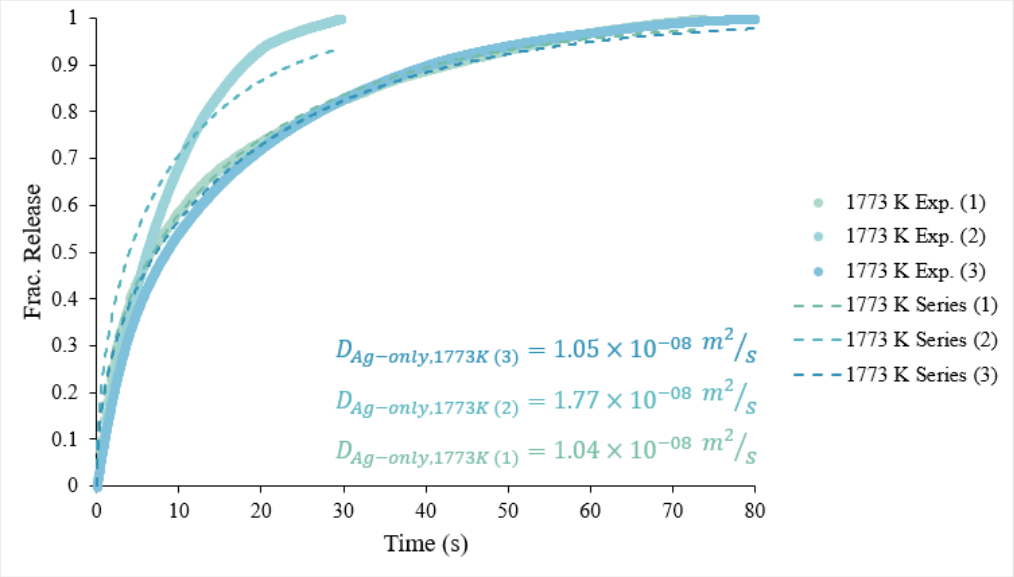

Figure A.6: Fractional release of Ag from spheres of IG-110 graphite loaded with Ag-only at 1773 K/

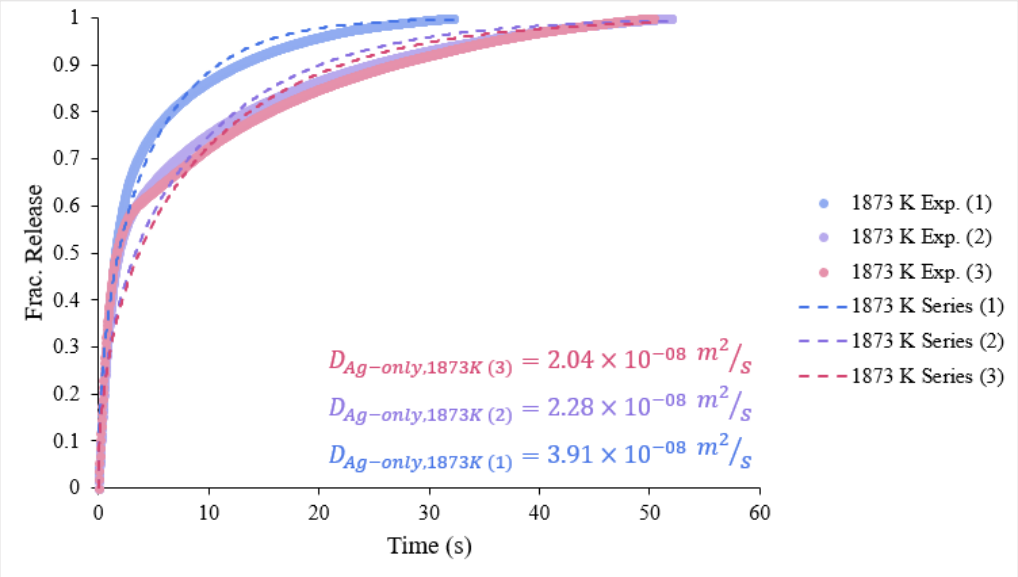

Figure A.7: Fractional release of Ag from spheres of IG-110 graphite loaded with Ag-only 1873 K.

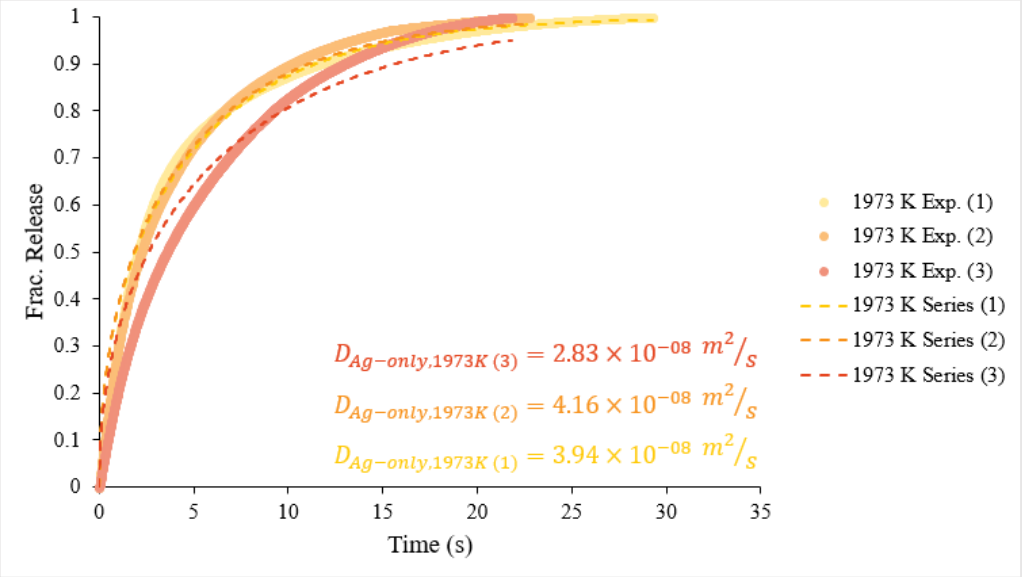

Figure A.8: Fractional release of Ag from spheres of IG-110 graphite loaded with Ag-only 1923 K.

A.2. Ag (+Pd)

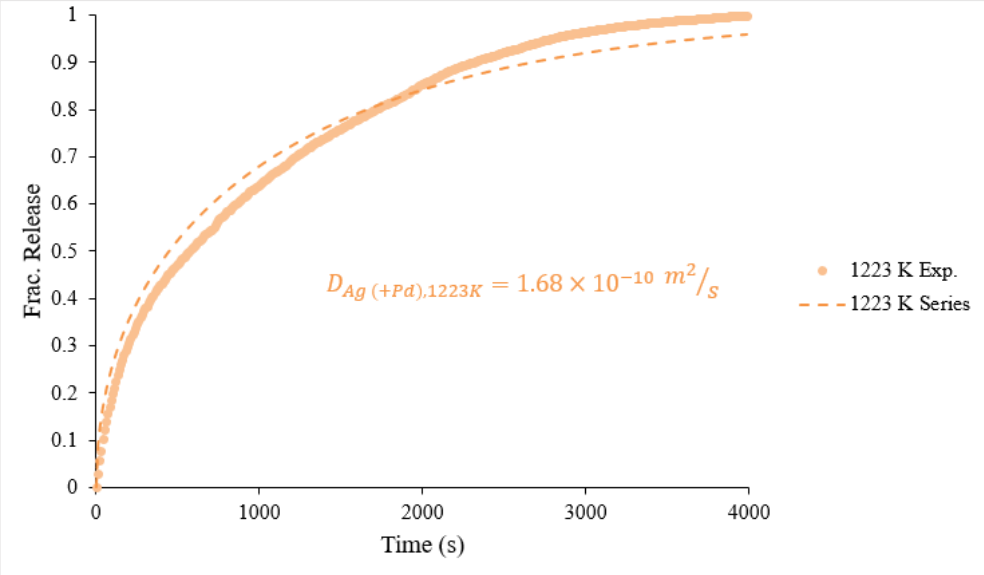

Figure A.9: Fractional release of Ag from spheres of IG-110 graphite loaded with Ag (+Pd) at 1223 K.

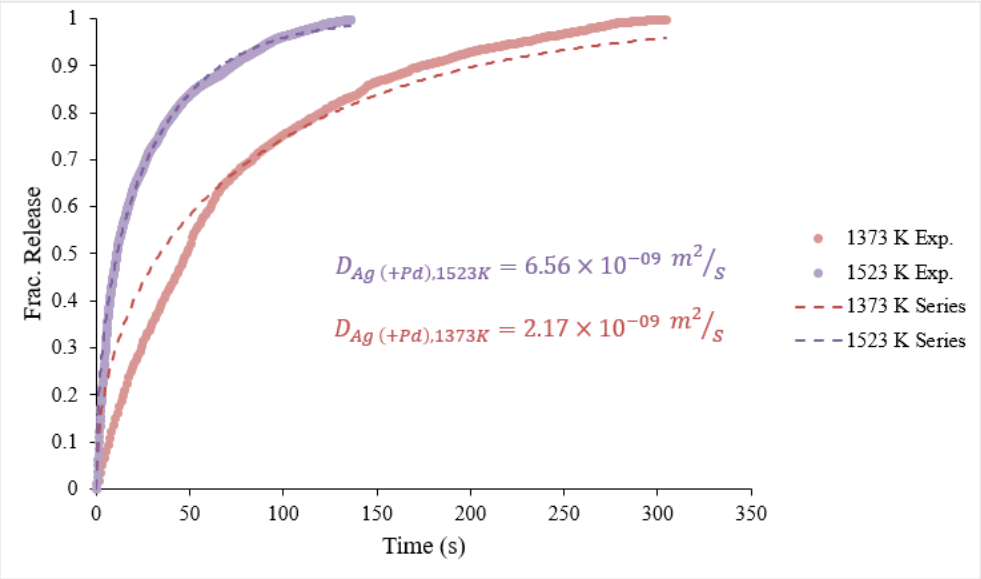

Figure A.10: Fractional release of Ag from spheres of IG-110 graphite loaded with Ag (+Pd) at 1523K and 1373 K.

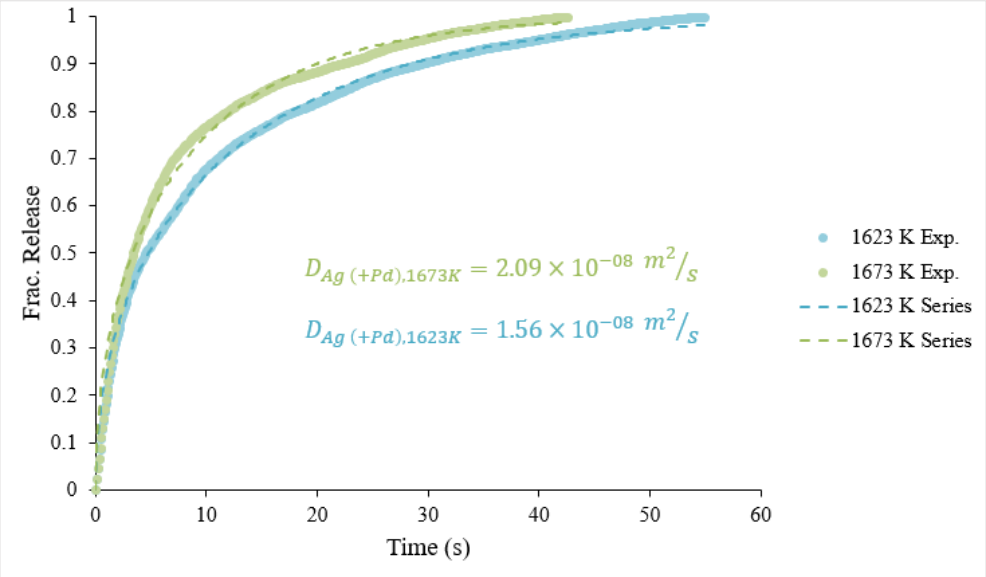

Figure A.11: Fractional release of Ag from spheres of IG-110 graphite loaded with Ag (+Pd) at 1623K and 1673 K.

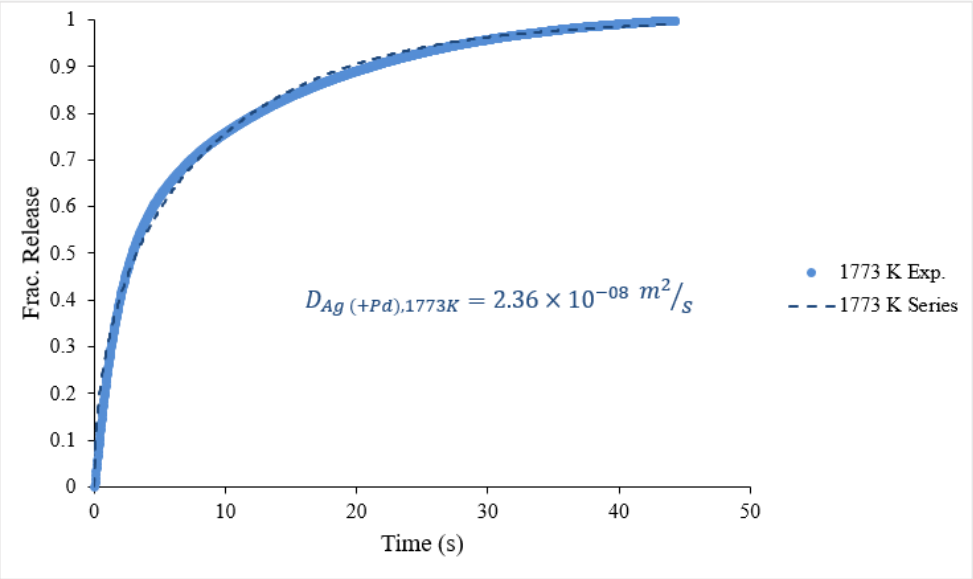

Figure A.12: Fractional release of Ag from spheres of IG-110 graphite loaded with Ag (+Pd) at 1773 K.

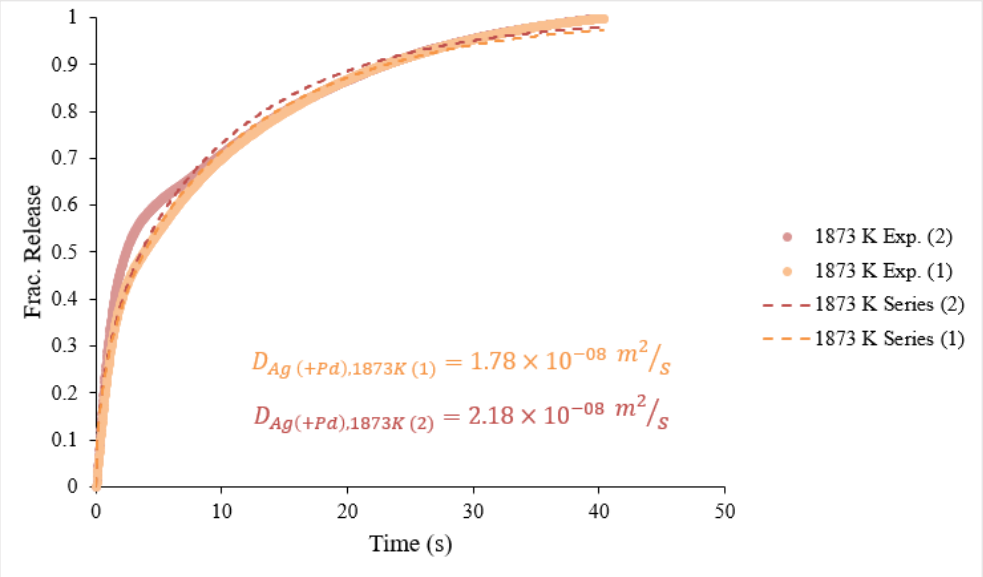

Figure A.13: Fractional release of Ag from spheres of IG-110 graphite loaded with Ag (+Pd) at 1873 K.

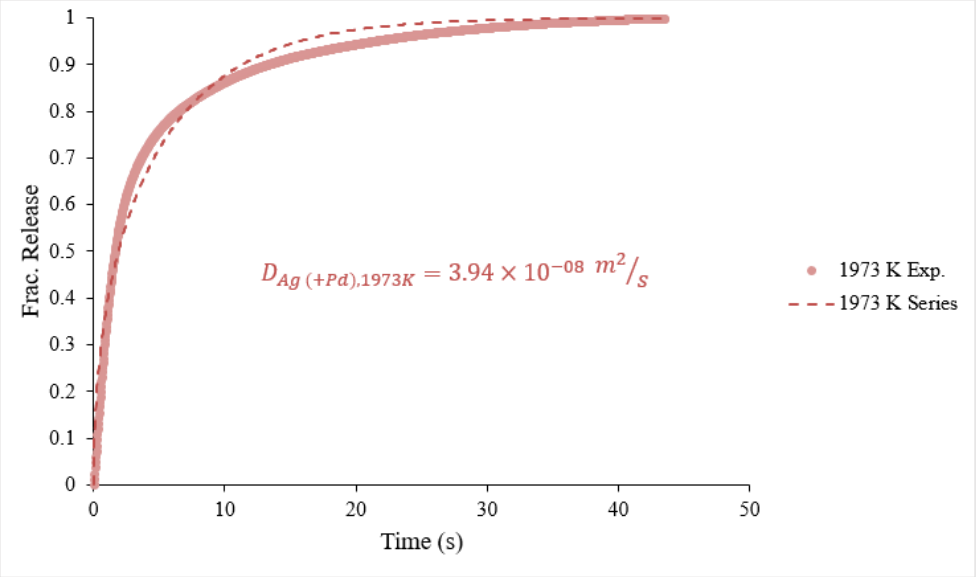

Figure A.14: Fractional release of Ag from spheres of IG-110 graphite loaded with Ag (+Pd) at 1973 K.

A.3. Pd (+Ag)

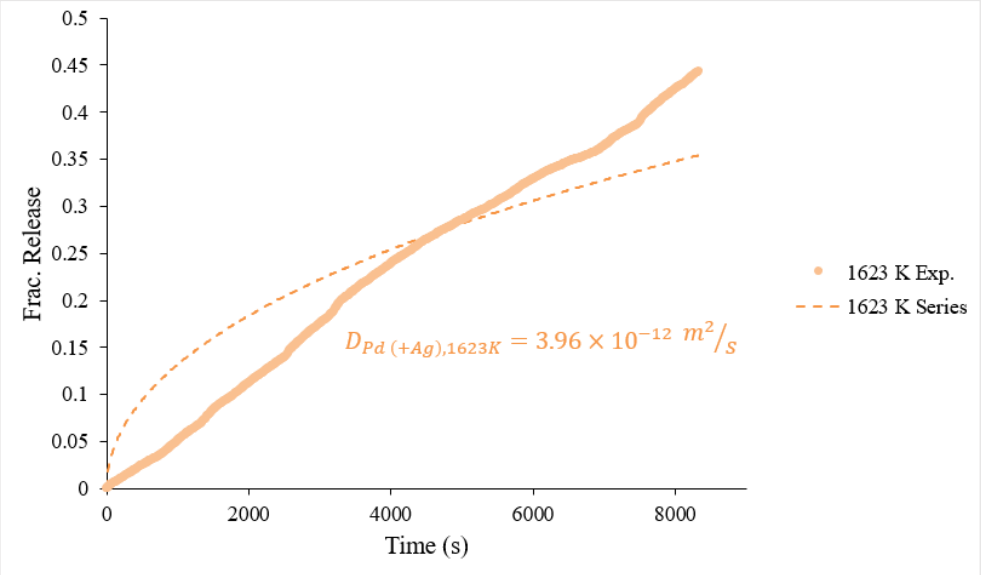

Figure A.15: Fractional release of Pd from spheres of IG-110 graphite loaded with Pd (+Ag) at 1623 K.

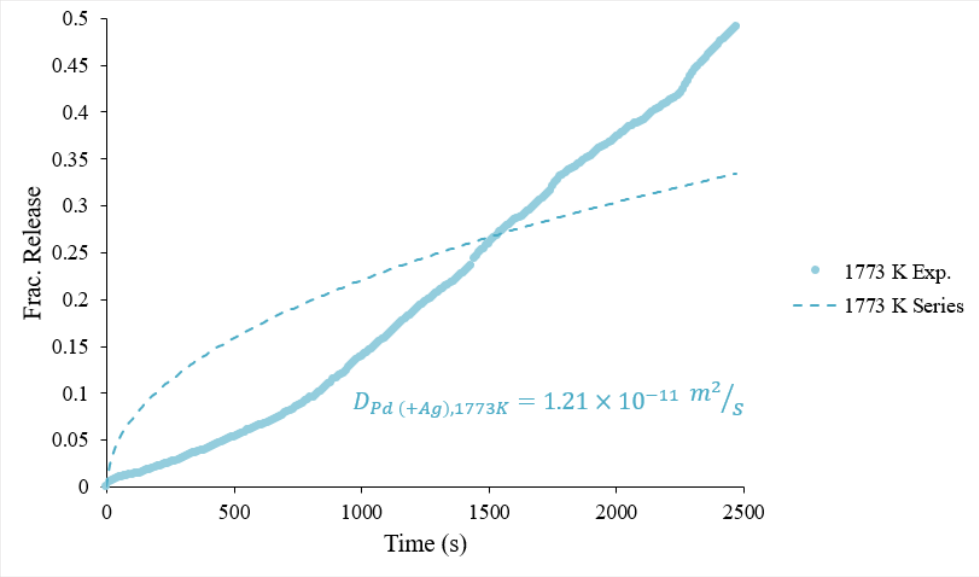

Figure A.16: Fractional release of Pd from spheres of IG-110 graphite loaded with Pd (+Ag) at 1623 K.

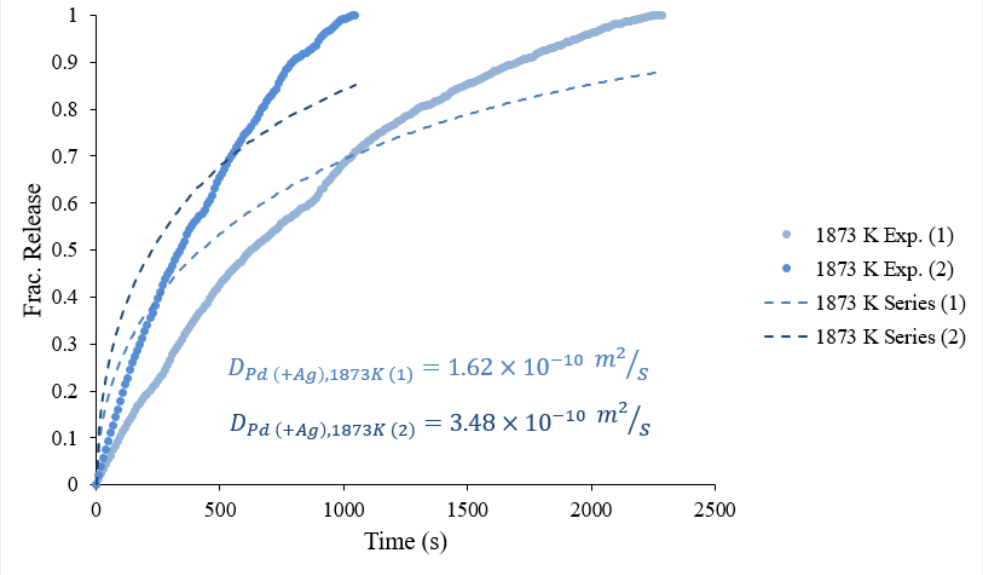

Figure A.17: Fractional release of Pd from spheres of IG-110 graphite loaded with Pd (+Ag) at 1873 K.

Table A.1: Initial and final masses of Ag and Pd and experimental temperatures.

Tested Diffusant(s)	Initial Mass (μg)		Final Mass (μg)		Temperature (K)	Diffusion Coefficient (m^2/s)	
	Ag	Pd	Ag	Pd		Ag	Pd
Ag	0.85	N/A	0.55	N/A	1073	4.01×10^{-12}	N/A
Ag	0.92	N/A	0.61	N/A	1073	3.34×10^{-12}	N/A
Ag	1.02	N/A	0.70	N/A	1073	3.14×10^{-12}	N/A
Ag	0.87	N/A	0.00	N/A	1223	9.48×10^{-11}	N/A
Ag	1.33	N/A	0.00	N/A	1223	8.75×10^{-11}	N/A
Ag	1.09	N/A	0.00	N/A	1223	6.70×10^{-11}	N/A
Ag	0.84	N/A	0.00	N/A	1373	6.85×10^{-10}	N/A
Ag	0.80	N/A	0.00	N/A	1373	6.31×10^{-10}	N/A
Ag	1.52	N/A	0.00	N/A	1373	8.13×10^{-10}	N/A
Ag	1.11	N/A	0.00	N/A	1523	7.16×10^{-9}	N/A
Ag	1.08	N/A	0.00	N/A	1523	6.07×10^{-9}	N/A
Ag	1.42	N/A	0.00	N/A	1523	5.08×10^{-9}	N/A
Ag	0.92	N/A	0.00	N/A	1673	2.16×10^{-8}	N/A
Ag	0.89	N/A	0.00	N/A	1673	3.98×10^{-8}	N/A
Ag	1.25	N/A	0.00	N/A	1673	5.43×10^{-9}	N/A
Ag	1.30	N/A	0.00	N/A	1673	5.47×10^{-9}	N/A
Ag	1.26	N/A	0.00	N/A	1673	3.63×10^{-9}	N/A
Ag	0.92	N/A	0.00	N/A	1773	1.04×10^{-8}	N/A
Ag	0.62	N/A	0.00	N/A	1773	1.77×10^{-8}	N/A
Ag	1.42	N/A	0.00	N/A	1773	1.05×10^{-8}	N/A
Ag	0.70	N/A	0.00	N/A	1873	3.91×10^{-8}	N/A
Ag	0.96	N/A	0.00	N/A	1873	2.28×10^{-8}	N/A
Ag	0.12	N/A	0.00	N/A	1873	2.04×10^{-8}	N/A
Ag	0.92	N/A	0.00	N/A	1973	3.94×10^{-8}	N/A
Ag	0.78	N/A	0.00	N/A	1973	4.16×10^{-8}	N/A
Ag	0.86	N/A	0.00	N/A	1973	2.83×10^{-8}	N/A
Ag + Pd	0.61	1.08	0.57	1.02	1073	1.81×10^{-13}	N/A
Ag + Pd	0.45	1.16	0.00	1.02	1223	1.68×10^{-10}	N/A
Ag + Pd	0.61	0.83	0.00	0.88	1373	2.17×10^{-9}	N/A
Ag + Pd	0.46	1.06	0.00	0.90	1523	6.56×10^{-9}	8.36×10^{-13}
Ag + Pd	0.47	1.00	0.00	0.54	1623	1.56×10^{-8}	3.96×10^{-12}
Ag + Pd	0.42	0.94	0.00	0.58	1673	2.09×10^{-8}	3.64×10^{-12}
Ag + Pd	0.57	1.13	0.00	0.28	1773	2.36×10^{-8}	1.21×10^{-11}
Ag + Pd	0.47	0.73	0.00	0.00	1873	1.78×10^{-8}	1.62×10^{-10}
Ag + Pd	0.66	1.14	0.00	0.00	1873	2.18×10^{-8}	3.48×10^{-10}
Ag + Pd	0.73	0.91	0.00	0.00	1973	3.94×10^{-8}	5.18×10^{-10}
Pd	N/A	1.38	N/A	1.31	1623	N/A	N/A
Pd	N/A	1.32	N/A	0.38	1673	N/A	4.10×10^{-13}
Pd	N/A	1.33	N/A	0.00	1973	N/A	N/A

APPENDIX B:

SUPPLEMENTARY INFORMATION FOR CHAPTER 6

B.1. Set B

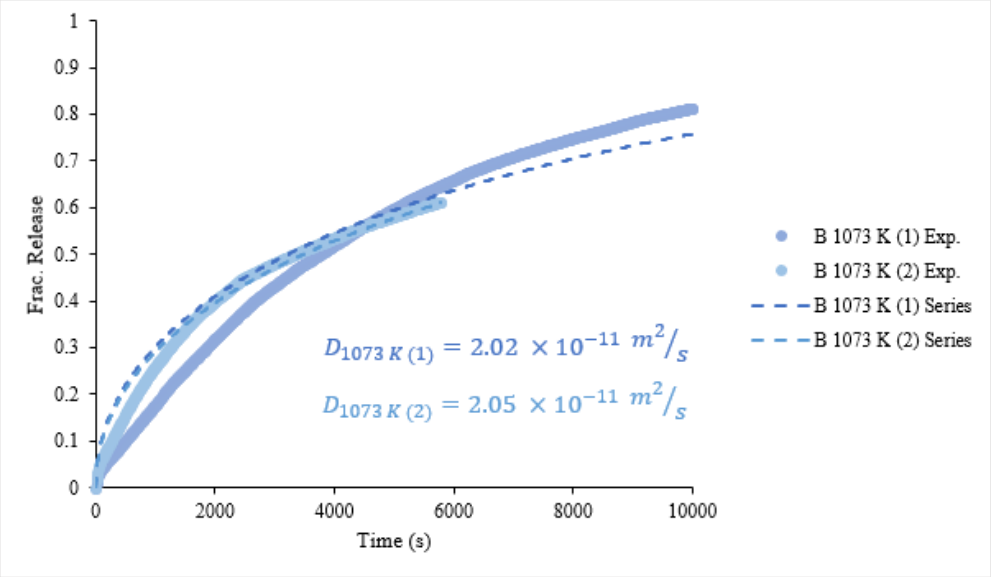

Figure B.1: Fractional release of Cs at 1073 K from unoxidized IG-110 graphite loaded with ~276 $\mu g_{Cs}/g_{graphite}$.

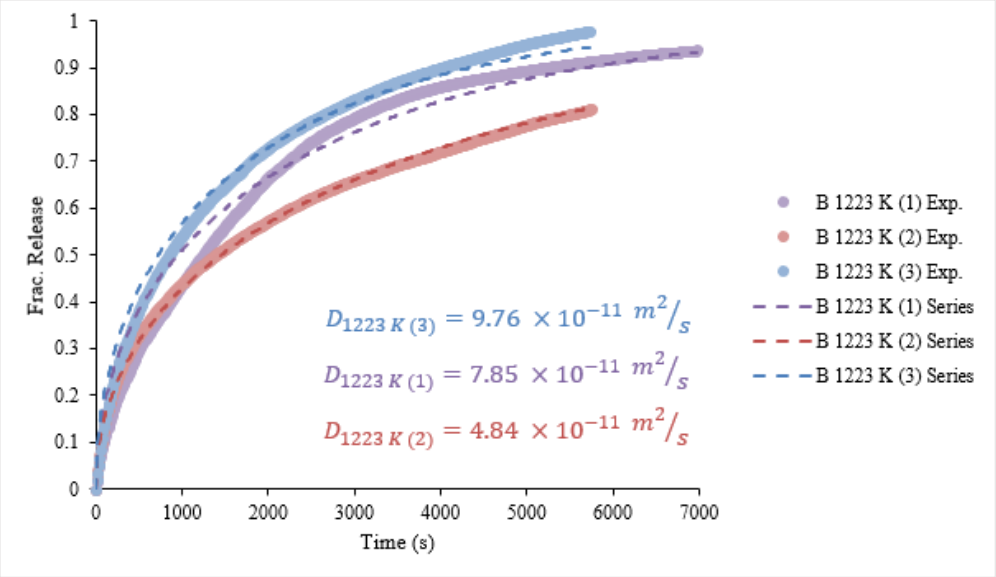

Figure B.2: Fractional release of Cs at 1223 K from unoxidized IG-110 graphite loaded with ~276 $\mu g_{Cs}/g_{graphite}$.

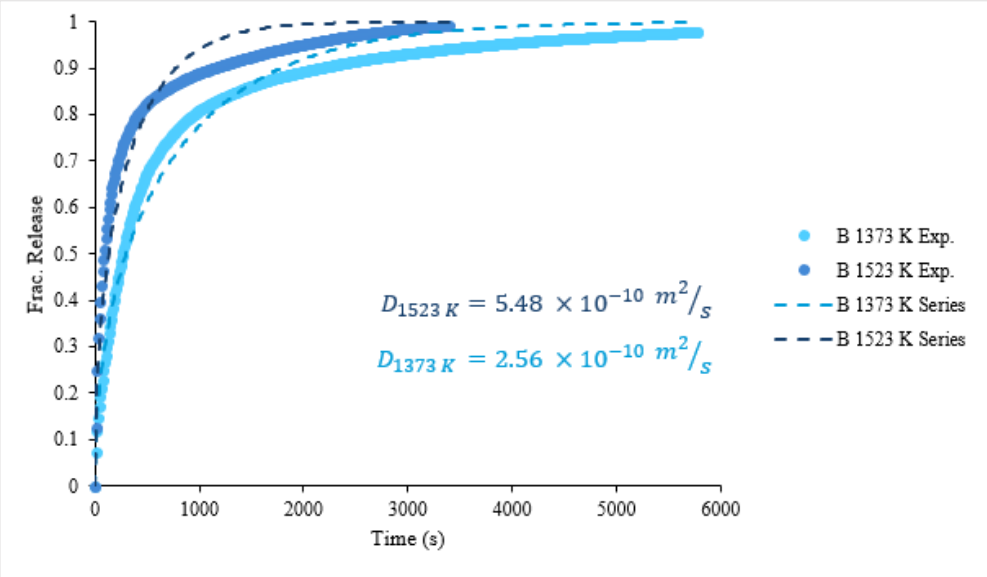

Figure B.3: Fractional release of Cs at 1373 K and 1523 K from unoxidized IG-110 graphite loaded with ~276 $\mu g_{Cs}/g_{graphite}$.

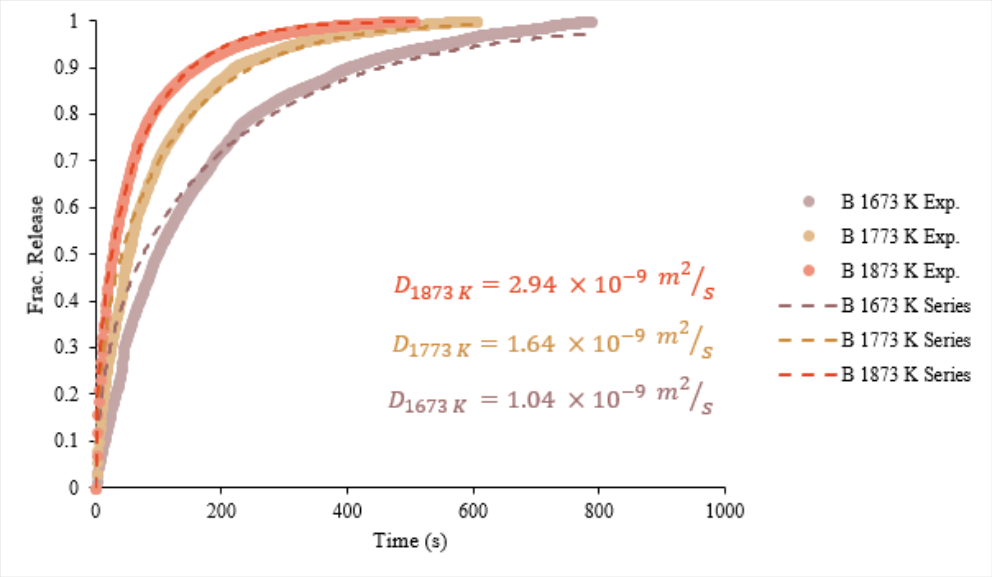

Figure B.4: Fractional release of Cs at 1673K, 1773 K, and 1873 K from unoxidized IG-110 graphite loaded with ~276 $\mu g_{Cs}/g_{graphite}$.

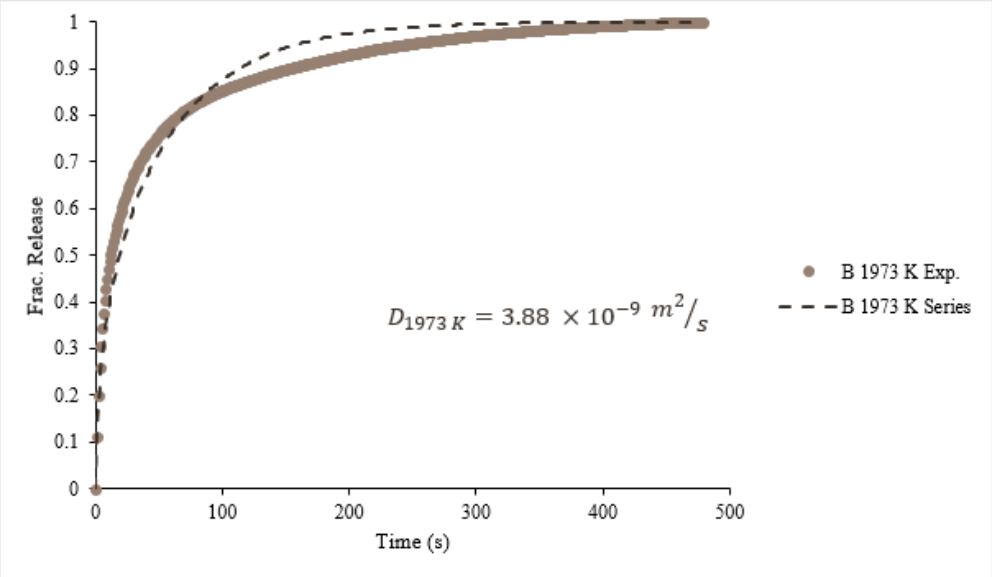

Figure B.5: Fractional release of Cs at 1973 K from unoxidized IG-110 graphite loaded with ~276 $\mu g_{Cs}/g_{graphite}$.

B.2. Set C

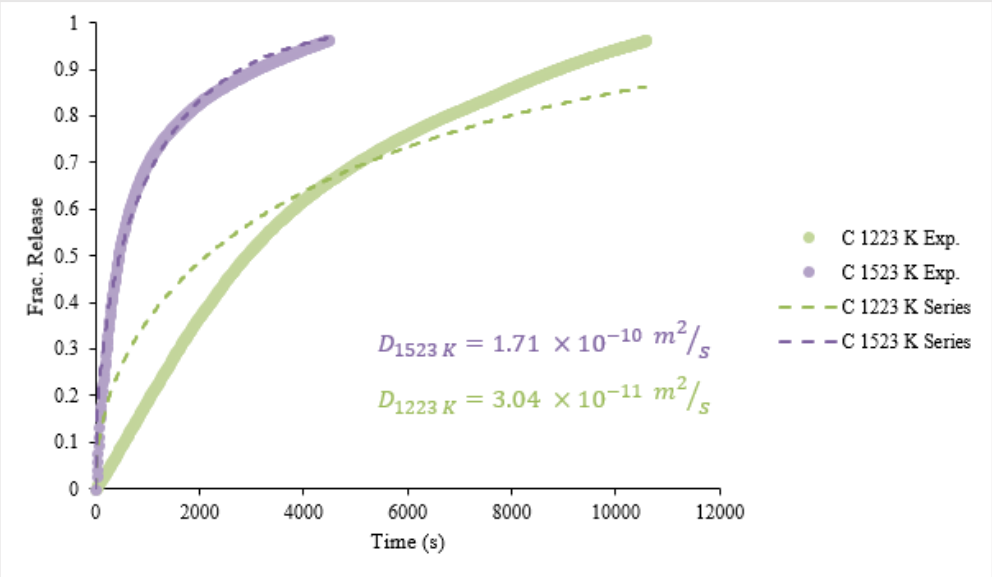

Figure B.6: Fractional release of Cs at 1223 K and 1523 K from unoxidized IG-110 graphite loaded with ~34 $\mu g_{Cs}/g_{graphite}$.

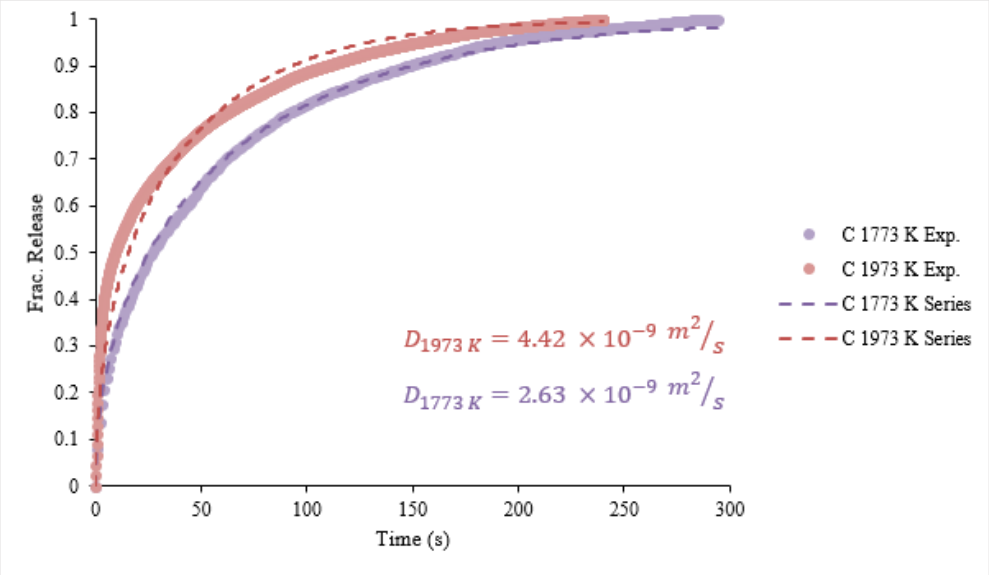

Figure B.7: Fractional release of Cs at 1773 K and 1973 K from unoxidized IG-110 graphite loaded with ~34 $\mu g_{Cs}/g_{graphite}$.

B.3. Set ox30

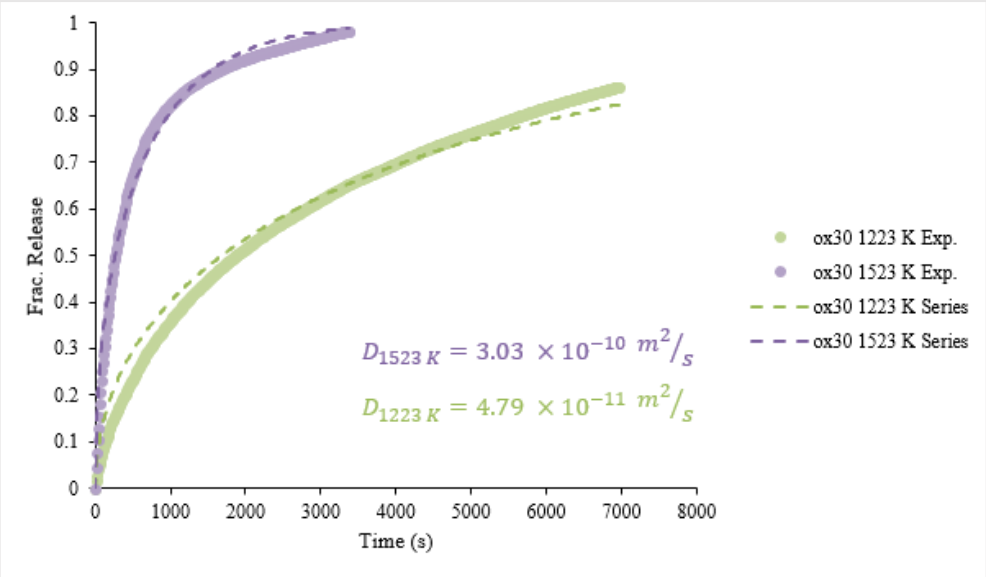

Figure B.8: Fractional release of Cs at 1223 K and 1523 K from 30-minute oxidized IG-110 graphite loaded with ~141 $\mu g_{Cs}/g_{graphite}$.

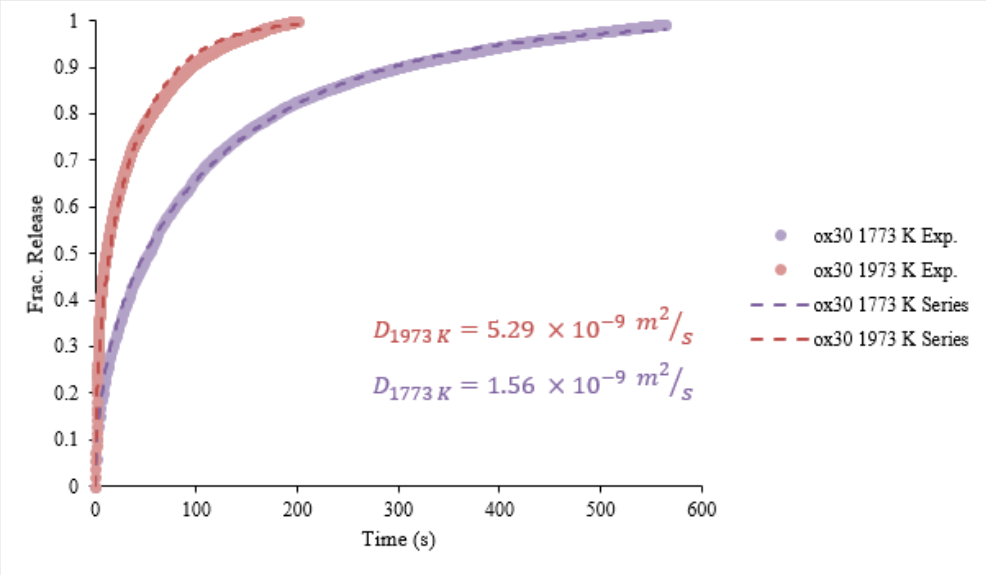

Figure B.9: Fractional release of Cs at 1773 K and 1973 K from 30-minute oxidized IG-110 graphite loaded with ~141 $\mu g_{Cs}/g_{graphite}$.

B.4. Set ox30 control

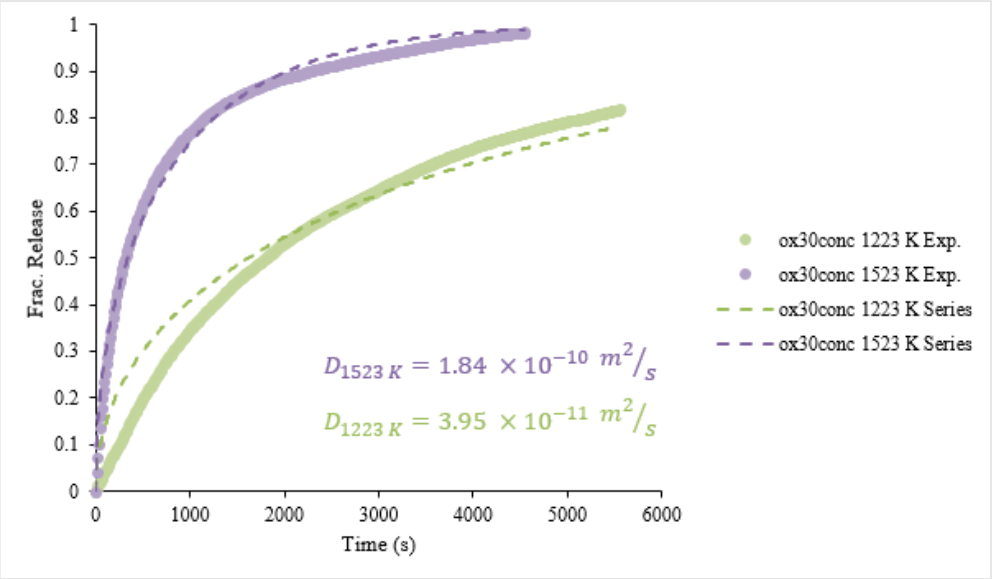

Figure B.10: Fractional release of Cs at 1223 K and 1523 K from unoxidized IG-110 graphite loaded with ~163 $\mu g_{Cs}/g_{graphite}$.

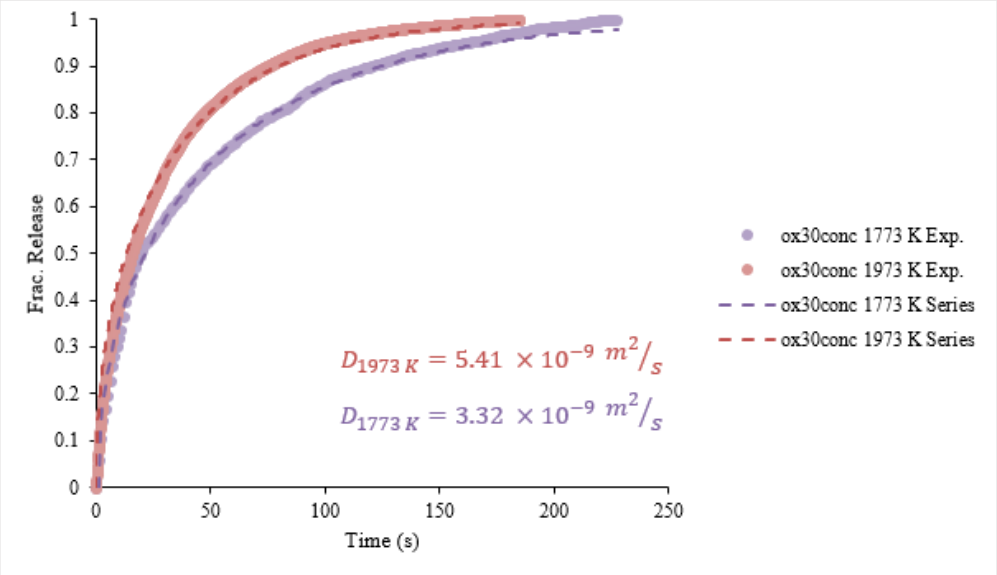

Figure B.11: Fractional release of Cs at 1773 K and 1973 K from unoxidized IG-110 graphite loaded with ~163 $\mu g_{Cs}/g_{graphite}$.

B.5. Set ox60

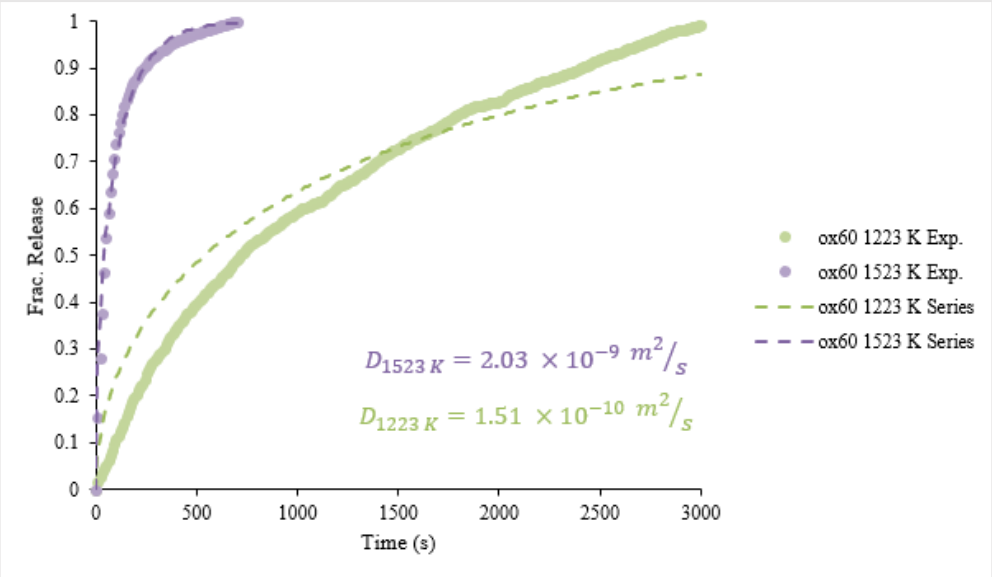

Figure B.12: Fractional release of Cs at 1223 K and 1523 K from 60-minute oxidized IG-110 graphite loaded with ~57 $\mu g_{Cs}/g_{graphite}$.

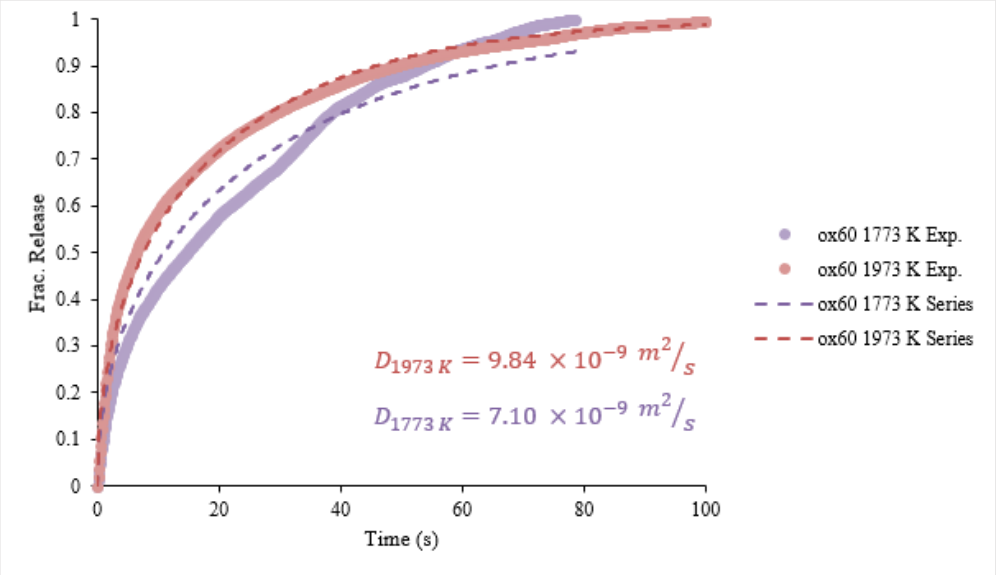

Figure B.13: Fractional release of Cs at 1773 K and 1973 K from 60-minute oxidized IG-110 graphite loaded with ~57 $\mu g_{Cs}/g_{graphite}$.

B.6. Set ox60 control

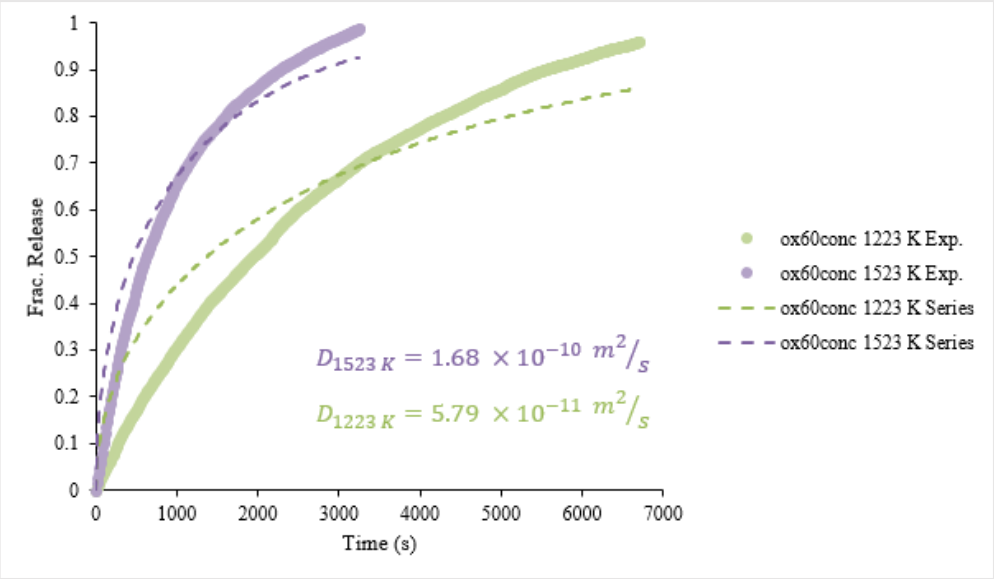

Figure B.14: Fractional release of Cs at 1223 K and 1523 K from unoxidized IG-110 graphite loaded with ~49 $\mu g_{Cs}/g_{graphite}$.

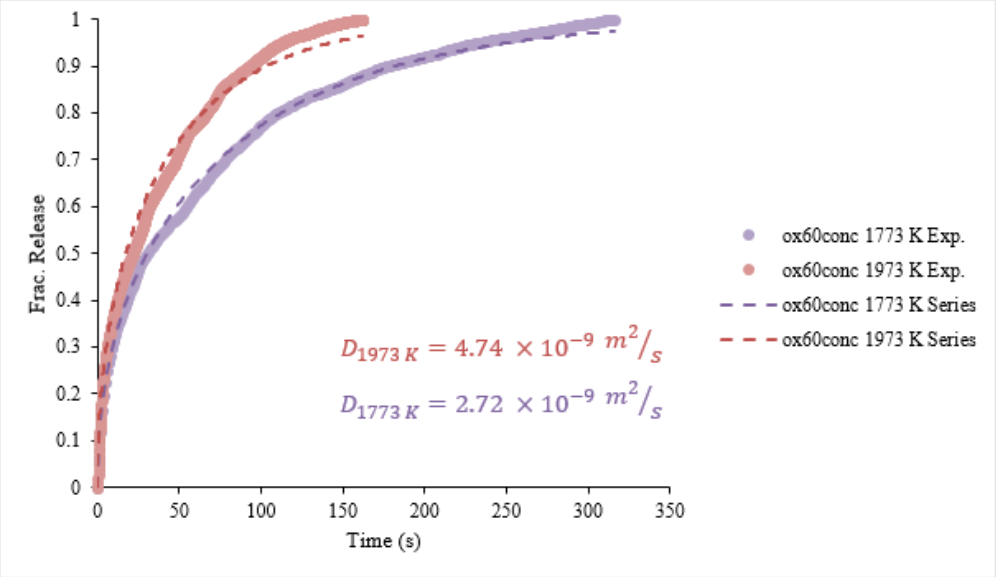

Figure B.15: Fractional release of Cs at 1773 K and 1973 K from unoxidized IG-110 graphite loaded with ~49 $\mu g_{Cs}/g_{graphite}$.

APPENDIX C:
COMPUTATION OF HEAT TRANSFER IN THE DIFFUSION CELL

A simple model for multi-physics simulation was used to determine any cooling effects from the flowing helium gas into the diffusion cell assembly. A conjugate heat transfer model with radiative heat transfer was implemented in COMSOL Multiphysics using Heat Transfer in Solids and Fluids, Laminar Flow, and Surface to Surface Radiation physics modules. Figure C.1 shows the SiC diffusion cell assembly and a representation of the furnace chamber. Information on the size and position of the heating elements could not be obtained for the simulation. Tables C.1 and C.2 provide the selected physics on the domains and boundaries, respectively, for each COMSOL physics module. Material data commonly available to the COMSOL program were used. Thus, AISI 4340 was chosen for the endcap instead of setting up data for stainless steel.

The model assumes the inserted portion of the diffusion cell assembly is heated in an air enclosure with fixed temperature walls. The size of the chamber is 0.2 m × 0.2 m × 0.2 m. The diffusion cell assembly portion outside the chamber was allowed to cool with natural convection and radiant energy. For natural convection, the heat transfer coefficient was 5 $W/(m^2 K^1)$. The helium flow from the spark generator was split between the diffusion cell assembly and HEPA filter, such that helium flow into the diffusion cell is 1 L/min. The Reynolds number at the inlet was estimated to be about 50, where the gas is at ambient temperature (293 K), and the kinematic viscosity is at its lowest. The Reynolds number will decrease throughout the diffusion cell, ensuring laminar flow. At the current gas density, no slip was assumed at the Wall boundary

conditions for the Laminar flow. All fluid walls were also gray diffusive surfaces for the Surface to Surface radiation, as seen in Table C.2. Chamber wall emissivity was chosen to be 0.8. The remaining material properties were from COMSOL's material library.

The temperature distribution around the graphite sphere would be due to the furnace design and heat losses through the port at the top of the furnace for the diffusion cell assembly. The magnitude of the linear flow velocity is given in Fig. C.2. The helium flow is relatively slow in the annular region of the assembly compared to the flow exiting through the inner SiC tube. The valve at the top of the diffusion cell assembly would create a higher resistance to the flow than in the model. The temperature distribution is given in Figs. C.3 and C.4. The model shows that the sphere is approximately 48 K lower than the chamber walls at 1973 K. However, the model does not account for the heat exchange between the SiC tube assembly and the insulation or the fact that the thermocouple that regulates the oven temperature is 2.5 cm from the sample location in the center of the furnace chamber. The model shows the temperature of the sphere to be 40 K lower than the chamber walls at 1823 K, which is 21 degrees below the boiling point of Eu metal. With the model assumptions, no cooling occurs until outside of the chamber. While fixed wall temperatures are not realistic, the ST-1700-888 is heavily insulted at the walls and door. The model confirms that the sample temperature is not significantly cooled during the experiment.

Table C.1: Domain materials and physics for COMSOL model.

Domain	**Material**	**Physics**		
		Heat Transfer in Solids and Fluids	Laminar Flow	Surface to Surface Radiation
SiC Tubes and Nozzle	Silicon Carbide	Solid	N/A	Opaque
Endcap	Steel AISI 4340	Solid	N/A	Opaque
Graphite Sphere	Graphite	Solid	N/A	Opaque
Helium	Helium	Fluid	Fluid	Transparent
Air	Air	Fluid	Fluid	Transparent

Table C.2: Boundary conditions for various surfaces for each physics module used in the model.

Boundary	**Physics**		
	Heat Transfer in Solids and Fluids	Laminar Flow	Surface-to-Surface Radiation
Endcap			
Exterior	Surface-Ambient Radiation Heat Flux	N/A	N/A
Bottom	N/A	Wall (No Slip)	Diffusive Surface
Outer Tube Exposed			
Exterior	Surface-Ambient Radiation Heat Flux	N/A	N/A
Interior	N/A	Wall (No Slip)	Diffusive Surface
Outer Tube Heated Zone	N/A	Wall (No Slip)	Diffusive Surface
Inner Tube/Nozzle	N/A	Wall (No Slip)	Diffusive Surface
Chamber Walls	Temperature	Wall (No Slip)	Diffusive Surface
Graphite Sphere	NA	Wall (No Slip)	Diffusive Surface
Helium			
Inlet	Inflow	Inlet	N/A
Outlet	Outflow	Outlet	N/A

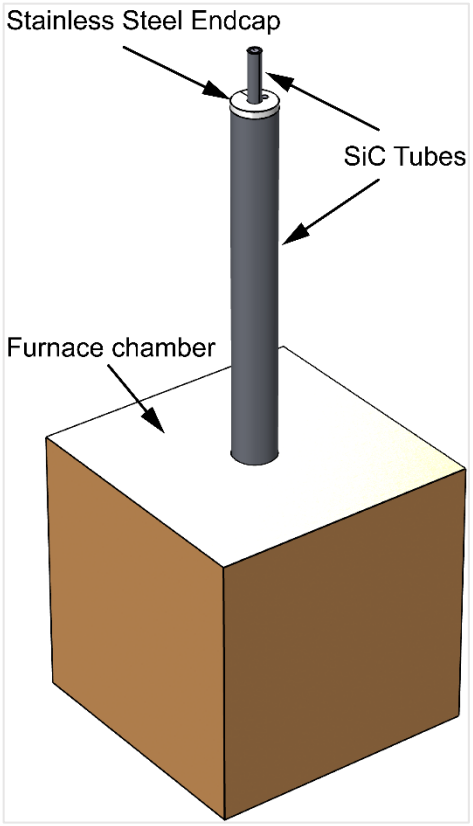

Figure C.1: Rendered geometry used for conjugate heat transfer with radiant heat transfer in COMSOL.

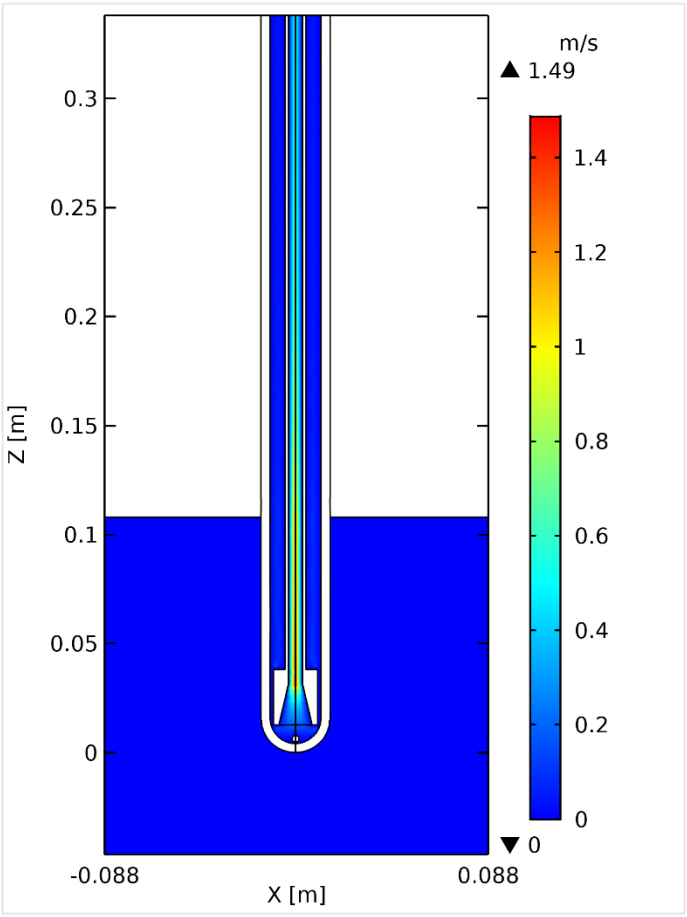

Figure C.2: Magnitude linear velocity of helium in the SiC diffusion in the XZ-plane at y=0.

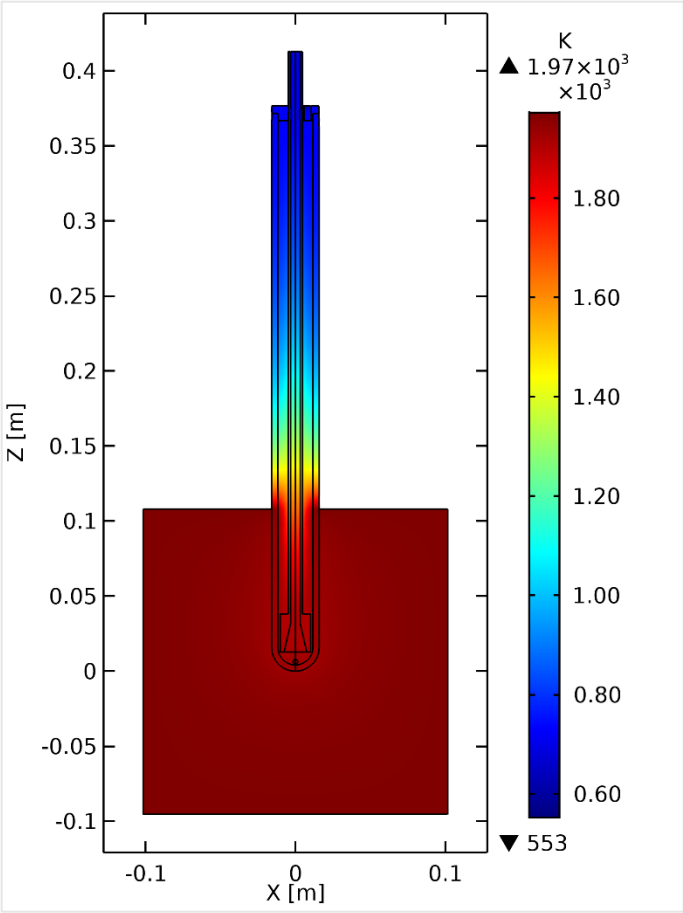

Figure C.3: Temperature distribution in the XZ-plane at y=0.

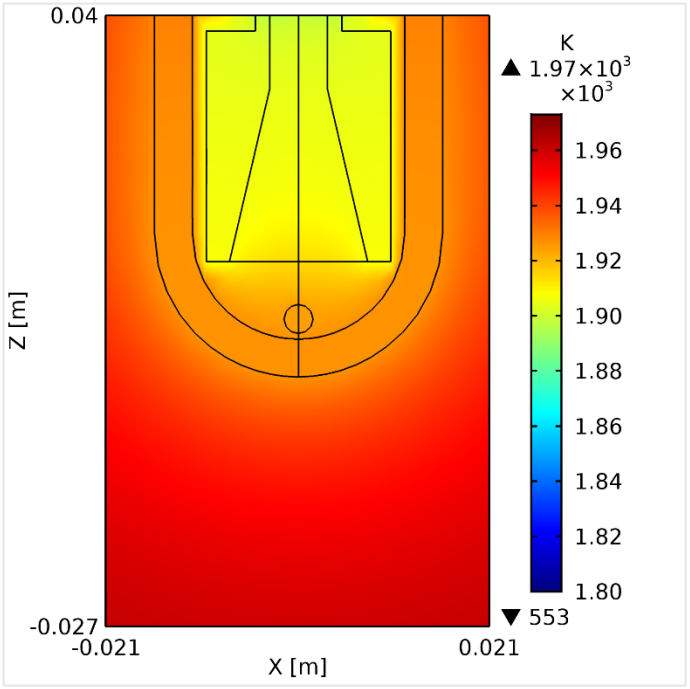

Figure C.4: Temperature distribution in the XZ-plane at y=0.

APPENDIX D:

SUPPLEMENTARY INFORMATION FOR CHAPTER 8

Table D.1: Complete list of wet-mass elemental concentrations in honey samples. Elements marked with an asterisk were measured using INAA.

µg/g	RF Rec	Spike Rec	Montana (N = 9)		North Dakota (N = 10)		South Dakota (N = 9)		LOD ICP-MS	LOD INAA
			Mean ± S.D.	Range	Mean ± S.D.	Range	Mean ± S.D.	Range		
B	-	96%	5.98 ± 1.29	4.59 – 8.18	9.88 ± 1.84	7.06 – 11.87	10.86 ± 1.81	8.71 – 13.64	0.25	-
Na	289%	100%	11.92 ± 5.04	6.63 – 20.21	14.15 ± 6.16	8.86 – 30.82	10.90 ± 1.25	9.25 – 13.64	0.050	0.060
Mg	-	100%	9.73 ± 1.34	7.89 – 11.56	14.51 ± 2.89	10.53 – 19.24	12.90 ± 2.91	9.56 – 16.49	0.039	-
Al	-	103%	0.12 ± 0.04	0.06 – 0.17	0.15 ± 0.08	0.08 – 0.30	0.11 ± 0.03	0.07 – 0.18	0.051	-
P	-	100%	35.45 ± 4.72	28.90 – 41.31	40.64 ± 6.68	30.60 – 52.12	40.39 ± 9.56	27.54 – 55.95	1.74	-
Cl*	-	-	99.47 ± 36.20	49.64 – 157.6	70.83 ± 15.55	41.59 – 93.16	73.65 ± 29.14	45.26 – 137.0	-	13.0
K	102%	98%	229.7 ± 69.1	130.6 – 355.2	196.7 ± 51.8	145.2 – 325.2	179.5 ± 37.3	135.1 – 243.6	0.53	-
Ca	97%	102%	43.04 ± 9.06	32.72 – 59.09	56.03 ± 9.71	44.55 – 71.32	64.91 ± 12.53	39.98 – 77.29	1.37	-
Mn	102%	102%	0.20 ± 0.07	0.14 – 0.37	0.37 ± 0.07	0.26 – 0.50	0.44 ± 0.07	0.34 – 0.55	0.0031	-
Fe	51%	99%	0.57 ± 0.28	0.38 – 1.28	1.13 ± 0.62	0.37 – 2.10	0.54 ± 0.20	0.34 – 0.97	0.038	0.300
Cu	94%	98%	0.09 ± 0.02	0.07 – 0.12	0.09 ± 0.02	0.07 – 0.12	0.11 ± 0.03	0.07 – 0.17	0.00086	-
Zn	100%	101%	0.27 ± 0.05	0.23 – 0.36	0.38 ± 0.19	0.22 – 0.74	0.28 ± 0.06	0.19 – 0.36	0.032	0.040
Br*	-	-	0.15 ± 0.06	0.08 – 0.28	0.17 ± 0.06	0.08 – 0.30	0.27 ± 0.25	0.12 – 0.86	-	0.020
Rb	113%	107%	0.29 ± 0.13	0.12 – 0.52	0.23 ± 0.06	0.16 – 0.35	0.22 ± 0.08	0.14 – 0.37	0.00057	-
Sr	-	99%	0.11 ± 0.04	0.05 – 0.17	0.15 ± 0.08	0.06 – 0.27	0.20 ± 0.08	0.06 – 0.27	0.0047	-

ng/g	RF Rec	Spike Rec	Mean ± S.D.	Range	Mean ± S.D.	Range	Mean ± S.D.	Range	LOD ICP-MS	LOD INAA
Li	-	-	-	<LOD – 28.7	32.89 ± 15.41	14.8 – 57.5	-	<LOD – 45.7	12.3	-
Be	-	-	-	<LOD	-	<LOD	-	<LOD	0.64	-
Sc*	-	-	0.15 ± 0.05	0.06 – 0.24	0.11 ± 0.05	0.05 – 0.19	0.09 ± 0.03	0.05 – 0.12	-	0.04
Ti	-	-	-	<LOD	-	<LOD	-	<LOD	11.8	-
V	-	-	-	<LOD – 0.53	-	<LOD – 1.23	-	<LOD – 0.93	0.43	-
Cr	-	-	9.00 ± 2.29	5.39 – 13.72	11.60 ± 2.70	8.67 – 16.01	11.01 ± 1.23	8.80 – 12.97	4.10	5.00
Co	67%	98%	2.37 ± 0.78	1.41 – 3.58	5.03 ± 1.52	2.90 – 7.72	6.20 ± 2.49	4.20 – 12.40	0.25	-
Ni	-	-	8.75 ± 4.43	4.29 – 16.77	16.30 ± 7.04	9.53 – 33.75	14.48 ± 2.16	11.64 – 17.59	1.15	-
Ga	-	-	-	<LOD	-	<LOD	-	<LOD	0.68	-
As	96%	-	-	<LOD – 3.11	-	<LOD – 2.18	-	<LOD – 1.94	1.52	-
Se*	0%	-	-	<LOD – 6.86	-	<LOD – 15.79	-	<LOD – 68.99	162.6	5.00
Y	-	-	-	<LOD – 0.25	-	<LOD – 2.01	0.21 ± 0.05	0.13 – 0.27	0.11	-
Mo	105%	112%	5.26 ± 2.09	2.02 – 7.29	4.59 ± 2.09	2.10 – 7.47	4.95 ± 2.00	1.92 – 8.03	1.00	-
Ru	-	-	-	<LOD	-	<LOD	-	<LOD	0.35	-
Pd	-	-	-	<LOD	-	<LOD	-	<LOD	0.30	-
Ag	-	-	-	<LOD – 0.24	-	<LOD – 0.73	-	<LOD	0.40	-
Cd	97%	-	-	<LOD – 0.52	-	<LOD – 0.50	-	<LOD – 0.47	0.40	-

Sn	-	-	2.89 ± 0.94	1.41 – 3.99	2.65 ± 2.49	1.03 – 8.46	1.60 ± 0.58	0.97 – 2.96	0.57	-
Sb	-	-	-	<LOD – 0.45	0.59 ± 0.24	0.30 – 1.03	0.66 ± 0.52	0.31 – 1.99	0.29	-
Cs	-	110%	1.19 ± 1.08	0.22 – 3.71	0.45 ± 0.41	0.11 – 1.45	0.21 ± 0.09	0.11 – 0.35	0.10	-
Ba	-	106%	60.48 ± 13.74	32.60 – 72.55	70.18 ± 36.08	17.46 – 117.1	80.35 ± 33.24	17.95 – 109.8	1.21	-
La	-	-	0.17 ± 0.08	0.09 – 0.35	0.24 ± 0.10	0.11 – 0.42	0.24 ± 0.19	0.09 – 0.74	0.075	-
Ce	-	110%	0.31 ± 0.11	0.16 – 0.49	0.42 ± 0.19	0.21 – 0.83	0.32 ± 0.07	0.14 – 0.37	0.088	-
Pr	-	-	-	<LOD – 0.10	-	<LOD – 0.11	-	<LOD – 0.07	0.037	-
Nd	-	-	-	<LOD	-	<LOD	-	<LOD	0.40	-
Sm	-	-	-	<LOD	-	<LOD – 0.12	-	<LOD – 0.12	0.11	-
Eu	-	-	-	<LOD – 0.04	-	<LOD – 0.04	-	<LOD – 0.03	0.028	-
Gd	-	-	-	<LOD – 0.14	-	<LOD – 0.09	-	<LOD – 0.07	0.061	-
Tb	-	-	-	<LOD – 0.02	-	<LOD – 0.02	-	<LOD – 0.01	0.013	-
Dy	-	-	-	<LOD – 0.11	-	<LOD – 0.08	-	<LOD – 0.09	0.039	-
Ho	-	-	-	<LOD – 0.02	-	<LOD – 0.02	-	<LOD – 0.01	0.013	-
Er	-	-	-	<LOD – 0.04	-	0.02 – 0.05	-	<LOD – 0.06	0.019	-
Tm	-	-	-	<LOD – 0.01	-	<LOD – 0.01	-	<LOD – 0.01	0.0074	-
Yb	-	-	-	<LOD – 0.02	-	<LOD	-	<LOD	0.019	-
Lu	-	-	-	<LOD	-	<LOD – 0.02	-	<LOD – 0.09	0.011	-
Ir	-	-	-	<LOD	-	<LOD	-	<LOD	0.025	-
Pt	-	-	-	<LOD – 0.18	-	<LOD – 0.68	-	<LOD – 1.34	0.17	-
Hg*	-	-	-	<LOD	-	<LOD	-	<LOD	-	2.00
Tl	-	-	0.86 ± 0.63	0.20 – 2.05	1.98 ± 1.83	0.16 – 4.67	-	<LOD – 4.76	0.12	-
Pb	-	-	9.92 ± 15.92	2.45 – 52.07	4.80 ± 3.61	0.81 – 10.81	1.68 ± 0.96	0.58 – 3.37	0.46	-
Bi	-	-	-	<LOD	-	<LOD – 37.5	-	<LOD	0.23	-
Th	-	-	-	<LOD	-	<LOD	-	<LOD	0.38	-
U	-	-	0.09 ± 0.02	0.06 – 0.13	-	<LOD – 0.14	-	<LOD – 0.10	0.056	-

Table D.2: Full Pearson correlation matrix for elements listed in Table 8.2.

	B	Na	Mg	Al	P	Cl	K	Ca	Mn	Fe	Cu	Zn	Br	Rb	Sr	Co	Mo	Cs	Ba	Ce
B	1																			
Na	-0.091	1																		
Mg	0.462*	0.319	1																	
Al	-0.145	0.503**	0.222	1																
P	0.074	0.222	0.396*	0.345	1															
Cl	-0.554**	0.306	-0.048	0.006	0.418*	1														
K	-0.540**	0.297	0.015	0.219	0.604**	0.722**	1													
Ca	0.618**	0.314	0.158	-0.030	0.374	-0.023	-0.108	1												
Mn	0.729**	0.134	0.512**	-0.164	0.364	-0.218	-0.160	0.783**	1											
Fe	-0.033	0.514**	0.570**	0.529**	0.127	0.026	0.162	-0.206	-0.093	1										
Cu	0.192	0.107	0.080	0.121	0.654**	0.315	0.316	0.482**	0.313	-0.184	1									
Zn	-0.099	0.489**	0.280	0.650**	0.633**	0.212	0.489**	0.144	0.188	0.435*	0.303	1								
Br	0.110	0.000	0.542**	-0.014	0.685**	0.500**	0.439*	0.188	0.337	0.088	0.536**	0.253	1							
Rb	-0.518**	0.542**	0.199	0.122	0.420*	0.770**	0.804**	-0.029	-0.055	0.279	0.237	0.318	0.495**	1						
Sr	0.318	0.298	-0.152	-0.050	0.364	0.090	0.064	0.860**	0.603**	-0.369	0.468*	0.217	0.074	0.034	1					
Co	0.625**	0.207	0.672**	0.128	0.459*	-0.230	-0.077	0.532**	0.731**	0.204	0.319	0.213	0.358	-0.031	0.258	1				
Mo	0.249	-0.143	-0.215	-0.326	-0.345	-0.144	-0.238	0.047	-0.089	-0.307	0.088	-0.255	-0.243	-0.302	-0.084	-0.106	1			
Cs	-0.755**	0.366	-0.115	0.213	0.099	0.655**	0.754**	-0.408*	-0.475*	0.282	-0.132	0.293	0.149	0.798**	-0.252	-0.453*	-0.223	1		
Ba	0.077	0.078	-0.338	0.251	0.382*	0.067	0.121	0.577**	0.305	-0.374	0.357	0.425*	-0.028	-0.131	0.774**	0.053	-0.137	-0.127	1	
Ce	0.228	0.480**	0.126	0.699**	0.174	-0.232	-0.099	0.341	0.171	0.245	0.049	0.533**	-0.166	-0.143	0.327	0.153	-0.163	-0.051	0.513**	1

* Correlation is significant at the 0.05 level (2-tailed)
** Correlation is significant at the 0.01 level (2-tailed)

Table D.3: ICP-MS and INAA comparison.

µg/g		Montana (N = 9)		North Dakota (N = 10)		South Dakota (N = 9)		LOD
		Mean ± S.D.	Range	Mean ± S.D.	Range	Mean ± S.D.	Range	
Na	ICP-MS	11.92 ± 5.04	6.63 – 20.21	14.15 ± 6.16	8.86 – 30.82	10.90 ± 1.25	9.25 – 13.64	0.050
	INAA	11.47 ± 4.85	6.50 – 20.18	12.98 ± 5.20	8.19 – 26.76	10.18 ± 1.08	8.72 – 12.24	0.060
Fe	ICP-MS	0.57 ± 0.28	0.38 – 1.28	1.13 ± 0.62	0.37 – 2.10	0.54 ± 0.20	0.34 – 0.97	0.038
	INAA	1.48 ± 1.78	0.58 – 6.13	1.23 ± 0.66	0.43 – 2.53	0.71 ± 0.19	0.53 – 1.13	0.300
Zn	ICP-MS	0.27 ± 0.05	0.23 – 0.36	0.38 ± 0.19	0.22 – 0.74	0.28 ± 0.06	0.19 – 0.36	0.032
	INAA	0.26 ± 0.05	0.20 – 0.36	0.35 ± 0.18	0.19 – 0.74	0.26 ± 0.05	0.21 – 0.35	0.040

ng/g		Mean ± S.D.	Range	Mean ± S.D.	Range	Mean ± S.D.	Range	LOD
Cr	ICP-MS	9.00 ± 2.29	5.39 – 13.72	11.60 ± 2.70	8.67 – 16.01	11.01 ± 1.23	8.80 – 12.97	4.10
	INAA	12.85 ± 10.80	4.57 – 33.34	14.76 ± 4.59	6.93 – 21.60	21.59 ± 7.70	11.55 – 37.03	5.00

Table D.4: INAA Summary.

µg/g	Montana (N = 9)		North Dakota (N = 10)		South Dakota (N = 9)		LOD
	Mean ± S.D.	Range	Mean ± S.D.	Range	Mean ± S.D.	Range	
Na	11.47 ± 4.85	6.50 – 20.18	12.98 ± 5.20	8.19 – 26.76	10.18 ± 1.08	8.72 – 12.24	0.060
Cl	99.5 ± 36.2	49.6 – 157.6	70.8 ± 15.5	41.6 – 93.2	73.7 ± 29.1	45.3 – 137.0	13.0
Fe	1.48 ± 1.78	0.58 – 6.13	1.23 ± 0.66	0.43 – 2.53	0.71 ± 0.19	0.53 – 1.13	0.300
Zn	0.26 ± 0.05	0.20 – 0.36	0.35 ± 0.18	0.19 – 0.74	0.26 ± 0.05	0.21 – 0.35	0.040
Br	0.15 ± 0.06	0.08 – 0.28	0.17 ± 0.06	0.08 – 0.30	0.27 ± 0.25	0.12 – 0.87	0.020
ng/g	Mean ± S.D.	Range	Mean ± S.D.	Range	Mean ± S.D.	Range	LOD
Sc	0.15 ± 0.05	0.06 – 0.24	0.11 ± 0.05	0.05 – 0.19	0.09 ± 0.03	0.05 – 0.12	0.04
Cr	12.85 ± 10.80	4.57 – 33.34	14.76 ± 4.59	6.93 – 21.60	21.59 ± 7.70	11.55 – 37.03	5.00
Se	-	<LOD – 6.86	-	<LOD – 15.79	-	<LOD – 68.99	5.00
Hg	-	<LOD	-	<LOD	-	<LOD	2.00

VITA

Taylor Mae Weilert was born in 1995 in Panama City Beach, FL. She graduated from Troy University in Troy, AL in 2017 with a Bachelor of Science degree in Chemistry. She was accepted into the Ph. D. program at the University of Missouri – Columbia where she studied radiochemistry and analytical chemistry under the mentorship of Dr. John D. Brockman. She is expected to complete her degree in Summer 2022.